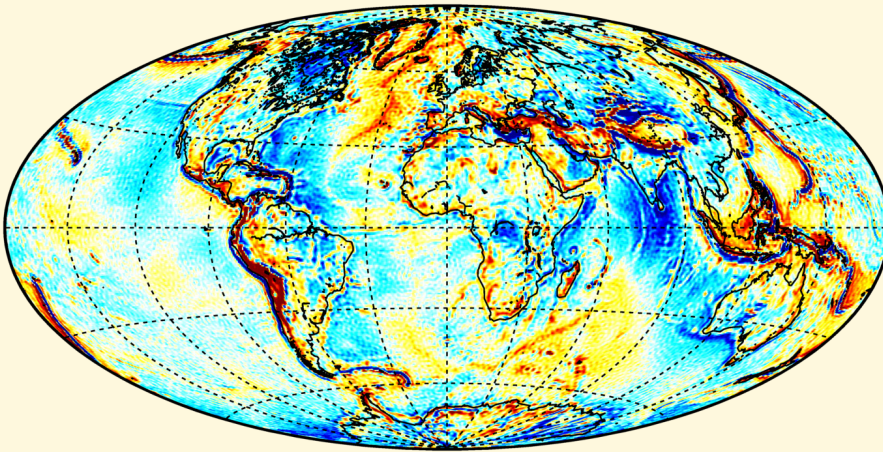


Modelling the Earth's static and time-varying gravity field using a combination of GRACE and GOCE data

Hassan Hashemi Farahani



Modelling the Earth's static and time-varying gravity field
using a combination of GRACE and GOCE data

Modelling the Earth's static and time-varying gravity field using a combination of GRACE and GOCE data

Hassan Hashemi Farahani

Publications on Geodesy 83

NCG Nederlandse Commissie voor Geodesie Netherlands Geodetic Commission

Delft, December 2013

Modelling the Earth's static and time-varying gravity field using a combination of GRACE and GOCE data

Hassan Hashemi Farahani
Publications on Geodesy 83
ISBN: 978 90 6132 345 7
ISSN 0165 1706

Published by: NCG, Nederlandse Commissie voor Geodesie, Netherlands Geodetic Commission, Delft, the Netherlands

Cover image: Gravity anomalies from DGM-1S (– 80 till 80 mGal).

Copyright ©2013 by H. H. Farahani

All rights reserved. No part of the material protected by this copyright notice may be reproduced or utilized in any form or by any means, electronic or mechanical, including photocopying, recording or by any information storage and retrieval system, without written permission of the author.

NCG, Nederlandse Commissie voor Geodesie, Netherlands Geodetic Commission
P.O. Box 5030, 2600 GA Delft, the Netherlands
T: + 31 (0)15 278 21 03
E: info@ncg.knaw.nl
W: www.ncg.knaw.nl

The NCG, Nederlandse Commissie voor Geodesie, Netherlands Geodetic Commission is part of the Royal Netherlands Academy of Arts and Sciences (KNAW).

Summary

Modelling the Earth’s static and time-varying gravity field using a combination of GRACE and GOCE data The main focus of the thesis is modelling the static and time-varying parts of the Earth’s gravity field at the global scale based on data acquired by the Gravity Recovery And Climate Experiment (GRACE) and Gravity field and steady-state Ocean Circulation Explorer (GOCE). In addition, a new methodology is proposed to validate global static gravity field models. Furthermore, the added value of GOCE data to the static and time-varying gravity field retrieval is assessed. Finally, low-frequency noise in GRACE observables derived from its K-band ranging (KBR) data is studied and a new way to cope with it is proposed.

GRACE/GOCE global static gravity field modelling: DGM-1S A new global static gravity field model entitled DGM-1S (Delft Gravity Model, release 1, Satellite-only) is computed by a statistically optimal combination of GRACE and GOCE data. The model is based on seven years of GRACE KBR data, four years of GRACE satellites’ kinematic orbits, 14 months of GOCE kinematic orbits, and 10 months of GOCE Satellite Gravity Gradiometry (SGG) data. Kinematic orbit and KBR data are processed with a variant of the acceleration approach, in which these data are respectively transformed into “three-dimensional (3-D) average acceleration vectors” and “range combinations” (\approx inter-satellite accelerations) with a three-point differentiation. Gravity gradients are processed in the instrument frame. Stochastic models of data noise are built with an auto-regressive moving-average (ARMA) process. The usage of ARMA models ensures that (i) coloured noise in data is appropriately dealt with; and (ii) data are combined in a statistically optimal manner. DGM-1S is compiled up to spherical harmonic degree 250 with a Kaula regularization applied above degree 179. It is found that (a) the usage of GOCE kinematic orbits may not lead to an improvement of a static gravity field model if GRACE data and GOCE gravity gradients are already incorporated; and (b) GOCE gravity gradients manifest their contribution in a combined GRACE/GOCE model above degree 150. For the purpose of an assessment, the DGM-1S, GOCO01S, EIGEN-6S (only its static part), and GOCO02S geoid models are used to compute the corresponding oceanic mean dynamic topography models by subtracting the DNSC08 mean sea surface model. The results are confronted with the state-of-the-art CNES-CLS09 mean dynamic topography model, which shows the best agreement for DGM-1S. Furthermore, the test suggests that the GRACE/GOCE satellite-only models are

influenced by a relatively strong high-frequency noise above degree 200. In addition, the test indicates that problems still seem to exist in satellite-only GRACE/GOCE models over the Pacific ocean, where considerable deviations of these models from EGM2008 are detected.

Validating global static gravity field models: quantifying GOCE mission’s added value and inspecting data combination optimality in models produced with surface data The ability of satellite gravimetry data to validate global static gravity field models is studied. Two types of control data are considered: GRACE KBR data and GOCE gravity gradients. The validation is based on an analysis of misfits computed as differences between data observed and those computed with a force model that includes, in particular, a static gravity field model to be assessed. Only “independent” data are used in the model validation, i.e., those that were not used in the production of models under assessment. The methodology is applied to eight models: EGM2008 (truncated at degree 250), EIGEN-6C (only its static part and truncated at degree 250), two GRACE-only models (ITG-Grace03 and ITG-Grace2010s), and four GRACE/GOCE models: GOCO01S, EIGEN-6S (only its static part), GOCO02S, and DGM-1S. The validation shows that independent data of both types allow a difference in performance of the models to be observed, despite the fact that the duration of these data is much shorter than that of data used to produce those models. The KBR and SGG control data demonstrate relatively high inaccuracies of EGM2008 in 5 – 22 mHz (27 – 120 cycles-per-revolution, cpr) and 10 – 28 mHz (54 – 150 cpr) frequency ranges, respectively. The latter data also reveal inaccuracies of ITG-Grace2010s in 25 – 37 mHz (135 – 200 cpr) frequency range. The validation in the spatial domain shows that EGM2008 performs weaker than the GRACE/GOCE models. Considering root mean square (RMS) misfits related to the zz gravity gradient component (with z being the nadir axis of the instrument frame), the performance difference in the continental areas poorly covered by terrestrial gravimetry data (Himalayas, South America, and Equatorial Africa) is 76 – 83 %. This difference is explained mostly by a loss of information content of ITG-Grace03 when it was combined with terrestrial gravimetry/satellite altimetry data to produce EGM2008. Furthermore, the revealed performance differences are 4 – 16 % in the continental areas well covered by those data (Australia, North Eurasia, and North America) and 11 % in the world’s oceans. These differences are related to the GOCE mission’s added value to the static gravity field retrieval. It is shown that EIGEN-6C also suffers from a loss of information during data combination, but in a much less pronounced manner. In South America, for instance, this model is found to perform poorer than its satellite-only counterpart, i.e., EIGEN-6S, by only

12 %. The GRACE/GOCE models show in the poorly surveyed continental areas a higher accuracy than ITG-Grace2010s: by 23 – 36 %, which is attributed to the GOCE mission’s added value. The quantified added value is shown to be almost entirely related to the coefficients below degree 200. DGM-1S and GOCO02S show an almost similar performance against GOCE control gravity gradients. Nevertheless, the former model shows a slightly better agreement with KBR control data. Both models agree with control data of both types better than EIGEN-6S.

Assessing GOCE mission’s added value to time-varying gravity field modelling Temporal gravity field variations recovered from KBR data suffer, among others, from a limited spatial resolution and a relatively low accuracy of the East-West changes. I investigate whether a retrieval of these variations can be improved by incorporating GOCE data. To that end, I compare monthly solutions up to degree 120 computed (i) from KBR data alone and (ii) using a statistically optimal combination of KBR data with GOCE kinematic orbit and gravity gradients. The impact of GOCE data is analysed in the context of unconstrained solutions and after an optimal anisotropic filtering. This impact in these two cases is found to be radically different. In the case of unconstrained solutions, a usage of GOCE data allows the noise in these solutions to be reduced by 1 – 2 orders of magnitude. I demonstrate, however, that this reduction is a stabilization effect and is not driven by the information content in GOCE data. In the case of the filtered solutions, the impact stays, in average, at sub-millimeter level in terms of equivalent water heights. This is below the GRACE noise level. The peak impacts reach about 1 cm. This holds true for the combined impact of GOCE kinematic orbit data and gravity gradients as well as for the impact of these data types individually. Relatively, the peak impacts do not exceed 5 – 7 % of the signal amplitude, because they always occur at locations where the time-varying gravity field signal is strong. Nevertheless, I refrain from concluding that added value of GOCE data to the retrieval of temporal gravity changes is always negligible. A number of scenarios are discussed, in which the impact of GOCE data may exceed the level quantified in the study presented.

GRACE global time-varying gravity field modelling: DMT-2 The Delft Mass Transport model, release 2 (DMT-2), similar to its predecessor, i.e., DMT-1, is produced from KBR data. The model consists of a time series of 94 monthly solutions (February 2003 – December 2010). Each solution consists of spherical harmonic coefficients up to degree 120 with respect to DGM-1S. Both unconstrained and optimally filtered solutions are produced. The improvements applied in the production of this new model as compared

to its predecessor are usage of: (i) an improved estimation and elimination of the low-frequency noise in residual range combinations, so that strong mass transport signals are not damped; (ii) an improved frequency-dependent data weighting, which allows statistically optimal solutions to be compiled; (iii) release 2 of GRACE level-1B data; (iv) a recent a priori static gravity field model, i.e., DGM-1S; (v) release 5 of the AOD1B model of non-tidal mass re-distribution in the atmosphere and ocean; (vi) the recent ocean tide model EOT11a; and (vii) an improved calibration scheme of the satellites' accelerometers. It is shown that DMT-2 substantially outperforms its predecessor in terms of spatial resolution, which is proven to be mainly associated with the usage of a more advanced frequency-dependent data weighting. Furthermore, it is confirmed that the usage of release 2 of GRACE level-1B data leads to an elimination of the East-West artifacts. Finally, it is shown that choosing the maximum spherical harmonic degree lower than 120 in the context of monthly gravity field modelling could lead to an underestimation of the signal amplitude and the presence of the so-called "Gibbs" phenomenon in the vicinity of areas with strong mass variations. However, the higher spatial resolution of models produced up to degree 120 is almost entirely attributed to the optimal filtering and is not driven by the information content in unconstrained spherical harmonic coefficients.

The contributions of the thesis The primary contributions of this thesis are as follows:

1. Computing new global static gravity models of a competitive quality.
2. Development of a new methodology to validate global static gravity field models.
3. Quantification of the GOCE mission's added value to the static and time-varying gravity field modelling.
4. Inspection of data combination optimality in models produced with satellite gravimetry and surface data. This paves the way to developing better strategies to combine satellite and surface gravimetry data in the production of future models.
5. Computing a new GRACE time-varying gravity field model, DMT-2.
6. Demonstrating the importance of an accurate computation and a proper exploitation of stochastic models of noise in satellite gravimetry data in the context of global gravity field modelling.
7. Identifying the origin of low-frequency noise in GRACE KBR-based observables and proposing a new way to cope with it.

Contents

Summary	i
1 Introduction	1
1.1 Background and motivations	1
1.1.1 Static gravity field	1
1.1.2 Time-varying gravity field	6
1.2 Objectives	7
1.3 Outline	9
2 GRACE/GOCE global gravity field modelling: methodology	11
2.1 Introduction	11
2.2 Functional models	13
2.2.1 Functional model for kinematic orbits	13
2.2.2 Functional model for KBR data	13
2.2.3 Functional model for gradiometry data	14
2.3 Computing residual data	14
2.3.1 Computing GRACE residual range combinations	15
2.3.2 Computing GRACE/GOCE residual 3-D average accel- eration vectors	16
2.3.3 Computing GOCE residual gravity gradients	16
2.4 Inversion	17
3 GRACE/GOCE global static gravity field modelling: results	19
3.1 Introduction	19
3.2 Residual data	20
3.3 Noise analysis	21
3.3.1 Noise in GRACE residual range combinations	22
3.3.2 Noise in GRACE residual 3-D average acceleration vectors	24
3.3.3 Noise in GOCE residual 3-D average acceleration vectors	24
3.3.4 Noise in GOCE residual gravity gradients	25
3.3.4.1 Impact of the low-frequency noise	27
3.3.4.2 Improvement of the noise model	29
3.4 Contribution of GOCE data to a GRACE model	31
3.5 DGM-1S: comparison and validation	34
3.5.1 Preliminary analysis	35
3.5.2 Validation with an independent MDT model	37
3.5.2.1 Methodology	37

3.5.2.2	Application and analysis	39
3.6	Summary, discussion, and conclusions	47
4	Validating gravity models with KBR and gradiometry data	51
4.1	Introduction	51
4.2	Methodology	53
4.2.1	Validation data	53
4.2.2	Computing misfit data	53
4.2.3	Suppressing noise	54
4.3	Application	56
4.3.1	Validation against GRACE KBR data	56
4.3.1.1	Validation in the spectral domain	56
4.3.1.2	Validation in the spatial domain	57
4.3.2	Validation against GOCE SGG data	65
4.3.2.1	Validation in the spectral domain	65
4.3.2.2	Validation in the spatial domain	67
4.4	Summary, discussion, and conclusions	72
5	Assessing models produced using surface data	81
5.1	Introduction	81
5.2	Inspections	82
5.2.1	EGM2008 versus ITG-Grace03	82
5.2.2	EIGEN-6C versus EIGEN-6S	86
5.3	Summary, discussion, and conclusions	87
6	Assessing GOCE added value to temporal gravity field modelling	91
6.1	Introduction	91
6.2	Unconstrained gravity field solutions	92
6.2.1	Computing monthly solutions	92
6.2.1.1	Computing residual data	93
6.2.1.2	Computing stochastic models of noise	95
6.2.1.3	Inversion	96
6.2.2	Impact of GOCE data onto unconstrained solutions	97
6.3	Optimally filtered gravity field solutions	103
6.3.1	Filtering procedure	103
6.3.2	Impact of GOCE data onto optimally filtered solutions	104
6.3.3	Attempt of an alternative definition of impact of GOCE data	114
6.4	Summary, discussion, and conclusions	116

7	GRACE global temporal gravity field modelling: DMT-2	119
7.1	Introduction	119
7.2	Unconstrained gravity field solutions	120
7.2.1	Improvements	120
7.2.1.1	Data- and force model-related improvements	120
7.2.1.2	Methodology-related improvements	122
7.2.2	DMT-2 versus DMT-1: unconstrained solutions	123
7.3	Optimally filtered gravity field solutions	125
7.3.1	DMT-2 versus DMT-1: optimally filtered solutions	125
7.3.2	Contribution of the latest releases of GRACE level-1B data and AOD1B model	128
7.4	Maximum degree recoverable from KBR data	130
7.5	Summary and conclusions	136
8	Global static gravity field retrieval with EGM96 as a priori	137
8.1	Introduction	137
8.2	Data processing modifications and their effects	138
8.2.1	Geometrical corrections and their effect	139
8.2.1.1	Geometrical correction of residual range combinations	139
8.2.1.2	Geometrical correction of residual 3-D average accelerations	140
8.2.1.3	Effect of geometrical corrections	141
8.2.2	An iterative improvement of noise models	143
8.2.3	An iterative improvement of the static gravity model	145
8.3	Assessment of TUD-GRACE01S	146
8.3.1	Preliminary comparison	146
8.3.2	Validation	146
8.3.2.1	Validation against GRACE KBR control data	147
8.3.2.2	Validation against GOCE SGG control data	148
8.4	Summary and conclusions	150
9	Understanding low-frequency noise in GRACE KBR data	153
9.1	Introduction	153
9.2	Methodology	153
9.2.1	Linking the average acceleration approach to the classical acceleration approach	153
9.2.2	Identifying the origin of the low-frequency noise in residual range combinations	156
9.3	Summary, discussion, and conclusions	159

10 Conclusions and recommendations	161
10.1 Conclusions	161
10.2 Recommendations	164
A Linking 3-D average accelerations to spherical harmonics coefficients	167
B Linking gravity gradients to spherical harmonic coefficients	171
References	173
Samenvatting	189
Acknowledgements	195
Curriculum vitae	197

1 Introduction

1.1 Background and motivations

The accurate modelling of the static (i.e., long-term mean) and time-varying parts of the Earth's gravity field at the global scale is essential for a variety of vastly inter-connected applications. Global static gravity field models greatly contribute to, e.g., geoid computation (Rapp, 1997; Rapp and Jekeli, 1980; Rummel, 1980; Wittwer, 2009), height datum unification (Jekeli, 2000; Gatti et al., 2013; Gerlach and Rummel, 2013), geoid's gravity potential value estimation (Burša et al., 1997, 2007; Nesvorný and Šíma, 1994), satellite orbit determination (Schutz et al., 1994; Scharroo and Visser, 1998; Perosanz et al., 1997), studying the Earth's inner density structure (Chao, 2005; Ricard et al., 2006; Braitenberg and Ebbing, 2009), and studying the oceanic circulations (Andersen and Knudsen, 2009; Gourdeau et al., 2003; Knudsen et al., 2011; Rio and Hernandez, 2004). Global time-varying gravity field models play an important role in quantifying and monitoring large scale mass transport in the Earth's system, which is mainly associated with earthquakes (Han et al., 2006, 2011), accumulation and depletion of continental water stocks (Wahr et al., 1998; Swenson et al., 2003; Klees et al., 2007, 2008a), postglacial rebound (van der Wal et al., 2008), ocean tides (Han et al., 2005), ice mass loss in the polar areas (Luthcke et al., 2006; Wouters et al., 2008; Baur and Sneeuw, 2011; Siemes et al., 2013), and the subsequent sea level rise (Bamber et al., 2009).

1.1.1 Static gravity field

An accurate determination of the Earth's gravity field at the global scale requires globally and homogeneously distributed gravity measurements. This can only be achieved by satellite gravimetry missions. Three dedicated satellite gravity field missions have been launched since 2000: CHAMP, GRACE, and GOCE.

CHAMP One of the main objectives of the CHALLENGING Minisatellite Payload (Reigber et al., 1996, 1999) satellite mission was to improve the knowledge about the static part of the gravity field. The mission, which lasted from July 2000 till September 2010, was carried out by a satellite entered an orbit with an initial altitude of about 454 km. It was equipped with a geodetic-quality receiver to collect measurements of the Global Positioning System (GPS), namely, GPS code and carrier phase

measurements. These measurements are often referred to as so-called “Satellite-to-Satellite Tracking (SST)” data in the “high-low” mode. They are typically converted into time-series of three-dimensional (3-D) satellite positions called “kinematic orbit” (e.g., Bock et al., 2007). The CHAMP satellite was also equipped with a three-axis accelerometer to measure non-gravitational accelerations, which are caused by, e.g., atmospheric drag and solar radiation. These accelerations were measured in a satellite-fixed frame, whose orientation with respect to the celestial reference frame was obtained by the on-board attitude control system. The influence of these accelerations onto orbital perturbations is unwanted in the gravity field retrieval and, therefore, must be corrected for. High-low SST data (i.e., GPS code and carrier phase measurements) can be used either directly for the gravity field modelling (e.g., Reigber et al., 2002, 2003) or subsequent to a transformation into a kinematic orbit (e.g., Ditmar et al., 2006; Jäggi et al., 2011). Numerous global static gravity field models have been produced in this way. Examples are EIGEN-1 (Reigber et al., 2002), EIGEN-2 (Reigber et al., 2003), TUM-1S (Gerlach et al., 2003), EIGEN-CHAMP03S (Reigber et al., 2004), TUM-2Sp (Földvary et al., 2005), ITG_Champ01 (Mayer-Gurr et al., 2005), DEOS_CHAMP-01C (Ditmar et al., 2006), AIUB-CHAMP01S (Prange et al., 2008), and EIGEN-CHAMP05S (Flechtner et al., 2010). All these models are fully based on CHAMP data and resolve the gravity field up to spherical harmonic degree 60 – 150, which corresponds to spatial scales of 335 – 135 km half wavelength. The recent CHAMP-only models, e.g., EIGEN-CHAMP05S, demonstrate an accuracy of about 6 cm in terms of cumulative geoid heights up to degree 70 (i.e., at spatial scale of about 285 km half wavelength). This accuracy is about six times better than that of the earlier state-of-the-art models, e.g., EGM96 (Lemoine et al., 1998).

GRACE The global modelling of the gravity field is the main objective of the Gravity Recovery And Climate Experiment satellite mission (Tapley et al., 2004a,b). This mission, launched in March 2002, consists of two identical satellites co-orbiting with an along-track separation of about 220 km at an altitude of below 500 km in a near polar orbit with an inclination of 89.5° . Their primary scientific payload is a K-Band Ranging (KBR) system, which measures the inter-satellite distance variations with a precision of a few microns. These measurements, however, do not contain information about the actual inter-satellite ranges due to an arbitrary bias, which is a consequence of phase ambiguities. Such data are often referred to as SST data in “low-low” mode. Furthermore, the GRACE satellites acquire GPS data using geodetic-quality receivers. In

addition, the satellites are equipped with accelerometers to measure non-gravitational accelerations. They obtain their attitudes with respect to the celestial reference frame with the on-board star cameras. The data delivered by the GRACE mission have substantially contributed to recovery of the static part of the gravity field up to approximately degree 150 (i.e., spatial scales larger than 135 km half wavelength). Exemplarily, I refer to a few of the most recent models produced based solely (or mainly) on these data: GGM02S (Tapley et al., 2005), EIGEN-GL04S1 (Förste et al., 2008a), ITG-Grace03 (Mayer-Gürr, 2006; Mayer-Gürr et al., 2010a), EIGEN-5S (Förste et al., 2008b), GGM03S (Tapley et al., 2007), AIUB-GRACE02S (Jäggi et al., 2009, 2012), ITG-Grace2010s (Mayer-Gürr et al., 2010a,b), and AIUB-GRACE03S (Beutler et al., 2011), which are complete to degree 150 – 180. The latest GRACE-only models, e.g., ITG-Grace2010s, are shown to be of an accuracy of 3 – 4 cm and 4 – 5 cm in terms of cumulative geoid heights up to degree 70 and 150, respectively (Gruber et al., 2011). The accuracy achieved up to degree 70 is almost two times better than that of the latest CHAMP-only models, e.g., EIGEN-CHAMP05S.

GOCE The Gravity field and steady-state Ocean Circulation Explorer satellite mission (Drinkwater et al., 2003; Floberghagen et al., 2011) was designed exclusively to deliver global static gravity field models of a high accuracy and spatial resolution: 1 – 2 cm in terms of geoid heights at a spatial scale of 100 km half wavelength, i.e., up to spherical harmonic degree 200. The GOCE satellite was launched in March 2009 into a sun-synchronous orbit with an inclination of 96.7° . The satellite reached an altitude of 254.9 km after a few months. Its primary measurements are accelerations obtained with three pairs of three-axis accelerometers located at three mutually orthogonal axes forming a three-axis gradiometer (e.g., Müller, 2003). These measurements are dealt with in two different modes, namely, so-called “common mode” and “differential mode”, in which measurements belonging to one pair of accelerometers are summed up and subtracted, respectively. The former operation provides non-gravitational satellite accelerations, which are then fed to the on-board drag-free control system for a real-time compensation for the effects of along-track non-gravitational forces. This enables the satellite to maintain itself at such an extraordinary low altitude. The differential mode operation yields the second order (spatial) derivatives of the gravitational potential plus the contribution of the satellite’s rotation. The latter effect is unwanted in the gravity field retrieval and, therefore, must be corrected for. The measurements of the second order derivatives of the gravitational potential are often referred to as “Satel-

lite Gravity Gradiometry (SGG)” data, a collection of which at a given measurement epoch forms a matrix known as the gravity gradient tensor. This tensor is measured in a gradiometer-fixed frame, whose orientation with respect to the celestial reference frame is acquired with an attitude determination system. These measurements are most accurate in the frequency range 5 – 100 mHz, which is known as the measurement frequency band (e.g., Rummel et al., 2011). They are the main input for the GOCE-based gravity field modelling. In addition, the GOCE satellite acquires GPS data with a high-quality receiver. On the basis of the acquired gravity gradients and GPS measurements, a number of global static gravity field models have been computed. The latest ones based solely on GOCE data are GO_CONS_GCF_2_TIM_R4 (Pail et al., 2010a, 2011), GO_CONS_GCF_2_DIR_R2 (Bruinsma et al., 2010a), GO_CONS_GCF_2_SPW_R2 (Migliaccio et al., 2011), and ITG-Goce02 (Schall et al., 2013). They resolve the static gravity field up to degree 240 – 250, i.e., signals at spatial scales larger than 85 – 80 km half wavelength. The accuracy achieved so far, e.g., in the case of GO_CONS_GCF_2_TIM_R2, is about 5 cm up to spherical harmonic degree 160 in terms of cumulative geoid heights (Gruber et al., 2011). This is by about 15 % better than that of the latest GRACE-only models, e.g., ITG-Grace2010s, but still not in line with the GOCE mission objectives. Nevertheless, the mission is still operational and keeps collecting new measurements. An incorporation of the new measurements collected before the end of 2012 will presumably improve the models to such an extent that the mission objective will be met (Fehring et al., 2012).

The GRACE KBR data and GOCE gravity gradients are nowadays the primary sources of information in the global static gravity field modelling. They complement each other in a number of ways. GOCE gravity gradients provide a higher sensitivity to signals at small spatial scales. Therefore, they allow models of a higher spatial resolution to be computed. Furthermore, KBR data are characterized by an anisotropic sensitivity, i.e., their signal content is mostly limited to the along-track (almost the North-South) gravity field variations. Therefore, an unconstrained model based solely on these data suffers from a poor estimation of sectorial and near-sectorial coefficients. This limitation leads to along-track artifacts, so-called “stripes”, in the spatial domain. On the contrary, SGG measurements are isotropic. They provide information about the gravity field spatial variations in all directions. Thus, along-track stripes in a GRACE-only unconstrained model may be mitigated by employing GOCE gravity gradients in a combined modelling. On the other hand, SGG data are contaminated by an increased noise at the frequencies below 5 mHz,

i.e., the lower bound of the measurement frequency band. This noise is caused primarily by the sensor noise and secondarily by inaccuracies in the satellite's attitude data, which are used to compute and remove the terms related to the frame rotation in the differential mode operation (Rummel et al., 2011). Given the satellite's orbital revolution time, i.e., nearly 1.5 hours, this corresponds to $5400 \text{ s} \times 0.005 \text{ Hz} \approx 27$ cycles-per-revolution (cpr) frequency. The range limited by this frequency comprises all signals associated with coefficients of degree 27 and less. This implies that GOCE gravity gradients cannot be used for determining coefficients below degree 27, i.e., signals at spatial scales larger than 745 km half wavelength. On the other hand, KBR data are extremely sensitive to signals at low degrees and, therefore, substantially contribute to an accurate retrieval of such large-scale features. In addition, due to its orbital inclination, the GOCE satellite's spatial coverage suffers from the 1500 km wide (in diameter) polar gaps, which lead to a numerical instability in a stand-alone processing of its measurements. This problem manifests itself in a poor estimation of zonal and near-zonal coefficients up to the highest maximum degree (e.g., van Gelderen and Koop, 1997). In contrast, the GRACE configuration does not suffer from a polar gap problem as much due to its nearly polar orbit. Given a high ability of KBR data to retrieve coefficients up to degree 150 – 180, this problem for zonal coefficients of at least these degrees can be fixed by using KBR data in conjunction with GOCE gravity gradients. Finally, GRACE KBR data and GOCE gravity gradients both show a high sensitivity in the frequency range 10 – 22 mHz or 54 – 119 cpr (Farahani et al., 2013a), which corresponds to signals at spatial scales of 370 – 170 km half wavelength. This implies that a statistically optimal combination of data of the two types naturally increases the accuracy and reliability of models at these spatial scales. These mutual benefits trigger a need to compile static gravity field models using GRACE KBR and GOCE SGG data, jointly. Six satellite-only models of this kind have been presented so far: GOCO01S (Pail et al., 2010b), GOCO02S (Goiginger et al., 2011), EIGEN-6S (Förste et al., 2011), GOCO03S (Mayer-Gürr et al., 2012), GO_CONS_GCF_2_DIR_R3, and GO_CONS_GCF_2_DIR_R4 (Bruinsma et al., 2010a), which represent the static part of the gravity field up to degree 224 – 260. EIGEN-6S describes the time-varying part, too (with a bias, linear trend, annual and semi-annual sinusoidal terms up to degree 50).

Generally speaking, a physical model prior to its usage has to be validated. A global static gravity field model is not an exception. Nevertheless, the high accuracy of the new models makes their validation a challenging task. There are a number of ways that have been traditionally used for that purpose based on different sets of control data: (i) applying a model to compute satellite orbit parameters, which are then confronted with Satellite Laser Ranging (SLR) and/or on-board GPS measurements (e.g., Visser et al., 2009;

Gruber et al., 2011); (ii) synthesis of gravity anomalies or deflections of the vertical at the Earth's surface with a subsequent comparison of them with terrestrial gravimetry or astro-geodetic measurements, respectively (e.g., Hirt et al., 2011; Ihde et al., 2010); (iii) usage of a model to compute the geoid height differences between various locations with a subsequent comparison of the results with GPS/levelling derived geoid values (e.g., Gruber, 2009; Gruber et al., 2011); and (iv) synthesis of the oceanic mean dynamic topography and/or of geostrophic velocities of the oceanic currents with a subsequent comparison with an independent, i.e., oceanographic, model of the mean dynamic topography or in situ measurements of geostrophic velocities, respectively (e.g., Gruber, 2009; Farahani et al., 2013b). Unfortunately, these validation techniques are not free of certain limitations. Firstly, the accuracy of the new combined GRACE/GOCE models is so high that an assessment of them using control SLR- and/or GPS-based satellite orbit data mostly reveals errors in those data, so that different models may demonstrate a very similar performance. Secondly, the control data mentioned above, except for those collected by on-board GPS receivers, are not globally distributed, which makes the validation results obtained on their basis insufficiently representative. Thirdly, due to the spectral distribution of signal versus that of noise in the control data stated above, their frequency content is practically limited either to very low degrees or to very high degrees. That is, satellite orbit data are only sensitive to low-degree spherical harmonic coefficients, whereas the other types of control data stated above are primarily sensitive to high-degree coefficients. These limitations necessitate developing new methodologies for validating global static gravity field models.

1.1.2 Time-varying gravity field

The GRACE KBR data have also enabled research centres to produce global time-varying gravity field models with an unprecedented accuracy and spatial resolution. Numerous models of this type have been produced. They are complete to degree 60 – 120, which corresponds to signals at spatial scales larger than 500 – 165 km half wavelength (e.g., Bettadpur, 2007, 2012; Flechtner, 2007a; Watkin and Ning, 2007; Kurtenbach et al., 2009; Dahle et al., 2012; Bruinsma et al., 2010b; Liu, 2008; Liu et al., 2010; Mayer-Gürr et al., 2010a,b; Meyer et al., 2012; Watkin and Ning, 2012). Their temporal resolution is typically limited to one month. A few of them, e.g., those produced by Kurtenbach et al. (2009) and Bruinsma et al. (2010b), are of a higher temporal resolution (from daily to 10-day), but with a reduced spatial resolution. Furthermore, the accuracy of unconstrained GRACE-only solutions rapidly degrades as the spatial scale decreases. In terms of geoid height error per degree, for instance, the noise level in these solutions starts to exceed that of signal at degree 20

– 30 (Sasgen et al., 2006). In addition, unconstrained GRACE-only solutions suffer from pronounced stripes, due to the previously mentioned anisotropic sensitivity of KBR data. To suppress noise in these solutions, one typically applies a filter. Examples are the de-stripping procedure (Swenson and Wahr, 2006) combined with a Gaussian filter (Wahr et al., 1998), a de-correlating non-isotropic filter (Kusche, 2007; Kusche et al., 2009), a statistically-optimal anisotropic filter (Klees et al., 2008b), and a so-called “Fan” filter (Zhang et al., 2009). Unfortunately, filtering not only suppresses noise, but also partly removes signal in the models produced. This triggers an idea of an improvement of such models not by applying a filter, but by using other sources of information, e.g., GOCE SST data and gravity gradients, in a combined modelling. Furthermore, an obvious way to improve GRACE time-varying gravity field models is to implement and utilise more advanced schemes to process KBR data when producing these models.

The GRACE global monthly gravity field models produced by different research centres are complete to different maximum spherical harmonic degrees: 60 to 120. It is, however, unclear what spatial resolution can be actually achieved from KBR data in this context and what maximum degree ensures that no information content is lost. Therefore, an investigation of this issue is still needed.

1.2 Objectives

In view of the outlined motivation, the study presented in this thesis pursues eight main objectives listed below.

1. The study is to produce new global models of the static part of the Earth’s gravity field based on GRACE and GOCE data. To that end, a special care is to be taken for a statistically optimal combination of data of different types and sources.
2. In view of the limitations of the traditional approaches for validating global static gravity field models, the study is to extend the list of validation methodologies. To that end, an alternative methodology is to be developed, in which the accuracy of models is to be assessed in terms of their ability to forecast data delivered by satellite gravimetry missions themselves. Two types of control data are to be considered: GRACE KBR data and GOCE gravity gradients.
3. An important task subsequent to a new experiment is to study the extent to which data acquired by that experiment have improved the existing knowledge. This is highly relevant for the latest satellite gravimetry mission: GOCE. Thus, I intend to study the added value of this mission to

the static gravity field modelling. To that end, the validation methodology stated above is to be utilised. In that way, GRACE/GOCE satellite-only models will be compared with state-of-the-art models produced in the absence of GOCE data and conclusions regarding GOCE mission's added value will be drawn.

4. Despite the recent progress made in the field of satellite gravimetry, the spatial resolution of global static gravity field models produced solely based on satellite gravity data is limited to about 100 km half wavelength. Thus, efforts have been made to combine GRACE and GOCE data with surface gravity data, namely, terrestrial gravimetry and satellite altimetry measurements, to produce ultra-high degree models. Examples are EGM2008 (Pavlis et al., 2008, 2012) and EIGEN-6C (Förste et al., 2011), which have been developed without and with GOCE data to degree 2159 and 1420, respectively. However, a statistically optimal combination of satellite and surface data is by no means a trivial task due to, among others, their different spectral information contents and spatial coverages. Thus, I intend to investigate how successfully this combination has been conducted in the case of the aforementioned two models. To that end, the validation methodology stated earlier is to be utilized.
5. In view of the limitations of GRACE-only global time-varying gravity field models, a possible improvement of those models using GOCE data is to be studied. To that end, KBR data are to be jointly processed with GOCE kinematic orbit and gravity gradients in a statistically optimal manner. Conclusions are to be drawn based on a comparison between GRACE-only solutions and the GRACE/GOCE ones.
6. The study is to produce new global time-varying gravity field models based on GRACE KBR data taking into account the latest developments in this area of study. Furthermore, an investigation is to be performed on the spatial resolution achievable from KBR data in the context of time-varying gravity field modelling at the global scale.
7. The concept of dynamic orbit integration plays in one way or another a central role in dealing with SST data, in particular GRACE KBR measurements. For instance, the functional model, which links these data with spherical harmonic coefficients, can be established directly on the basis of this concept (Reigber, 1989). The link established by this concept is notoriously non-linear (Montenbruck and Gill, 2000). This implies that a gravity field model based on these data is, in essence, produced as a residual field with respect to an a priori model in line with

the so-called “remove-compute-restore” approach. I intend to investigate the sensitivity of the gravity field retrieval based on KBR data to the choice of the a priori model taking into account the non-linear link between these data and the gravity field parameters. To that end, I will deliberately consider an a priori gravity field model that is far from the truth.

8. GRACE KBR data are contaminated with an increased noise level at low frequencies up to approximately 5 cpr. This noise maps itself onto zonal and near-zonal coefficients up to the highest degree considered in the global gravity field retrieval (Colombo, 1986). A pragmatic approach to deal with this noise is to apply an empirical high-pass filter prior to the model production (Colombo, 1984; Kim, 2000; Liu, 2008; Liu et al., 2010). Nevertheless, an empirical filtering not only eliminates noise but may also partly remove signal in the range of low frequencies. Therefore, I find it necessary to identify the origin of this low-frequency noise and propose better ways to cope with it.

1.3 Outline

In chapter 2, the methodology that I use to produce global gravity field models is described. The next seven chapters (chapters 3 – 9) document my findings in a pursuit of the aforementioned eight main objectives. In chapter 3, my findings in the combined GRACE/GOCE global static gravity field modelling are documented. Chapter 4 describes a procedure proposed to validate global static gravity field models. The results of its application to various models, including the one produced in this thesis, are presented as well. Importantly, this leads to an analysis of GOCE mission’s added value to the static gravity field modelling. In chapter 5, I use the proposed validation procedure to inspect data combination optimality in global static gravity field models produced in the presence of surface measurements. In chapter 6, an investigation on the possible added value of GOCE data to the time-varying gravity field modelling is presented. In chapter 7, I present my findings in the GRACE-only global time-varying gravity field modelling. This includes, among others, an inspection of the spectral sensitivity of KBR data to the temporal gravity field variations. A new global time-varying gravity field model is presented in chapter 7, too. In chapter 8, I investigate whether an attempt of the static gravity field retrieval could lead to a model of a competitive quality if a relatively inaccurate model such as EGM96 is used as the a priori. Chapter 9 is devoted to identifying the origin of the low-frequency noise in KBR data. Chapter 10 is left for conclusions and recommendations.

2 GRACE/GOCE global gravity field modelling: methodology

2.1 Introduction

The Earth's gravitational potential V in the global gravity field modelling is commonly approximated above the Earth's surface by the series of the spherical harmonic functions (Heiskanen and Moritz, 1967):

$$V(\lambda, \phi, r) \approx \frac{GM}{R} \times \sum_{n=0}^L \left(\frac{R}{r}\right)^{n+1} \sum_{m=0}^n (\bar{c}_{nm} \cos m\lambda + \bar{s}_{nm} \sin m\lambda) \bar{P}_{nm}(\sin \phi). \quad (2.1)$$

Herein, λ (longitude), ϕ (geocentric latitude) and r (geocentric radius) are the spherical coordinates of a point of interest, GM is the gravitational constant times the Earth's mass, R is the Earth's equatorial radius, \bar{P}_{nm} are normalized associated Legendre's functions of degree n and order m , \bar{c}_{nm} and \bar{s}_{nm} are the corresponding (4π -normalized) spherical harmonic coefficients, and L denotes the maximum degree. The degree zero coefficient \bar{c}_{00} in Eq. (2.1) is set equal to 1 due to the fact that M is the total mass of the Earth. The degree one coefficients are related to the location of the Earth's centre of mass, namely, $\bar{c}_{10} = \frac{1}{R}z_c^{\text{TRF}}$, $\bar{c}_{11} = \frac{1}{R}x_c^{\text{TRF}}$, and $\bar{s}_{11} = \frac{1}{R}y_c^{\text{TRF}}$, where x_c^{TRF} , y_c^{TRF} , and z_c^{TRF} , are the Cartesian coordinates of the Earth's centre of mass with respect to a realization of the Terrestrial Reference Frame (TRF) (e.g., Altamimi et al., 2011) with x_c^{TRF} and z_c^{TRF} being related to the TRF's Greenwich- and the North Pole-oriented axes, respectively. The degree one coefficients in the global gravity field modelling from GRACE or GOCE data are often excluded from the list of the unknown parameters due to the assumption that x_c^{TRF} , y_c^{TRF} , and z_c^{TRF} are zero, i.e., that the TRF's origin coincides with the Earth's centre of mass.

The spherical harmonic coefficients in this thesis are to be estimated based on GRACE and GOCE SST data plus GOCE gravity gradients. The latter ones are direct measurements of the second order derivatives of the gravitational potential. Thus, their links with the unknown coefficients are straightforward (Ditmar and Klees, 2002; Ditmar et al., 2003a). The SST data, on the other hand, are not direct measurements of the gravity field observables. At least, five approaches have been developed so far to establish links between them

and the unknown coefficients: “energy balance approach” (Jekeli, 1999; Han, 2003, 2004; Gerlach et al., 2003), “variational equations approach” (Reigber, 1989; Reigber et al., 2002, 2003; Tapley et al., 2005; Beutler et al., 2010a,b; Prange et al., 2008; Jäggi et al., 2010), “short-arc approach” (Mayer-Gürr et al., 2005; Mayer-Gürr, 2006; Mayer-Gürr et al., 2010a), “point-wise acceleration approach” (Reubelt et al., 2003, 2006), and “average acceleration approach” (Ditmar and van Eck van der Sluijs, 2004; Ditmar et al., 2006; Liu, 2008; Liu et al., 2010).

The functional model in the energy balance approach is based on the energy conservation law. In the context of kinematic orbits, the corresponding functional model, unlike those in the other approaches, exploits information about the along-track component of the gravity field only. Thus, this functional model fails to fully exploit the information content of these measurements, which is a drawback. In the context of GRACE KBR data, the functional model of the energy balance approach suffers from a different problem. It allows observed GRACE inter-satellite range-rates to be converted into the gravitational potential differences between the GRACE satellites (plus an unknown constant) under the assumption that the mean of the velocity vectors of the two satellites at a given time is parallel to their line-of-sight. This is a poor approximation, which makes the functional model rather inaccurate (Jekeli, 1999). The functional models of the other approaches are all based on the Newton’s equation of motion. Thus, they are theoretically equivalent. This means that in practice they could also lead to results of a similar quality, provided that statistically optimal methodologies are followed to process data. In this thesis, I utilize the functional models based on the average acceleration approach to deal with GRACE KBR data and kinematic orbits of the GRACE and GOCE satellites.

The methodology followed in this dissertation in order to estimate spherical harmonic coefficients consists of three steps: (i) data pre-processing: transforming data of different types into sets of residual (gravitational) data with respect to an a priori static gravity field model; (ii) inversion: optimally combining and inverting residual data sets into residual coefficients in the least squares sense; and (iii) adding coefficients of the a priori model back to those estimated. The latter step can be done with ease, and therefore, does not require further discussions. In the first section, I describe functional models exploited to deal with data of different types. The second section describes how I compute sets of residual data. The approach followed for a joint inversion of them into residual spherical harmonic coefficients is discussed in the third section.

2.2 Functional models

2.2.1 Functional model for kinematic orbits

The average acceleration approach in the context of kinematic orbit data has been developed by Ditmar and van Eck van der Sluijs (2004) and Ditmar et al. (2006). The functional model is defined based on 3-D average acceleration vectors $\bar{\mathbf{a}}(t)$ derived from satellite orbit with a three-point differentiation scheme:

$$\bar{\mathbf{a}}(t) = \frac{\mathbf{r}(t - \Delta t) - 2\mathbf{r}(t) + \mathbf{r}(t + \Delta t)}{(\Delta t)^2}, \quad (2.2)$$

where $\mathbf{r}(t)$ is the satellite 3-D position vector at measurement epoch t and Δt denotes the sampling interval. All the vectors in this equation are associated with the satellite's centre of mass and given in an inertial frame, e.g., a realization of the Celestial Reference Frame (CRF) (e.g., Fey et al., 2009). Ditmar and van Eck van der Sluijs (2004) have shown that the outcome of the differentiation given by Eq. (2.2) can be interpreted as a 3-D point-wise acceleration vector $\mathbf{a}(t)$ averaged with weight $\frac{\Delta t - |s|}{(\Delta t)^2}$ in the differentiation time interval $s \in [-\Delta t, \Delta t]$:

$$\bar{\mathbf{a}}(t) = \int_{-\Delta t}^{\Delta t} \frac{\Delta t - |s|}{(\Delta t)^2} \mathbf{a}(t + s) ds. \quad (2.3)$$

The proof of this equation can be easily achieved by integrating its right-hand side by parts. Equation (2.3), which is in essence an averaging filter, allows the link between a 3-D average acceleration vector and spherical harmonic coefficients to be established. To that end, it is sufficient to apply the gradient operator and then the averaging filter of Eq. (2.3) to both sides of Eq. (2.1). Practical aspects of the latter operation have been documented in detail in (Ditmar and van Eck van der Sluijs, 2004; Ditmar et al., 2006; Ditmar, 2009). I describe them in Appendix A, too.

2.2.2 Functional model for KBR data

Liu (2008) and Liu et al. (2010) have modified the functional model described in the previous subsection to process GRACE KBR data. So-called ‘‘range combinations’’ are obtained from bias-corrected inter-satellite ranges at three successive epochs with a similar three-point differentiation scheme:

$$\bar{a}(t) = \frac{\mathbf{e}(t - \Delta t) \cdot \mathbf{e}(t)\rho(t - \Delta t) - 2\rho(t) + \mathbf{e}(t) \cdot \mathbf{e}(t + \Delta t)\rho(t + \Delta t)}{(\Delta t)^2}. \quad (2.4)$$

Herein, \cdot denotes the inner product, $\rho(t)$ are measured bias-corrected inter-satellite ranges, and $\mathbf{e}(t)$ are the line-of-sight unit vectors pointing from the trailing satellite towards the leading one. Liu (2008) has shown that the left-hand-side of Eq. (2.4) can be interpreted as the difference between 3-D average acceleration vectors of the two GRACE satellites, defined by Eq. (2.3), projected onto their line-of-sight:

$$\bar{a}(t) = \{\bar{\mathbf{a}}_2(t) - \bar{\mathbf{a}}_1(t)\} \cdot \mathbf{e}(t), \quad (2.5)$$

where indices 1 and 2 refer to the trailing and leading GRACE satellites, respectively. The proof of this statement can be easily achieved by inserting Eq. (2.2) into Eq. (2.5) and then replacing the 3-D positions with ranges $\rho(t)$. Since the link between 3-D average acceleration vectors with spherical harmonic coefficients has already been established in the previous subsection and in Appendix A, the link of a range combination with these coefficients is straightforward.

2.2.3 Functional model for gradiometry data

The GOCE gravity gradients are acquired in the Gradiometer Reference Frame (GRF): a right-handed satellite-fixed Cartesian frame whose axes nominally point in the along-track (flight), cross-track (orthogonal to the orbital plane), and nadir directions with an approximation of a few degrees (Rummel et al., 2011). I process these measurements in the same frame to avoid amplifying their noise as a consequence of a transformation into another frame. In the model production, I exploit only the diagonal components of the gravity gradient tensor, which are the most accurately measured components (Rummel et al., 2011). To link the gravity gradients measured in the GRF with spherical harmonic coefficients, it is sufficient to represent the full gravity gradient tensor in the form of the spherical harmonic expansion using Eq. (2.1) and then to transform this tensor into the GRF. This transformation requires, among others, the orientation of the GRF with respect to the inertial frame, which is provided by the GOCE on-board star camera. Details in establishing these links have been well documented in (Ditmar and Klees, 2002; Ditmar et al., 2003a). I document them, too (Appendix B).

2.3 Computing residual data

The data are reduced to residual ones by subtracting their a priori counterparts. The latter ones are computed based on a model describing the forces acting on the satellites. In this context, it is worth reminding that observations naturally refer to the instantaneous gravity field. This field experiences temporal variations, which are caused by, e.g., tidal perturbations. In addition,

the satellite measurements, in particular KBR data, are heavily influenced by non-gravitational perturbations. Therefore, it is required that the force model in addition to an a priori gravity field model takes these nuisance signals (associated with temporal gravity field variations and, possibly, non-gravitational forces) into account. Details about computation of residual data of different types are presented in sections 2.3.1 – 2.3.3

2.3.1 Computing GRACE residual range combinations

The average acceleration approach has been applied to KBR data by Liu (2008) and Liu et al. (2010) to produce the Delft Mass Transport, release 1 (DMT-1) model. To compute residual range combinations, I exploit the experience collected in that research. The computation of these residuals involves the following steps.

As it will be shown in chapter 9, the usage of Eq. (2.4) in computing range combinations requires GRACE satellites' line-of-sight unit vectors, i.e., $\mathbf{e}(t)$, to be accurately known. Thus, I compute dynamic orbits. These orbits in the context of the model production are hereafter referred to as a priori orbits. To compute them, I perform dynamic orbit integration. To this end, I use the software package Positioning And Navigation Data Analyst (PANDA) developed at the GNSS Research Centre of Wuhan University (Zhao, 2004). These a priori orbits are computed in the form of six-hour arcs separately for either GRACE satellite using the force model. The computation of orbital arcs includes a least squares adjustment of the initial state vector elements and accelerometer's six calibration parameters (a bias and a scaling factor per axis). To perform this adjustment, a preliminary variant of the a priori orbits is first produced based on initial values of the aforementioned twelve parameters. The initial values of the state vector elements are extracted from reduced-dynamic orbits, i.e., orbits produced by fitting kinematic orbits to a force model (e.g., Montenbruck and Gill, 2000; Montenbruck et al., 2005). The initial values associated with the accelerometer's bias and scaling parameters are set to zero and one, respectively. Then, the aforementioned adjustment is performed by fitting the preliminary a priori orbits to kinematic ones. In case kinematic orbits are unavailable, reduced-dynamic orbits are instead used to perform this adjustment. In my study, GRACE kinematic and reduced-dynamic orbits are produced and provided by the GNSS Research Centre of Wuhan University in accordance with (Zhao, 2004). For almost three years at the beginning of the GRACE mission (i.e., February 2003 – December 2005), only reduced-dynamic orbits are available to me. Those orbits are produced and provided by Kroes et al. (2005).

Observed inter-satellite ranges are provided in KBR1B product as a part of GRACE level-1B data (Case et al., 2004). The a priori orbits are used to esti-

mate (in a least squares sense) and remove their bias, one value per continuous time segment, in which there are no phase breaks or cycle slips. In addition, the a priori orbits are used to compute a priori inter-satellite ranges. Subsequently, residual inter-satellite ranges are obtained by subtracting the a priori inter-satellite ranges from the observed bias-corrected ones. Residual range combinations are obtained from the residual inter-satellite ranges by applying Eq. (2.4).

2.3.2 Computing GRACE/GOCE residual 3-D average acceleration vectors

There are two theoretically equivalent approaches to compute residual 3-D average acceleration vectors. One is to compute residual orbits by subtracting a priori orbits from kinematic ones. Subsequently, residual accelerations are produced by applying Eq. (2.2) to residual orbits. The second approach is to produce observed 3-D average acceleration vectors by applying Eq. (2.2) to kinematic orbits. Their a priori counterparts are evaluated based on the force model using Eq. (2.3). Subsequently, residual accelerations are produced by subtracting the a priori quantities from the observed ones. These approaches are fully equivalent, provided that the same force model is used to produce a priori orbits and a priori accelerations. Since I compute a priori orbits only for the GRACE satellites, I follow the first approach in the case of the GRACE mission and the second one in the case of the GOCE mission. The second approach was also used by Ditmar et al. (2006) when they produced DEOS_CHAMP-01C from CHAMP kinematic orbit data. In this thesis, I exploit the experience accumulated in that activity to compute GOCE residual 3-D average acceleration vectors. In doing so, I extract the satellite's locations at which I evaluate the a priori quantities from reduced-dynamic orbits subsequent to an interpolation at kinematic orbit epochs with an eleventh-order Legendre interpolation scheme. GOCE kinematic and reduced-dynamic orbits have been determined by Bock et al. (2011). These orbits are provided in SST_PSO_2 product as a part of GOCE level-2 data (Gruber et al., 2010; de Witte, 2011).

2.3.3 Computing GOCE residual gravity gradients

GOCE observed gravity gradients are provided in EGG_NOM_2 product as a part of GOCE level-2 data. They are provided in the GRF and supplied with orientation parameters of this frame with respect to the inertial one. Residual gravity gradients are produced in the GRF, too. I produce them by subtracting the a priori gravity gradients from the observed ones in the GRF. The a priori quantities are evaluated based on the force model at satellite's locations. These

locations are extracted from GOCE reduced-dynamic orbits interpolated at gradiometer’s measurement epochs with an interpolation scheme similar to that mentioned in the previous subsection.

2.4 Inversion

An optimal combination of residual data sets requires an accurate stochastic description of their noise. The residual data sets are known to be contaminated by colored, i.e., frequency-dependent, noise (e.g., Ditmar et al., 2007). Therefore, I use the concept of frequency-dependent data weighting for all of them. To that end, I assume that their noise is Gaussian and stationary, so that its full stochastic description can be made in the form of Power Spectral Density (PSD). To estimate noise in residual data, I follow an iterative scheme. Initially, I assume sets of residual data to be realizations of their noise, too. With this assumption, a preliminary gravity field model is produced. It is reasonable to expect that this preliminary model is of a higher quality than the a priori gravity field model. Thus, the post-fit residuals computed after the gravity field retrieval are expected to be more accurate realizations of noise. These post-fit residuals are produced in the same manner as described in the case of residual data sets involved in the gravity field retrieval. This scheme for noise estimation is iterated until a convergence of results is achieved. Further details on this iterative scheme are provided later when I present the conducted numerical experiments.

Technically, frequency-dependent data weighting is realized with Auto-Regressive Moving-Average (ARMA) models, i.e., parameterized models that best fit noise PSD’s (Klees and Broersen, 2002; Klees et al., 2003; Klees and Ditmar, 2004). It is worth noting that building ARMA models does not necessarily require computing noise PSD’s. However, it is advisable to compute these noise PSD’s always, as they provide insight into the distribution of noise over frequency.

The built ARMA models allow the noise covariance matrices associated with sets of residual data to be adequately represented in their combined inversion:

$$\mathbf{x} = \left(\sum_i \mathbf{A}_i^T \mathbf{C}_i^{-1} \mathbf{A}_i + \alpha \mathbf{R} \right)^{-1} \left(\sum_i \mathbf{A}_i^T \mathbf{C}_i^{-1} \mathbf{d}_i \right). \quad (2.6)$$

Herein, \mathbf{x} is a vector composed of estimated residual spherical harmonic coefficients, \mathbf{A}_i , \mathbf{C}_i , and \mathbf{d}_i are respectively design matrix, noise covariance matrix, and vector of residual data associated with data set i . The design matrices in the case of the GRACE-based data sets are assembled using a priori orbits, whereas those related to the GOCE-based data sets are formed using reduced-dynamic orbits. The terms \mathbf{R} and α denote a regularization matrix

and the corresponding regularization parameter. A good review of different regularization matrices in the context of the static gravity field retrieval from GOCE gradiometry data can be found in (Ditmar et al., 2003b). Different methods to obtain the optimal value of the regularization parameter has been documented in (Kusche and Klees, 2004; Koch and Kusche, 2002; Kusche, 2003) in the same context. In many numerical experiments to be conducted in this thesis, no regularization is imposed. In those cases, α is obviously set as zero. When I do apply a regularization, I use the Kaula regularization matrix in the context of the static gravity field modelling. In that context, I find the regularization parameter in an empirical manner: by minimizing the difference between the model to be produced and a state-of-the-art model. In the context of the time-varying gravity field modelling, I define the regularization matrix as the inverse of the full covariance matrix of the time-varying gravity field signal (Klees et al., 2008b). The regularization parameter in the latter case is set as one. Equation (2.6) involves multiple matrix to vector multiplications. The multiplication of a noise covariance matrix to a vector in the context of a large least squares problem is performed with a scheme described in (Klees and Ditmar, 2004). Algorithms for an efficient multiplication of a design matrix to a vector have been described by Ditmar and Klees (2002) and Ditmar and van Eck van der Sluijs (2004) in the same context. Efficient algorithms for solving the linear system of equations, e.g., the method of pre-conditioned conjugate gradients, have been discussed by them, too.

3 GRACE/GOCE global static gravity field modelling: results

This chapter is based on the study documented in (Farahani et al., 2013b). In that manuscript, (i) various aspects of the combined GRACE/GOCE global static gravity field modelling were investigated, e.g., individual contribution of SST and SGG data from the GOCE mission; (ii) a new combined GRACE/GOCE model, namely, Delft Gravity Model, release 1, Satellite-only (DGM-1S), was presented; and (iii) a validation of that model and of some of the alternative ones, e.g., GOCO03S, was performed based on different sets of control data, including a state-of-the-art oceanographic model of the mean dynamic topography.

3.1 Introduction

This chapter primarily presents a new global static gravity field model, entitled DGM-1S: Delft Gravity Model, release 1, Satellite-only. The model has been produced in terms of spherical harmonic coefficients up to degree 250 based on a statistically optimal combination of GRACE KBR data, GOCE gravity gradients, and GRACE and GOCE satellites' kinematic orbits. Prior to its presentation, I additionally analyse a number of preliminary models produced to understand various aspects of the combined GRACE/GOCE static gravity field modelling. This includes quantifying (i) the influence of the low-frequency noise in GOCE gravity gradients; (ii) the impact of the usage of an accurate estimation of noise in these data; and (iii) the contribution of GOCE kinematic orbit data and gravity gradients to the static gravity field modelling, separately and jointly. Furthermore, a validation of DGM-1S is performed by comparing its quality with that of three alternative models, namely, GOCO01S, EIGEN-6S (only its static part), and GOCO02S. The validation is based on an analysis of the ability of these models to synthesize a model of the oceanic Mean Dynamic Topography (MDT), which is compared against an independent, i.e., oceanographic, state-of-the-art MDT model. I include ITG-Grace2010s and EGM2008 in this assessment as well. ITG-Grace2010s is a state-of-the-art GRACE-only model and EGM2008 is a state-of-the-art model based on GRACE and terrestrial gravimetry/satellite altimetry data. Thus, their inclusion allows studying the added value of the GOCE mission to the static gravity field modelling over the oceanic areas.

Table 3.1: The sets of GRACE and GOCE data involved in the static gravity field modelling.

Residual data	Duration (months)	Time interval	Sampling (seconds)
GRACE range combinations	82	Feb 2003–Dec 2009	5
GRACE 3-D average accelerations	48	Jan 2006–Dec 2009	30
GOCE 3-D average accelerations	14	Aug 2009–Dec 2010	30
GOCE gravity gradients	10	Nov 2009–Dec 2010	1

Here is the outline of the chapter. Section 3.2 introduces sets of residual data involved in the static gravity field modelling. Section 3.3 analyses their noise in the spectral domain and also in the spatial domain in the case of sets of GOCE data. In section 3.4, I study the contribution of GOCE kinematic orbit data and gravity gradients, separately and jointly, to a GRACE-only model in the absence of regularization. DGM-1S is the primary subject of section 3.5, where a preliminary assessment of its quality is made by comparing it as well as ITG-Grace2010s, GOCO01S, EIGEN-6S, and GOCO02S with EGM2008. In section 3.5, I also present results of a validation of these six models against independent data. Section 3.6 is left for a summary, discussion, and conclusions.

3.2 Residual data

The sets of data utilized in the production of static gravity field models are listed in Table 3.1. The force model exploited to produce them is comprised of the following contributors:

- (i) Static gravity field defined by ITG-Grace2010s up to its maximum degree, i.e., 180.
- (ii) Linear trends in five low-degree spherical harmonic coefficients of the gravity field, i.e., \bar{c}_{20} , \bar{c}_{30} , \bar{c}_{40} , \bar{c}_{21} , and \bar{s}_{21} , according to (Flechtner, 2007a). These linear trends are used to correct the corresponding coefficients of ITG-Grace2010s per measurement for the time difference between the reference epoch of this model and that of the measurement epochs.
- (iii) Astronomical (direct) tidal perturbations based on the Jet Propulsion Laboratory (JPL) DE405/LE405 lunar and planetary ephemerides (Standish, 1998).

- (iv) Solid Earth tides and pole tides defined in accordance with the conventions of the International Earth Rotation and Reference Systems Service (IERS) adopted in 2003 (McCarthy and Petit, 2004).
- (v) Ocean tides described by the FES2004 model (Lyard et al., 2006) up to spherical harmonic degree 80.
- (vi) Non-tidal atmospheric and oceanic variability described by the fourth release of the Atmosphere and Ocean De-aliasing level-1B (AOD1B) model (Flechtner, 2007b) up to spherical harmonic degree 100.

In addition, the high sensitivity of KBR data to temporal gravity field variations (Wahr et al., 1998) and the presence of strong non-gravitational signals in these data require an extension of the force model applied in the context of GRACE data with the following contributors:

- (a) Ocean pole tide described by the model of Desai (2002) up to spherical harmonic degree 30.
- (b) General relativity corrections according to the IERS 2003 conventions (McCarthy and Petit, 2004).
- (c) Non-gravitational accelerations. They are accounted for using GRACE accelerometer and attitude data, which are respectively provided in ACC1B and SCA1B products as parts of GRACE level-1B data (Case et al., 2004). These accelerations are not accounted for in the case of GOCE gravity gradients, because they do not influence differential accelerometry data, provided that they are perfectly calibrated (e.g., Siemes et al., 2012). They are not considered in the case of GOCE kinematic orbit data either in view of two reasons. Firstly, it has been demonstrated in (Ditmar et al., 2007) that these forces are of a minor impact if proper stochastic models of noise in accelerations are used. Secondly, these forces are largely (i.e., fully along-track) compensated by the on-board drag-free system.

Furthermore, Earth's rotation parameters released by the IERS on the daily basis are used to compute matrices describing the rotation between the terrestrial and inertial reference frames, which are required throughout the data pre-processing (see Appendices A and B).

3.3 Noise analysis

In this section, I analyse noise in the residual data sets involved in the static gravity field retrieval. This analysis, in some cases, leads to introducing additional steps in the data pre-processing schemes, which are explained, too.

To obtain noise PSD's, I use the residual data sets themselves. Since ITG-Grace2010s is a rather accurate model, I assume that sets of residual data, with the exception of GOCE residual gravity gradients, contain mostly noise. In the case of GRACE residual range combinations, long-term mass transport signals (due to, e.g., accumulation or depletion of continental water stocks, polar ice mass variations, or post-glacial rebound) are present. As it will be shown in chapter 6, an inclusion of these signals in the force model (using a GRACE-based mass transport model) would reduce PSD of these residuals in the frequency range 0.5 – 10 mHz (3 – 54 cpr), which can be related to signals at spatial scales of 7200 – 400 km half wavelength. These signals in the context of this chapter are noise. Thus, I shall not remove them from the sets of residual range combinations when I obtain the corresponding noise PSD's. As far as the GOCE residual gravity gradients are concerned, they contain gravity field signal not captured by ITG-Grace2010s. Thus, their noise PSD's are considered as initial ones. I improve them iteratively prior to the production of DGM-1S. The details of this iterative scheme are discussed in section 3.3.4.2.

3.3.1 Noise in GRACE residual range combinations

The following inputs are used in order to compute the GRACE residual range combinations: (i) 5-second observed inter-satellite ranges; (ii) 30-second reduced-dynamic orbits in February 2003 – December 2005, determined and provided by (Kroes et al., 2005); and (iii) 30-second kinematic and reduced-dynamic orbits in January 2006 – December 2009, determined and provided by the GNSS research centre of Wuhan University in accordance with (Zhao, 2004).

The square-root of noise PSD, hereafter referred to as $\text{PSD}^{\frac{1}{2}}$, of the GRACE residual range combinations is shown for 12 months of 2006 (as examples) in Fig. 3.1a. As it will be demonstrated in chapter 9, the increased noise level at low-frequencies (up to approximately 3 cpr) is a consequence of inaccuracies in the a priori orbits. This noise leads to an inaccurate estimation of zonal and near-zonal coefficients up to the highest degree considered in the gravity field retrieval. I eliminate this noise at the pre-processing stage using an empirically defined seven-parameter high-pass filter proposed by Colombo (1984) and Kim (2000):

$$r(t) = x_0 + x_1t + x_2 \cos \omega t + x_3 \sin \omega t + x_4t \cos \omega t + x_5t \sin \omega t + x_6t^2. \quad (3.1)$$

Herein, $r(t)$ are the values (in this case, GRACE residual range combinations) given by the analytical function, $\omega = \frac{2\pi}{T}$ is the orbital angular velocity with T being the orbital revolution time, and x_0 till x_6 are unknown coefficients. The latter ones are estimated per orbital revolution by fitting the analytical

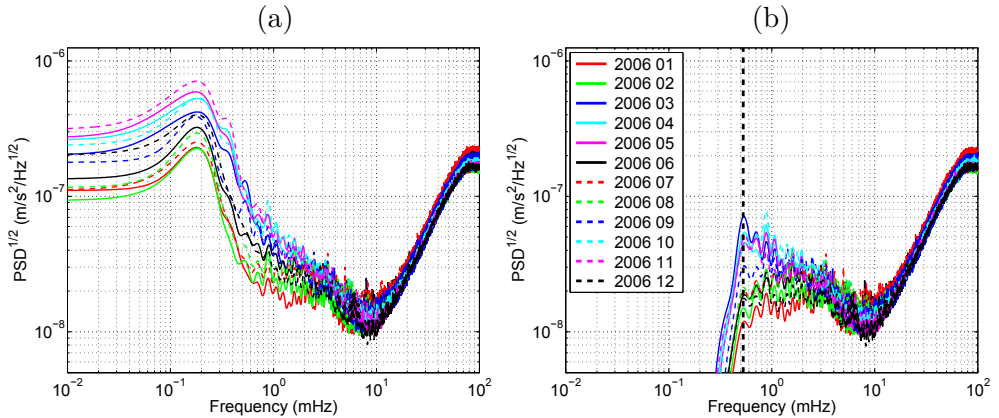


Figure 3.1: The noise $\text{PSD}^{\frac{1}{2}}$ of the GRACE residual range combinations (a) before and (b) after eliminating their low-frequency noise for 12 months of 2006. The vertical line marks the 0.5 mHz (3 cpr) frequency. A Gaussian smoothing has been applied for a better visualization.

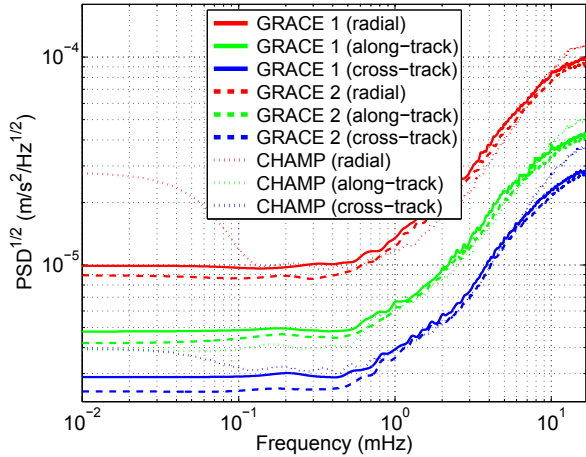
function $r(t)$ to the residual data in the least squares sense. Subsequently, the values estimated with the analytical function are subtracted from the residual data. The noise $\text{PSD}^{\frac{1}{2}}$ of the GRACE residual range combinations subsequent to this operation is shown for the same 12 months in Fig. 3.1b. A comparison of Figs. 3.1a and 3.1b demonstrates that the usage of the high-pass filter eliminates the noise in the low-frequency range up to nearly 0.5 mHz (3 cpr) frequency.

Unfortunately, the filter removes not only noise but also possible signals below 3 cpr frequency, which can be associated with low-degree spherical harmonic coefficients (particularly of degree 2 and 3). Given the fact that low-degree coefficients (at least below degree 27) in a combined GRACE/GOCE model predominantly rely on KBR data, this implies that an application of this high-pass filter to residual range combinations leads to a model bias towards the a priori static gravity field model at very low degrees. A need to mitigate this effect is the major motivation to incorporate GRACE and GOCE kinematic orbits in the gravity field modelling, as they may provide additional contribution to the estimation of low-degree coefficients.

To account for a temporal variability of noise in the residual range combinations, which can be clearly seen in Fig. 3.1, individual ARMA models are built on a monthly basis. They are highly detailed (not shown).

One may argue that the time-variability of noise in the residual range combinations is an evidence of the presence of long-term mass transport signals in these residuals. Nonetheless, as it will be shown in chapter 6, a similar variability is also observed when these signals are removed.

Figure 3.2: The noise PSD $^{\frac{1}{2}}$'s for the residual 3-D average acceleration vectors derived from the GRACE kinematic orbits in 2006 and CHAMP kinematic orbits in 2003. The solid, dashed, and dotted lines are associated with GRACE-1, GRACE-2, and CHAMP, respectively. The radial, along-track, and cross-track components are plotted in red, green, and blue, respectively. A Gaussian smoothing has been applied for a better visualization.



3.3.2 Noise in GRACE residual 3-D average acceleration vectors

Figure 3.2 shows the noise PSD $^{\frac{1}{2}}$'s for the along-track, cross-track, and radial components of GRACE satellites' residual 3-D average acceleration vectors based on data of 2006. They are similar to those of noise in CHAMP data of this type (Ditmar et al., 2007), which are also shown in Fig. 3.2 as references. This is an expected outcome, because kinematic orbits for these two missions are based on data collected by GPS receivers of a similar quality. The noise PSD $^{\frac{1}{2}}$'s shown in Fig. 3.2 are used to build ARMA models for different components of these residuals.

Furthermore, I find it worth noting that CHAMP as compared to GRACE shows slightly higher noise in the very low frequency range (below 0.1 mHz) for the radial and cross-track components. The reason for that is not known to me.

3.3.3 Noise in GOCE residual 3-D average acceleration vectors

The GOCE kinematic orbits are provided with 1-second sampling. The results to be presented in this thesis are based on a subset of them obtained by picking up every thirtieth epoch. Figure 3.3 shows the noise PSD $^{\frac{1}{2}}$'s for the along-track, cross-track, and radial components of the obtained residuals for November 2009. A comparison between Figs. 3.2 and 3.3 shows that there is a similarity between the spectra of the GRACE and GOCE-based residuals. Nevertheless, in the low-frequency range, the PSD $^{\frac{1}{2}}$'s in the case of GOCE-based residuals are higher for the radial and cross-track components. The reason for that is not known to me. One may argue that this an indication

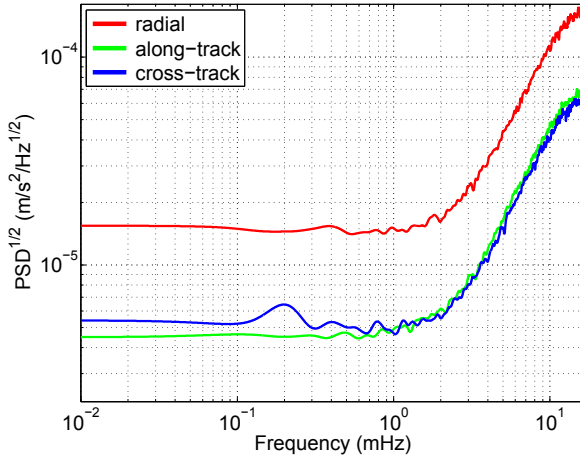


Figure 3.3: The noise $\text{PSD}^{\frac{1}{2}}$'s for the GOCE residual 3-D average acceleration vectors derived from the kinematic orbits in November 2009. A Gaussian smoothing has been applied for a better visualization.

of the presence of the gravity field signal in the GOCE-based residuals. However, I also obtained these noise PSD's by computing post-fit residuals using a combined GRACE/GOCE static gravity field model. Those noise PSD's (not shown) turned out to be similar to those shown in Fig. 3.3.

The noise $\text{PSD}^{\frac{1}{2}}$'s exhibited in Fig. 3.3 are utilized to build ARMA models for different components of the GOCE residual 3-D average acceleration vectors. I find it important to mention that I also processed the 1-second GOCE kinematic orbits. Unfortunately, the noise $\text{PSD}^{\frac{1}{2}}$'s in that case turn out to be larger than that of the 30-second data in the entire spectrum. That did not allow me to use the 1-second GOCE kinematic orbits in the gravity field modelling. My personal communications with T. Reubelt (Geodätisches Institut, Universität Stuttgart) have led me to a hypothesis that noise in the 1-second residual accelerations is highly non-stationary, and therefore, the dependence of data accuracy on time must be somehow taken into account. This means that the 1-second covariance information of GOCE kinematic orbit data, provided in `SST_PSO_2`, must be used. This hypothesis is currently being investigated by my co-promoter, P. Ditmar, and myself (outside the framework of this thesis).

3.3.4 Noise in GOCE residual gravity gradients

Figure 3.4a shows the initial noise $\text{PSD}^{\frac{1}{2}}$'s of the GOCE residual gravity gradients for the $V_{xx} = \frac{\partial^2 V}{\partial x^2}$, $V_{yy} = \frac{\partial^2 V}{\partial y^2}$, and $V_{zz} = \frac{\partial^2 V}{\partial z^2}$ components with x , y , and z being the GRF's along-track, cross-track, and nadir axes, respectively. These components are hereafter referred to as xx , yy , and zz , respectively. One can see in Fig. 3.4 that noise in all three components is close to 10^{-2} Eötvös per square root of Hertz ($\text{E}/\text{Hz}^{\frac{1}{2}}$) in the measurement frequency band, which is

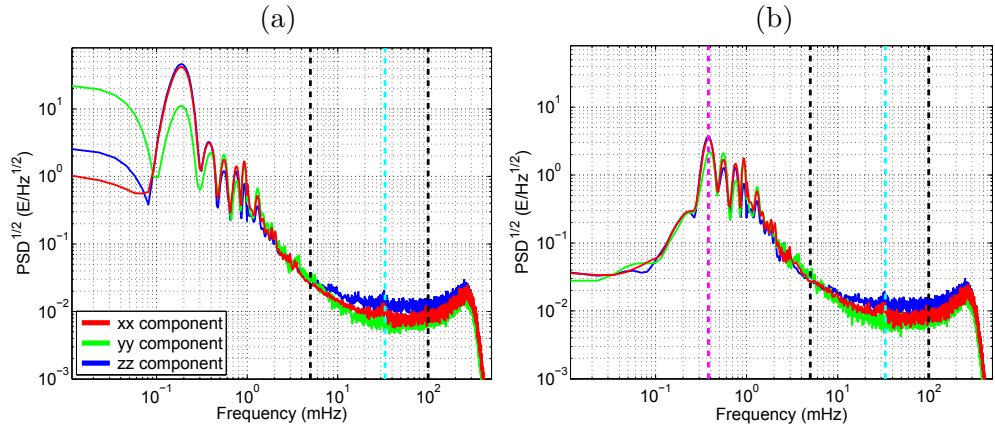


Figure 3.4: The initial noise $\text{PSD}^{\frac{1}{2}}$'s of the GOCE residual gravity gradients (a) before and (b) after eliminating the low-frequency noise using the 4-parameter high-pass filter. They are based on data of May 19, 2010. Two black vertical lines mark the measurement frequency band. The purple and cyan vertical lines mark the frequencies 0.3 mHz (2 cpr) and 30 mHz (180 cpr), respectively. A Gaussian smoothing has been applied at high frequencies for a better visualization.

consistent with other estimations (e.g., Rummel et al., 2011). Furthermore, a high level of noise at low frequencies and prominent peaks at the frequencies of 1, 2, ... cpr can be observed for all three components, which is consistent with the findings of the closed loop simulations (Bouman et al., 2004). Another features are the peaks at approximately 30 mHz (180 cpr) frequency, which reflect the fact that the exploited a priori static gravity field model is complete only to degree 180 (Ditmar et al., 2012). This is lower than what GOCE gravity gradients are to resolve. The increased noise below 30 mHz could be probably explained by a relatively low accuracy of ITG-Grace2010s at high degrees. Furthermore, a drop in noise beyond 30 mHz probably means that zero coefficients for the a priori static gravity field model beyond degree 180 are closer to the truth than the coefficients of ITG-Grace2010s near this degree.

The initial noise $\text{PSD}^{\frac{1}{2}}$'s exhibited in Fig. 3.4a are utilized to build initial ARMA models of noise in residual gravity gradients for the three components. The built ARMA models are highly detailed (not shown).

In the remaining two parts of this subsection, I compile a number of preliminary static gravity field models in order to (i) investigate the impact of the low-frequency noise in GOCE residual gravity gradients in the absence of a regularization (section 3.3.4.1); and (ii) improve the stochastic models of noise in these residuals (section 3.3.4.2). I analyse the resulting preliminary models on the basis of their geoid height differences with respect to EGM2008.

The differences are analysed per-degree and in the form of global maps over a $0.5^\circ \times 0.5^\circ$ grid, excluding the polar gaps in the GOCE satellite's spatial coverage.

3.3.4.1 Impact of the low-frequency noise

In this section, I investigate the impact of the low-frequency noise in GOCE residual gravity gradients below 2 cpr. To that end, I analyse the ability of three empirical high-pass filters to eliminate this noise prior to the inversion. One of them is the 7-parameter high-pass filter defined earlier by Eq. (3.1). The other two are defined by the first four and six terms of this equation. They are hereafter referred to as the 4- and 6-parameter high-pass filters, respectively. These filters are built and applied to GOCE residual gravity gradients in the same manner as in the case of GRACE residual range combinations. The initial noise $\text{PSD}^{\frac{1}{2}}$'s of the residual gravity gradients after the application of the 4-parameter high-pass filter are shown in Fig. 3.4b. A comparison of Figs. 3.4a and 3.4b indicates that the application of this filter eliminates the low-frequency noise up to nearly 0.3 mHz (2 cpr). The initial noise $\text{PSD}^{\frac{1}{2}}$'s associated with the 6- and 7-parameter filters (not shown) expectedly show the noise elimination up to a slightly higher frequency: 0.5 mHz (3 cpr). These initial noise $\text{PSD}^{\frac{1}{2}}$'s are transformed into highly detailed initial ARMA models (not shown).

I produce four combined GRACE/GOCE models in which the residual gravity gradients and the corresponding initial ARMA models are used without and with elimination of the low-frequency noise by means of the 4-, 6-, and 7-parameter filters. The models are complete to degree 250. The choice of maximum degree is to ensure that the gravity field signal present in GOCE gravity gradients is fully captured. The coefficients up to degree 180 are estimated as corrections with respect to ITG-Grace2010s, and above that degree as total ones. No regularization is applied. The produced models are presented in Figs. 3.5 and 3.6 respectively in terms of per-degree geoid height differences and of global maps of geoid height differences with respect to EGM2008 up to degree 250. Only the map associated with the 4-parameter filter is shown in Fig. 3.6, because the 6- and 7-parameter filters lead to very similar results. The Root Mean Square (RMS) of differences associated with the model compiled without elimination of the low-frequency noise is 1.084 m, whereas elimination of this noise using the 4-, 6-, and 7-parameter filters reduces this number to 0.387 m, 0.387 m, and 0.399 m, respectively (by about 64 %). The low-frequency noise manifests itself in the spatial domain as large differences distributed over the entire globe including the oceans (Fig. 3.6a). Given the high accuracy of EGM2008 in the oceans, these differences must largely reflect inaccuracies in the model compiled in the presence of this noise.

Figure 3.5: The unconstrained combined GRACE/GOCE static gravity field models in terms of per-degree geoid height differences with respect to EGM2008. The GOCE residual gravity gradients and the corresponding initial ARMA models of noise are used without and with elimination of the low-frequency noise by means of the 4-, 6-, and 7-parameter empirical high-pass filters.

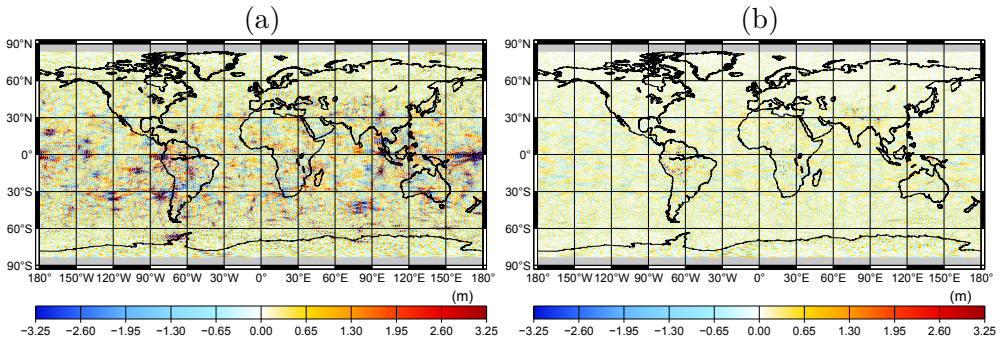
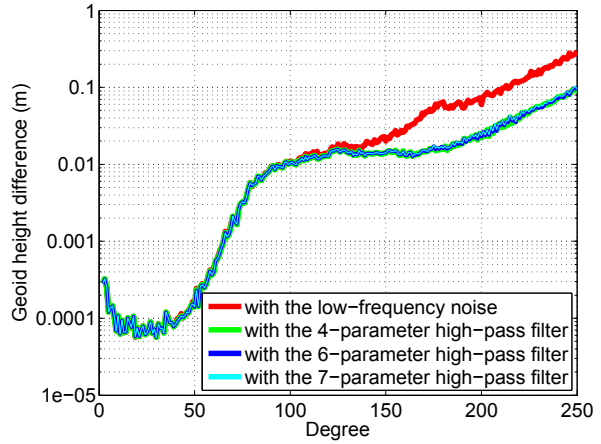


Figure 3.6: The unconstrained combined GRACE/GOCE static gravity field models in the form of global maps of geoid height differences with respect to EGM2008 up to spherical harmonic degree 250. The GOCE residual gravity gradients and the corresponding initial ARMA models of noise are used (a) without and (b) with elimination of the low-frequency noise by means of the 4-parameter empirical high-pass filter. The maps are generated over a $0.5^\circ \times 0.5^\circ$ equiangular grid, excluding the polar gaps in the GOCE satellite's spatial coverage. Their RMS values are (a) 1.084 m and (b) 0.387 m.

As one can see in Fig. 3.5, elimination of the low-frequency noise results in a reduction of per-degree differences at relatively high degrees. I explain this by the fact that the GRACE/GOCE model at low degrees is predominately determined by KBR data. The noise reduction starts to play a role from approximately degree 100 and gradually reaches 60 – 75 % at degrees 175 – 250. Furthermore, Fig. 3.5 reveals a very similar accuracy of the models compiled with the 4-, 6-, and 7-parameter filters. However, it still allows one to pick up slightly higher per-degree differences beyond degree 150 for the model compiled with the 7-parameter filter. The RMS value related to this model is also by 3 % larger than the ones obtained for the models compiled with the 4- and 6-parameter filters. Hereafter, I proceed with the 4-parameter filter. It is one of the two filters that leads to the smallest RMS value and, at the same time, less aggressive than the 6-parameter filter and as such is expected to less manipulate the signal content.

3.3.4.2 Improvement of the noise model

The production of the DGM-1S model consists of two iterations. In the first iteration, I compute a preliminary gravity field model for which purpose the initial ARMA models of noise in the GOCE residual gravity gradients are exploited. This preliminary model is also compiled up to degree 250. Then, this preliminary model is used instead of ITG-Grace2010s in the force model to obtain its misfits to the sets of the observed gravity gradients. The low-frequency noise in the obtained sets of misfits is eliminated by the 4-parameter high-pass filter. The filtered misfits are used to compute improved noise PSD's and improved ARMA models. This iterative scheme converges after only two iterations. The changes obtained in the third iteration are found to be negligible (not shown).

Both the preliminary and definitive gravity field models are compiled with a Kaula-type regularization (see Ditmar et al., 2003b) applied above degree 179. The optimal value for the regularization parameter is obtained in each case by minimizing RMS geoid height differences from EGM2008 up to degree 250 (over the same $0.5^\circ \times 0.5^\circ$ grid defined in the previous subsection).

Figure 3.7 shows the initial and improved noise $\text{PSD}^{\frac{1}{2}}$'s for the residual gravity gradients in the frequency range 5 – 45 mHz (i.e., inside the measurement frequency band) where they slightly differ. One can see in Fig. 3.7 that the peaks that are visible at the frequency 180 cpr in the initial noise PSD's do not exist in their improved counterparts.

The improved noise PSD's are transformed into highly detailed ARMA models at the three gravity gradient components (not shown). In contrast to their initial counterpart, the improved ARMA models do not contain the peaks at the frequency 180 cpr.

Figure 3.7: The initial and improved noise PSD $^{1/2}$'s of the GOCE residual gravity gradients based on data of May 19, 2010. The vertical line marks the frequency 30 mHz (180 cpr). The solid and dashed lines are related to the initial and improved noise PSD $^{1/2}$'s, respectively. The xx , yy , and zz gravity gradient components per case are plotted in red, green, and blue, respectively. A Gaussian smoothing has been applied to facilitate the comparison.

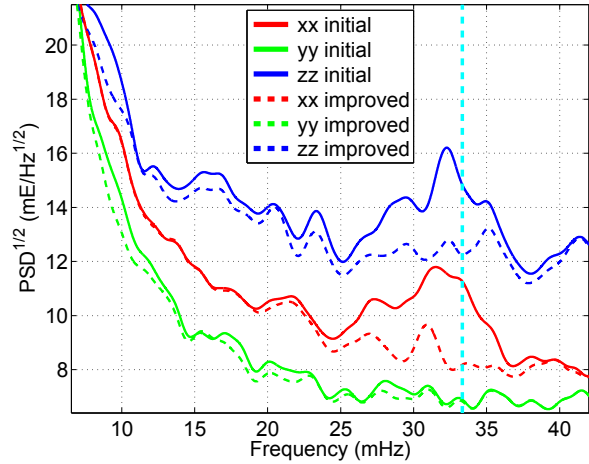


Figure 3.8: The preliminary and definitive combined GRACE/GOCE static gravity field models in terms of per-degree geoid height differences with respect to the EGM2008 model.

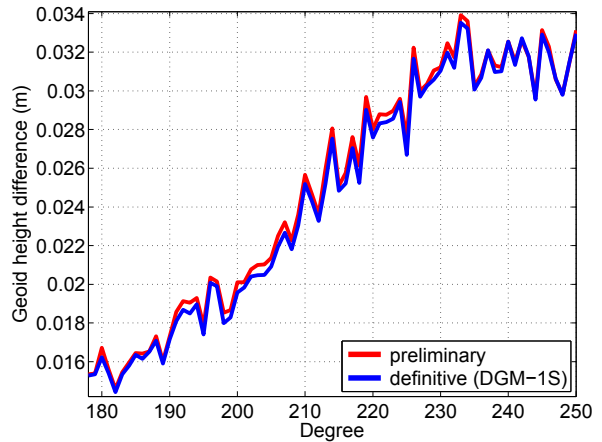


Figure 3.8 presents the preliminary and definitive models in terms of per-degree geoid height differences with respect to EGM2008 above degree 178, where one can identify slightly smaller differences for the definitive model. Given the high quality of EGM2008 at high degrees, this difference reflects a marginal improvement of the definitive model as opposed to the preliminary one. The RMS differences associated with the preliminary and definitive models in the spatial domain are respectively 0.238 m and 0.236 m, which indicate about 1 % reduction as a result of the usage of the improved ARMA models. Thus, I proceed with the improved stochastic models of noise in the residual gravity gradients.

3.4 Contribution of GOCE data to an unconstrained GRACE-only static gravity field model

In this section, I investigate the contribution of the GOCE kinematic orbits and gravity gradients, individually and jointly, to an unconstrained static gravity field recovery in the presence of the GRACE kinematic orbit and KBR data. First, I compile a GRACE-only model up to degree 180. In addition, I produce three combined ones using the GRACE data in combination with the GOCE kinematic orbit data alone, its gravity gradients alone, and the combination of the latter two data sets. The models into which the gravity gradients are incorporated are produced up to degree 250, whereas the others up to degree 180. The models are analysed in the same manner as in the previous section. They are presented in terms of geoid height differences from EGM2008: per-degree (Fig. 3.9a) and as a map (Fig. 3.10). For a fair comparison in the spatial domain, the models compiled in the presence of the gravity gradients are truncated at degree 180. The model produced from all the data sets is not shown in Fig. 3.10, because the results obtained in that case are very similar to those based on the combination of the GRACE data and GOCE gravity gradients alone. The RMS difference (computed up to degree 180) associated with the GRACE-only model is 0.501 m and those related to the GRACE/GOCE models are 0.301 m in the presence of only the GOCE kinematic orbits and 0.121 m in the presence of the GOCE gravity gradients, no matter whether or not the GOCE kinematic orbits are used.

According to Fig. 3.9a, GOCE gravity gradients start to manifest their contribution above degree 120. Reduction of per-degree geoid height differences gradually reaches about 90 % at degree 180. It results in about 75 % reduction of RMS geoid height differences in the spatial domain (when the maximum degree is set as 180). Undoubtedly, this reduction is partly explained by the fact that these data provide extra information about the gravity field. However, they also have another effect: stabilization of the system of linear equations when the normal matrix related to the GOCE gravity gradients is incorporated. This leads, in particular, to a more accurate estimation of high-degree sectorial and near sectorial coefficients, which are associated with the meridional stripes. As a result, these stripes are significantly reduced, particularly in the tropical areas, where an unconstrained GRACE-only model suffers from the anisotropic sensitivity of KBR data the most. This can be clearly observed from a comparison between Fig. 3.10a (related to the GRACE-only model) and Fig. 3.10c (related to the combined one produced in the presence of only the gravity gradients). To demonstrate this stabilization effect even more explicitly, I re-compile the model after replacing the actual gravity gradients with time series filled with zeroes. In other words, I compile an auxiliary

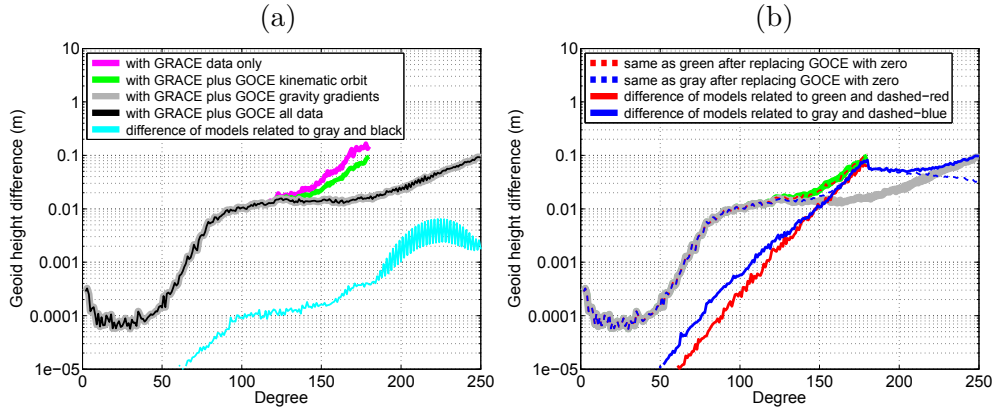


Figure 3.9: The unconstrained static gravity field model compiled solely from the GRACE data (purple) as well as the ones produced from the combinations of these data with the GOCE kinematic orbits alone (green), with the GOCE gravity gradients alone (gray), and with the latter two data sets together (black), which are all shown in the left picture. In addition, two auxiliary models are plotted in the right picture in dashed-red and dashed-blue. They are respectively the same as the models plotted in the left picture in green and gray, but after replacing the corresponding sets of GOCE data with time series filled with zeroes. That is, they are produced from the GRACE data using the normal matrices related to the GOCE data sets as regularization matrices. All the aforementioned models are presented in terms of per-degree geoid height differences from EGM2008. Besides, three curves reflect per-degree geoid height differences between three pairs of the above-described models. One is shown in cyan in the left picture, which shows the difference between model produced with all the data (black) and the one produced with the GRACE data and the GOCE gravity gradients alone (gray). The second curve is plotted in red in the right picture, which shows the difference between the model produced with the GRACE data plus the GOCE kinematic orbits alone (green) and the auxiliary counterpart of this model when the GOCE kinematic orbits are replaced with the time series filled with zero (dashed-red). Finally, the third curve is plotted in blue in the right picture, which shows the difference between the model produced with the GRACE data plus the GOCE gravity gradients alone (gray) and the auxiliary counterpart of this model when the GOCE gravity gradients are replaced with the time series filled with zero (dashed-blue).

model based on the GRACE data and using the normal matrix related to the gravity gradients as a regularization matrix. The auxiliary model is shown in Fig. 3.9b in terms of per-degree geoid height differences from EGM2008. This model also shows reduction of per-degree difference above degree 120 that gradually reaches about 45 % at degree 180. This implies that almost half of the already stated 90 % reduction is explained by the stabilization impact of the gradiometry-related normal matrix. The geoid height differences in the spatial domain (not shown) computed for the auxiliary model up to the

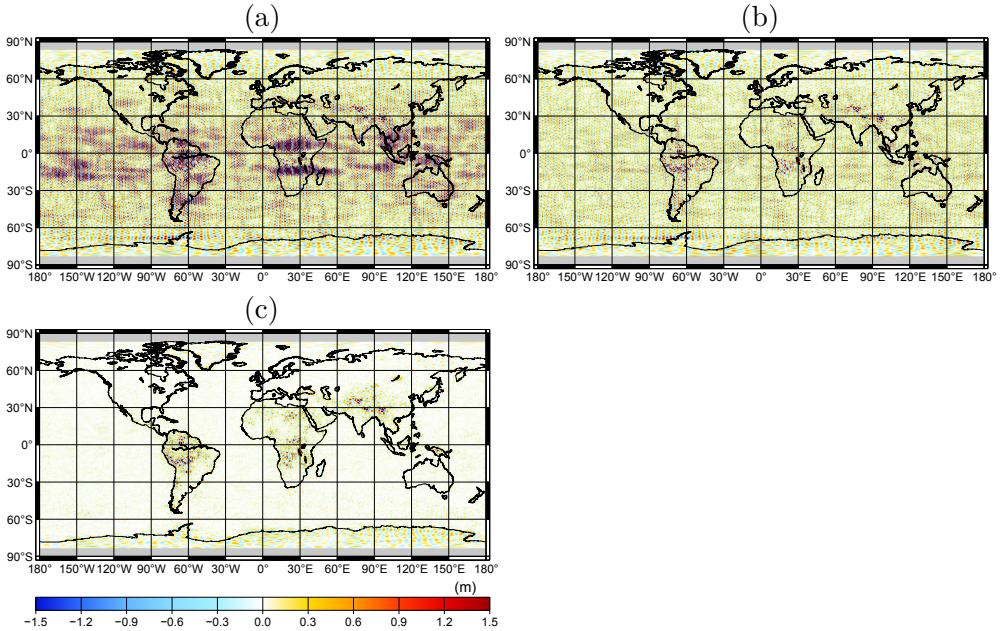


Figure 3.10: Unconstrained static gravity field models compiled (a) solely from the GRACE data sets and from the combinations of these data with (b) the GOCE kinematic orbits alone and (c) the GOCE gravity gradients alone. The results are presented in terms of geoid height differences from EGM2080 up to degree 180. The maps are generated over a $0.5^\circ \times 0.5^\circ$ grid, excluding the polar gaps in the GOCE satellite’s spatial coverage. Their RMS values are (a) 0.501 m, (b) 0.301 m, and (c) 0.121 m.

same degree also show a reduction of the meridional stripes with the RMS being reduced by almost 50 %, which explains two thirds of the aforementioned 75 % reduction when the actual gravity gradients participated. The per-degree differences between the combined model produced with the actual gravity gradients and its auxiliary counterpart is also included in Fig. 3.9b, which are at the sub-centimetre level below degree 150. This implies that the non-trivial contribution of the GOCE gravity gradients, i.e., the part of their contribution that cannot be explained by their stabilization effect, are mostly related to the coefficients above degree 150.

In the absence of the GOCE gravity gradients, an incorporation of its kinematic orbits also leads to a reduction of per-degree geoid height differences (Fig. 3.9a). This reduction also starts at degree 120, gradually reaching about 36 % at degree 180. This is in contradiction with the fact that kinematic orbits are mostly sensitive to gravity field signals in the range of low degrees. The obtained results are explained by the impact of the normal matrix related to GOCE kinematic orbits on a stabilization of the linear system of equations.

This can be clearly seen from a comparison between Fig. 3.10a (related to the GRACE-only model) and Fig. 3.10b (related to the model based on the GRACE data and GOCE kinematic orbits alone). The incorporation of the GOCE kinematic orbits has led to a reduction of meridional stripes as a result of a more accurate estimation of high-degree sectorial and near-sectorial coefficients. To provide further support for this explanation, I compile a second auxiliary model by replacing these data with time series filled with zeroes. This auxiliary model is presented in Fig. 3.9b in terms of per-degree geoid height differences from EGM2008. One can see that the corresponding curve almost coincides with its counterpart related to the model based on the actual GOCE kinematic orbits. In the spatial domain, the map of geoid height differences of the auxiliary model from EGM2008 (not shown) is also very similar to the one related to the model produced with the actual GOCE kinematic orbits (Fig. 3.10b). The RMS differences related to the former model is 0.319 m, which means that approximately 36 % out of the 40 % reduction in the RMS value after the incorporation of the GOCE kinematic orbits is related to the impact of their normal matrix.

The obtained results also suggest that an incorporation of GOCE kinematic orbits does not lead to a further improvement of a static gravity field model when GRACE data and GOCE gravity gradients are already incorporated. This can be clearly seen from a comparison of the GRACE/GOCE model produced from all the data sets and the one compiled in the presence of only the gravity gradients, which yield almost coinciding curves (Fig. 3.9a). The per-degree geoid height differences between these two models (also shown in Fig. 3.9a) are at the sub-millimetre level below degree 190 and hardly exceed a few millimetres above that degree. In addition, practically no difference can be visually identified in the spatial domain between the maps of geoid height differences of these two models from EGM2008 (not shown). The corresponding RMS differences equal 0.387 m for both models. Furthermore, the RMS geoid height differences between these two models themselves (up to degree 250) is only 0.008 m. Thus, I associate the added value of the GOCE mission to the static gravity field modelling entirely with its gravity gradients.

3.5 DGM-1S: comparison and validation

In this section, I present a preliminary analysis of DGM-1S by comparing it and three alternative GRACE/GOCE models, namely, GOCO01S, EIGEN-6S, and GOCO02S, as well as ITG-Grace2010s with EGM2008 in terms of geoid heights (the first subsection). Furthermore, I perform a validation of DGM-1S and the other five models under consideration using an independent model of the oceanic MDT (the second subsection).

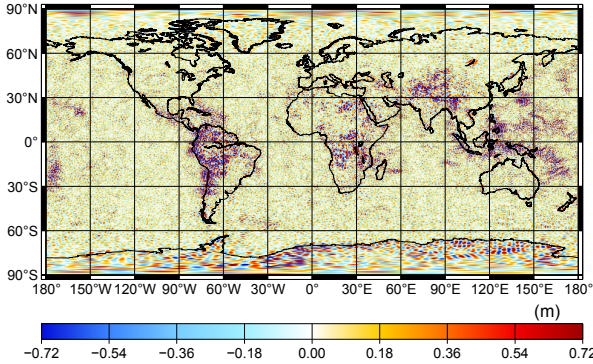


Figure 3.11: DGM-1S in terms of geoid height differences with respect to EGM2008 up to spherical harmonic degree 250. The map is generated over a $0.5^\circ \times 0.5^\circ$ global grid. The RMS of the difference is equal to 0.237 m.

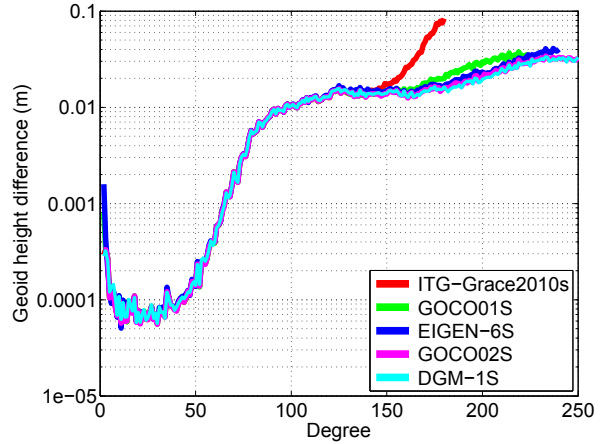
The procedure applied to produce DGM-1S is already described in sections 3.2 and 3.3. A brief description of the other models is given below.

- (i) ITG-Grace2010s is complete to degree 180 and based on seven years of GRACE KBR and kinematic orbit data (August 2002 – August 2009).
- (ii) GOCO01S is complete to degree 224 and based on a combination of ITG-Grace2010s with two months of GOCE SGG data (November – December 2009).
- (iii) GOCO02S is complete to degree 250 and based on a combination of ITG-Grace2010s with eight months of GOCE SGG data, 12 months of GOCE kinematic orbit data, eight years of the CHAMP kinematic orbit data, and five years of SLR data from five satellites.
- (iv) EIGEN-6S is complete to degree 240 and based on 7.5 years of GRACE KBR and kinematic orbit data (January 2003 – June 2009), 6.7 months of GOCE SGG data (November 2009 – June 2010), and 6.5 years of SLR data from Laser Geodynamics Satellites (LAGEOS). I recall that I only consider the static part of this model.
- (v) EGM2008 is complete to degree 2159 with some coefficients to degree 2190. It is based on a combination of ITG-Grace03 with an extended set of terrestrial gravimetry and satellite altimetry data.

3.5.1 Preliminary analysis

DGM-1S is presented in Fig. 3.11 in the spatial domain in terms of geoid height differences from EGM2008 up to degree 250. Expectedly, it reveals relatively large differences over the continental areas with a poor coverage with terrestrial gravimetry measurements (Equatorial Africa, Himalayas, and South America), where the quality of EGM2008 is relatively low. The opposite is,

Figure 3.12: Per-degree geoid height differences between EGM2008 and the other five gravity field models under assessment.



however, observed over the continental areas well covered with these measurements (Australia, North America, and the northern part of Eurasia), where EGM2008 represents the static part of the gravity field quite well. Since it is unreasonable to expect a degraded performance of the GOCE mission over the poorly surveyed continental areas, I interpret larger differences there as mostly inaccuracies in EGM2008. This issue is confirmed in chapter 4. Furthermore, Fig. 3.11 expectedly reveals relatively small differences over the majority of the oceanic areas, where EGM2008 shows a high accuracy due to the usage of satellite altimetry data (see Sandwell and Smith, 2009). At the same time, it reveals relatively large differences in a few oceanic areas that are mostly located in the Pacific Ocean. This issue is discussed in section 3.5.2.

I compare DGM-1S and the other five models under consideration with EGM2008 in terms of geoid height differences. The results are presented in terms of per-degree differences (Fig. 3.12) and of cumulative RMS differences for selected degrees (Table 3.2). The latter ones are computed globally over a $0.5^\circ \times 0.5^\circ$ grid. Figure 3.12 and Table 3.2 reveal some differences in the consistency of the five models with EGM2008, particularly below degree 60 and above degree 150. DGM-1S shows in most cases a similar or a better agreement with EGM2008 as compared to the other models, particularly at high degrees. Nevertheless, such a comparison hardly allows conclusions to be drawn regarding the actual accuracy of DGM-1S or the other five models under consideration. The following questions remain open: (1) How to interpret the disagreement between EGM2008 on the one hand and the other five models on the other hand that rapidly increases above degree 50? Is it an evidence of a lower quality of EGM2008 or an indication of an insufficient accuracy of the other five models? (2) Is it fair to interpret a relatively poor agreement of ITG-Grace2010s, GOCO01S, and EIGEN-6S with EGM2008 as an indication of a lower accuracy of these three models as compared to GOCO02S

Table 3.2: The cumulative RMS geoid height differences (in centimetres) between five gravity field models and EGM2008. They are computed globally over a $0.5^\circ \times 0.5^\circ$ grid.

Degree	ITG-Grace2010s	GOCO01S	EIGEN-6S	GOCO02S	DGM-1S
10	0.05	0.11	0.18	0.06	0.05
15	0.05	0.11	0.18	0.06	0.06
30	0.06	0.11	0.18	0.06	0.06
60	0.11	0.15	0.21	0.11	0.11
90	2.22	2.22	2.23	2.22	2.22
120	5.88	5.87	5.94	5.88	5.90
150	9.41	9.05	9.43	9.03	9.12
180	25.4	12.8	12.6	12.0	12.1
210	-	19.4	17.1	16.2	15.9
224	-	22.8	20.1	18.8	18.5
240	-	-	24.6	22.2	21.8
250	-	-	-	24.1	23.6

and DGM-1S? (3) Is it fair to state that the accuracy of models that match EGM2008 equally well is equal? Thus, a fair comparison between the models under consideration requires a validation of them against independent sets of control data. To that end, in the next subsection, I utilize one of traditional validation approaches. That is, I utilize an independent model of the oceanic MDT to perform a validation of all the six global static gravity field models under consideration.

3.5.2 Validation with an independent MDT model

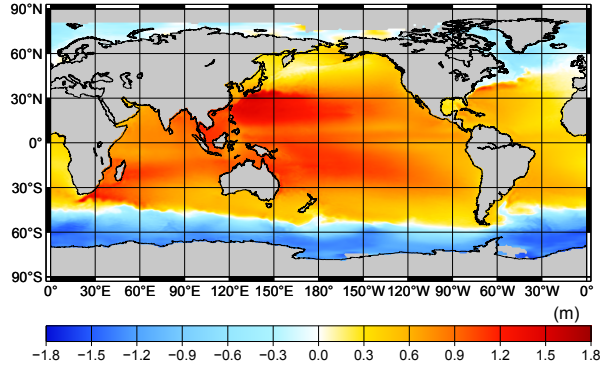
The first part of this subsection describes the method that I use to validate a static gravity field model against an independent MDT model. In addition, the input data required for an application of this method are introduced in the first part. The second part presents and analyses the results of its application to the global static gravity field models under consideration.

3.5.2.1 Methodology

The MDT ζ is defined as difference of ellipsoidal heights of the Mean Sea Surface (MSS) h and those of the geoid N (e.g., Wunsch and Gaposchkin, 1980), provided that h and N are defined in a geometrically consistent manner (i.e., that they are assigned to the same reference ellipsoid and the same permanent tide system):

$$\zeta = h - N. \quad (3.2)$$

Figure 3.13: The CNES-CLS09 MDT model. It is provided on a $0.25^\circ \times 0.25^\circ$ grid covering the world's oceans in the latitudinal range $79.125^\circ\text{S} - 80.625^\circ\text{N}$. Its minimum, maximum, and mean values are -1.695 m, 1.807 m, and 0.256 m, respectively.



I use this equation to transform static gravity field models under consideration into MDT models. To mitigate the spectral inconsistency between MSS and satellite-only geoid models (see, e.g., Losch et al., 2002; Albertella and Rummel, 2009; Slobbe et al., 2012), I augment the latter ones with a band-limited geoid model based on EGM2008.

I use CNES-CLS09 MDT model (Rio et al., 2011) as control, against which I compare the MDT models obtained from the gravity field models. CNES-CLS09 is available over a $0.25^\circ \times 0.25^\circ$ grid covering the world's oceans in the latitudinal range $79.125^\circ\text{S} - 80.625^\circ\text{N}$ (Fig. 3.13). It is fully independent from GOCE data. However, it is to some extent dependent on GRACE data, as a GRACE-based preliminary MDT model was used as the initial guess. Rio et al. (2011) obtained this initial guess using Eq. (3.2) and a GRACE-only geoid model. Before using it, they filtered this initial guess to remove noise at spatial scales smaller than 400 km. Thus, CNES-CLS09 cannot be considered as an independent source of information about the MDT at the spatial scales larger than 400 km. I ignore this limitation. There is another limitation. It lies within the fact that Rio et al. (2011) improved their initial guess by incorporating, among others, satellite-altimetric sea level anomalies. They are partly from the same sources as those contributed to the development of EGM2008. Those data were used in the production of EGM2008 after a filtering to remove their noise at the spatial scales larger than 180 km wavelength (Sandwell and Smith, 2009). This undermines the independence of validation results to be obtained for EGM2008 at the spatial scales smaller than 180 km. I ignore this limitation, too.

In the conversion of the gravity field models into the corresponding MDT models, I use the DNSC08 MSS model, which is available over the world's oceans on a $1' \times 1'$ grid (Andersen and Knudsen, 2009). I apply to it a $0.25^\circ \times 0.25^\circ$ non-weighted averaging to make it consistent with the grid of CNES-CLS09.

DGM-1S is used to compute the geoid heights on a $0.25^\circ \times 0.25^\circ$ grid to be

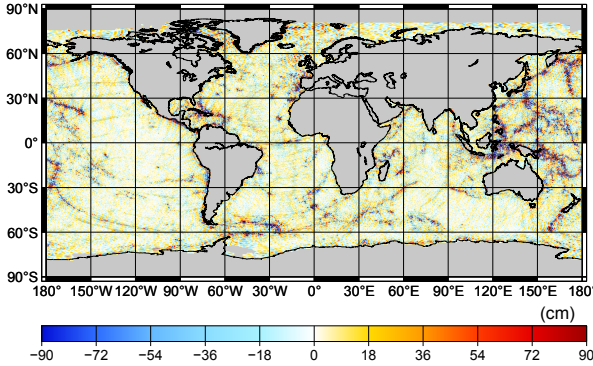


Figure 3.14: The band-limited geoid model synthesized from EGM2008 in the degree range 251 till 720 over the world's ocean on a $0.25^\circ \times 0.25^\circ$ grid. Its peak and RMS values are 5.806 m and 0.261 m, respectively.

consistent with the grid of CNES-CLS09. It is augmented with a band-limited geoid model synthesized from EGM2008 in the range from degree 251 till 720 to be of the same spatial resolution as CNES-CLS09 (i.e., 0.25°). This band-limited geoid model is exhibited in Fig. 3.14. One identifies in this picture the gravitational signature of the oceanic trenches, reaching 6 m. This signature is present in DNSC08, too. Ignoring it in a geoid model would lead to large errors in the resulting MDT model.

In the computation of the MDT model, I exclude data points where the MDT exceeds ± 2.5 m (715 data points out of a grand total of 629,447). In view of the range of CNES-CLS09 (i.e., between -1.695 m and 1.807 m), these points are considered as outliers. It is found that they are mostly located along the coasts. Hence, their likely origin is DNSC08, considering the fact that satellite altimetry data are relatively inaccurate over shallow waters.

3.5.2.2 Application and analysis

The MDT model obtained from DGM-1S is shown in Fig. 3.15a. For a comparison, five more MDT models are obtained with Eq. (3.2) from the other gravity field models and using the same procedure. For the sake of brevity, I hereafter address the obtained MDT models by the name of the corresponding gravity field models. A comparison between Figs 3.15 and 3.13 allows me to conclude that in general there is a good agreement between these MDT models and CNES-CLS09. Nevertheless, ITG-Grace2010s and the combined GRACE/GOCE MDT models show high frequency spatial features, which cannot be seen in CNES-CLS09. These features are not consistent with the nature of the MDT either. Later, I inspect them further.

The difference between the MDT models obtained from the gravity field models under consideration is plotted in Fig. 3.16. Hereafter, I formulate differences between the models in the form of percentages. To that end, in a comparison between a pair of models, I assign 100 % to the one whose misfit to the control data is larger. With this in mind, RMS misfits shown in the

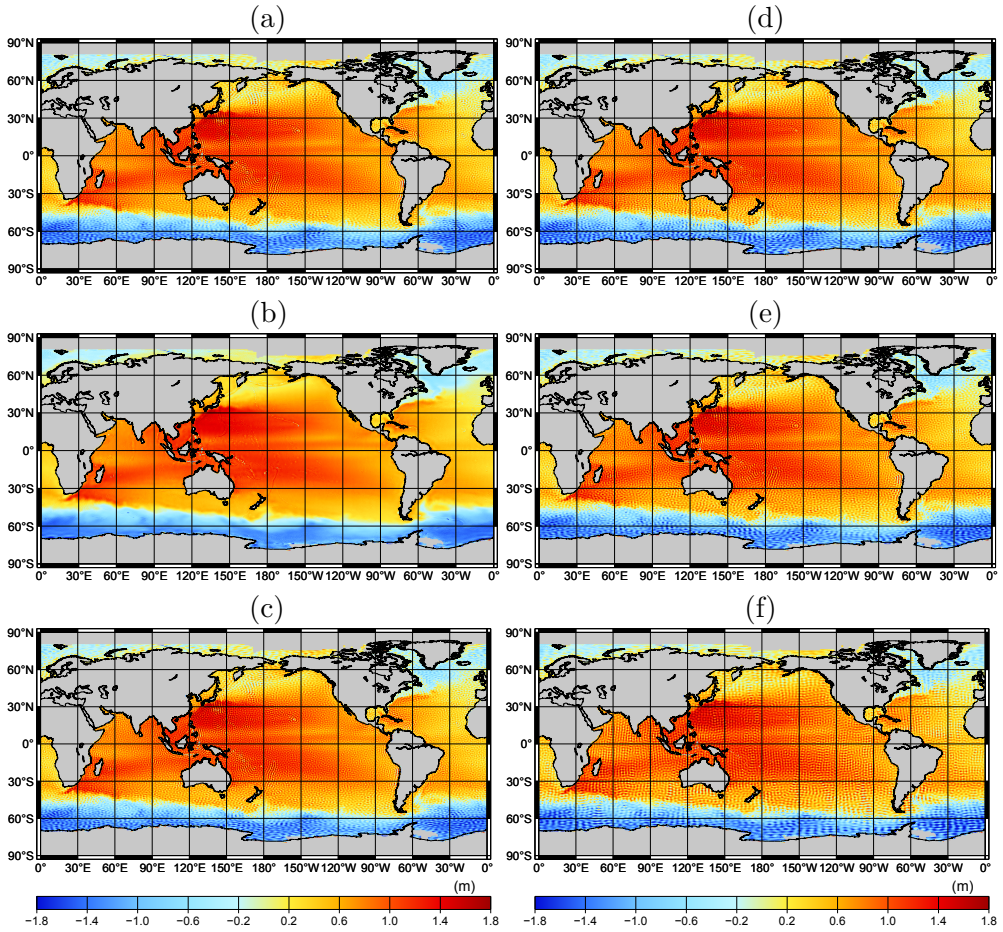


Figure 3.15: The (a) DGM-1S, (b) EGM2008, (c) GOCO02S, (d) EIGEN-6S, (e) GOCO01S, and (f) ITG-Grace2010s MDT models. The maps are generated on a $0.25^\circ \times 0.25^\circ$ grid.

caption to Fig. 3.16 suggest that DGM-1S agrees with CNES-CLS09 better than GOCO02S by about 3 %. Figure 3.16 allows one to visually identify slightly smaller differences in the case of DGM-1S as opposed to GOCO02S, particularly at high latitudes. Importantly, Fig. 3.16g reveals expected stripes in ITG-Grace2010s.

Furthermore, the RMS misfits suggest that ITG-Grace2010s, GOCO01S, and EIGEN-6S MDT models agree with the control data worse than DGM-1S by about 16 %, 2 %, and 8 %, respectively. One may argue that this may have been caused by the fact that the former models are complete respectively to degree 180, 224, and 240, whereas the latter one to degree 250. To verify that, I truncate all the models at degree 180, 224, and 240. In addition, I truncate

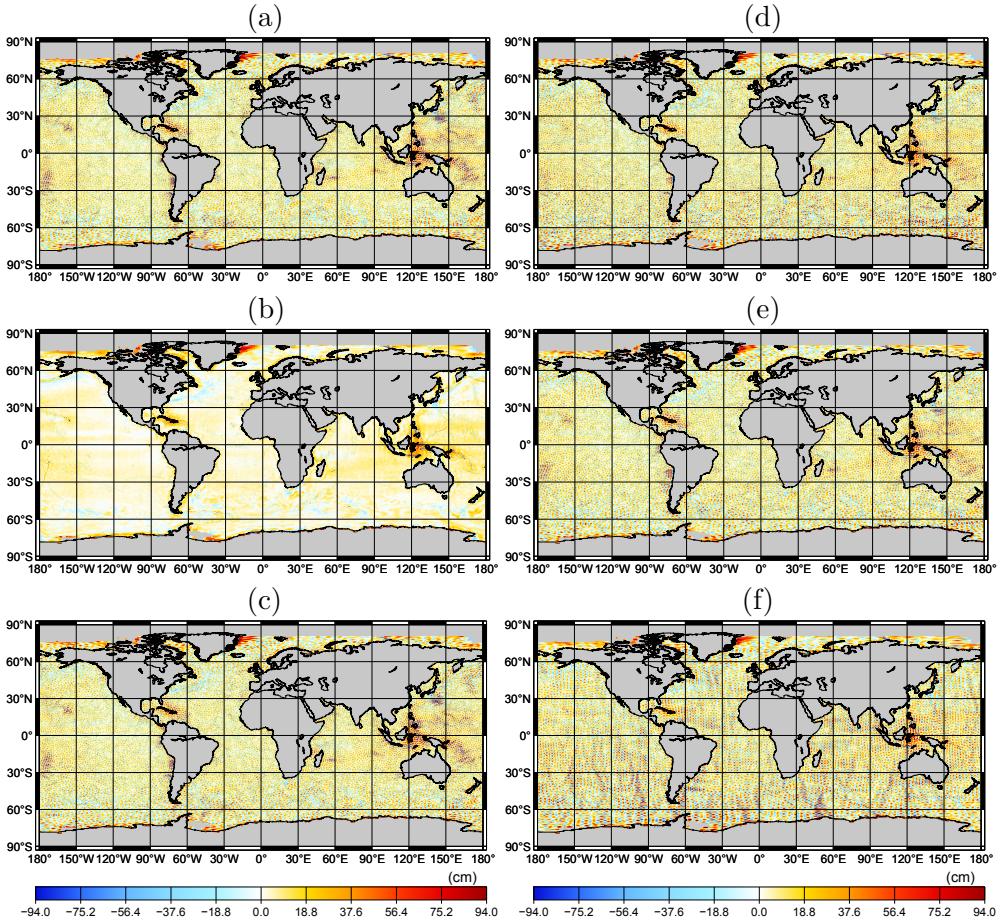


Figure 3.16: The difference of (a) DGM-1S, (b) EGM2008, (c) GOCO02S, (d) EIGEN-6S, (e) GOCO01S, and (f) ITG-Grace2010s MDT models from CNES-CLS09. The maps are generated on a $0.25^\circ \times 0.25^\circ$ grid and their respective RMS values are (a) 0.254 m, (b) 0.179 m, (c) 0.261 m, (d) 0.277 m, (e) 0.258 m, and (f) 0.304 m.

them at degree 200, i.e., the maximum degree to which an accurate GOCE gravity field retrieval is expected according to the mission objectives. Then, I repeat the procedure. The RMS misfits related to all the six models are presented in Table 3.3. In addition, differences of the DGM-1S MDT model from CNES-CLS09 obtained after the truncation at degree 240, 224, and 180 are shown in Fig. 3.17. Table 3.3 shows that DGM-1S agrees with CNES-CLS09 better than ITG-Grace2010s, GOCO01S, and EIGEN-6S by respectively 40 %, 16 %, and 13 % when DGM-1S is truncated consistently at maximum degree of the latter models. Thus, the differences are now even larger than those in the initial setup. This can also be visually identified by comparing the maps shown in Fig. 3.17 with those shown in the right panel of Fig. 3.16.

Table 3.3: The RMS misfits (in meters) of the obtained MDT models from the CNES-CLS09 MDT model as a function of spherical harmonic degree above which the corresponding geoid models are augmented with the EGM2008 model. They are computed in the world's oceans in the latitudinal range $79^{\circ}\text{S} - 81^{\circ}\text{N}$ over a $0.25^{\circ} \times 0.25^{\circ}$ global grid.

Degree	EGM2008	ITG- Grace2010s	GOCO01S	EIGEN- 6S	GOCO02S	DGM- 1S
250	0.179	-	-	-	0.261	0.254
240	0.179	-	-	0.277	0.247	0.240
224	0.179	-	0.258	0.236	0.221	0.216
200	0.179	-	0.214	0.199	0.192	0.190
180	0.179	0.304	0.190	0.186	0.183	0.183

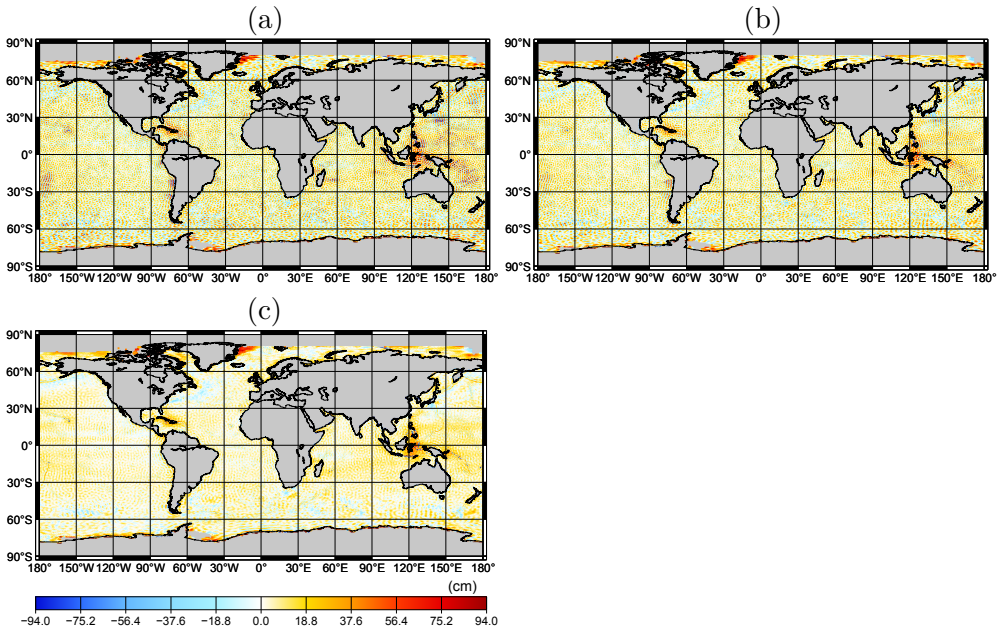


Figure 3.17: The difference of the DGM-1S MDT model from the CNES-CLS09 MDT model after the truncation at spherical harmonic degree (a) 240, (b) 224, and (c) 180. The maps are respectively consistent with those related to EIGEN-6S, GOCO01S, and ITG-Grace2010s (Figs. 3.16d – 3.16f) in maximum spherical harmonic degree. They are generated on a $0.25^{\circ} \times 0.25^{\circ}$ global grid and their RMS values are (a) 0.240 m, (b) 0.216 m, and (c) 0.183 m.

It is worth noting that GOCO01S in the initial setup shows smaller RMS misfit than GOCO02S. I explain it by the fact that the former model in the initial setup is augmented above degree 224 unlike the latter model, which is augmented above degree 250. This means that GOCO01S in the initial setup benefits more from the high quality of EGM2008 at high degrees. When GOCO02S is truncated at degree 224, it shows a better match to the control data than GOCO01S (Table 3.3).

On the other hand, the MDT models based on DGM-1S and the other combined GRACE/GOCE models show a much worse agreement with CNES-CLS09 than the EGM2008 MDT model (by 30 – 35 %). In particular, they systematically show relatively large differences in the Pacific Ocean. They show an increased level of inconsistency at high spatial frequencies, too. This is likely due to a relatively poor performance of DGM-1S and the other combined GRACE/GOCE models at high degrees, particularly above degree 200. Figure 3.18 presents the differences between these MDT models and CNES-CLS09 obtained after the truncation of the combined GRACE/GOCE models at degree 200. The map related to EGM2008 is also included to facilitate the comparison. One can see from Fig. 3.18 and Table 3.3 that the MDT models based on the combined GRACE/GOCE models still agree with CNES-CLS09 worse than EGM2008, but the differences are now reduced to only 6 – 16 %. A part of the high-frequency inconsistencies identified in the case of the GRACE/GOCE models may have been also caused by an artificial jump introduced when these models are augmented with EGM2008. To verify this hypothesis, I introduce a transition range where coefficients are defined via a weighted averaging using the tapered cosine function as the averaging weight. This range is defined as 200 – 224 in the case of GOCO01S, 200 – 240 in the case of EIGEN-6S, and 200 – 250 in the case of GOCO02S and DGM-1S. The differences between the resulting MDT models and CNES-CLS09 still show high-frequency inconsistencies (Fig. 3.19). The RMS differences in this setup for GOCO01S, EIGEN-6S, GOCO02S, and DGM-1S are 0.228 m, 0.218 m, 0.212 m, and 0.208 m respectively. Thus, EGM2008 as opposed to these models still shows a better agreement with CNES-CLS09 (by 15 – 22 %). Thus, the tests conducted so far do not allow added value of GOCE data in the oceanic areas to be seen.

To investigate this issue further, I produce MDT models based on the considered gravity field models up to truncation degree in the range 2 – 250 in the same manner as in the initial setup (i.e., without a tapered cosine weighting). The RMS differences of the resulting MDT models from CNES-CLS09 are plotted in Fig. 3.20 as a function of the truncation degree. The results related to ITG-Grace2010s are included for the completeness. One can see in Fig. 3.20b that three of the combined GRACE/GOCE MDT models, namely, GOCO01S, GOCO02S, and DGM-1S, do show slightly smaller RMS misfits

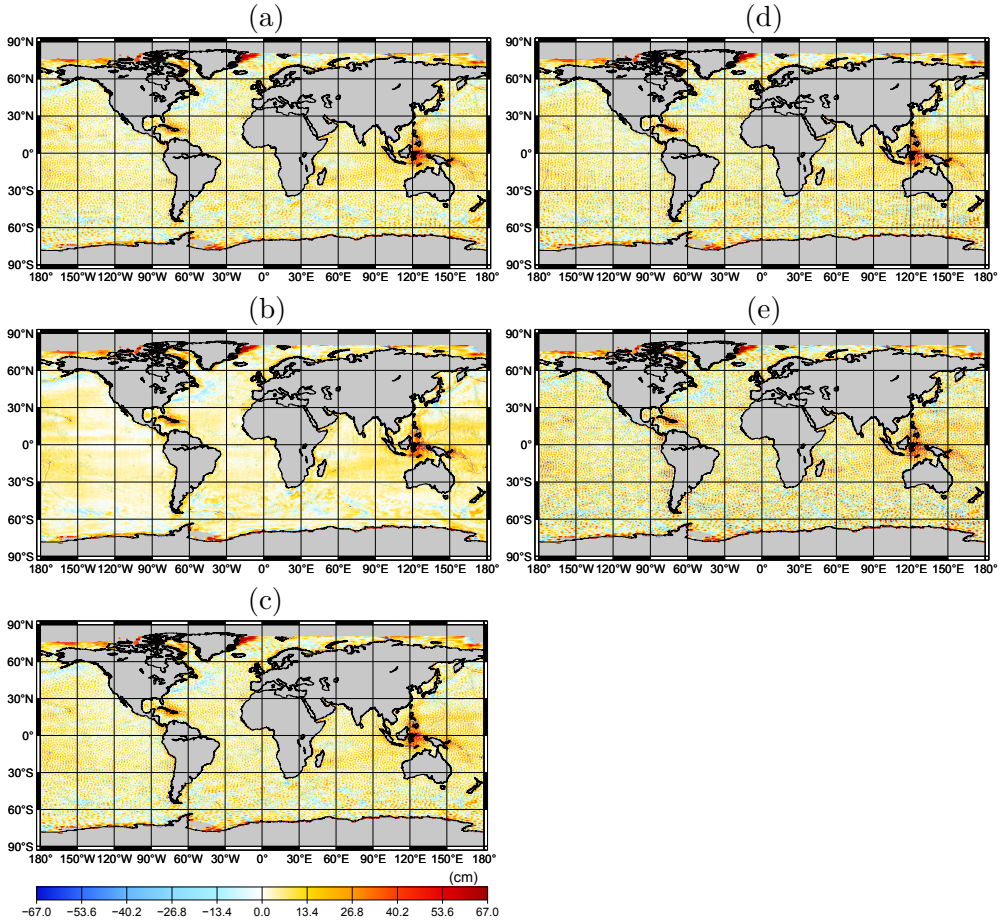


Figure 3.18: The difference of the (a) DGM-1S, (b) EGM2008, (c) GOCO02S, (d) EIGEN-6S, and (e) GOCO01S MDT models from CNES-CLS09 when the combined GRACE/GOCE models are truncated at degree 200. The maps are generated on a $0.25^\circ \times 0.25^\circ$ grid. Their RMS values are (a) 0.190 m, (b) 0.179 m, (c) 0.192 m, (d) 0.199 m, and (e) 0.214 m.

than EGM2008 in the degree range 110 – 155. In the case of a higher truncation degree, RMS misfits for all the considered combined GRACE/GOCE models rapidly exceed that of EGM2008. It is worth noticing in Fig. 3.20b the range of degree from 80 till 110, where DGM-1S and the other combined GRACE/GOCE models show slightly larger RMS misfits than EGM2008. I explain it by the previously mentioned jump between the coefficients of the combined GRACE/GOCE models and those of EGM2008 at the degree above which the former models are augmented with the latter one. To demonstrate that, I perform such a combination at each degree via a weighted averaging the weights being defined by the tapered cosine function. To that end, I define

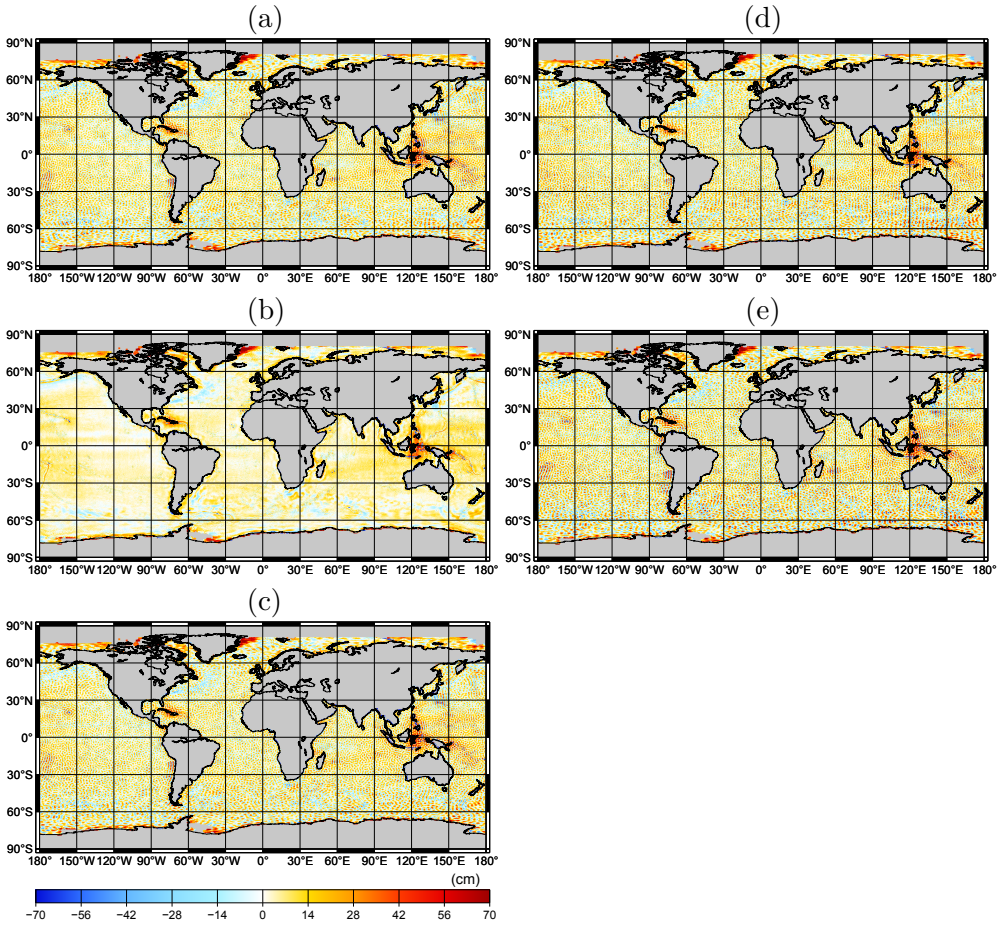


Figure 3.19: The difference of the (a) DGM-1S, (b) EGM2008, (c) GOCO02S, (d) EIGEN-6S, and (e) GOCO01S MDT models from CNES-CLS09 when the combination of EGM2008 and the combined GRACE/GOCE models is performed via a weighted averaging using the tapered cosine function as the averaging weight. The maps are generated on a $0.25^\circ \times 0.25^\circ$ grid. Their RMS values are (a) 0.208 m, (b) 0.179 m, (c) 0.212 m, (d) 0.218 m, and (e) 0.228 m.

for each truncation degree a 40-degree wide transition range centred at that degree. The RMS differences of the resulting MDT models from CNES-CLS09 are plotted in Fig. 3.21. One can see that the increased discrepancy in the degree range 80 – 110 observed in Fig. 3.20b now disappears.

Another positive outcome of this setup is that Fig. 3.21 as compared to Fig. 3.20b allows one to identify a larger degree range where DGM-1S shows smaller RMS misfits than EGM2008: 80 – 170. It also reveals the differences in this degree range in a slightly more pronounced manner. Those differences are, however, still marginal (not more than 1 %). Besides, they can only be

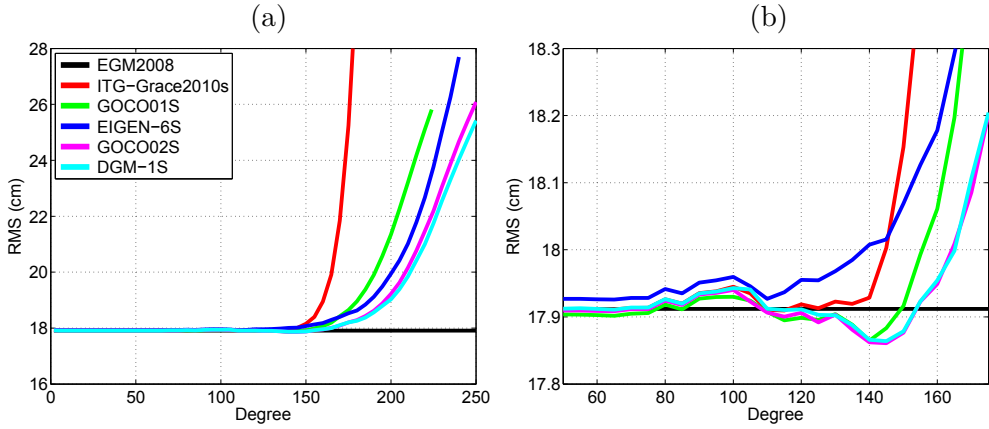
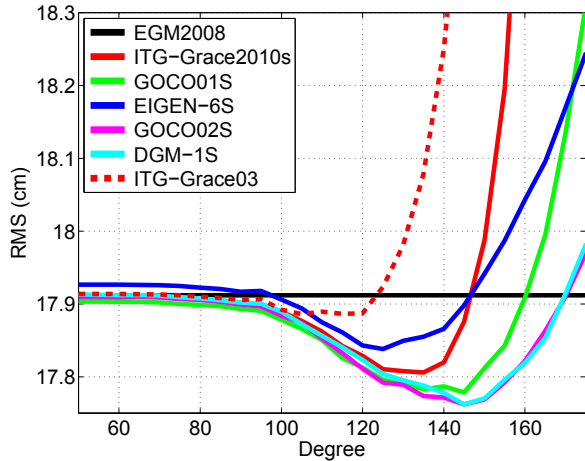


Figure 3.20: The cumulative RMS differences of the obtained MDT models from CNES-CLS09 as a function of truncation spherical harmonic degree. The considered degree range is (a) 2 – 250 and (b) 50 – 175.

Figure 3.21: The same as Fig. 3.20b, but the combination of the EGM2008 model and the other gravity field models at each truncation spherical harmonic degree is performed with a weighted averaging using the tapered cosine function as the averaging weight.



partly related to the added value of the GOCE data as ITG-Grace2010s also shows smaller RMS misfits than EGM2008 in a large part of the aforementioned degree range.

Given the fact that EGM2008 uses ITG-Grace03 as GRACE pseudo data, there may be two explanations for the latter observation: (i) the usage of more GRACE data in ITG-Grace2010s than its predecessor, i.e., ITG-Grace03; and (ii) a loss of information content of ITG-Grace03s in the production of EGM2008. To verify these hypotheses, I also include in Fig. 3.21 the results related to ITG-Grace03. A comparison between these results and those related to ITG-Grace2010s allows me to conclude that the first explanation is likely close to the truth. However, the second one has also played a role. In the next two chapters, I will demonstrate using the other sources of independent data that EGM2008 has experienced a loss of information content of ITG-Grace03 in some areas, including the oceans.

The validation of DGM-1S based on an independent MDT model provides useful insights into its quality over the world's oceans. To assess its accuracy also in the continental areas, I develop and perform a novel validation methodology based on independent satellite gravimetry data. This allows the accuracy of DGM-1S and the other considered gravity field models to be further analysed over the oceanic areas, too. This new validation methodology and the results of its application are documented in the next chapter.

3.6 Summary, discussion, and conclusions

A new combined GRACE/GOCE model entitled DGM-1S was developed. In its production, KBR data were used in the form of range combinations. Gravity gradients were processed in the GRF. Kinematic orbits were used in the form of 3-D average accelerations. All these data were reduced to residuals from ITG-Grace2010s. Frequency-dependent data weighting was applied to deal with the colored noise and ensure an optimal data combination. It was found that noise in residual range combinations shows rather strong month-to-month time variability. To account for that, I built and used individual stochastic noise model for each month.

In the production of DGM-1S, I used GRACE data in February 2003 – December 2009. One may argue that these data in February 2003 – August 2009 were already incorporated into ITG-Grace2010s so that it was unnecessary to consider them again. However, I did not have an access to the full noise covariance matrix of that model, so that a re-usage of GRACE data was needed to combine them with GOCE data in a statistically optimal manner. Besides, this matrix is huge in size and it would be technically problematic to use it anyway.

The analysis performed in the absence of regularization indicated that the low-frequency noise in GOCE residual gravity gradients should be eliminated up to 1 cpr frequency prior to the inversion. It was shown that this noise could lead to a degradation of the model quality above degree 100 in the combined GRACE/GOCE gravity field retrieval. One may view this as counter-intuitive. However, this can be explained by the facts that (i) low-frequency noise in the time domain maps onto zonal and nearly zonal coefficients to the highest degree considered in the static gravity field modelling (in the case of a nearly-polar satellite orbit); and (ii) the quality of a combined GRACE/GOCE model below degree 120 is predominately controlled by KBR data.

In the production of DGM-1S, it was shown that an improvement of the stochastic model of noise in GOCE residual gravity gradients using a newly computed GRACE/GOCE model leads to only a marginal improvement of the final gravity field model and only at relatively high degrees (above degree 180).

Prior to the production of DGM-1S, I attempted to identify the contribution of GOCE kinematic orbits and gravity gradients, separately and jointly, in the unconstrained gravity field retrieval in the presence of GRACE data. In doing so, I found it important to distinguish between the non-trivial contribution of GOCE data and the trivial one. The latter is a part of their contribution that can be explained by the stabilization effect of the normal matrix related to them. I refer to it as trivial, because it can also be achieved by a regularization and without a need to use real data. GOCE kinematic orbits in the absence of gravity gradients were found to provide a contribution above degree 120. That was, however, shown to be almost entirely trivial. The experiment allowed the contribution of GOCE gravity gradients to be identified above degree 120. At degree 180, the usage of those data led to a 75 % reduction of geoid height errors. However, nearly two thirds of this reduction was found to be trivial. The non-trivial portion of the contribution was found to be related to the coefficients above degree 150. Furthermore, it was found that the incorporation of GOCE kinematic orbits in the presence of GRACE data and GOCE gravity gradients does not lead to a trivial or not-trivial contribution. The implication is that the added value of the GOCE mission to static gravity field models is fully linked to the gravity gradiometry data acquired by this mission.

The performance of DGM-1S was compared with that of three of alternative GRACE/GOCE models (GOCO01S, EIGEN-6S, and GOCO02S) using CNES-CLS09: an oceanographic MDT model, fully independent from GOCE data, and covering almost the entire world's oceans. DGM-1S was found to match CNES-CLS09 better than GOCO01S, EIGEN-6S, and GOCO02S by about 16 %, 13 %, and 3 %, respectively, in terms of RMS misfits (having considered DGM-1S up to the maximum degree of the model against which it is compared). ITG-Grace2010s and EGM2008 were included in this test, too.

The combined GRACE/GOCE models were found to perform much better than ITG-Grace2010s in this test. Importantly, the test succeeded to reveal the expected stripes in ITG-Grace2010s. To perform an assessment of the added value of the GOCE mission over the oceanic areas, I looked into the test results obtained for the combined (satellite-only) GRACE/GOCE models and those related to EGM2008. The test did not allow the GOCE mission's added value in the world's ocean to be seen when DGM-1S (or the other considered combined GRACE/GOCE models) were considered up to their maximum degree. In contrast, it suggested that these models are influenced by a high-frequency random noise mostly above degree 200. When these models were truncated at degree 200 or lower degrees, the results obtained for three of the combined GRACE/GOCE models (DGM-1S, GOCO01S, and GOCO02S) did eventually reveal a marginal model improvement in the degree range 80 – 170 due to the usage of GOCE data.

Importantly, from the validation based on the control MDT model, the relatively large geoid height differences between DGM-1S and EGM2008 (Fig. 3.11) in some areas in the Pacific ocean (reaching in most cases ± 70 cm) were found to be mostly related to inaccuracies of DGM-1S. The reason for that remains to be identified.

In this thesis, GOCO03S, i.e., a latest combined GRACE/GOCE model, is not included in the list of models assessed. That model uses 18 months of GOCE gravity gradients. This is much more than that was used in the production of the combined GRACE/GOCE models tested. Nevertheless, it has been shown in (Farahani et al., 2013b) that all the problems that are revealed for the combined GRACE/GOCE models in the validation against the control MDT model (i.e., the presence of systematic errors in the Pacific ocean and high-frequency random inaccuracies) are present in GOCO03S, too. Of course, these problems manifest themselves in that model in a slightly less pronounced manner. For instance, GOCO03S as compared to EGM2008 shows a larger RMS misfit to CNES-CLS09: by about 4 % (when GOCO03S is augmented with EGM2008 above degree 200). In the case of GOCO02S, this mismatch was found to be only slightly larger: about 7 %.

Finally, it is worth mentioning that in my dissertation (with the exception of chapter 7) I extracted KBR data from the release 1 of GRACE level-1B data. These data contain systematic inaccuracies identified by Horwath et al. (2011). Besides, I used an early release of GOCE gravity gradients in my research. More specifically, those re-produced based on the improved calibration methodology (Siemes et al., 2012) were not used in my work. Therefore, more accurate gravity field models might be produced with the presented methodology when the latest releases of these data are used. In addition, GOCE satellite is still delivering new data, which are highly anticipated to improve gravity field models further.

4 Validating global static gravity field models using KBR and gradiometry data

This chapter is based to a large part on a manuscript published by Farahani et al. (2013a), who developed a new procedure for validating global static gravity field models using independent GRACE KBR data and GOCE gravity gradients, i.e., data that have not been used in the production of models under consideration. They applied that procedure to a number of recent models: GRACE-only models (e.g., ITG-Grace2010s), combined satellite-only GRACE/GOCE models (e.g., DGM-1S), and EGM2008. That application led not only to a validation of those models, but also to a quantification of the added value of the GOCE mission to the static gravity field modelling all over the globe, including the oceans.

4.1 Introduction

The primary objective of this chapter is to extend the set of tools for validation of global static gravity field models. To that end, I introduce an alternative validation procedure, in which the accuracy of models is assessed in terms of their ability to forecast data delivered by satellite gravity missions themselves. Two types of control data are considered: KBR data from the GRACE mission and gravity gradients from the GOCE mission. Each of them has its pros and cons. The KBR measurements contain extremely accurate information about the gravity field. These measurements are particularly sensitive to signals at relatively low degrees, so that even temporal gravity field variations due to, e.g., natural mass transport, can be reliably sensed (Wahr et al., 1998). They contain also some information about the gravity field signal up to high degrees: 180 or even higher (Ditmar et al., 2012). In addition, these data cover practically the entire surface of the Earth due to a nearly polar orbit of the GRACE satellites. Unfortunately, the sensitivity of KBR data is highly anisotropic. They are much more sensitive to the North-South variations of the gravity field than to the East-West ones. This can be easily understood from the fact that the GRACE configuration can be seen as a realization of a very large, one-component, along-track gradiometer (Keller and Sharifi, 2005).

Most of the time, the arm of this gradiometer is nearly parallel to the meridional direction and, therefore, almost “blind” to the East-West gravity gradients. The implication is that a validation based on KBR data alone cannot provide comprehensive information about the quality of models. In contrast, GOCE gravity gradients contain information about spatial variations of the gravity field in all directions. Furthermore, the extraordinary low altitude of the GOCE satellite facilitates a high sensitivity of these measurements to small-scale spatial variations of the gravity field, namely, to signals up to degree 200 – 250. A drawback of these measurements is an increased noise level at low frequencies, especially at those associated with spherical harmonics of degree 27 and below (Rummel et al., 2011). Furthermore, the geographical distribution of GOCE measurements suffers from polar gaps of approximately 1500 km in diameter. Thus, I find it essential to consider control data of both types to benefit from the advantages of each of them.

Generally, it is always advisable to utilise only independent data for the model validation. In this thesis, I define independent data as those that have not been incorporated into models under consideration. In this manner, I reduce the likelihood of misleadingly obtaining the most favourable results for the models in the computation of which GRACE KBR data and/or GOCE gravity gradients have been over-weighted. Fortunately, acquiring independent data of these types is currently not a problem, as both the GRACE and GOCE missions are still operational and keep delivering new measurements.

In this chapter, I apply the proposed validation methodology to DGM-1S and five other global static gravity field models already mentioned in the previous chapter: EGM2008 as a state-of-the-art pre-GOCE model based on GRACE and terrestrial gravimetry/satellite altimetry data; ITG-Grace2010s as a state-of-the-art GRACE-only model; and three combined satellite-only GRACE/GOCE models, namely, GOCO01S, EIGEN-6S, and GOCO02S. A brief description of these five models can be found in the previous chapter (section 3.5).

The chapter is structured as follows. Section 4.2 is devoted to the description of the validation methodology. The results of its application to the six considered models (EGM2008, ITG-Grace2010s, GOCO01S, EIGEN-6S, GOCO02S, and DGM-1S) are presented in section 4.3. In that section, I (i) compare the performance of the combined GRACE/GOCE models; and (ii) study the added value of the GOCE mission to the static gravity field modelling. The latter is performed by comparing the performance of the combined (satellite-only) GRACE/GOCE models with that of either EGM2008 or ITG-Grace2010s depending on which of the two performs better in a given geographical region. Section 4.4 is left for a summary, discussion, and conclusions.

4.2 Methodology

In this section, I describe (i) the way in which GRACE KBR and GOCE SGG control data are exploited in the validation methodology (the first subsection); (ii) the way in which misfit of static gravity field models to these data are computed (the second subsection); and (iii) further steps that are required prior to the usage of misfit data for an assessment of the quality of the models (the third subsection).

4.2.1 Validation data

Similar to the model production, described in the previous chapter, GOCE gravity gradients in the validation procedure are processed in the GRF. Importantly, these measurements can be considered as “in situ”. This means that each of them reflects the gravity field only in the vicinity of the measurement point. In other words, the functional model that relates parameters of the gravitational field with these data is “local”. Only the accurately measured components in these data are used in the validation of the models. This includes the diagonal components plus the only accurately measured off-diagonal component, i.e., $V_{xz} = \frac{\partial^2 V}{\partial x \partial z}$, which is hereafter referred to as the xz component.

Local functional models are definitely preferable for a model validation, because they facilitate the model assessment in different geographical regions individually. Thus, I utilise a local functional model in the context of KBR control data, too. More specifically, I continue to use these data in the form of range combinations.

4.2.2 Computing misfit data

The validation procedure makes use of misfits between model-based quantities and observations. They are hereafter referred to as “GRACE misfit range combinations” and “GOCE misfit gravity gradients”. The comparison between sets of misfit data associated with various static gravity field models allows conclusions to be drawn regarding the quality of those models.

The sets of GRACE misfit range combinations and GOCE misfit gravity gradients are obtained with respect to static gravity field models to be assessed. A set of these misfits is obtained in the same manner as a residual set of the corresponding data type is produced with respect to an a priori gravity field model in the context of model production (see section 2.3 in chapter 2). The force model exploited to that end includes a static gravity field model to be tested. Apart from that, the force model accounts for all the other contributors mentioned in chapter 3 (section 3.2). Additionally, in view of the high

sensitivity of KBR data to the temporal variations of the gravity field (Wahr et al., 1998), the long-term (i.e., with a characteristic time longer than one month) gravity field variations are included in the force model. The need to account for these variations is explained in the following. At many geographical locations, a prominent annual cycle of mass variations of hydrological origin takes place. Moreover, in some regions (mostly located in the polar areas), a steady accumulation or loss of mass occurs due to the postglacial rebound and shrinking of polar ice sheets. Therefore, a discrepancy between a static gravity field model and KBR control data collected at a certain moment of time may reveal not only inaccuracies of the model, but also an evolution of the gravity field in the course of time.

To mitigate the latter effect, I complement the force model with a term described by Eq. (4.1), namely, a model $m^{(LT)}(t)$ of long term (LT) gravity field variations. To that end, I use the release 4 of the Centre for Space Research (CSR)'s GRACE-based monthly gravity field solutions $m^{(CSR)}(t)$ (Betadpur, 2007) processed with an anisotropic filter in accordance with (Kusche et al., 2009). Before using these solutions, I correct them for a non-zero mean $\overline{m^{(CSR)}(t)}$:

$$m^{(LT)}(t) = m^{(CSR)}(t) - \overline{m^{(CSR)}(t)}. \quad (4.1)$$

The latter is computed as the mean of the monthly gravity field solutions in the time interval that coincides with the one covered by KBR data used in the production of the static gravity field model under assessment. The necessity of this operation can be understood from the fact that the long-term variations of the gravity field are not removed from KBR data prior to the computation of a static gravity field model. Since KBR data are practically the only source of information about the temporal gravity field variations, such a model is nothing but the mean gravity field in the time interval covered by KBR data used in its computation. Thus, by subtracting the non-zero mean $\overline{m^{(CSR)}(t)}$ computed over the same time interval, I ensure that $m^{(LT)}(t)$ approximates nothing but the deviation of the instantaneous gravity field from the reference level defined by the static gravity field model under consideration. This deviation includes, among others, the annual variations and the linear trend.

4.2.3 Suppressing noise

In the first instance, the validation is performed in the spectral domain on the basis of the PSD of the obtained misfit data. However, a spectral analysis of misfits does not allow identifying the geographical regions responsible for those misfits. Therefore, I find it essential to analyse the misfit data sets in the spatial domain as well. This requires improving signal-to-noise ratio in

the sets of misfit data. It is worth noting that “signal” in the context of the model validation is defined as inaccuracies of a given static gravity field model propagated into the corresponding sets of misfit data.

As it was mentioned earlier, the misfit data of both types show an increased level of noise at low frequencies. This noise exceeds the noise level at mid-frequencies (which I define as 0.5 – 10 mHz and 5 – 100 mHz for GRACE range combinations and GOCE gravity gradients, respectively) approximately 30 and 300 times in the case of the GRACE and GOCE misfit data, respectively. In the misfits of the former type, this noise is eliminated using a high-pass filter based on the seven-parameter empirical model, defined in the previous chapter (section 3.3.1). The elimination of the low-frequency noise in the case of GOCE misfit gravity gradients is achieved in a similar manner, but the empirical model includes a bias, a linear trend, and periodic terms up to the frequency 27 cpr:

$$r(t) = x_0 + x_1 t + \sum_{k=1}^{27} \{x_{(2k)} \cos k\omega t + x_{(2k+1)} \sin k\omega t\}, \quad (4.2)$$

where x_0 , x_1 , ..., and x_{55} are unknown parameters. The application of this filter eliminates noise in GOCE misfit gravity gradients up to the frequency 27 cpr, which corresponds to the lower bound of the gradiometer measurement band, i.e., 5 mHz.

Furthermore, I find it essential to suppress noise as a whole, including that in the high-frequency range where the instrumental noise is particularly strong (above 25 mHz and 100 mHz in the case of GRACE KBR data and GOCE gravity gradients, respectively). To that end, I map the misfits onto the Earth’s surface and compute their mean per $\Delta^\circ \times \Delta^\circ$ block, where Δ° is the block size in degrees. In the case of KBR data, each block-mean value is computed based on all measurements for which the mid-point between the GRACE satellites is located inside that block. Assuming that noise in different orbital tracks is uncorrelated, computation of block-mean values results in the suppression of noise at least by the factor equal to the square root of the average number of orbital tracks crossing the blocks. Thus, the longer the duration of a control data set is, the better signal-to-noise ratio is expected.

The computation of block-mean values also leads to another positive outcome. It acts as a low-pass filter. The GRACE and GOCE satellites cross the distance of Δ° in about $t_{\Delta^\circ} \approx \frac{(\Delta^\circ \times \pi / 180^\circ) \times 6370}{v}$ seconds, where $v \approx 7.4 \frac{\text{km}}{\text{s}}$ and $v \approx 8 \frac{\text{km}}{\text{s}}$ respectively denote the GRACE and GOCE satellites’ ground speed and 6370 is the Earth’s mean equatorial radius in kilometers. Thus, noise and signal at the frequencies above $f_{\Delta^\circ} = \frac{1}{t_{\Delta^\circ}}$ Hz or equivalently above $f_{\Delta^\circ} \times 5400$ cpr (with 5400 being the satellites’ orbital revolution period in seconds) are largely averaged out. The frequency $f_{\Delta^\circ} \times 5400$ cpr can be approximately associated

with spherical harmonic coefficients of degree $L_{\Delta^\circ} = f_{\Delta^\circ} \times 5400$ and less. This means that the validation of a model becomes largely limited to its coefficients below degree L_{Δ° . For instance, choosing Δ° equal to 6° or 3° associates the outcome of the validation largely with the coefficients of models below degree 60 or 120, respectively. Given a unique sensitivity of KBR data to low degree spherical harmonics of the gravity field, this is extremely beneficial when assessment of low degree coefficients of a model is the primary focus. In that case, it is sufficient to choose Δ° in accordance with the maximum degree up to which the validation of a model is to be performed.

4.3 Application

In this section, I use the methodology described above to perform a validation of DGM-1S and the other five previously mentioned static gravity field models (ITG-Grace2010s, GOCO01S, EIGEN-6S, GOCO02S, and EGM2008). I recall that a brief description of these five models can be found in the previous chapter (section 3.5). I truncate EGM2008 at degree 250 to be consistent with the maximum degree of at least two of the combined GRACE/GOCE models (GOCO02S and DGM-1S) and speed up the computations. In any case, the satellite control data used in this study are hardly sensitive to signals above degree 250.

The control data utilised for a validation of the static gravity field models under consideration are: (i) GRACE range combinations covering all 12 months of 2010 (5-second sampling); and (ii) GOCE gravity gradients from March to May 2011 (1-second sampling). Importantly, these data have not been used in the production of any of the considered models. The original data are converted into sets of misfits associated with these models as described in the previous section. In the validation of the models, I also compare the ability of GRACE KBR data and GOCE gravity gradients to reveal model inaccuracies. To make this comparison equitable, I find it important to ensure the same length of the data sets. Therefore, in addition to the yearly set of GRACE range combinations, I also consider a subset of it with the length equal to that of the considered GOCE gravity gradients (i.e., three months) using the data collected in August – October 2010.

4.3.1 Validation against GRACE KBR data

4.3.1.1 Validation in the spectral domain

Figure 4.1 shows the PSD $^{\frac{1}{2}}$ of the sets of GRACE misfit range combinations associated with the six aforementioned models. They are computed based on data of February 2010. The shown frequency range in Fig. 4.1a is limited to

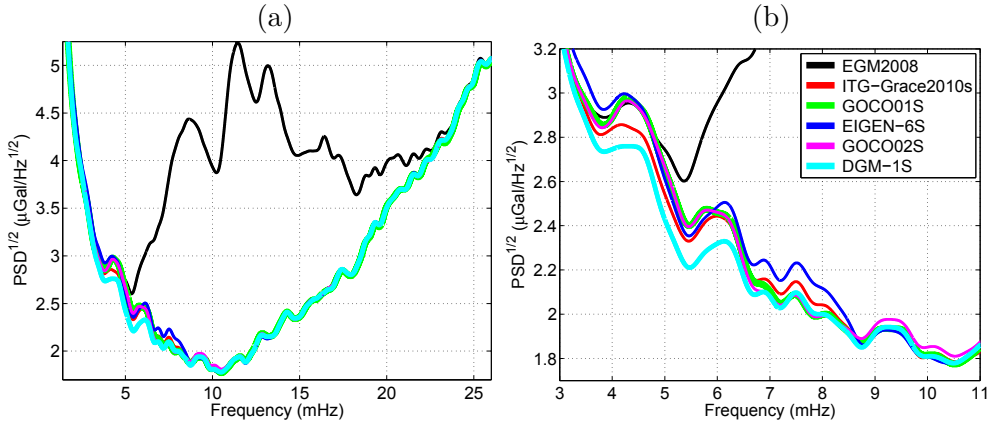


Figure 4.1: The $\text{PSD}^{\frac{1}{2}}$ of the GRACE misfit range combinations in the frequency ranges (a) 1.5 – 26 mHz and (b) 3 – 11 mHz. They are based on data of February 2010. A Gaussian smoothing has been applied to facilitate the comparison between the curves.

the one in which a pronounced difference is observed between the performance of EGM2008 and that of the other five models, whereas Fig. 4.1b zooms in the frequency range 3 – 11 mHz, where some differences are observed between consistencies of the latter models with the KBR control data.

Figure 4.1a allows one to conclude that EGM2008 is of much lower accuracy than all the other considered models in the frequency range 5 – 22 mHz (27 – 120 cpr), which corresponds to signals at spatial scales of 800 – 180 km half wavelength. Practically no difference can be identified in Fig. 4.1a between the performance of the considered models above the upper bound of this frequency range. ITG-Grace2010s and the four combined GRACE/GOCE models in this representation seem to match the KBR control data almost equally well, so that the corresponding five curves are hardly distinguishable in Fig. 4.1a. However, the zoomed-in picture (Fig. 4.1b) allows some differences in the model performance to be revealed in the frequency range 4 – 10 mHz (22 – 54 cpr), which corresponds to signals at spatial scales of 990 – 400 km half wavelength. In this frequency range, DGM-1S shows a slightly better agreement with the control data than the other combined GRACE/GOCE models and ITG-Grace2010s.

4.3.1.2 Validation in the spatial domain

To begin with, I set Δ° equal to 1° , which results in the elimination of the high-frequency noise in misfit range combinations above 66 mHz. It also leads to a suppression of noise as a whole with a factor of about $\sqrt{33} \approx 5.7$, where 33 is the average number of orbital tracks crossing one block in 2010. For the

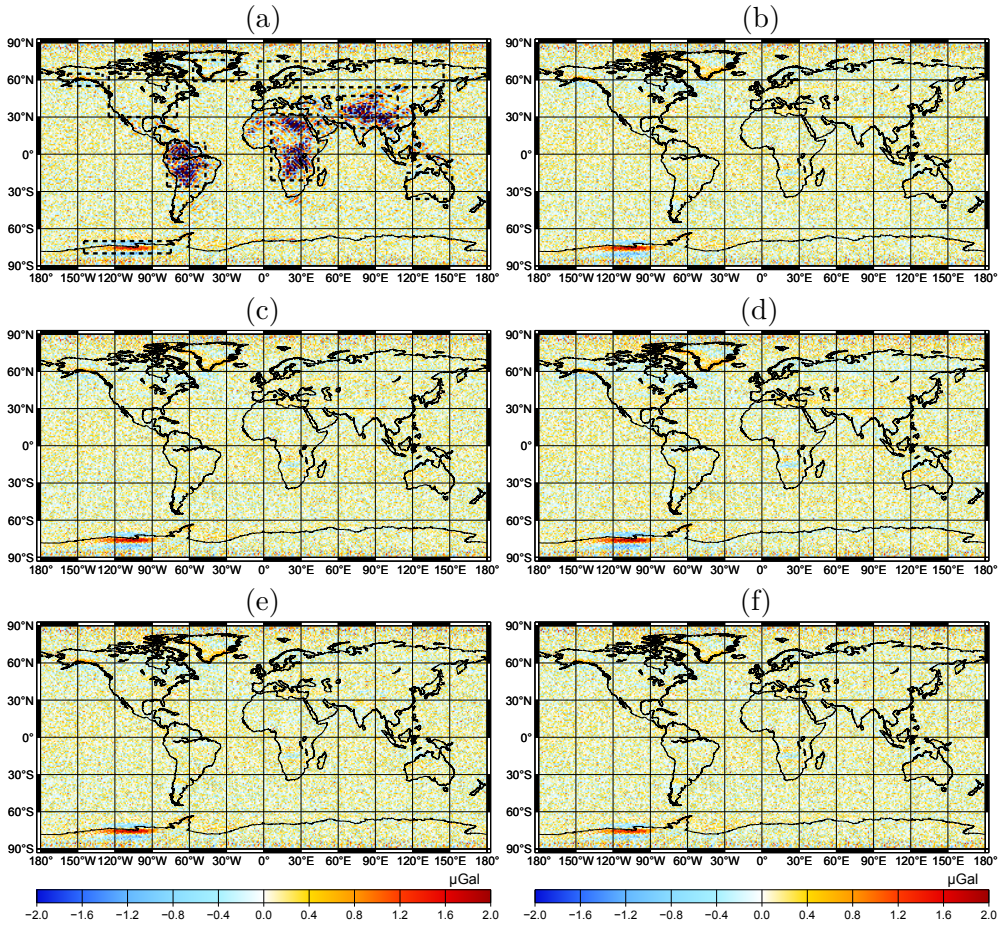


Figure 4.2: The GRACE $1^\circ \times 1^\circ$ block-mean misfit range combinations obtained for (a) EGM2008, (b) ITG-Grace2010s, (c) GOCO01S, (d) EIGEN-6S, (e) GOCO02S, and (f) DGM-1S on the basis of the 1-year data set. The RMS misfits are (a) $0.667 \mu\text{Gal}$, (b) $0.382 \mu\text{Gal}$, (c) $0.382 \mu\text{Gal}$, (d) $0.387 \mu\text{Gal}$, (e) $0.382 \mu\text{Gal}$, and (f) $0.378 \mu\text{Gal}$. The nine rectangular regions for which regional RMS misfits are computed are marked in Fig. 4.2a with black dashed lines.

3-month data subset, this factor reduces to 3. It is important to note that the chosen size of the blocks allows the gravity field signal to be largely preserved, since a full suppression of the signal would occur only around degree 360, whereas all the considered gravity field models are complete, at maximum, up to degree 250. This means that the “total” accuracy of the models is analysed to the extent possible with KBR data. Figure 4.2 shows the sets of GRACE $1^\circ \times 1^\circ$ block-mean misfit range combinations globally. The 112-km wide (in diameter) polar gaps in the GRACE satellites’ spatial coverage are absent in these maps.

A visual inspection of the pictures presented in Fig. 4.2 suggests splitting the continental areas into three categories: (1) areas that have a poor coverage with terrestrial gravimetry measurements, where EGM2008 shows a relatively poor agreement with the KBR control data, whereas the other considered models match them much better (e.g., the Himalayas, the Northern part of South America, and the Equatorial Africa); (2) areas that are well surveyed by terrestrial gravimetry campaigns, where all the six models visually demonstrate a good match to the control data (e.g., Australia, North America, and the Northern part of Eurasia); and (3) polar areas with a systematic linear trend in mass variations (which is mainly caused by a steady ice mass loss there), where all the six models show an increased level of disagreement with the control data (e.g., the South coast of Alaska, the Southern part of Greenland, and the coast of Amundsen sea in Antarctica). In addition, I introduce the fourth category: the world's oceans within the latitudes 65°S and 65°N , which is characterized by an excellent coverage with TOPEX/Poseidon satellite altimetry data (see Sandwell and Smith, 2009). A good match with the KBR control data is observed there for all the six considered gravity field models.

In order to obtain some quantitative estimates, I define three rectangular regions in the areas of the first, second, and third categories (nine regions in total), which are marked in Fig. 4.2a with black dashed lines. In Table 4.1, the RMS of the sets of GRACE $1^{\circ} \times 1^{\circ}$ block-mean misfit range combinations associated with the considered gravity field models are presented for each of these nine rectangular regions as well as for the world's oceans ($65^{\circ}\text{S} - 65^{\circ}\text{N}$) and for the entire globe, both for the 1-year data set and the 3-month data subset.

In this chapter, I continue to formulate performance differences between the tested gravity field models in the form of percentages. To that end, in a comparison between a pair of models, similar to the previous chapter, I assign 100 % to the one with a larger misfit to control data. The exception is when one of the models in a pair is EGM2008. In that case, I find it more convenient to always assign 100 % to this model no matter whether it performs better or worse.

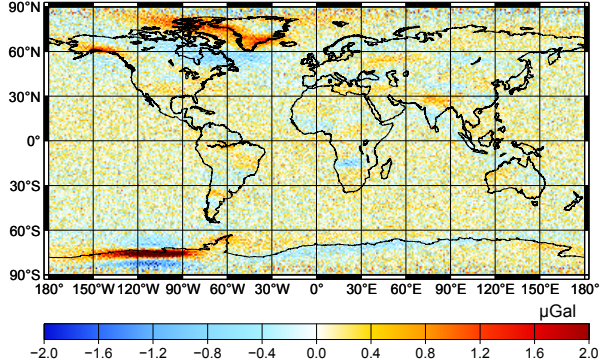
Table 4.1: The RMS of the GRACE $1^\circ \times 1^\circ$ block-mean misfit range combinations (in μGal) per region, obtained from the 1-year data set (in the numerator) and from the 3-month subset (in the denominator). The nine considered rectangular regions are defined by longitudinal and latitudinal boundaries marked in Fig. 4.2a with dashed, black lines.

Cat.	Region	Longitudinal	Latitudinal	EGM2008	ITG-Grace2010s		GOCO01S		EIGEN-6S		GOCO02S		DGM-1S
1	"Himalayas"	63°E–108°E	21°N–47°N	2.323	0.363	0.358	0.370	0.361	0.354				
				2.452	0.599	0.596	0.604	0.594	0.592				
				2.211	0.347	0.351	0.356	0.350	0.352				
"South America"	78°W–47°W	26°S–9°N	2.335	0.557	0.559	0.562	0.559	0.557					
			1.656	0.354	0.356	0.357	0.354	0.351					
			1.768	0.563	0.563	0.568	0.562	0.562					
"Equatorial Africa"	6°E–44°E	21°S–32°N	0.386	0.356	0.353	0.357	0.352	0.351					
			0.626	0.614	0.612	0.609	0.607	0.608					
			0.385	0.357	0.356	0.366	0.356	0.356					
2	"North Eurasia"	5°W–145°E	50°N–75°N	0.588	0.569	0.568	0.576	0.568	0.568				
				0.368	0.350	0.353	0.358	0.350	0.346				
				0.567	0.553	0.559	0.561	0.553	0.553				
"North America"	125°W–70°W	30°N–65°N	0.458	0.453	0.449	0.458	0.450	0.418					
			0.657	0.641	0.640	0.644	0.640	0.610					
			0.701	0.743	0.745	0.791	0.746	0.639					
3	"Amundsen sea coast"	145°W–75°W	80°S–70°S	0.872	0.913	0.915	0.959	0.917	0.823				
				0.444	0.406	0.405	0.431	0.405	0.372				
				0.659	0.638	0.640	0.661	0.640	0.614				
"South Greenland"	57°W–20°W	59°N–76°N	0.386	0.343	0.343	0.344	0.343	0.343					
			0.595	0.568	0.567	0.568	0.567	0.567					
			0.667	0.382	0.382	0.387	0.382	0.378					
4	"World's oceans"	180°W–180°E	65°S–65°N	0.846	0.630	0.629	0.632	0.629	0.629				
				0.667	0.382	0.382	0.387	0.382	0.378				
				0.846	0.630	0.629	0.632	0.629	0.629				
"Globe"	180°W–180°E	89°S–89°N	0.667	0.382	0.382	0.387	0.382	0.378					
			0.846	0.630	0.629	0.632	0.629	0.629					
			0.667	0.382	0.382	0.387	0.382	0.378					

According to Table 4.1, the 1-year data set as compared to the 3-month data subset shows a significant reduction of misfit to the considered models: by 20 – 42 %. This is probably a consequence of a more efficient suppression of random noise when a longer data set is considered. The exception is EGM2008 in the regions of the first category, where this reduction is only 5 – 6 %. This is probably caused by the signal-to-noise ratio being in this case significantly higher than in the other cases. On the other hand, for some combinations of the region and model, this reduction approaches a factor of $\sqrt{\frac{12}{3}} = 2$ (with 12 and 3 respectively being the lengths of the one-year data set and the three-month subset in months), which is the maximum value one can expect under the assumption that noise time series in different months are not correlated with each other. This allows me to conclude that random noise in the control data plays a substantial, if not dominant, role in the obtained RMS misfits. Nevertheless, these RMS values still show some differences between the models and between the regions, which means that they also contain valuable information for a model validation. Further analysis is fully based on the misfits to the 1-year data set, as they are proven to be less contaminated by random noise.

The RMS misfits indicate that ITG-Grace2010s and the combined GRACE/GOCE models demonstrate a much higher accuracy than EGM2008 in the regions from the first category: by 79 – 85 %. I find it worth discussing the origin of this difference. EGM2008 utilised GRACE data by including the GRACE-based ITG-Grace03 into the data combination. ITG-Grace03 uses approximately one and half time less GRACE data than ITG-Grace2010s. Therefore, the latter model is statistically expected to be more accurate than the former one by a factor of only $\sqrt{1.5} \approx 1.2$ (or 20 %). This statistically expected better performance will be confirmed in the next chapter (section 5.2.1) in the validation against the GOCE control gravity gradients. This means that only a small portion of the performance difference between ITG-Grace2010s and EGM2008 in the first category regions can be attributed to the contribution of the extra KBR data incorporated into ITG-Grace2010s. The rest of it can only be explained by a lower accuracy of EGM2008 as compared to ITG-Grace03 in these areas. One may find this as an unexpected outcome. Ideally, in an optimal combination of a GRACE-only model with terrestrial gravimetry measurements, the resulting model should perform in the gravimetrically poorly surveyed continental areas at least as well as the GRACE-only model. Nevertheless, as reported by Pavlis et al. (2012) themselves, a loss of information content of ITG-Grace03 has indeed occurred in the production of EGM2008 over the areas that are poorly surveyed gravimetrically. In the next chapter (section 5.2.1), I utilise the proposed validation procedure to analyse this deficiency further and present a quantification of its severity.

Figure 4.3: The GRACE $1^\circ \times 1^\circ$ block-mean misfit range combinations obtained based on DGM-1S without complementing the force model with the long-term gravity field variations, i.e., Eq. (4.1). The RMS number is $0.443 \mu\text{Gal}$.



Furthermore, Table 4.1 allows me to conclude that ITG-Grace2010s and the combined GRACE/GOCE models consistently demonstrate a slightly higher accuracy than EGM2008 in the regions from the second category (by 5 – 9 %) and in the “World’s oceans” (by about 11 %). In addition, Table 4.1 reveals a comparable performance of ITG-Grace2010s and of the four combined GRACE/GOCE models in the regions belonging to the first and second categories as well as in the “World’s oceans”. In most cases, DGM-1S matches the KBR control data slightly better than the other models. For instance, in “Himalayas” DGM-1S seems to outperform ITG-Grace2010s (or GOCO02S), GOCO01S, and EIGEN-6S by about 2 %, 1 %, and 4 %, respectively. Given the fact that ITG-Grace2010s is fully independent from GOCE data and GOCO01S uses only a very limited set of these data, I find it worth noting that these two models show practically the same agreement with the KBR control data as EIGEN-6S, GOCO02S, and DGM-1S. They even show a slightly smaller misfit than EIGEN-6S in some regions (e.g., in “Himalayas” and “North Eurasia”: by 2 – 3 %). I explain this by a relatively low sensitivity of the KBR control data to the contribution of the GOCE gravity gradients exploited in the production of the combined GRACE/GOCE models, which manifests itself at relatively high degrees (see Fig. 3.12 in the previous chapter).

In the regions from the third category, DGM-1S fits the KBR control data by 9 – 19 % better than the other models. Though such a difference seems to be substantial, I recommend interpreting it with a caution. The time-varying gravity field signals in the regions of the third category are very strong. To demonstrate that, I re-compute block-mean misfit range combinations without including the CSR monthly solutions into the force model. The results obtained in this way on the basis of DGM-1S are shown in Fig. 4.3. A comparison of it with Fig. 4.2f demonstrates that these signals are largely removed in the model validation procedure. It is very likely, however, that the CSR solutions are unable to remove these signals from KBR data completely. This may

Table 4.2: The RMS of the GRACE $3^\circ \times 3^\circ$ (in the numerator) and $6^\circ \times 6^\circ$ (in the denominator) block-mean misfit range combinations (in μGal) per region obtained from the 1-year data set.

Region	EGM 2008	ITG- Grace2010s	GOCO 01S	EIGEN- 6S	GOCO 02S	DGM- 1S
“Himalayas”	<u>0.993</u>	<u>0.116</u>	<u>0.116</u>	<u>0.130</u>	<u>0.116</u>	<u>0.104</u>
	<u>0.184</u>	<u>0.059</u>	<u>0.057</u>	<u>0.072</u>	<u>0.058</u>	<u>0.052</u>
“South America”	<u>0.963</u>	<u>0.086</u>	<u>0.086</u>	<u>0.101</u>	<u>0.086</u>	<u>0.092</u>
	<u>0.138</u>	<u>0.040</u>	<u>0.039</u>	<u>0.062</u>	<u>0.039</u>	<u>0.050</u>
“Equatorial Africa”	<u>0.783</u>	<u>0.094</u>	<u>0.095</u>	<u>0.101</u>	<u>0.095</u>	<u>0.089</u>
	<u>0.124</u>	<u>0.047</u>	<u>0.048</u>	<u>0.052</u>	<u>0.048</u>	<u>0.041</u>
“Australia”	<u>0.113</u>	<u>0.096</u>	<u>0.094</u>	<u>0.101</u>	<u>0.095</u>	<u>0.088</u>
	<u>0.049</u>	<u>0.057</u>	<u>0.053</u>	<u>0.059</u>	<u>0.056</u>	<u>0.048</u>
“North Eurasia”	<u>0.097</u>	<u>0.093</u>	<u>0.090</u>	<u>0.118</u>	<u>0.090</u>	<u>0.084</u>
	<u>0.036</u>	<u>0.065</u>	<u>0.060</u>	<u>0.101</u>	<u>0.061</u>	<u>0.053</u>
“North America”	<u>0.092</u>	<u>0.111</u>	<u>0.109</u>	<u>0.135</u>	<u>0.109</u>	<u>0.097</u>
	<u>0.040</u>	<u>0.079</u>	<u>0.078</u>	<u>0.106</u>	<u>0.078</u>	<u>0.063</u>
“South Alaska”	<u>0.266</u>	<u>0.263</u>	<u>0.261</u>	<u>0.260</u>	<u>0.263</u>	<u>0.209</u>
	<u>0.134</u>	<u>0.216</u>	<u>0.215</u>	<u>0.173</u>	<u>0.219</u>	<u>0.149</u>
“Amundsen sea coast”	<u>0.475</u>	<u>0.569</u>	<u>0.571</u>	<u>0.623</u>	<u>0.572</u>	<u>0.452</u>
	<u>0.032</u>	<u>0.186</u>	<u>0.191</u>	<u>0.156</u>	<u>0.192</u>	<u>0.124</u>
“South Greenland”	<u>0.230</u>	<u>0.256</u>	<u>0.258</u>	<u>0.303</u>	<u>0.259</u>	<u>0.200</u>
	<u>0.143</u>	<u>0.216</u>	<u>0.220</u>	<u>0.264</u>	<u>0.221</u>	<u>0.158</u>
“World’s oceans”	<u>0.099</u>	<u>0.080</u>	<u>0.079</u>	<u>0.081</u>	<u>0.079</u>	<u>0.077</u>
	<u>0.040</u>	<u>0.044</u>	<u>0.042</u>	<u>0.044</u>	<u>0.042</u>	<u>0.039</u>
“Globe”	<u>0.262</u>	<u>0.116</u>	<u>0.116</u>	<u>0.127</u>	<u>0.116</u>	<u>0.105</u>
	<u>0.072</u>	<u>0.083</u>	<u>0.083</u>	<u>0.096</u>	<u>0.083</u>	<u>0.068</u>

have been caused by a variety of reasons, e.g., a limited temporal resolution of the CSR solutions (one month), a limited spatial resolution of them (degree 60), or a suppression of signal due to the anisotropic filtering. Consequently, the RMS misfits obtained in the third category regions may be contaminated with relatively large systematic errors.

Globally, the agreement of the EGM2008 model with the KBR control data is worse than that of the other five models: by 42 – 43 %. The latter models agree with these control data globally almost equally well (DGM-1S matches these data by 1 – 2 % better than ITG-Grace2010s, GOCO01S, EIGEN-6S, and GOCO02S).

Due to the fact that the accuracy of satellite-only models reduces with increasing degrees (see Fig. 3.12 in the previous chapter), the validation based on $1^\circ \times 1^\circ$ blocks may be insufficiently sensitive to errors in the low-degree coefficients. To shed more light on this issue, I perform the validation of the

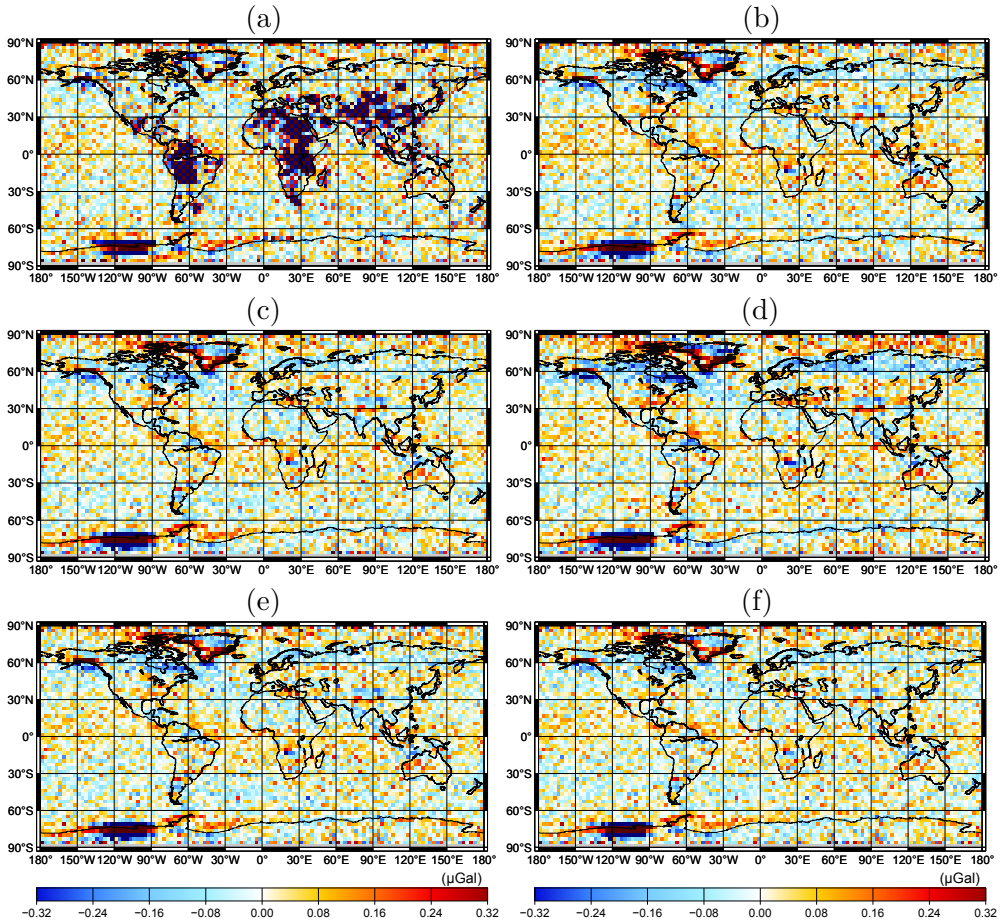


Figure 4.4: The GRACE $3^\circ \times 3^\circ$ block-mean misfit range combinations obtained for (a) EGM2008, (b) ITG-Grace2010s, (c) GOCO01S, (d) EIGEN-6S, (e) GOCO02S, and (f) DGM-1S on the basis of the 1-year data set. The RMS misfits are (a) $0.262 \mu\text{Gal}$, (b) $0.116 \mu\text{Gal}$, (c) $0.116 \mu\text{Gal}$, (d) $0.127 \mu\text{Gal}$, (e) $0.116 \mu\text{Gal}$, and (f) $0.105 \mu\text{Gal}$.

models using $3^\circ \times 3^\circ$ and $6^\circ \times 6^\circ$ block-mean misfit range combinations obtained from the 1-year data set. The average number of GRACE orbital tracks crossing the $3^\circ \times 3^\circ$ and $6^\circ \times 6^\circ$ blocks in year 2010 is 112 and 228, respectively. This allows noise in the sets of misfit range combinations to be suppressed by a factor of $\sqrt{112} \approx 11$ and $\sqrt{228} \approx 15$, respectively. Figures 4.4 and 4.5 show the obtained sets of $3^\circ \times 3^\circ$ and $6^\circ \times 6^\circ$ block-mean misfits, respectively. The corresponding RMS values computed in the previously defined regions are presented in Table 4.2. The conducted analysis shows, in particular, that the low-degree part of DGM-1S is globally by up to 10 % more consistent with the KBR control data than the other models. I find it also remarkable that

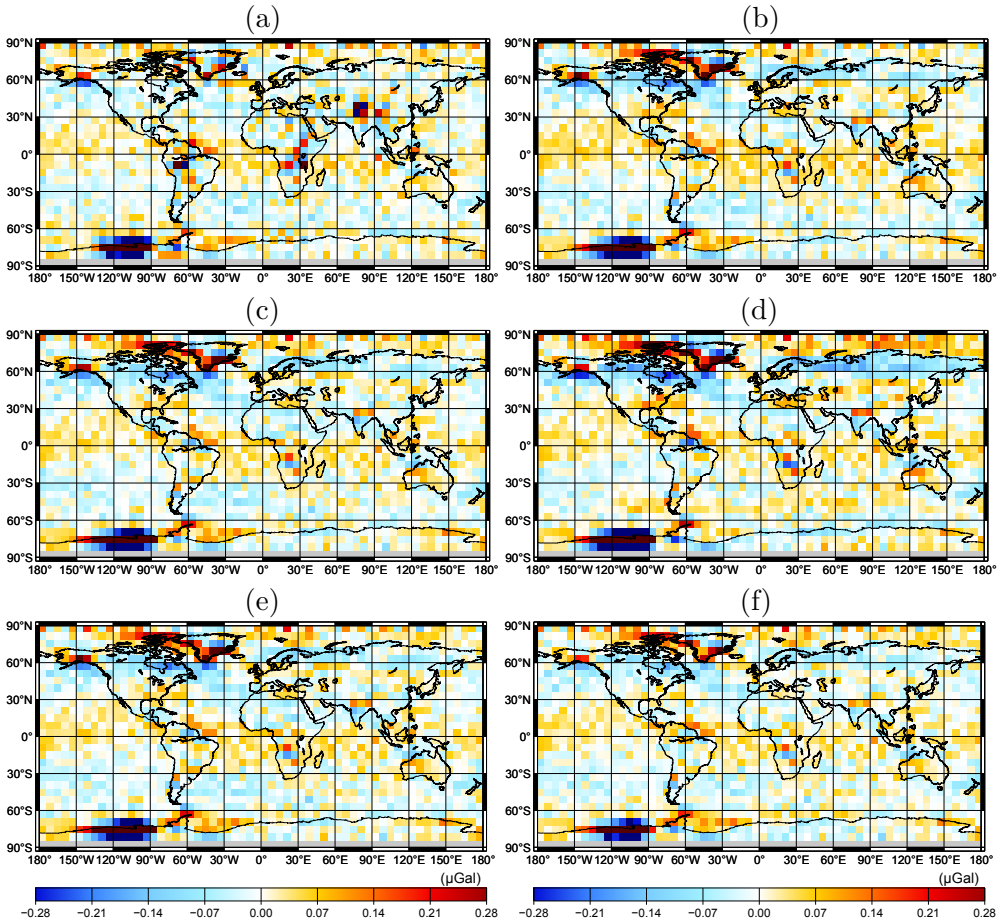


Figure 4.5: The GRACE $6^\circ \times 6^\circ$ block-mean misfit range combinations obtained for (a) EGM2008, (b) ITG-Grace2010s, (c) GOCO01S, (d) EIGEN-6S, (e) GOCO02S, and (f) DGM-1S on the basis of the 1-year data set. The RMS misfits are (a) $0.072 \mu\text{Gal}$, (b) $0.083 \mu\text{Gal}$, (c) $0.083 \mu\text{Gal}$, (d) $0.096 \mu\text{Gal}$, (e) $0.083 \mu\text{Gal}$, and (f) $0.068 \mu\text{Gal}$.

in the case of $6^\circ \times 6^\circ$ blocks, EGM2008 demonstrates globally and outside the poorly-studied continental areas a higher level of consistency with the KBR control data than the other models.

4.3.2 Validation against GOCE SGG data

4.3.2.1 Validation in the spectral domain

Figure 4.6 shows the spectra of the GOCE misfit gravity gradients associated with all the six gravity field models under consideration. They are computed

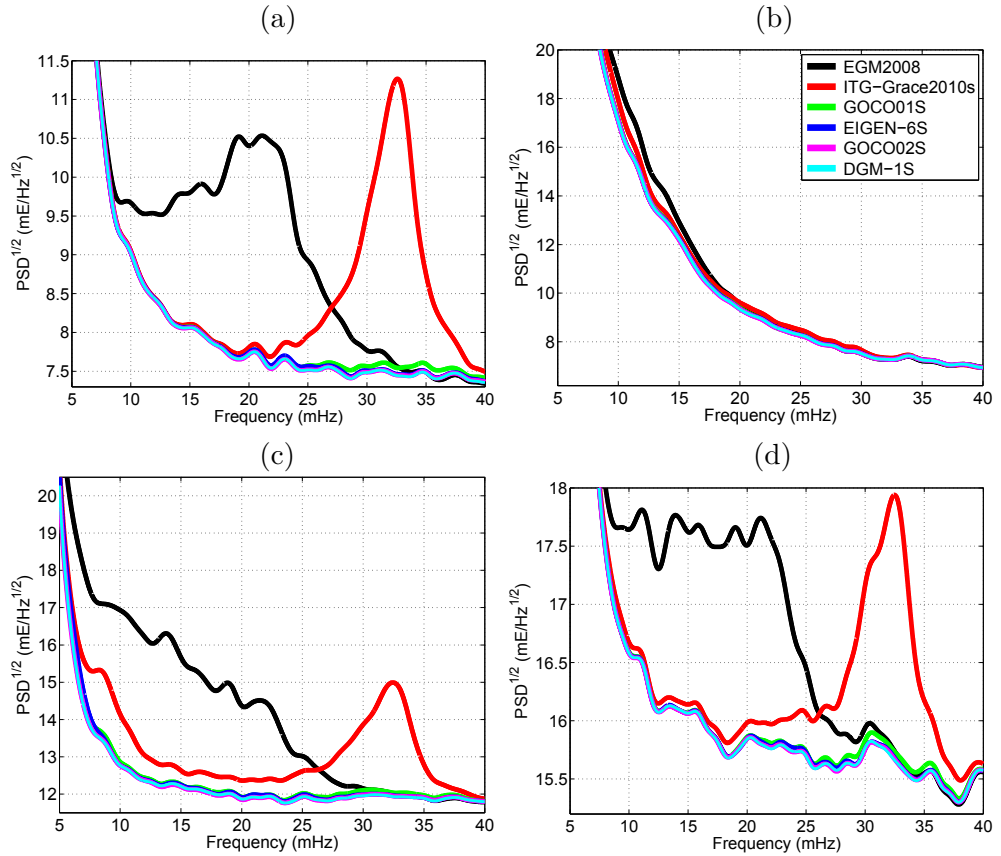


Figure 4.6: The $\text{PSD}^{\frac{1}{2}}$ of the (a) xx , (b) yy , (c) zz , and (d) xz components of the GOCE misfit gravity gradient tensor for May 2011. A Gaussian smoothing has been applied to facilitate the comparison.

based on data of May 2011. The shown frequency range in these pictures is limited to the one in which differences between the models can be visually identified.

These pictures demonstrate a lower performance of EGM2008 as compared to the other five models in the frequency range 10 – 28 mHz (54 – 150 cpr), which corresponds to signals at spatial scales of 390 – 140 km half wavelength. This largely confirms the outcome of the validation against the KBR control data, though the pronounced differences in that case appeared at lower frequencies: 5 – 22 mHz. Furthermore, Fig. 4.6 demonstrates a much higher accuracy of EGM2008 and the combined GRACE/GOCE models as opposed to ITG-Grace2010s in the frequency range 25 – 37 mHz or 135 – 200 cpr (signal at spatial scales of 155 – 105 km half wavelength). This can be explained by the high-frequency information content in GOCE gravity gradients

exploited in the combined GRACE/GOCE models and that in the terrestrial gravimetry and satellite altimetry measurements exploited in the production of EGM2008. As far as the combined GRACE/GOCE models are concerned, the curves associated with them are practically indistinguishable in the plots. An exception is the frequency range 27 – 37 mHz or 146 – 200 cpr (signal at spatial scales of 140 – 105 km half wavelength), where GOCO01S shows slightly larger misfits to the control gravity gradients at the xx component. The yy gravity gradient component in Fig. 4.6 does not reveal performance differences as pronounced as the other considered components. Besides, the PSD's at the yy component shows for the combined GRACE/GOCE models a much higher level than at the xx component. This contradicts to the fact that these two components are of an almost similar quality under normal circumstances. A possible explanation for these peculiarities is discussed in the next section.

4.3.2.2 Validation in the spatial domain

In order to perform the validation of the models in the spatial domain, I utilize the sets of GOCE misfit gravity gradients to compute $1^\circ \times 1^\circ$ block-mean misfits. The results for the xx , yy , zz , and xz gravity gradient components are globally plotted in Figs. 4.7 – 4.10, respectively. Only the maps associated with EGM2008, ITG-Grace2010s, and DGM-1S are shown, because the maps for the other three models are practically indistinguishable from DGM-1S at most geographical locations. The 1500 km wide (in diameter) polar gaps in GOCE data are absent in these maps. The RMS values are presented in Table 4.3 for all the four gravity gradient components and for all the six models under consideration. They are obtained globally as well as for the nine rectangular regions defined in section 4.3.1.2 and for the world's oceans ($65^\circ\text{S} - 65^\circ\text{N}$).

From Figs. 4.7 – 4.9 and Table 4.3, one can see that the obtained results are, in general, in agreement with those based on the GRACE KBR control data. In particular, ITG-Grace2010s and the combined GRACE/GOCE models as compared to EGM2008 demonstrate in the regions from the first category a better consistency with the control data at all the four gravity gradient components. At the zz component, for instance, the RMS misfits obtained for ITG-Grace2010s and the combined GRACE/GOCE models are smaller than those for EGM2008 by 69 – 75 % and 76 – 83 %, respectively. In the regions from the second category, the combined GRACE/GOCE models also demonstrate a higher accuracy than EGM2008. The difference in performance is particularly large for the zz component over North Eurasia: nearly 15 %. For the other two regions of this category, the difference is 3 – 4 %. There are, however, a few exceptions. For instance, EIGEN-6S shows in “Australia” larger

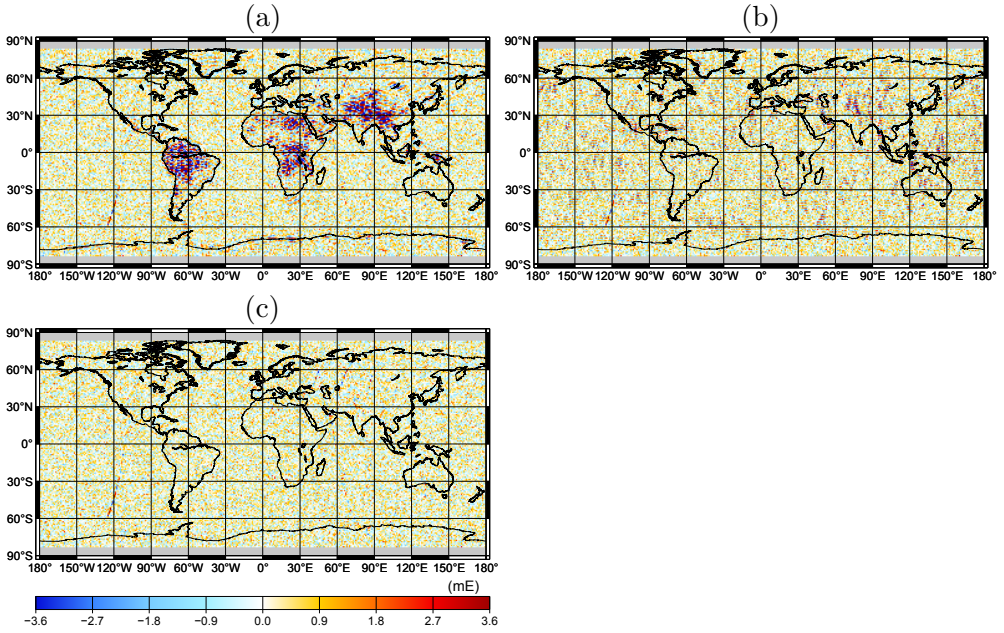


Figure 4.7: The GOCE $1^\circ \times 1^\circ$ block-mean misfit gravity gradients for the xx component obtained for (a) EGM2008, (b) ITG-Grace2010s, and (c) DGM-1S. The RMS misfits are (a) 1.199 mE, (b) 0.944 mE, and (c) 0.729 mE.

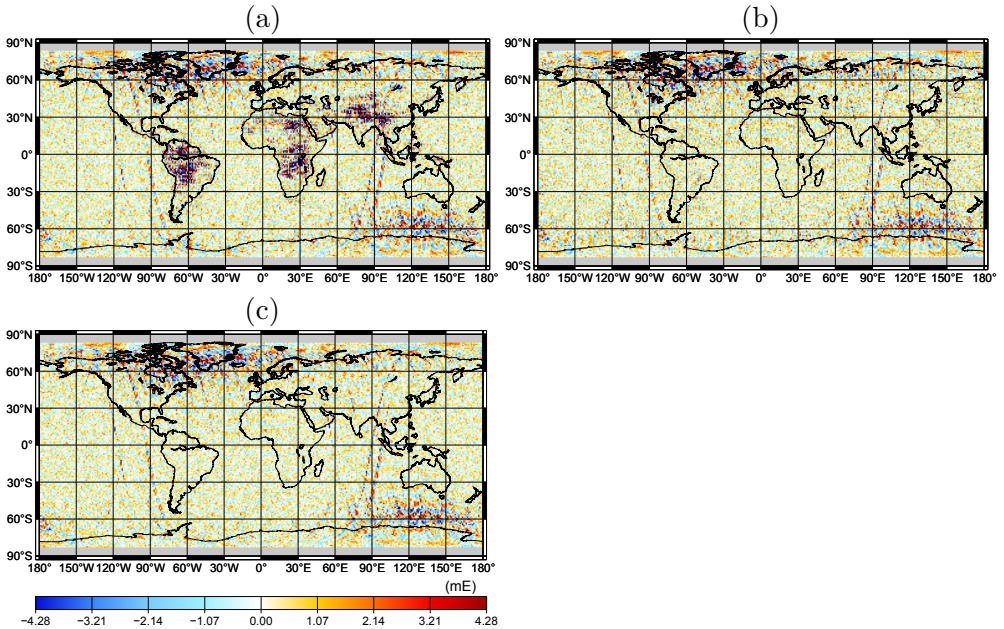


Figure 4.8: The GOCE $1^\circ \times 1^\circ$ block-mean misfit gravity gradients for the yy component obtained for (a) EGM2008, (b) ITG-Grace2010s, and (c) DGM-1S. The RMS misfits are (a) 1.426 mE, (b) 1.226 mE, and (c) 1.103 mE.

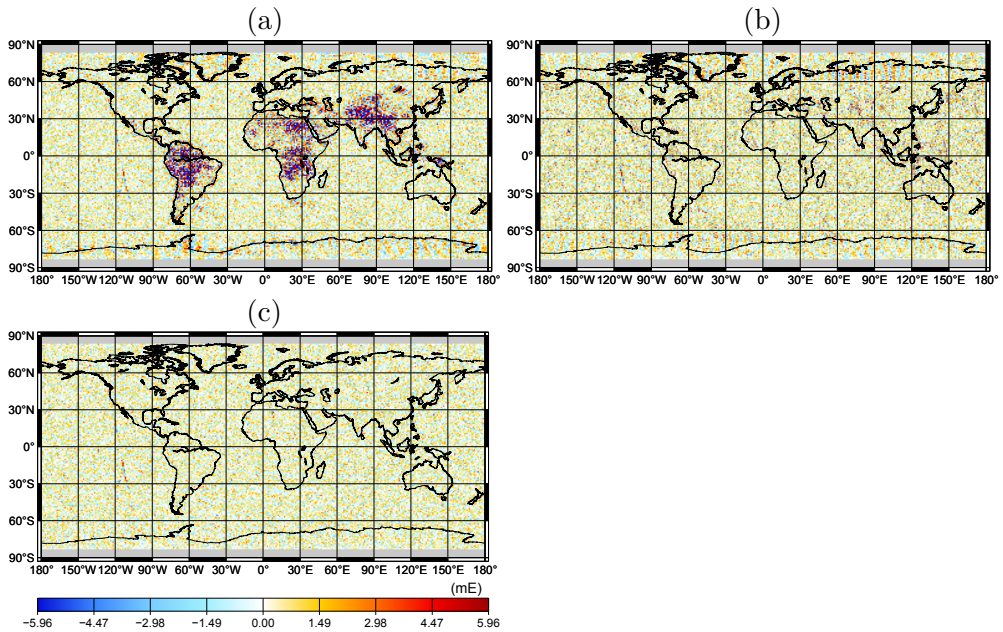


Figure 4.9: The GOCE $1^\circ \times 1^\circ$ block-mean misfit gravity gradients for the zz component obtained for (a) EGM2008, (b) ITG-Grace2010s, and (c) DGM-1S. The RMS misfits are (a) 1.981 mE, (b) 1.426 mE, and (c) 1.073 mE.

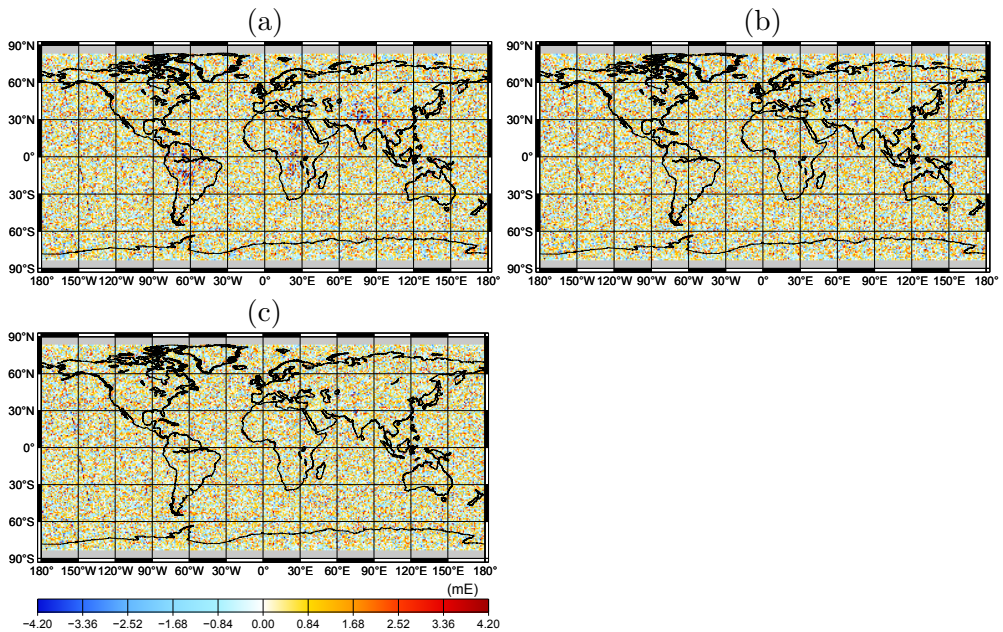


Figure 4.10: The GOCE $1^\circ \times 1^\circ$ block-mean misfit gravity gradients for the xx component obtained for (a) EGM2008, (b) ITG-Grace2010s, and (c) DGM-1S. The RMS misfits are (a) 1.405 mE, (b) 1.366 mE, and (c) 1.344 mE.

Table 4.3: The RMS of the GOCE $1^\circ \times 1^\circ$ block-mean misfit gravity gradients (in mE), per region. The top to bottom numbers in a quartet correspond to the xx , yy , zz , and xz components, respectively.

Region	EGM 2008	ITG- Grace2010s	GOCO 01S	EIGEN- 6S	GOCO 02S	DGM- 1S
"Himalayas"	4.018	1.307	0.846	0.975	0.817	0.811
	3.475	1.124	1.027	1.060	0.993	0.998
	6.625	1.783	1.187	1.332	1.133	1.138
	1.963	1.387	1.371	1.365	1.367	1.369
"South America"	3.505	0.914	0.718	0.699	0.692	0.693
	3.525	0.979	0.759	0.747	0.724	0.722
	6.232	1.531	1.112	1.110	1.074	1.075
	1.947	1.378	1.357	1.355	1.354	1.352
"Equatorial Africa"	2.531	0.931	0.741	0.729	0.727	0.722
	2.556	0.913	0.772	0.778	0.749	0.749
	4.551	1.431	1.129	1.130	1.100	1.099
	1.688	1.361	1.351	1.350	1.350	1.350
"Australia"	0.703	1.042	0.696	0.681	0.683	0.682
	0.847	1.006	0.850	0.879	0.823	0.829
	1.104	1.493	1.086	1.094	1.056	1.055
	1.355	1.360	1.348	1.350	1.347	1.347
"North Eurasia"	0.855	0.912	0.780	0.773	0.770	0.769
	1.455	1.626	1.416	1.416	1.401	1.401
	1.273	1.551	1.094	1.099	1.070	1.067
	1.361	1.371	1.345	1.345	1.344	1.344
"North America"	0.766	0.902	0.747	0.753	0.744	0.745
	1.567	1.645	1.570	1.579	1.560	1.563
	1.171	1.397	1.136	1.147	1.106	1.112
	1.392	1.400	1.389	1.389	1.387	1.388
"South Alaska"	0.821	0.876	0.759	0.760	0.754	0.750
	1.330	1.473	1.252	1.233	1.247	1.264
	1.322	1.499	1.197	1.188	1.147	1.140
	1.338	1.362	1.339	1.338	1.336	1.330
"Amundsen sea coast"	0.943	0.839	0.770	0.764	0.765	0.758
	1.022	0.964	0.915	0.901	0.907	0.900
	1.369	1.200	1.051	1.041	1.033	1.045
	1.330	1.285	1.272	1.267	1.266	1.271
"South Greenland"	1.004	0.930	0.779	0.766	0.769	0.763
	2.858	2.976	2.815	2.816	2.808	2.798
	1.452	1.585	1.110	1.098	1.075	1.064
	1.392	1.403	1.346	1.337	1.338	1.337
"World's oceans"	0.778	0.954	0.736	0.726	0.721	0.720
	1.054	1.118	1.017	1.026	1.004	1.005
	1.207	1.419	1.110	1.106	1.076	1.075
	1.370	1.378	1.365	1.365	1.363	1.363
"Globe"	1.199	0.944	0.744	0.738	0.731	0.729
	1.426	1.226	1.114	1.121	1.102	1.103
	1.981	1.426	1.105	1.104	1.073	1.073
	1.405	1.366	1.347	1.346	1.345	1.344

misfits to the yy component of the control gravity gradients than EGM2008 (by about 4 %).

In the “World’s oceans”, the combined GRACE/GOCE models also demonstrate a better match to the control gravity gradients than EGM2008. At the xx , yy , zz , and xz components, the observed difference is about 7 %, 5 %, 11 %, and 1 %, respectively.

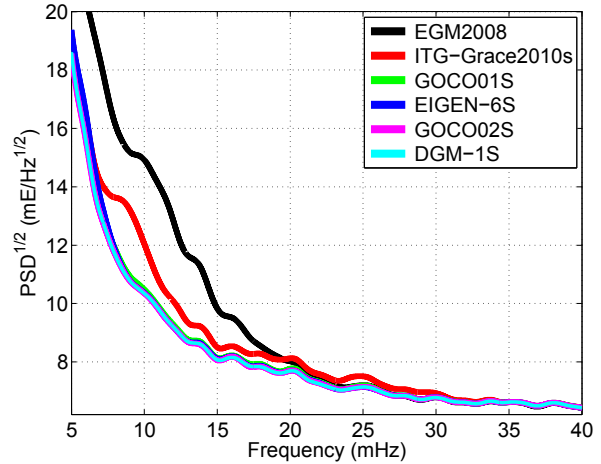
GOCO02S and DGM-1S show, in general, a better consistency with the control gravity gradients than EIGEN-6S. At the zz component, for instance, the difference in most regions and globally is 3 – 4 %. In “Himalayas”, the difference reaches about 17 % and 15 % in the case of the xx and zz components, respectively.

On the other hand, there are some disagreements between the results based on the GOCE control gravity gradients and those obtained earlier against the GRACE KBR control data. First, ITG-Grace2010s shows a much lower accuracy than EGM2008 in the regions from the second category and in the “World’s oceans”. At the zz component, the difference reaches 19 – 35 % and 18 %, respectively. These differences are even more pronounced at the xx component: 18 – 48 % and 23 %, respectively. Second, the GOCE control gravity gradients, unlike the KBR control data, clearly show a lower performance of EGM2008 as compared to the combined GRACE/GOCE models in the regions from the third category. At the zz component, the difference reaches 12 – 25 %. Third, the control gravity gradients reveal an expected better performance of DGM-1S and GOCO02S as compared to GOCO01S: by 4 – 5 % at the zz component. Fourth, practically no difference can be seen in the performance of GOCO02S and DGM-1S. Fifth, all the combined GRACE/GOCE models under consideration consistently demonstrate a higher accuracy than ITG-Grace2010s in all the considered regions. At the zz component, for instance, the difference is 13 – 36 %.

In addition, it is worth noticing that the xz gravity gradient component demonstrates a less sensitivity to the gravity field signal as compared to the diagonal components of the gravity gradient tensor. This can be clearly observed by comparing the inconsistencies of EGM2008 associated with the diagonal components (Figs. 4.7a, 4.8a, and 4.9a) with those associated with the xz component (Fig. 4.10a) in the regions from the first category, where this model is relatively inaccurate. At the xx , yy , and zz components, the performance of this model is worse than that of GOCO02S by 71 – 80 %, 71 – 79 %, and 76 – 83 %, respectively, whereas at the xz component the difference is only 20 – 30 %. This allows me to conclude that the xz component is least informative in the gravity field modelling. This justifies the fact that it is usually not exploited in the model production.

Furthermore, one can observe large disagreements between all the considered models and the yy gravity gradient component of the GOCE control gravity

Figure 4.11: The same as Fig. 4.6b, but using the data only in the latitudinal band $45^\circ\text{S} - 45^\circ\text{N}$.



gradients (particularly, around the magnetic poles of the Earth, but also along some individual orbital tracks). This leads to a significant spatial variability of the RMS misfits associated with this component. For instance, this component shows much larger RMS misfits than the other ones in “North Eurasia”, “South Alaska”, “South Greenland”, and “North America”. Since these discrepancies are observed for all the six models under consideration, I interpret them as an evidence of a low accuracy of the yy gravity gradient component in the control data. This finding is consistent with the results of Siemes et al. (2012), who explain this phenomenon by a contamination of the yy component with the cross-track non-gravitational acceleration signals due to an imperfect gradiometer calibration.

These inaccuracies may also explain a peculiar behaviour of the yy gravity gradient component in the validation of the models in the spectral domain. To validate this hypothesis, I re-compute the PSD’s related to this component with the same data as in the case of Fig. 4.6, but only using the latitudinal band $45^\circ\text{S} - 45^\circ\text{N}$, where the accuracy of the yy component is less degraded. The square-root of the resulting PSD’s are exhibited in Fig. 4.11. This picture does reveal the model differences though only in the low-frequency range: 10 – 27 mHz. Furthermore, a comparison of the curves in Fig. 4.11 with those shown earlier for the xx gravity gradient component (Fig. 4.6a) in the context of the combined GRACE/GOCE models allows an expectedly comparable quality of these two components to be observed.

4.4 Summary, discussion, and conclusions

With this chapter, I demonstrated that both GRACE KBR data and GOCE gravity gradients could be utilized as control data for a validation and com-

parison of global static gravity field models. In order to facilitate the model assessment on a region-by-region basis, I recommend to pre-process GRACE KBR data in such a way that they can be related to the gravity field spatial variations locally: e.g., to transform them into range combinations with Eq. (2.4).

The validation can be performed in both the frequency and spatial domain. In the latter case, it is advised to represent misfit data in the form of block-mean values, so that random inaccuracies in the control data are suppressed. An advantage of the validation in the spatial domain is that the model performance can be assessed on a regional basis. Nevertheless, an analysis in the spectral domain can be informative, too. Firstly, it can provide valuable information about the model performance at different spatial scales. Secondly, it can clearly show which parts of the spectrum are overwhelmed by noise and, therefore, should be subjected to filtering prior to the validation in the spatial domain.

In this chapter, I performed a validation and comparison of six global static gravity field models: one model based on a combination of satellite and surface data (EGM2008, considered up to degree 250 only), one GRACE-only model (ITG-Grace2010s), and four satellite-only combined GRACE/GOCE models (GOCO01S, EIGEN-6S, GOCO02S, and DGM-1S). Table 4.4 shows a summary of the validation results in the spatial domain. This table presents the RMS values of the $1^\circ \times 1^\circ$ block-mean misfits globally as well as for the pre-defined nine rectangular regions and for the “World’s oceans” in terms of percentages, defining that RMS misfit obtained for a given region for EGM2008 is 100 %. Since the RMS misfits for EGM2008 in most cases is the largest among all the models, the chosen presentation manner in Table 4.4 allows me to highlight the difference between the observed performance of EGM2008 on the one hand and of the other models on the other hand. The results based on both the KBR and SGG control data are included. The GRACE-based values correspond to the 3-month subset, so that their comparison with the GOCE-based numbers is more equitable. As far as the GOCE-based values are concerned, the minimum of the numbers obtained for the considered components are shown. In other words, I consider the best-case validation scenario among those based on the control gravity gradients. It is worth noting that these smallest numbers are in most cases related to the zz component. It is important to note that Table 4.4 additionally contains the results associated with two other models: ITG-Grace03 and EIGEN-6C. In a pursuit of the objective defined for the next chapter, I will apply the presented validation methodology (using the same control data sets) to these two models, too. Thus, for the sake of completeness, I include the numbers related to these two models in this table, too.

Table 4.4: The RMS of the GRACE $1^\circ \times 1^\circ$ block-mean misfit range combinations (in numerator) and of GOCE $1^\circ \times 1^\circ$ block-mean misfit gravity gradients (in denominator) obtained for eight static gravity field models. They are shown in terms of percentage with respect to RMS value obtained for EGM2008 in a given region. The GRACE-based values are computed from the 3-month data subset. The GOCE-based values are related to the minimum of those obtained for the four considered gravity gradient components. In most cases, the minimum numbers are obtained for the zz component.

Region	EGM2008	ITG-Grace03	ITG-Grace2010s	GOCO01S	EIGEN-6S	EIGEN-6C	GOCO02S	DGM-1S
"Himalayas"	100.0%	24.4%	24.4%	24.3%	24.6%	24.6%	24.2%	24.1%
	100.0%	36.7%	26.9%	17.9%	20.1%	20.3%	17.1%	17.2%
"South America"	100.0%	23.9%	23.9%	23.9%	24.1%	24.2%	23.9%	23.9%
	100.0%	30.8%	24.6%	17.8%	17.8%	19.9%	17.2%	17.2%
"Equatorial Africa"	100.0%	31.8%	31.8%	31.8%	32.1%	32.1%	31.8%	31.8%
	100.0%	38.2%	31.4%	24.8%	24.8%	25.1%	24.2%	24.1%
"Australia"	100.0%	98.1%	98.1%	97.8%	97.3%	97.8%	97.0%	97.1%
	100.0%	155.2%	118.8%	98.4%	96.9%	94.9%	95.7%	95.6%
"North Eurasia"	100.0%	96.8%	96.8%	96.6%	98.0%	98.1%	96.6%	96.6%
	100.0%	116.7%	106.7%	85.9%	86.3%	85.0%	84.1%	83.8%
"North America"	100.0%	96.6%	97.5%	98.6%	98.9%	98.4%	97.5%	97.5%
	100.0%	128.5%	105.0%	97.0%	98.0%	94.5%	94.4%	95.0%
"South Alaska"	100.0%	96.3%	97.6%	97.4%	98.0%	98.6%	97.4%	92.8%
	100.0%	119.6%	106.7%	90.5%	89.9%	88.1%	86.8%	86.2%
"Amundsen sea coast"	100.0%	98.6%	104.7%	104.9%	110.0%	109.9%	105.2%	94.4%
	100.0%	95.4%	87.7%	76.8%	76.0%	76.3%	75.5%	76.3%
"South Greenland"	100.0%	94.1%	96.8%	97.1%	100.3%	100.9%	97.1%	93.2%
	100.0%	94.7%	92.6%	76.4%	75.6%	73.8%	74.0%	73.3%
"World's oceans"	100.0%	95.3%	95.5%	95.3%	95.5%	95.5%	95.3%	95.3%
	100.0%	137.5%	106.1%	92.0%	91.6%	89.1%	89.1%	89.1%
"Globe"	100.0%	74.1%	74.5%	74.3%	74.7%	74.8%	74.3%	74.0%
	100.0%	89.7%	72.0%	55.8%	55.7%	54.8%	54.2%	54.2%

Table 4.4 demonstrates, in particular, a significantly poorer performance of EGM2008 in the regions of the first category as compared to the other models, including ITG-Grace2010s. The implication is that the added value of the GOCE mission to determining the gravity field in continental areas void of high-quality terrestrial gravimetry measurements can be quantified more fairly by comparing the performance of the combined (satellite-only) GRACE/GOCE models with ITG-Grace2010s rather than with EGM2008. In view of that, the validation of the models against the GRACE KBR control data does not allow this added value to be revealed. The validation of the models against the control gravity gradients, on the other hand, quantifies the GOCE mission's added value in these regions as an improvement of model quality by 21 – 36 %.

At the same time, validation against the GOCE control gravity gradients indicates a higher performance of EGM2008 as compared to ITG-Grace2010s in the regions of the second category as well as in the “World's oceans”. The implication is that it is fairer to quantify the added value of the GOCE satellite mission in those areas by comparing the performance of the combined (satellite-only) GRACE/GOCE models with that of EGM2008. In the context of the validation against the control gravity gradients, this added value turns out to be 4 – 16 % in the second category regions and about 11 % in the “World's oceans”.

Thus, quantification of the GOCE mission's added value in the oceans based on the control gravity gradients and on the control MDT model, utilized in the previous chapter, leads to contradictory results. In the former case, the model improvement is more than 10 %, whereas in the latter case it is marginal, if at all. I provide two explanations for this inconsistency. First, the validation against control gravity gradients is relatively insensitive to high-frequency inaccuracies due to the upward continuation effect and averaging of residuals over $1^\circ \times 1^\circ$ blocks. To prove this, I truncate the considered gravity field models at degree 200 and repeat the validation using the control gravity gradients. The RMS misfits obtained for EGM2008 and DGM-1S at the zz component in the oceans in this setup read as 1.222 mE and 1.088 mE, respectively. They are practically the same as their counterparts presented in Table 4.3 (i.e., 1.207 mE and 1.075 mE, respectively). I also compute RMS of the difference between the results based on the full gravity field models and based on the truncated ones. They read as 0.201 mE and 0.172 mE for EGM2008 and DGM-1S, respectively. These numbers are significantly smaller than those related to the original and truncated gravity field models. This implies that the GOCE mission's added value identified in the oceans based on the control gravity gradients is mostly associated with the coefficients below degree 200. The second explanation lies within the fact that the outcome of a validation against a control MDT model is sensitive to possible errors in this model as

well as in the MSS model. A high noise level in at least one of the two models (particularly, below degree 200) can make the performance of different gravity field models indistinguishable.

It could be argued that one should use a latest satellite-only combined GRACE/GOCE model, e.g., GOCO03S, when quantifying the added value of the GOCE mission. Such an analysis was conducted at a later stage of my research, and therefore, not documented in my Ph.D. thesis. Nevertheless, it has been shown that the usage of GOCO03S for that purpose only slightly increases the estimated GOCE mission's added value (Farahani et al., 2013b): 25 – 38 % in the poorly-surveyed continental areas, 7 – 17 % in the well surveyed continental areas, and 14 % in the world's oceans, considering the GOCE control gravity gradients at the zz component. These numbers are only marginally different from those obtained when DGM-1S or GOCO02S is used (i.e., 21 – 36 %, 4 – 16 %, and 11 %, respectively).

The results based on the 1-year GRACE KBR control data set and to some extent on the three-month data subset (summarized in Table 4.4) indicate that DGM-1S shows slightly smaller misfits than the other combined GRACE/GOCE models. One may argue that this is due to the fact that the same functional model based on range combinations is exploited to handle KBR data in both the model production and in the model validation. This is not the case for the other considered models, all of which utilize in one way or another KBR data in the form of range-rates. Therefore, I additionally performed the validation of the models using GRACE range-rates. In doing so, I firstly produced the sets of GRACE along-track inter-satellite velocities by applying a multi-point differentiation to the corresponding sets of GRACE satellites' dynamic orbits. Then, I generated sets of misfit range-rates by subtracting the observed range-rates, which are derived from the KBR measurements. Afterwards, I applied to them the high-pass filter of Eq. (3.1) to suppress their low-frequency noise. Subsequently, I computed the sets of GRACE $1^\circ \times 1^\circ$ block-mean misfit range-rates using the one-year data set. The corresponding RMS misfits obtained globally read as 59 nm/s, 55 nm/s, 49.4 nm/s, 49.8 nm/s, 49.4 nm/s, and 49.3 nm/s for EGM2008, ITG-Grace2010s, GOCO01S, EIGEN-6S, GOCO02S, and DGM-1S, respectively. Therefore, DGM-1S still shows a smaller or similar RMS misfit as compared to the other models.

The comparison of the validation results based on the KBR and SGG control data in the spectral domain (presented in Figs. 4.1 and 4.6, respectively) clearly shows a difference in sensitivity of these two data types to model inaccuracies. For instance, the KBR control data show inconsistencies with EGM2008 in the frequency range 5 – 22 mHz with the maximum at about 12 mHz \approx 65 cpr, which corresponds to spherical harmonic degree 65 and less. On the other hand, the control gravity gradients demonstrate inconsis-

tencies with this model at higher frequencies. For instance, the xx component shows inconsistencies in the frequency range 10 – 32 mHz with the maximum at 22.5 mHz \approx 120 cpr. I also note the frequency range 25 – 37 mHz, in which the control gravity gradients (particularly, the xx component), show large inconsistencies with ITG-Grace2010s, whereas the KBR control data do not allow these inconsistencies to be seen due to an increased noise level at high frequencies. In other words, control gravity gradients expectedly show the maximum sensitivity to model inaccuracies at higher degrees as compared to KBR control data.

The results obtained by the validation in the spatial domain, which are summarized in Table 4.4, offer another way to compare the sensitivity of KBR and SGG control data to model inaccuracies. One can see that the control gravity gradients, as compared to the KBR control data, reveal a larger discrepancy between the performances of the models. For instance, in the regions from the first and the second categories, the RMS misfits associated with the combined GRACE/GOCE models are respectively equal to 17 – 24 % and 80 – 96 % of those related to EGM2008 when the control gravity gradients are considered, versus 24 – 32 % and 94 – 98 % when the KBR control data are utilized. This indicates an expectedly higher sensitivity of GOCE gravity gradients. However, this conclusion is based on the mean values over $1^\circ \times 1^\circ$ blocks. The obtained values in this case may capture model inaccuracies up to degree 180 and even somewhat higher. Since model inaccuracies increase with degree, it is not surprising that the set of GOCE gravity gradients act as a more sensitive tool in this situation.

A different frequency sensitivity of KBR and SGG control data also explains why the data of the former type practically do not allow discrepancies between GOCO01S and GOCO02S to be observed, whereas those of the latter type reveal a difference of up to 4 % in terms of RMS misfits (see Table 4.4). As it is explained at the beginning of section 4.3, the major additional source of information exploited in the production of GOCO02S was six extra months of GOCE gravity gradients. Clearly, these data manifest their added value mostly at high degrees (see Fig. 3.12 in the previous chapter). The control data that are sensitive to the high-frequency signals offer the best way to sense this improvement.

A better ability of GOCE control gravity gradients to reveal model inaccuracies in the range of high degrees may also explain why these data indicate a much higher accuracy of EGM2008 than ITG-Grace2010s in the regions of the second category and in the “World’s oceans”, whereas the KBR control data show a slightly worse quality of the former model. Furthermore, a different spectral sensitivity of these two data types may also explain a contradiction in the validation outcome in the third category regions, where DGM-1S shows a significantly higher consistency with the KBR control data as compared to,

e.g., GOCO02S, whereas an almost comparable performance of these two models is observed there in the case of the control gravity gradients (see Table 4.4). This contradiction is in line with my hypothesis of an incomplete removal of the long-term mass transport signal from the KBR control data in the validation procedure. Since temporal variations of the gravity field occur mostly at low degrees (Wahr et al., 1998), they have no effect when a validation of the models is performed against the control gravity gradients.

The presented research proves that GOCE gravity gradients and GRACE KBR data can complement each other in different ways in the context of the model assessment. The GOCE gradiometer is a better tool to assess the integrated quality of a model up to a relatively high degree, i.e., 180, or even higher. Importantly, the collection of the GOCE gradiometry data at various components is sensitive to the gravity field variations in all directions, so that the validation results obtained on their basis can be considered as sufficiently comprehensive. Of course, the GOCE-based test in the spatial domain requires that the misfit gravity gradients are averaged over sufficiently small blocks, e.g., of the size $1^\circ \times 1^\circ$, so that the high sensitivity of gravity gradients at high frequencies can be exploited. At the same time, GOCE gravity gradients are less sensitive to possible model inaccuracies at lower degrees. Thus, a validation based on KBR data must be preferred when the model performance at low degrees is to be investigated, particularly, below degree 27. For this purpose, it is sufficient to increase the size of the block in computing the block-mean values. Of course, one should keep in mind the anisotropic sensitivity of GRACE KBR data, which limits their ability to assess the East-West gravity field variations. Another limitation of KBR data is an increased noise level at very low frequencies (cf. Fig. 4.1), which can make these data poorly sensitive to model inaccuracies at very low degrees, i.e., 2 – 4. Therefore, control data of other types, e.g., SLR data, may be needed when the accuracy of a model at very low degrees is the primary concern.

An important outcome of the conducted study is the demonstrated ability of satellite data to sense the difference in the performance of static gravity field models on a region-by-region basis, even if the length of the independent control data is much shorter than the length of data sets used in the production of models. In the considered examples, for instance, all the models were based on several years of GRACE KBR data. Nevertheless, even a 3-month subset of independent KBR data allowed a difference in the performance of EGM2008 and the combined GRACE/GOCE models to be seen. The 1-year set of these data made this difference even more pronounced, as it further improved signal-to-noise ratio in the pre-defined blocks.

None of the static gravity field models considered in my study uses the xz component of GOCE gravity gradients. Thus, this component is potentially the source of fully independent information for validation of models. This

encouraged me to include the xz component into the sets of control data. Nevertheless, this component was found to be least informative among all the considered gravity gradient components.

It is worth noting that the model performance shown in the case of EGM2008 is in a good agreement (in terms of geographical distribution of its errors) with the propagated error estimates of this model (Pavlis et al., 2012). It is a matter of future studies to inspect if this is also the case for the other tested models. To that end, it is sufficient to compare the actual errors of these models, a quantification of which is presented in this study, with their propagated error estimates.

Importantly, both GRACE KBR data and GOCE gravity gradients may suffer from systematic inaccuracies. Examples are inaccuracies related to calibration of GRACE attitude determination system (Horwath et al., 2011) and inaccuracies caused by an imperfect calibration of GOCE gravity gradients (Siemes et al., 2012). Such inaccuracies contaminate both data used for the production of models and those used for the validation of those models. Therefore, the proposed validation scheme may not reveal the impact of those inaccuracies, even if the control data are independent in line with my data independency definition. In the context of this chapter, this caveat does not apply to the validation of two of the tested models, namely, EGM2008 and ITG-Grace2010s, with the control gravity gradients since these models were produced without GOCE gravity gradients.

I conclude by saying that a validation based on independent GRACE KBR data and GOCE gravity gradients is a sufficiently general tool in the sense that it can be applied to any global static model of the Earth's gravity field, including the old ones. However, I find it important to emphasize that the proposed validation procedure represents only one way to test the model accuracy. A comprehensive evaluation of a model requires its validation against all types of independent control data, including the terrestrial ones.

5 Assessing data combination optimality in models produced using surface data

Farahani et al. (2013a) proposed a procedure to validate global static gravity field models using GRACE KBR and GOCE SGG control data. In that manuscript, they found it indispensable to document the findings of their inspection of how successfully surface gravity data (i.e., terrestrial gravimetry and satellite altimetry measurements) have been combined with satellite gravimetry data in the production of ultra-high resolution global gravity field models such as EGM2008 and EIGEN-6C. This chapter presents the findings of that inspection.

5.1 Introduction

In this chapter, as an example of another potential application of the validation methodology illustrated in the previous chapter, I inspect how successfully surface gravimetry measurements, i.e., terrestrial gravimetry and satellite altimetry measurements, have been combined with ITG-Grace03 in the production of EGM2008 and with GRACE and GOCE satellite data in the production of EIGEN-6C. To that end, I apply the proposed validation procedure to two additional static gravity field models: ITG-Grace03 and EIGEN-6C. Then, I analyse the difference in the performance (a) between EGM2008 and ITG-Grace03; and (b) between EIGEN-6C and its satellite-only counterpart, i.e., EIGEN-6S. I perform these two inspections in the spectral domain as well as in the spatial domain on the basis of the $1^\circ \times 1^\circ$ block-mean values of GRACE misfit range combinations associated with the one-year data set and on those of GOCE misfit gravity gradients at only the diagonal components of the gravity gradient tensor. It is worth reminding that the exploited sets of misfit data are associated with GRACE KBR data in 2010 and GOCE gravity gradients in August – October 2011, respectively (i.e., the same sets of control data as those used in the previous chapter). Importantly, these sets of data are not used in the production of the two newly added models to be assessed either. Thus, these control data are independent with respect to these two models, too. It is also important to note that EIGEN-6C is complete to degree 1420. I truncate this model similar to EGM2008 at degree 250. The reason for that

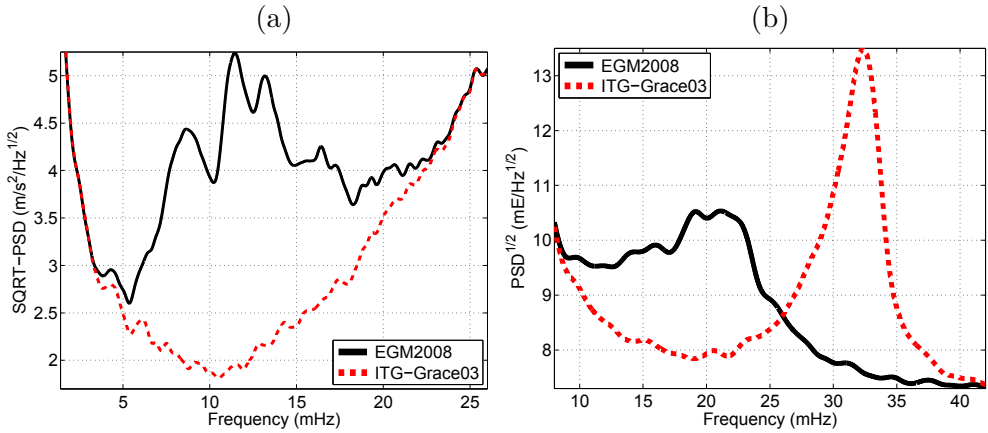


Figure 5.1: The $\text{PSD}^{\frac{1}{2}}$ of the (a) GRACE misfit range combinations and (b) GOCE xx misfit gravity gradients for February 2010 and May 2010, respectively. A Gaussian smoothing has been applied to facilitate the comparison.

is already given in the previous chapter at the beginning of section 4.3. Furthermore, similar to its satellite-only counterpart, I only consider the static part of EIGEN-6C.

Here is how the chapter has been structured. The outcome of the two aforementioned inspections, i.e., EGM2008 versus ITG-Grace03 and EIGEN-6C versus EIGEN-6S, is presented in section 5.2. Section 5.3 summarises the findings.

5.2 Inspections

The first subsection compares the validation results obtained based on the sets of control data of both types for the pair of models EGM2008 and ITG-Grace03, whereas the second subsection for the pair of models EIGEN-6C and EIGEN-6S.

5.2.1 EGM2008 versus ITG-Grace03

Figure 5.1 shows the $\text{PSD}^{\frac{1}{2}}$ of the GRACE misfit range combinations and that of the GOCE misfit gravity gradients at the xx component with respect to ITG-Grace03 and EGM2008. The shown frequency ranges are limited to those in which pronounced differences are observed. This figure clearly shows a significant loss of information content of ITG-Grace03 in the production of EGM2008 in 4 – 23 mHz (22 – 124 cpr) and 9 – 26 mHz (50 – 140 cpr) frequency ranges in the case of control KBR and SGG data, respectively. On

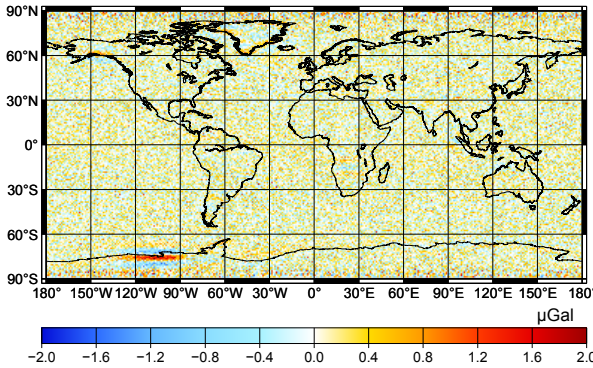


Figure 5.2: The GRACE $1^\circ \times 1^\circ$ block-mean misfit range combinations obtained for ITG-Grace03 on the basis of the yearly data set. The RMS misfit is $0.380 \mu\text{Gal}$.

the other hand, Fig. 5.1b confirms a substantial improvement of EGM2008 beyond the 26 mHz frequency due to the usage of terrestrial gravimetry and satellite altimetry data. I do not show the results in the spectral domain related to the yy component due to a relatively low ability of this component in such a domain to reveal model performance differences, as discussed in the previous chapter. The results related to the zz and xz components are not shown either, because they lead to similar findings as those based on the xx component.

The $1^\circ \times 1^\circ$ block-mean values of the GRACE misfit range combinations and of the GOCE misfit gravity gradients related to ITG-Grace03 are plotted in Figs. 5.2 and 5.3, respectively. The corresponding RMS misfits obtained globally as well as for the previously defined nine rectangular regions and for the “World’s oceans” are presented in Table 5.1. Those obtained for EGM2008 are also included there to facilitate the comparison. For the sake of completeness, the RMS misfits related to the 3-month subset of the KBR control data are also included.

From a comparison of Figs. 5.2 and 5.3 with their counterparts associated with EGM2008 (shown in the previous chapter as Figs. 4.2a and 4.7a – 4.9a, respectively), one can clearly see that the data combination performed in the production of EGM2008 has led to a significant deterioration of the model’s performance in the regions of the first category (i.e., poorly gravimetrically surveyed continental areas). The RMS misfits confirm that EGM2008 is of a much lower accuracy than ITG-Grace03 in those regions (by 79 – 85 % in the case of the KBR control data and by 59 – 69 % in the case of the control gravity gradients). Furthermore, the GRACE-based RMS misfits suggest that EGM2008 also performs slightly poorer than ITG-Grace03 in the other considered regions (up to maximum spectral ability of KBR control data). For instance, the difference in the regions of the second category (i.e., gravimetrically well surveyed continental areas) is 6 – 8 % and in the “World’s oceans” is about 11 %.

Table 5.1: The RMS of the GRACE $1^\circ \times 1^\circ$ block-mean misfit range combinations (in μGal) and the GOCE $1^\circ \times 1^\circ$ block-mean misfit gravity gradients (in mE) with respect to the EGM2008 and ITG-Grace03 models. The GRACE-based RMS misfits are presented for both the one-year data set (in the numerator) and for the three-month data subset (in the denominator). The top, middle, and bottom RMS numbers in a triad correspond to the xx , yy , and zz components of the GOCE control gravity gradients, respectively.

Region	GRACE-based misfits		GOCE-based misfits	
	ITG-Grace03	EGM2008	ITG-Grace03	EGM2008
“Himalayas”	$\frac{0.358}{0.599}$	$\frac{2.323}{2.452}$	$\frac{1.620}{1.535}$	$\frac{4.018}{3.475}$
			$\frac{2.433}{6.625}$	
“South America”	$\frac{0.352}{0.557}$	$\frac{2.211}{2.335}$	$\frac{1.142}{1.290}$	$\frac{3.505}{3.525}$
			$\frac{1.922}{6.232}$	
“Equatorial Africa”	$\frac{0.353}{0.562}$	$\frac{1.656}{1.768}$	$\frac{1.028}{1.135}$	$\frac{2.531}{2.556}$
			$\frac{1.740}{4.551}$	
“Australia”	$\frac{0.357}{0.614}$	$\frac{0.386}{0.626}$	$\frac{1.091}{1.324}$	$\frac{0.703}{0.847}$
			$\frac{1.824}{1.104}$	
“North Eurasia”	$\frac{0.354}{0.569}$	$\frac{0.385}{0.588}$	$\frac{0.998}{1.964}$	$\frac{0.855}{1.455}$
			$\frac{2.067}{1.273}$	
“North America”	$\frac{0.345}{0.548}$	$\frac{0.368}{0.567}$	$\frac{0.984}{2.067}$	$\frac{0.766}{1.567}$
			$\frac{1.988}{1.171}$	
“South Alaska”	$\frac{0.440}{0.633}$	$\frac{0.458}{0.657}$	$\frac{0.982}{1.603}$	$\frac{0.821}{1.330}$
			$\frac{1.881}{1.322}$	
“Amundsen sea coast”	$\frac{0.686}{0.860}$	$\frac{0.701}{0.872}$	$\frac{0.900}{1.085}$	$\frac{0.943}{1.022}$
			$\frac{1.405}{1.369}$	
“South Greenland”	$\frac{0.378}{0.620}$	$\frac{0.444}{0.659}$	$\frac{0.951}{3.157}$	$\frac{1.004}{2.858}$
			$\frac{2.092}{1.452}$	
“World’s oceans”	$\frac{0.344}{0.567}$	$\frac{0.386}{0.595}$	$\frac{1.097}{1.449}$	$\frac{0.778}{1.054}$
			$\frac{1.862}{1.207}$	
“Globe”	$\frac{0.380}{0.627}$	$\frac{0.667}{0.846}$	$\frac{1.076}{1.527}$	$\frac{1.199}{1.426}$
			$\frac{1.862}{1.981}$	

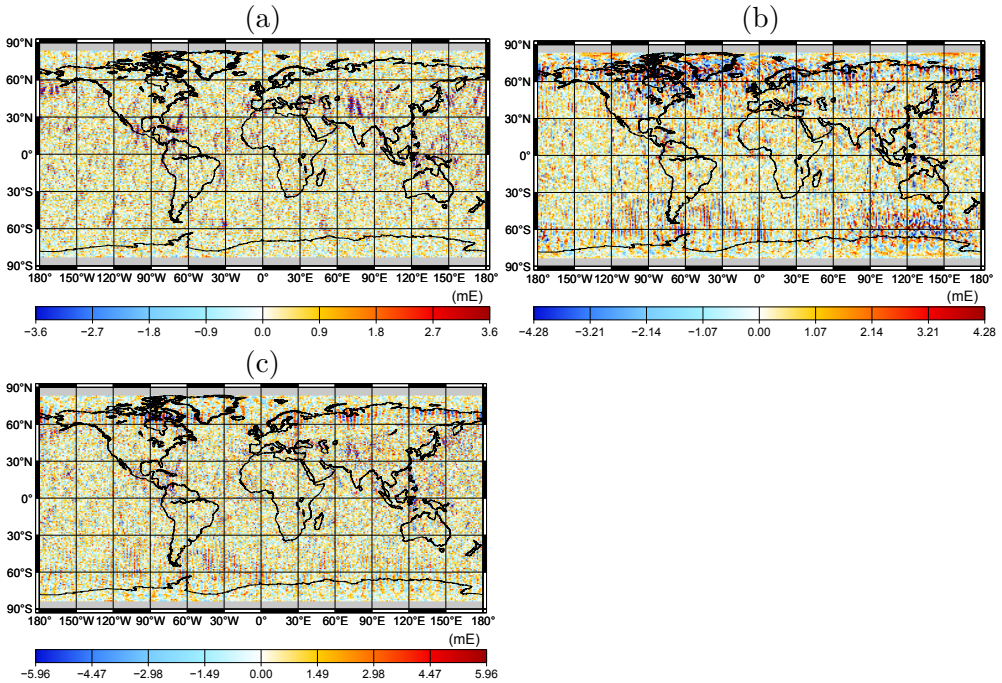


Figure 5.3: The GOCE $1^\circ \times 1^\circ$ block-mean misfit gravity gradients obtained for ITG-Grace03 at the (a) xx , (b) yy , and (c) zz components. The RMS misfits are (a) 1.076 mE, (b) 1.527 mE, and (c) 1.862 mE.

The conducted analysis confirms that the data combination in the production of EGM2008 has suffered from a partial loss of the information content of ITG-Grace03 in the areas with a poor coverage with terrestrial gravimetry data. Given the results related to the KBR control data, a minor loss of information of ITG-Grace03 may have occurred also in the well-studied areas (in the frequency range to which these data are sensitive). On the other hand, the GOCE control gravity gradients clearly demonstrate that EGM2008 performs much better in the gravimetrically well-studied continental regions, as well as in the oceanic areas, than ITG-Grace03. At the zz component, for instance, the difference in performance is 39 – 41 % and about 35 %, respectively.

Furthermore, it is worth noticing that a comparison of Fig. 5.2 with Figs. 5.3b and 5.3c shows that the GRACE-based test fails to reveal the meridional inaccuracies, so-called stripes, in the ITG-Grace03 model, whereas the results based on the GOCE zz control gravity gradients reveal them quite clearly. I explain this phenomenon by the anisotropic sensitivity of GRACE KBR data, which (as it has been already mentioned several times) is a serious limitation of these data.

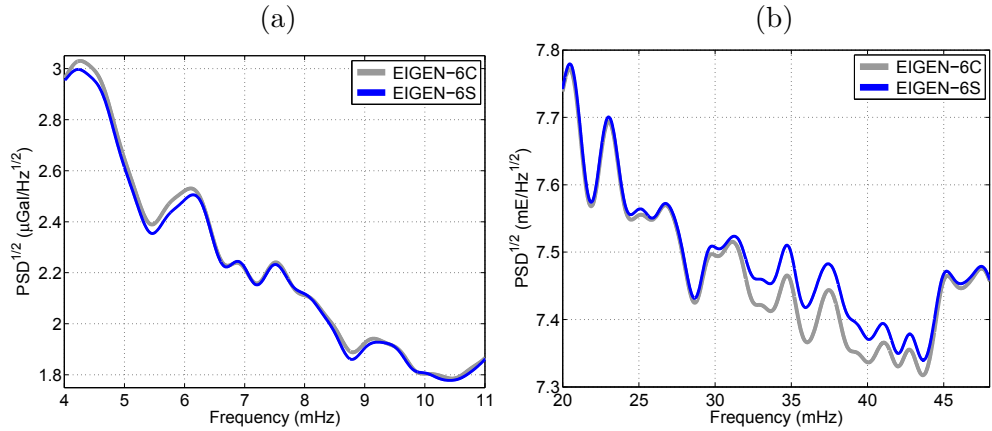


Figure 5.4: The $\text{PSD}^{\frac{1}{2}}$ of the (a) GRACE misfit range combinations and (b) GOCE xx misfit gravity gradients for February 2010 and May 2010, respectively. A Gaussian smoothing has been applied to facilitate the comparison.

Finally, it is worth noting that the global RMS misfit obtained for ITG-Grace03 based on the KBR control data (i.e., $0.380 \mu\text{Gal}$) is about 0.5 % smaller than that for ITG-Grace2010s. The reason for that is not understood.

5.2.2 EIGEN-6C versus EIGEN-6S

Figure 5.4 shows the $\text{PSD}^{\frac{1}{2}}$ of the GRACE misfit range combinations and that of the GOCE misfit gravity gradients at the xx component with respect to EIGEN-6C and its satellite-only counterpart, i.e., EIGEN-6S. The shown frequency ranges are limited to those in which some differences can be identified. The picture 5.4a only reveals minor performance differences, but importantly in favour of the satellite-only model. The implication is that a minor loss of information content of satellite data in the computation of EIGEN-6C may have also occurred. The spectral results related to the GOCE control gravity gradients fail to reveal these differences due to their weak sensitivity in the low-frequency range shown in Fig. 5.4a. Instead, Fig. 5.4b expectedly indicates a higher quality of EIGEN-6C as opposed to EIGEN-6S at higher frequencies (i.e., 20 – 46 mHz or 108 – 248 cpr). I attribute this to the incorporation of surface gravity measurements into the former model. The results related to the zz and xz control gravity gradients lead to a similar conclusion, and therefore, are not shown. Those related to the yy component are not shown either due to a relatively poor ability of this component to reveal performance differences in the models in the spectral domain (as discussed in the previous chapter).

The global maps of $1^\circ \times 1^\circ$ block-mean values of GRACE misfit range combinations and of GOCE misfit gravity gradients related to EIGEN-6C are not shown, as they turn out to be visually indistinguishable from those previously shown for EIGEN-6S. This by itself indicates that EIGEN-6C has not suffered from a loss of information content in satellite data as severely as EGM2008. To quantify a potential information loss, I present the RMS misfits related to EIGEN-6S and EIGEN-6C in Table 5.2 globally as well as in the previously defined regions. The results suggest that the combination of GRACE and GOCE data with terrestrial gravimetry measurements in the production of EIGEN-6C has led to only a minor performance degradation as compared to EIGEN-6S in the first category regions. The maximum loss of information content of satellite data is observed in “South America”: by about 6 % at the yy component, by about 11 % at the xx and zz components, and by about 1 % in the case of the KBR control data. A similar problem is also identified in “Equatorial Africa” but even in a less pronounced manner: by only 1 – 3 % in terms of RMS misfits to the GOCE control gravity gradients. In the well-studied continental and oceanic areas, EIGEN-6C expectedly outperforms its satellite-only counterpart: the difference reaches 2 – 4 % at the zz gravity gradient component. This level of performance difference is rather small. Most probably, this test is not sufficiently sensitive to the contribution of surface gravimetry data used in the production of EIGEN-6C.

5.3 Summary, discussion, and conclusions

It was shown that the combination of ITG-Grace03 and terrestrial gravimetry measurements in the production of EGM2008 has significantly worsened the quality of the resulting model as compared to ITG-Grace03 in the gravimetrically poorly studied continental areas. According to the KBR and SGG control data, this problem manifests itself in 4 – 23 mHz (22 – 124 cpr) and 9 – 26 mHz (50 – 140 cpr) frequency ranges, respectively. I relate this to an imperfection of the data weighting used in the data combination (e.g., due to a lacking stochastic description of noise in some input data). It is worth emphasizing that a loss of information content of ITG-Grace03 in the production of EGM2008 has been reported by Pavlis et al. (2012) themselves. The performance differences identified between these two models also explain a large part of those between ITG-Grace2010s and EGM2008 in continental areas with poor terrestrial gravity data. Furthermore, a minor loss of information content was also identified in the gravimetrically well surveyed continental areas.

In addition, I compared the performance of EIGEN-6C with that of its satellite-only counterpart, i.e., EIGEN-6S, to inspect whether the former

Table 5.2: The same as Table 5.1, but for EIGEN-6C and EIGEN-6S.

Region	GRACE-based misfits		GOCE-based misfits	
	EIGEN-6S	EIGEN-6C	EIGEN-6S	EIGEN-6C
“Himalayas”	$\underline{0.370}$	$\underline{0.371}$	$\underline{0.975}$	$\underline{0.967}$
	$\underline{0.604}$	$\underline{0.603}$	$\underline{1.060}$	$\underline{1.065}$
			$\underline{1.332}$	$\underline{1.342}$
“South America”	$\underline{0.356}$	$\underline{0.360}$	$\underline{0.699}$	$\underline{0.744}$
	$\underline{0.562}$	$\underline{0.564}$	$\underline{0.747}$	$\underline{0.837}$
			$\underline{1.110}$	$\underline{1.241}$
“Equatorial Africa”	$\underline{0.357}$	$\underline{0.356}$	$\underline{0.729}$	$\underline{0.736}$
	$\underline{0.568}$	$\underline{0.567}$	$\underline{0.778}$	$\underline{0.804}$
			$\underline{1.130}$	$\underline{1.144}$
“Australia”	$\underline{0.357}$	$\underline{0.359}$	$\underline{0.681}$	$\underline{0.673}$
	$\underline{0.609}$	$\underline{0.612}$	$\underline{0.879}$	$\underline{0.828}$
			$\underline{1.094}$	$\underline{1.048}$
“North Eurasia”	$\underline{0.366}$	$\underline{0.366}$	$\underline{0.773}$	$\underline{0.771}$
	$\underline{0.576}$	$\underline{0.577}$	$\underline{1.416}$	$\underline{1.406}$
			$\underline{1.099}$	$\underline{1.082}$
“North America”	$\underline{0.358}$	$\underline{0.359}$	$\underline{0.753}$	$\underline{0.745}$
	$\underline{0.561}$	$\underline{0.558}$	$\underline{1.579}$	$\underline{1.568}$
			$\underline{1.147}$	$\underline{1.107}$
“South Alaska”	$\underline{0.458}$	$\underline{0.460}$	$\underline{0.760}$	$\underline{0.752}$
	$\underline{0.644}$	$\underline{0.648}$	$\underline{1.233}$	$\underline{1.248}$
			$\underline{1.188}$	$\underline{1.165}$
“Amundsen sea coast”	$\underline{0.791}$	$\underline{0.790}$	$\underline{0.764}$	$\underline{0.768}$
	$\underline{0.959}$	$\underline{0.958}$	$\underline{0.901}$	$\underline{0.903}$
			$\underline{1.041}$	$\underline{1.044}$
“South Greenland”	$\underline{0.431}$	$\underline{0.433}$	$\underline{0.766}$	$\underline{0.764}$
	$\underline{0.661}$	$\underline{0.665}$	$\underline{2.816}$	$\underline{2.814}$
			$\underline{1.098}$	$\underline{1.071}$
“World’s oceans”	$\underline{0.344}$	$\underline{0.344}$	$\underline{0.726}$	$\underline{0.718}$
	$\underline{0.568}$	$\underline{0.568}$	$\underline{1.026}$	$\underline{1.008}$
			$\underline{1.106}$	$\underline{1.075}$
“Globe”	$\underline{0.387}$	$\underline{0.387}$	$\underline{0.738}$	$\underline{0.734}$
	$\underline{0.632}$	$\underline{0.633}$	$\underline{1.121}$	$\underline{1.111}$
			$\underline{1.104}$	$\underline{1.085}$

model has also experienced a loss of information content of satellite data in the course of data combination. The inspection did reveal this problem in the gravimetrically poorly surveyed continental areas, but in a significantly less pronounced manner than in the case of EGM2008. I relate this to the adopted data combination methodology. According to (Förste et al., 2011), the surface

gravity measurements were permitted to contribute to the production of this model only above degree 160, where the contribution of KBR and SGG data is not substantial. In the well-studied continental and oceanic areas, an expected better performance of EIGEN-6C was confirmed.

Furthermore, the analysis performed in the spatial domain demonstrates another limitation of GRACE KBR control data: their anisotropic sensitivity. These data fail to reveal the meridional errors (stripes) in ITG-Grace03 (Fig. 5.2). On the other hand, the test performed based on the yy and zz components of the GOCE control gravity gradients (Fig. 5.3) clearly reveals those errors.

Finally, I conclude by saying that the research presented in this chapter paves the way to an improved data weighting in the next generation ultra-high resolution combined global gravity field models to be produced using GOCE gravity gradients and GRACE KBR data.

6 Assessing GOCE mission's added value to the time-varying gravity field modelling

This chapter is based on the study documented in (Farahani et al., 2013c), where an investigation on the possible added value of GOCE data to GRACE-based time-varying gravity field models was performed. This chapter is included in this thesis, because, in conjunction with chapters 4 and 5, it completes my investigation on the added value of the GOCE mission to the retrieval of the static and time-varying parts of the Earth's gravity field.

6.1 Introduction

This chapter aims at investigating a possible improvement of models of the gravity field temporal variations retrieved from GRACE KBR data. An obvious way to improve models of this type is to combine KBR data with information from other sources. A potential source emerges from data acquired by the GOCE mission. In principle, this mission is exclusively designed to retrieve the static part of the gravity field. Nevertheless, it is not excluded that data from this mission could also improve the spatial resolution of models of the time-varying part once they are processed in conjunction with GRACE KBR data. This expectation is supported by experiments conducted by Ditmar and Liu (2007) and Han and Ditmar (2008) with simulated GRACE and GOCE data. The outcome of the former study indicated a reduction of random noise in GRACE-based unconstrained time-varying gravity field models as a result of an incorporation of GOCE data. The latter study demonstrated that mass transport caused by large earthquakes, such as the Sumatra-Andaman one occurred in 2004, could be alternatively detected by GOCE gravity gradients. In the context of real data, on the other hand, it has been demonstrated by, e.g., Flechtner et al. (2010), Weigelt et al. (2013), and Baur (2013), that even high-low SST data acquired by the CHAMP satellite mission contain time varying gravity field signals. Given a lower orbital altitude of the GOCE satellite, it is not unreasonable to expect that such signals are also present in GOCE SST data.

The main question I will try to answer is whether the time-varying gravity field signals present in GOCE SST data, and possibly in its gravity gradients,

could lead to a more accurate retrieval of the temporal gravity field variations if these data are processed in conjunction with KBR measurements. I perform this investigation in the context of the monthly gravity field modelling in terms of spherical harmonic coefficients up to degree 120. I consider data of both types acquired by the GOCE mission: (i) high-low SST data transformed into kinematic orbits; and (ii) gravity gradients in the instrument frame. To reach the study objectives, I conduct twin experiments. First, I produce monthly solutions by a stand-alone processing of KBR data. Second, I produce solutions using a statistically optimal combination of KBR and GOCE data. The difference between the obtained solutions of these two types allows conclusions to be drawn regarding the impact of GOCE data.

The chapter is structured as follows. In section 6.2, I study the impact of GOCE data on KBR-only unconstrained monthly gravity field solutions. In section 6.3, I analyse KBR-only and combined GRACE/GOCE monthly solutions as well as the differences between these solutions subsequent to a statistically optimal anisotropic filtering (Klees et al., 2008b). At this stage, I study not only the total impact of GOCE data, but also the impact of its SST data and gravity gradients, individually. Section 6.4 is left for a summary, discussion, and conclusions.

6.2 Unconstrained gravity field solutions

In the first subsection, I describe the methodology used to produce GRACE-only and combined GRACE/GOCE unconstrained monthly gravity field solutions. In the second subsection, I compare the solutions of these two types and study impact of GOCE data to unconstrained GRACE-only solutions.

6.2.1 Computing monthly solutions

In this chapter, I analyze multiple sets of monthly gravity field solutions produced in eleven months spanning the time interval November 2009 – December 2010. Three months (July, August, and September 2010) are excluded due to the lack of GOCE data. The computed solutions consist of residual spherical harmonic coefficients complete to degree 120. They describe monthly deviations of the gravity field from an a priori static gravity field model. The GRACE-only solutions are produced from KBR data alone. The combined GRACE/GOCE solutions are obtained by combining these data with GOCE SST and SGG data. The procedure consists of two steps: (1) computing residual data with respect to an a priori static gravity field model; and (2) optimally combining and inverting the residual data sets into residual spherical harmonic coefficients using the least squares adjustment. These two operations are performed in the same manner as described in chapter 2.

6.2.1.1 Computing residual data

The force model exploited to compute the sets of residual gravitational data makes use of DGM-1S as the a priori static gravity field model. The other contributors listed in chapter 3 (section 3.2) are incorporated into the force model, too.

In order to eliminate the low-frequency noise in GRACE residual range combinations, I make use of the same seven-parameter analytical function of Eq. (3.1). I build the high-pass filter in the same manner as described earlier in section 3.3.1, but using a new spatially dependent data weighting. As it was pointed out earlier, this high-pass filter eliminates not only noise at low frequencies (below 2 – 3 cpr), but also signals to be recovered at these spatial scales. Thus, the usage of a non-weighted least squares scheme to estimate the unknown seven parameters, as it was done in the case of the static gravity field modelling (chapter 3), may not lead to optimal results in the context of this chapter. The reason can be understood in the following. In a statistically optimal least squares adjustment, data weights must represent noise in data. By definition, noise in a least squares adjustment is the difference between the actual observations and the values predicted based on the “true” model. In particular, noise includes all the signals that cannot be explained by the adopted functional model. In the context under consideration, “noise” includes, for instance, the signals that are to be retrieved at a later stage in the course of the time-varying gravity field modelling. If the presence of this “noise” is ignored, as it is done in the non-weighted least squares adjustment, the functional model synthesized from the estimated parameters will tend to explain not only the low-frequency inaccuracies in residual range combinations, but also the time-varying gravity field signals present in these residuals. In order to mitigate this effect, I perform the least squares adjustment using a diagonal weight matrix. Each element of this matrix, which is associated with a given observational epoch, is defined as the inverse of the mass transport signal variance at the corresponding ground location of the GRACE inter-satellite mid-point. The adopted signal variances have been estimated in the course of the production of the DMT-1 model (Liu et al., 2010). The square-root of these variances, i.e., the signal standard deviations, is globally plotted in Fig. 6.1.

The map shows relatively small numbers in majority of the globe, including oceans and large deserts. At the same time, it reflects relatively large numbers in a few locations in the continental areas such as Greenland or Equatorial Africa. This means that the usage of this information to form the weight matrix ensures that residual data collected over areas with minor mass variations (e.g., in the oceanic areas and deserts) provide the largest contribution to building the high-pass filter, whereas those collected over the areas with

Figure 6.1: Mass transport signal standard deviations estimated from DMT-1 in the time interval February 2003 – December 2006. The map is shown in terms of equivalent water heights. It is generated on a $0.5^\circ \times 0.5^\circ$ grid.

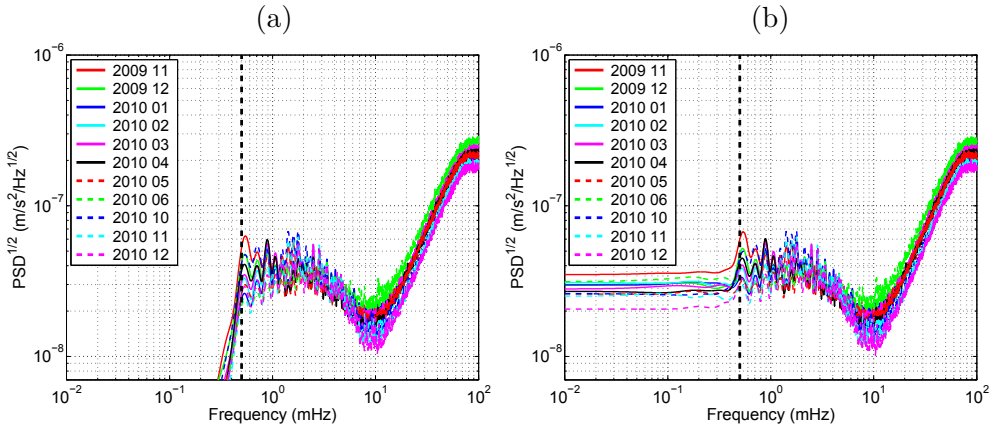
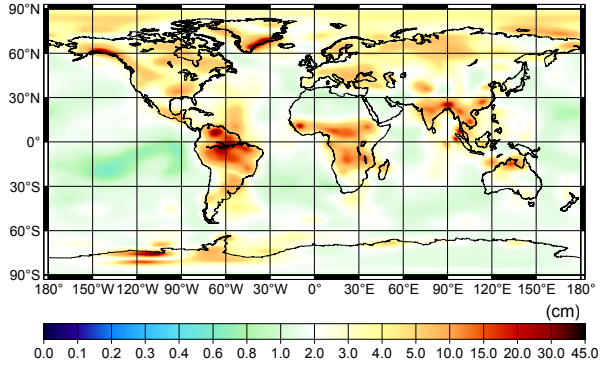


Figure 6.2: The $\text{PSD}^{\frac{1}{2}}$ of GRACE residual range combinations for the considered 11 months after elimination of their low-frequency noise (a) without and (b) with the spatially dependent data weighting. The vertical line marks the 3 cpr frequency. A Gaussian smoothing has been applied for a better visualization.

relatively strong mass variations (e.g., in Greenland, Antarctica, and Amazon) contribute the least to building this filter. This reduces damping the time varying gravity field signals in areas where these signals are relatively strong when applying the aforementioned high pass filter to residual range combinations.

To demonstrate the impact of this spatially dependent data weighting, I show in Fig. 6.2 the $\text{PSD}^{\frac{1}{2}}$ of the sets of residual range combinations for all the 11 months under consideration after elimination of the low frequency noise without and with the spatially dependent data weighting. Figure 6.2a shows that the non-weighted least squares scheme removes both noise and the time-varying gravity field signals below 3 cpr frequency, which is marked in this picture by a vertical line. This is not the case when the high-pass filter is built with the spatially dependent data weighting scheme (Fig. 6.2). In that case,

it is clearly seen that some information survive the high-pass filtering in this low frequency range. I consider this as a good indication that this approach reduces the loss of signal, thus providing an improved retrieval of the temporal gravity field variations.

To eliminate the extraordinary strong low-frequency noise in GOCE residual gravity gradients (i.e., up to 1 cpr), I follow the approach already described in chapter 3 (sections 3.3.4 and 3.3.4.1).

6.2.1.2 Computing stochastic models of noise

In line with a description provided in chapter 2 (section 2.4), the analysis of noise in sets of GRACE residual range combinations is performed in an iterative manner. In the first instance, the time series of these residuals itself is assumed to be a realization of its noise. On the basis of this assumption, an initial noise PSD is computed and the corresponding ARMA model is built. In view of an already mentioned noticeable time variability of noise in GRACE KBR data (Fig. 6.3), the ARMA models are built for each of the months in the considered tie interval individually. The built ARMA models are highly detailed (not shown). The initial ARMA models are exploited in the inversion, which results in a set of preliminary monthly gravity field solutions. Those solutions are included in the next iteration into the force model, thus allowing a more accurate estimation of noise in the residual range combinations to be acquired. It is sufficient to perform in this way only two iterations, as further changes in the estimated noise properties are found negligible. The initial and final noise PSD^{1/2}'s for all the 11 months under consideration are exhibited in Fig. 6.3.

A comparison of Figs. 6.3a and 6.3b shows that an inclusion of the preliminary monthly solutions in the force model expectedly reduces PSD of the residuals. This reduction is observed mostly in the frequency range 0.5 – 10 mHz (3 – 54 cpr, which corresponds to signals at spatial scales of 7200 – 400 km half wavelength), which is marked in Fig. 6.3 by two vertical lines. Interestingly, the noise time-variability is still observed in Fig. 6.3b with the same clarity as in Fig. 6.3a even when mass variation signals are removed from the residual range combinations. This confirms my statement in chapter 3 that the observed time variability of noise is not related to the presence or the absence of the time-varying gravity field signals in these residuals.

As far as the GOCE data are concerned, I found that it is sufficient to define noise realizations as residual data without any iterative improvement. This is because an addition of the produced monthly gravity field solutions to the force model leads to only negligible changes in the obtained noise PSD's. The noise PSD's are transformed into ARMA models. These models are similar to those obtained for these residuals in chapter 3 (not shown).

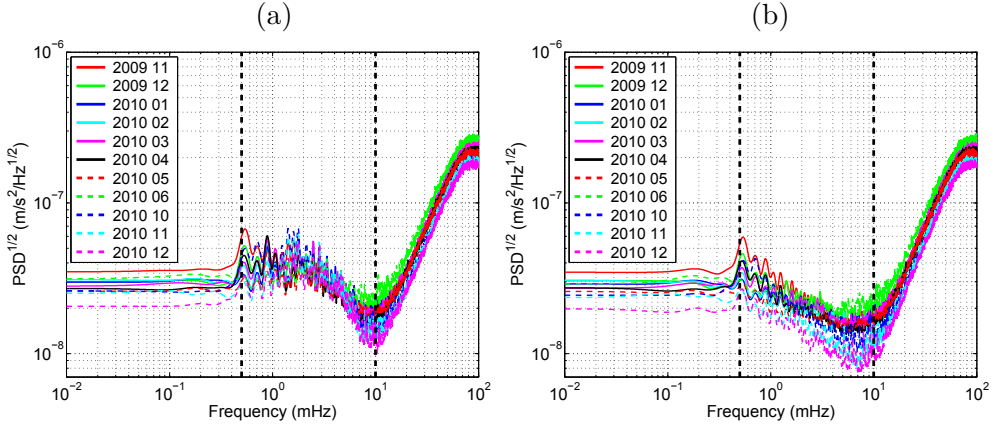


Figure 6.3: The (a) initial and (b) final, i.e., improved, noise $\text{PSD}^{\frac{1}{2}}$'s in the GRACE residual range combinations for the considered 11 months. The vertical lines mark the frequencies 3 and 54 cpr. A Gaussian smoothing has been applied for a better visualization.

6.2.1.3 Inversion

The sets of residual data are inverted into sets of residual spherical harmonic coefficients by solving the corresponding system of normal equations:

$$\mathbf{x}_{\text{UG}}^{(k)} = \left(\mathbf{N}_{\text{UG}}^{(k)} \right)^{-1} \left(\mathbf{A}_{\text{G}}^{(k)} \right)^T \left(\mathbf{C}_{\text{G}}^{(k)} \right)^{-1} \mathbf{d}_{\text{G}}^{(k)}, \quad (6.1)$$

or

$$\begin{aligned} \mathbf{x}_{\text{UC}}^{(k)} = & \left(\mathbf{N}_{\text{UC}}^{(k)} \right)^{-1} \left\{ \left(\mathbf{A}_{\text{G}}^{(k)} \right)^T \left(\mathbf{C}_{\text{G}}^{(k)} \right)^{-1} \mathbf{d}_{\text{G}}^{(k)} + \right. \\ & \left. + \left(\mathbf{A}_{\text{AA}}^{(k)} \right)^T \left(\mathbf{C}_{\text{AA}} \right)^{-1} \mathbf{d}_{\text{AA}}^{(k)} + \left(\mathbf{A}_{\text{GG}}^{(k)} \right)^T \left(\mathbf{C}_{\text{GG}} \right)^{-1} \mathbf{d}_{\text{GG}}^{(k)} \right\}, \end{aligned} \quad (6.2)$$

where $\mathbf{x}_{\text{UG}}^{(k)}$ is an unconstrained gravity field solution for the month k based on GRACE data alone and $\mathbf{x}_{\text{UC}}^{(k)}$ is an unconstrained solution based on a combination of KBR and GOCE data for the same month. The vectors $\mathbf{d}_{\text{G}}^{(k)}$, $\mathbf{d}_{\text{AA}}^{(k)}$, and $\mathbf{d}_{\text{GG}}^{(k)}$ denote the monthly time series of GRACE residual range combinations, GOCE residual 3-D average acceleration vectors, and GOCE residual gravity gradients, respectively. The terms $\mathbf{C}_{\text{G}}^{(k)}$, \mathbf{C}_{AA} , and \mathbf{C}_{GG} are the covariance matrices of noise in sets of residual data of the three considered types, respectively. Notice that the latter two matrices are independent from the month. The terms $\mathbf{A}_{\text{G}}^{(k)}$, $\mathbf{A}_{\text{AA}}^{(k)}$, and $\mathbf{A}_{\text{GG}}^{(k)}$ are the design matrices associated with the data of the three aforementioned types, respectively. Finally,

$$\mathbf{N}_{\text{UG}}^{(k)} = \left(\mathbf{A}_{\text{G}}^{(k)} \right)^T \left(\mathbf{C}_{\text{G}}^{(k)} \right)^{-1} \mathbf{A}_{\text{G}}^{(k)} \quad (6.3)$$

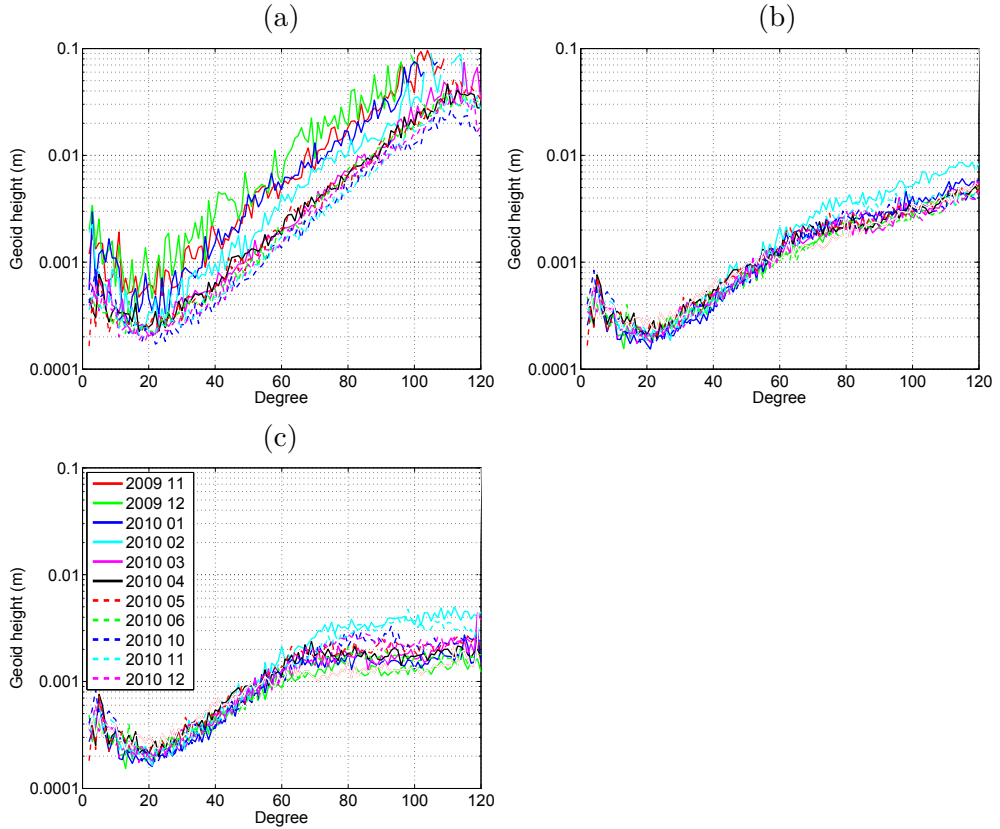


Figure 6.4: The unconstrained (a) GRACE-only (UG), (b) GRACE/GOCE combined (UC), and (c) pseudo-combined (UP) gravity field solutions for the considered 11 months in terms of per-degree geoid height differences from DGM-1S.

and

$$\mathbf{N}_{\text{UC}}^{(k)} = \left(\mathbf{A}_{\text{G}}^{(k)}\right)^T \left(\mathbf{C}_{\text{G}}^{(k)}\right)^{-1} \mathbf{A}_{\text{G}}^{(k)} + \left(\mathbf{A}_{\text{AA}}^{(k)}\right)^T \left(\mathbf{C}_{\text{AA}}\right)^{-1} \mathbf{A}_{\text{AA}}^{(k)} + \left(\mathbf{A}_{\text{GG}}^{(k)}\right)^T \left(\mathbf{C}_{\text{GG}}\right)^{-1} \mathbf{A}_{\text{GG}}^{(k)} \quad (6.4)$$

are the normal matrices associated with the GRACE-only and the combined GRACE/GOCE solutions, respectively.

6.2.2 Impact of GOCE data onto unconstrained solutions

The unconstrained GRACE-only solutions for the considered 11 months are shown in Fig. 6.4a in terms of per-degree geoid height differences from DGM-1S. Thereafter, these solutions are denoted as “UG”: Unconstrained GRACE-only. One can see that all these solutions show a similar behaviour. Below degree 20, their per-degree amplitudes decrease as the degree increases.

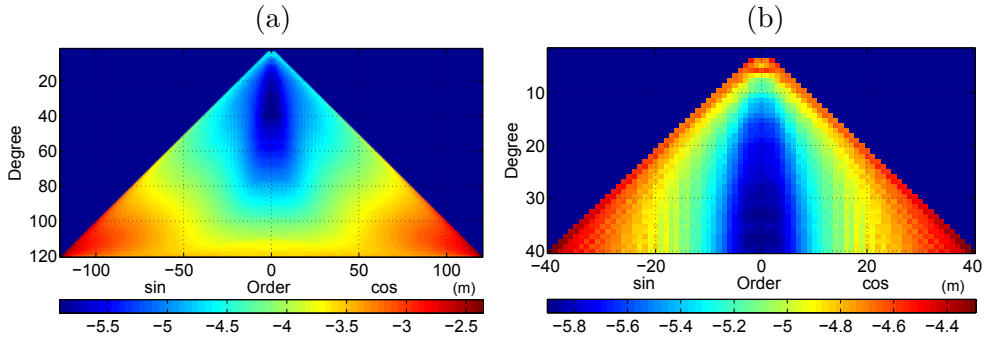


Figure 6.5: Logarithm with base 10 of formal errors in terms of geoid heights in the GRACE-only solution for November 2010 up to (a) the maximum degree and (b) degree 40.

This is consistent with the behaviour of signals caused by the Earth’s mass re-distribution (Wahr et al., 1998; Sasgen et al., 2006). Above that degree, however, the per-degree amplitudes increase, which is an evidence that noise gradually becomes the dominant contributor. The observed noise level is mostly associated with a poor estimation of sectorial and near-sectorial coefficients, caused by the previously mentioned anisotropic sensitivity of KBR data (Fig. 6.5).

It is worth noticing in Fig. 6.4a that the UG solutions produced for the first four months are characterized with a relatively large noise level in the entire range of degrees. This is due to the fact that the GRACE satellites’ orbits during that time interval were nearly repeating themselves after only seven days. For the sake of brevity, I hereafter refer to these four months as “bad” and to the remaining ones as “good”.

Fig. 6.4b presents a similar set of solutions, but produced by a combined inversion of KBR and GOCE data. Both GOCE SST data and its gravity gradients are exploited in these solutions. They are hereafter referred to as “UC”: Unconstrained Combined. The incorporation of GOCE data reduces noise quite significantly. For the “good” months, this reduction is mostly limited to the range of high degrees (above nearly degree 60). For the “bad” months, the impact of GOCE data is even more pronounced. It is observed in the entire range of degrees, so that the spectral behaviour of the UC solutions for the “bad” months and those for the “good” ones becomes quite similar. Furthermore, a comparison between the UG and UC solutions allows me to conclude that no model degradation is observed in the UC solutions due to the presence of the polar gaps in the GOCE spatial coverage. I explain this by the presence of KBR data in the joint inversion, as mentioned in the introductory part of the thesis.

It is tempting to conclude based on this experiment that the added value of GOCE data, at least for the months when GRACE satellites follow an orbit with a relatively short repeat period, may be substantial. One should bear in mind, however, that a reduction of noise in unconstrained solutions does not necessarily justify a need in real GOCE data. The actual added value can only be claimed when the data contain new information about the signals being studied. Otherwise, the reduction of noise is nothing more than constraining a model. Such a noise reduction can be achieved in the absence of real data, too. For that, it may be sufficient to replace real data with a realistic noise realization, which can be simulated numerically, or even to replace real data with zeroes. With this consideration in mind, I conduct the third experiment. I replace both the GOCE residual 3-D average accelerations and its residual gravity gradients with time series filled with zeros. Hereafter, I refer to these time series as “pseudo-data”. The compiled pseudo-data are inverted, together with the sets of GRACE residual range combinations, in the same manner as in the case of the real GOCE data, including the usage of the same stochastic models of data noise. In other words, I replace the GRACE-only normal matrix in Eq. (6.1) with the GRACE/GOCE combined normal matrix, i.e.,

$$\mathbf{x}_{\text{UP}}^{(k)} = \left(\mathbf{N}_{\text{UC}}^{(k)} \right)^{-1} \left(\mathbf{A}_{\text{G}}^{(k)} \right)^T \left(\mathbf{C}_{\text{G}}^{(k)} \right)^{-1} \mathbf{d}_{\text{G}}^{(k)}. \quad (6.5)$$

I hereafter denote the resulting set of solutions as “UP”: Unconstrained Pseudo-combined. These solutions are shown in Fig. 6.4c. From a comparison of Fig. 6.4b with Fig. 6.4c, one can conclude that the noise reduction in monthly solutions achieved by the incorporation of the GOCE pseudo-data seems to be close to that achieved using the real GOCE data. In other words, the impact of real GOCE data can be mostly explained by the incorporation of their normal matrix into the system of normal equations, i.e., it is similar to the impact of a regularization.

One may argue that the usage of the GOCE pseudo-data forces the solutions to be close to the a priori static gravity field model. Since this a priori model in my study is DGM-1S, which is partly based on GOCE data (see chapter 3), it is, strictly speaking, not fair to claim that the UP solutions do not exploit the information content of real GOCE data at all. However, I have also repeated the computations using another a priori model, EIGEN-5C (Förste et al., 2008b), which was compiled without GOCE data. The results (not shown) turned out to be quite similar to those demonstrated in Fig. 6.4.

Furthermore, it could be argued that the produced monthly solutions may reflect not only the temporal gravity field variations, but also deficiencies of the adopted a priori static gravity field model. A way to eliminate the latter effect is to consider differences between successive monthly solutions rather than the monthly solutions themselves. Therefore, I focus below on month-to-

month differential solutions. Two of such solutions are addressed explicitly: (i) “December 2009 minus November 2009”, which is associated with the “bad” months; and (ii) “December 2010 minus November 2010”, which corresponds to the “good” months. In addition, the linear trend in the entire time interval November 2009 till December 2010 is considered. It is obtained for each spherical harmonic coefficient together with five other parameters, namely, a bias and four parameters describing the annual and semi-annual sinusoidal variations, by a least squares adjustment, in which the observation equation per coefficient reads as follows:

$$x(\tau) = y_0 + y_1\tau + y_2 \cos(2\pi\tau) + y_3 \sin(2\pi\tau) + y_4 \cos(4\pi\tau) + y_5 \sin(4\pi\tau). \quad (6.6)$$

Herein, τ denotes the time difference between the middle of a considered month and the middle of the time interval under consideration after normalising (i.e., after dividing by the length of the time interval for which the unknowns are to be estimated), $x(\tau)$ is a value estimated for a given coefficient in the month associated with τ , y_0 represents the bias with respect to the a priori static gravity field model, y_1 describes the linear trend, and y_2 till y_5 account for the annual and semi-annual sinusoidal variations to be estimated. The unknown terms y_0 till y_5 are estimated from the 11 monthly values of a given coefficient. Figure 6.6 shows the derived products (i.e., the differential solutions “December 2009 minus November 2009”, differential solutions “December 2010 minus November 2010”, and the linear trends) in terms of per-degree geoid heights. The products based on the solutions of all the three types, namely, UG, UC, and UP, are presented, which facilitates their comparison. In addition, I include the per-degree differences between the UC- and UP-based products. One can see that in the range of low degrees (up to nearly degree 60), the difference between the UC- and UP-based products is indeed minor. This can be considered as a further justification of my earlier statement that the role of GOCE data is mostly limited to constraining the solutions, so that the information content of these data does not play a notable role. It is also remarkable that for the differential solution related to the “good” months under consideration, the incorporation of GOCE data or pseudo-data practically has no effect below degree 60. At higher degrees, the GOCE pseudo-data as compared to the real measurements of the mission result in a stronger reduction of noise in the solutions. Most probably, this is due to the fact that real GOCE data are contaminated by noise, which propagates into the spherical harmonic coefficients. Given the fact that the sensitivity of GRACE data to high-degree signals is relatively low, this noise propagation gradually becomes dominant as degree increases. Noise in the pseudo-combined solutions, on the other hand, is solely the outcome of GRACE data noise propagation. The other differential solutions reflect a similar pattern, and therefore, are not shown. At last, it is worth noting that the UG solution of the linear trend (Fig. 6.6c) shows

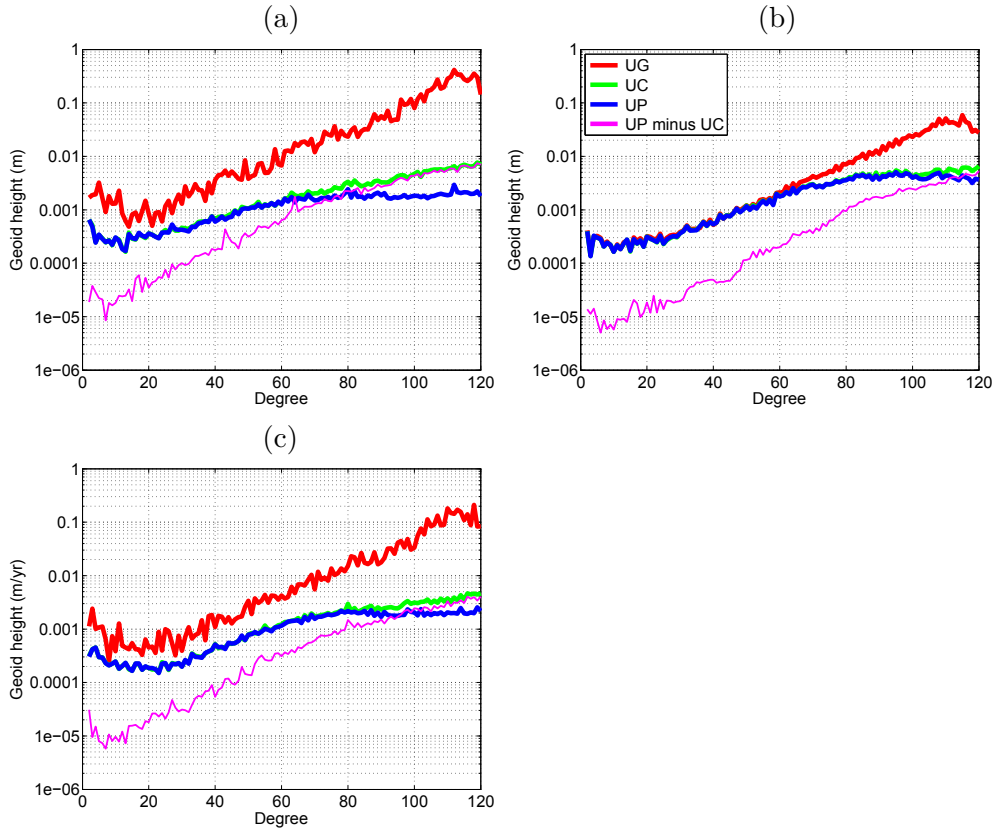


Figure 6.6: Products based on unconstrained GRACE-only (UG), GRACE/GOCE combined (UC), and pseudo-combined (UP) solutions: (a) differential solutions “December 2009 minus November 2009”, (b) differential solutions “December 2010 minus November 2010”, and (c) linear trends. In addition, the differences between the UP- and UC-based products are included. All the results are shown in terms of geoid height per degree.

a similar pattern as the differential solution derived from the “bad” months (Fig. 6.6a). I explain this by the fact that the relatively strong random noise in the UG solutions produced for the “bad” months influences the estimation of the linear trend in a negative manner.

I compare the solutions in the spatial domain, too. For instance, Fig. 6.7 shows the linear trends in terms of equivalent water heights derived from the UG, UC, and UP solutions. Noise in the UG-based trend is typical for unconstrained GRACE-only solutions: along-track stripes, which are especially pronounced in the tropical areas, where a solution of this type suffers the most from the anisotropic sensitivity of GRACE KBR data. Noise in the trend derived from the UC solutions, which are constrained by real GOCE data, is much lower,

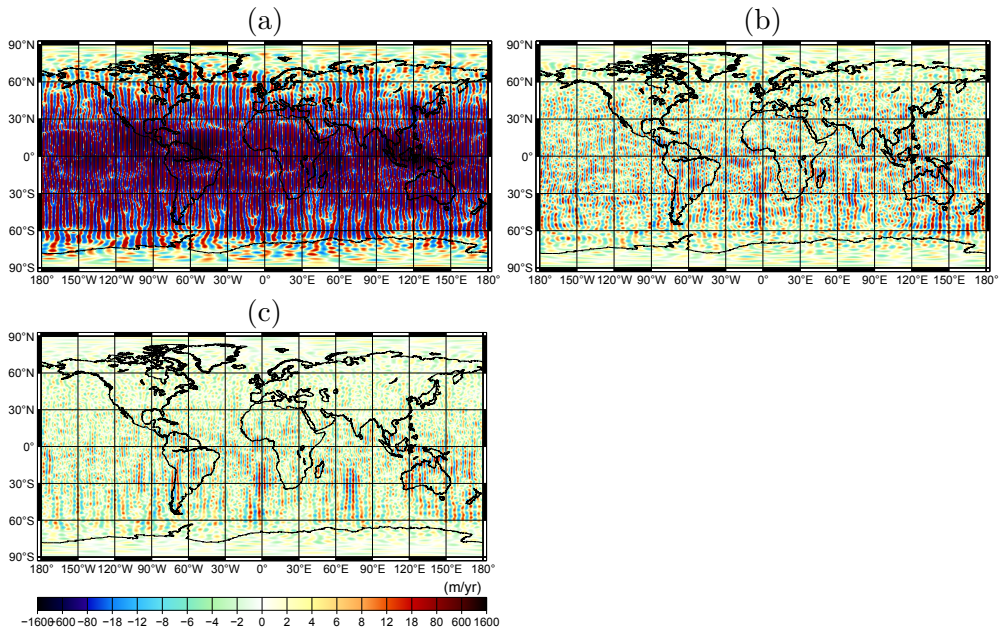


Figure 6.7: Linear trends in terms of equivalent water heights derived from the (a) unconstrained GRACE-only (UG), (b) GRACE/GOCE combined (UC), and (c) pseudo-combined (UP) solutions. The maps are generated on a $0.5^\circ \times 0.5^\circ$ grid. Their RMS values are (a) 165.5 m/yr, (b) 6.6 m/yr, and (c) 4.2 m/yr.

i.e., the stripes are much less pronounced. The trend derived from the UP solutions, which are constrained by the GOCE pseudo-data, shows the lowest noise level. The differential solutions behave in a similar way, and therefore, are not shown.

In addition, the produced solutions of all the three types (UG, UC, and UP) are compared in terms of globally obtained RMS values of equivalent water heights (Table 6.1). This table clearly shows that the GOCE pseudo-data lead to the lowest noise level in the produced solutions. It is of the order of 4 – 8 m in the case of the differential solutions and about 4 m/yr in the case of the linear trend. On the other hand, the observed noise level in all the cases is at least an order of magnitude higher than the expected signal level (e.g., Ditmar et al., 2010). Therefore, the analysis of the unconstrained solutions does not allow one to decide whether or not the usage of real GOCE data improves the retrieval of the mass transport.

In practice, the utilization of GRACE-based time-varying gravity field models requires that noise in them is reduced to a sufficiently low level. A common way to achieve this is to apply a properly defined filter. Studying the added value of GOCE data in the context of filtered monthly gravity field solutions is the primary subject of the next section.

Table 6.1: The global RMS equivalent water heights derived from UG-, UC-, and UP-based products. The equivalent water heights are computed at the nodes of an equiangular $0.5^\circ \times 0.5^\circ$ grid.

Product	UG	UC	UP
“December 2009 minus November 2009” (m)	350.3	10.2	4.1
“December 2010 minus November 2010” (m)	56.5	10.0	8.2
Linear trend (m/yr)	165.5	6.6	4.2

6.3 Optimally filtered gravity field solutions

The first subsection describes the filtering of the GRACE-only and combined GRACE/GOCE monthly gravity field solutions. The second subsection looks into the differences between the filtered solutions of these two types in an attempt to quantify the impact of GOCE data.

6.3.1 Filtering procedure

As it was pointed out in the introductory part of the thesis, multiple filters have been proposed to suppress noise in GRACE-based unconstrained models of the temporal gravity field variations. In this thesis, I limit myself to the optimal anisotropic filter described in (Klees et al., 2008b) and (Liu et al., 2010). The filter is statistically optimal in the sense that it minimizes the mean square differences between the true mass variations and the estimated filtered ones. In the case of the GRACE-only monthly solutions, this filter is defined as:

$$\mathbf{F}_G^{(k)} = \mathbf{D} \left(\mathbf{C}_{UG}^{(k)} + \mathbf{D} \right)^{-1}, \quad (6.7)$$

where \mathbf{D} denotes the full covariance matrix of the signal and $\mathbf{C}_{UG}^{(k)}$ is the full covariance matrix of noise in a GRACE-only solution produced by the inversion of the corresponding normal matrix: $\mathbf{C}_{UG}^{(k)} = (\mathbf{N}_{UG}^{(k)})^{-1}$. The optimal filter to be applied to a combined GRACE/GOCE monthly solution is defined similarly:

$$\mathbf{F}_C^{(k)} = \mathbf{D} \left(\mathbf{C}_{UC}^{(k)} + \mathbf{D} \right)^{-1}, \quad (6.8)$$

where $\mathbf{C}_{UC}^{(k)}$ is the full covariance matrix of noise in the combined solution: $\mathbf{C}_{UC}^{(k)} = (\mathbf{N}_{UC}^{(k)})^{-1}$. The filters defined in this way are spatially varying: the higher the signal-to-noise ratio at a particular location, the less smoothing is applied, and vice versa.

As it has been shown by Klees et al. (2008b), simple algebraic manipulations allow the terms in the expression for the optimal filter to be re-ordered. For instance, the filter $\mathbf{F}_G^{(k)}$ can be alternatively represented as

$$\mathbf{F}_G^{(k)} = \left\{ \left(\mathbf{C}_{\text{UG}}^{(k)} \right)^{-1} + \mathbf{D}^{-1} \right\}^{-1} \left(\mathbf{C}_{\text{UG}}^{(k)} \right)^{-1}. \quad (6.9)$$

The application of such a filter to an unconstrained GRACE-only solution yields:

$$\begin{aligned} \mathbf{F}_G^{(k)} \mathbf{x}_{\text{UG}}^{(k)} &= \\ \left\{ \left(\mathbf{C}_{\text{UG}}^{(k)} \right)^{-1} + \mathbf{D}^{-1} \right\}^{-1} \left(\mathbf{C}_{\text{UG}}^{(k)} \right)^{-1} \left(\mathbf{N}_{\text{UG}}^{(k)} \right)^{-1} \left(\mathbf{A}_G^{(k)} \right)^T \left(\mathbf{C}_G^{(k)} \right)^{-1} \mathbf{d}_G^{(k)} &= \\ \left\{ \mathbf{N}_{\text{UG}}^{(k)} + \mathbf{D}^{-1} \right\}^{-1} \left(\mathbf{A}_G^{(k)} \right)^T \left(\mathbf{C}_G^{(k)} \right)^{-1} \mathbf{d}_G^{(k)}. \end{aligned} \quad (6.10)$$

Thus, the optimal filtering is equivalent to the regularization of the solution, the regularization matrix being defined as \mathbf{D}^{-1} , i.e., the inverse signal covariance matrix. Obviously, a similar statement holds true also for the combined GRACE/GOCE solutions.

The procedure to compute the signal covariance matrix is discussed in detail in (Klees et al., 2008b) and (Liu et al., 2010). This matrix is computed with an iterative scheme, which initiates from a constant variance of mass transport signal worldwide. An accurate computation of this matrix requires a sufficiently long time series of time-varying gravity field solutions: the longer, the better. In my study, however, I deal with a relatively short time series of solutions. Therefore, in my analysis, I cannot accurately compute this matrix myself and have to make use of the one computed in the course of production of DMT-1.

6.3.2 Impact of GOCE data onto optimally filtered solutions

The optimal filters described in the previous subsection are applied to all the GRACE-only and the combined GRACE/GOCE monthly solutions one by one. Hereafter, GOCE SST and SGG data are treated not only combined but also separately. In other words, two additional variants of the GRACE/GOCE combined solutions are produced. To that end, I invert either of the aforementioned sets of GOCE data together with the KBR data and then apply the appropriately built optimal filter.

Prior to a further analysis, I subtract from the considered eleven-month time series the corresponding mean to eliminate the contribution of the GRACE and GOCE data to an improvement of the a priori static gravity field model. Furthermore, I consider derived products similar to those described in section 6.2.2: (i) nine differential solutions obtained by subtracting two successive

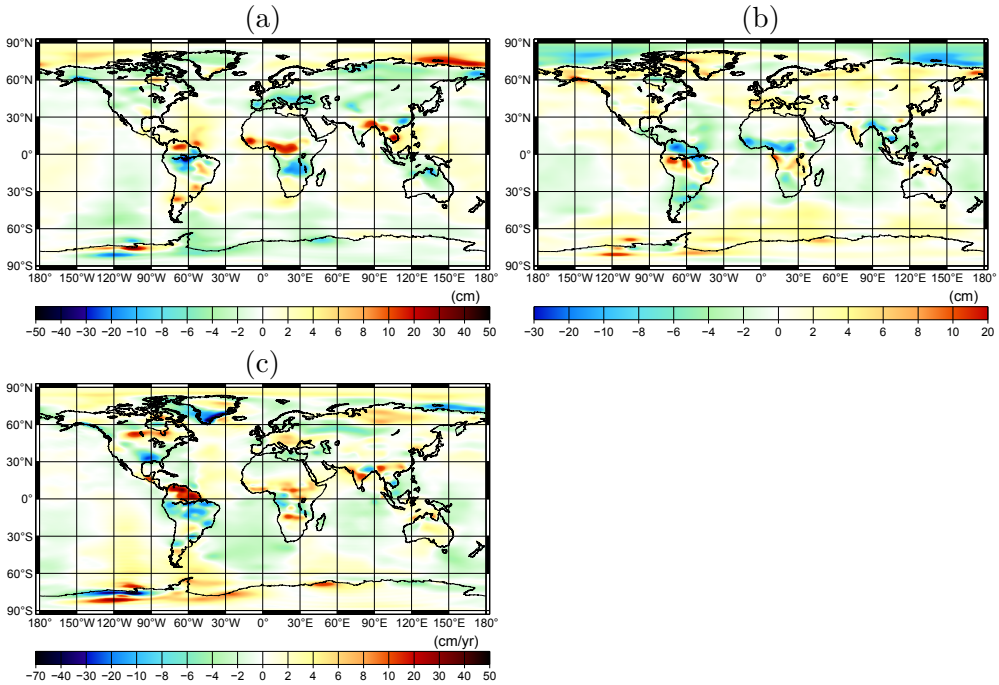


Figure 6.8: Some results based on the optimally filtered GRACE-only solutions: (a) the monthly solution of November 2009; (b) the differential solution “December 2009 minus November 2009”; and (c) the linear trend. All the results are shown in terms of equivalent water heights. The maps are generated on a $0.5^\circ \times 0.5^\circ$ grid. Their RMS values are (a) 2.8 cm, (b) 2.7 cm, and (c) 3.5 cm/yr.

monthly solutions; and (ii) linear trend in the time interval November 2009 – December 2010 computed from the filtered solutions with the same procedure as described in section 6.2.2.

Figure 6.8 shows some of the results obtained based on KBR data alone: (a) the monthly solution of November 2009; (b) the differential solution “December 2009 minus November 2009”; and (c) the linear trend. The first two products (Fig. 6.8a and 6.8b) show a particularly strong signal in the equatorial areas, which are known to show pronounced annual variations due to the accumulation and depletion of continental water stocks. Furthermore, positive signals are visible in the second product (Fig. 6.8b) in many continental areas above latitude 50°N . Most probably, they reflect the increasing accumulation of snow in winter. In the map of the linear trend (Fig. 6.8c), one can easily recognize, among others, a strong ice mass loss at the southeast coast of Greenland and at the coast of Amundsen sea in West Antarctica. The maps based on the filtered GRACE/GOCE combined solutions are visually quite similar to those related to the GRACE-only ones, and therefore, are not shown.

Both the optimal filtering and the usage of GOCE pseudo-data can be interpreted as applying a regularization to unconstrained GRACE-only solutions. A comparison of Figs. 6.7 and 6.8c allows one to conclude that the optimal filters constrain the solutions much heavier than the GOCE pseudo-data. One may, therefore, suggest that the impact of GOCE pseudo-data in the context of filtered solutions must be minor. The conducted experiments confirm this expectation. The difference between the optimally filtered UG and UP solutions is always at a sub-millimeter level everywhere. Therefore, the idea of using GOCE-pseudo data is not addressed below any further.

As it was previously mentioned, the filtered GRACE-only solutions are quite close to the filtered combined GRACE/GOCE ones. Therefore, the focus of my further analysis is on the differences between the solutions of these two types rather than on the solutions themselves. Below, a collection of these differences is treated in my study as a formal definition of the impact of GOCE data.

To quantify this impact, I compute its RMS in terms of equivalent water heights for all the monthly solutions and the products derived on their basis individually. In addition, the RMS values based on the entire time series are produced for the monthly and differential solutions. The obtained results are presented in Table 6.2, both in terms of equivalent water heights (cm or cm/yr in the case of the linear trend) and in the form of percentages with respect to the RMS value of the corresponding mass transport signal, which is always computed based on the GRACE-only solutions. First, Table 6.2 shows that the impact of GOCE data onto the optimally filtered solutions is, in average, quite modest: for most cases, it stays at the level of 1 – 3 % of the signal sensed by the GRACE. Furthermore, the average impact of GOCE SST data exceeds that of its gravity gradients up to 4 times. Finally, there is no obvious distinction between the impact of GOCE data in the “bad” months (November 2009 till February 2010) and that in the “good” ones (i.e., March 2010 till December 2010).

Furthermore, it is worth noticing that random errors in the filtered GRACE-based monthly solutions are of the order of 1 cm in terms of equivalent water heights or even larger (e.g., Liu et al., 2010). Thus, the average impact of GOCE data quantified in this study is well below the noise level.

Figure 6.9a shows the impact of GOCE data onto the differential solution “December 2009 minus November 2009” in terms of equivalent water heights. From a comparison of this picture with Fig. 6.8b, one can conclude that the impact of GOCE data closely correlates with the total mass transport signal. It is the largest in the continental areas near the equator, where large mass variations of the hydrological origin occur, as well as in the polar areas with a rapid ice mass change. At the same time, it is the smallest in the oceanic areas.

Table 6.2: The statistical information about the impact of the GOCE SST and SGG data onto the optimally filtered monthly GRACE-only gravity field solutions and the products derived on their basis. The numbers are given both in terms of equivalent water heights (cm or cm/yr for the linear trend) and in the form of percentages with respect to the RMS value of the corresponding signal computed on the basis of the GRACE-only solutions.

Product	Time interval	GOCE SST and SGG data combined		GOCE SST data alone		GOCE SGG data alone	
		cm or	per	cm or	per	cm or	per
		cm/yr	cent	cm/yr	cent	cm/yr	cent
Monthly solutions	November 2009	0.04	1.48%	0.04	1.33%	0.02	0.68%
	December 2009	0.03	1.67%	0.03	1.31%	0.02	1.00%
	January 2010	0.03	1.36%	0.02	0.98%	0.02	0.94%
	February 2010	0.03	1.22%	0.03	1.12%	0.01	0.50%
	March 2010	0.03	0.93%	0.02	0.77%	0.02	0.55%
	April 2010	0.04	1.38%	0.04	1.21%	0.02	0.68%
	May 2010	0.05	1.74%	0.05	1.62%	0.02	0.64%
	June 2010	0.08	2.89%	0.08	2.83%	0.02	0.67%
	October 2010	0.03	0.70%	0.02	0.59%	0.01	0.35%
	November 2010	0.03	0.87%	0.03	0.74%	0.02	0.44%
	December 2010	0.03	0.89%	0.02	0.77%	0.01	0.47%
	All solutions	0.04	1.40%	0.04	1.28%	0.02	0.59%
Differential solutions	Dec 2009 minus Nov 2009	0.06	2.02%	0.05	1.70%	0.03	1.07%
	Jan 2010 minus Dec 2009	0.04	1.78%	0.03	1.31%	0.03	1.21%
	Feb 2010 minus Jan 2010	0.04	1.66%	0.03	1.28%	0.02	1.05%
	Mar 2010 minus Feb 2010	0.04	1.81%	0.03	1.49%	0.02	1.04%
	Apr 2010 minus Mar 2010	0.05	2.23%	0.04	1.90%	0.03	1.20%
	May 2010 minus Apr 2010	0.07	2.72%	0.06	2.45%	0.03	1.21%
	Jun 2010 minus May 2010	0.09	3.54%	0.08	3.40%	0.03	1.08%
	Nov 2010 minus Oct 2010	0.03	1.11%	0.02	0.76%	0.02	0.81%
	Dec 2010 minus Nov 2010	0.03	1.31%	0.03	0.98%	0.02	0.89%
	All solutions	0.05	2.16%	0.04	1.89%	0.03	1.07%
Linear trend	Nov 2009 – Dec 2010	0.04	1.14%	0.04	1.03%	0.02	0.48%

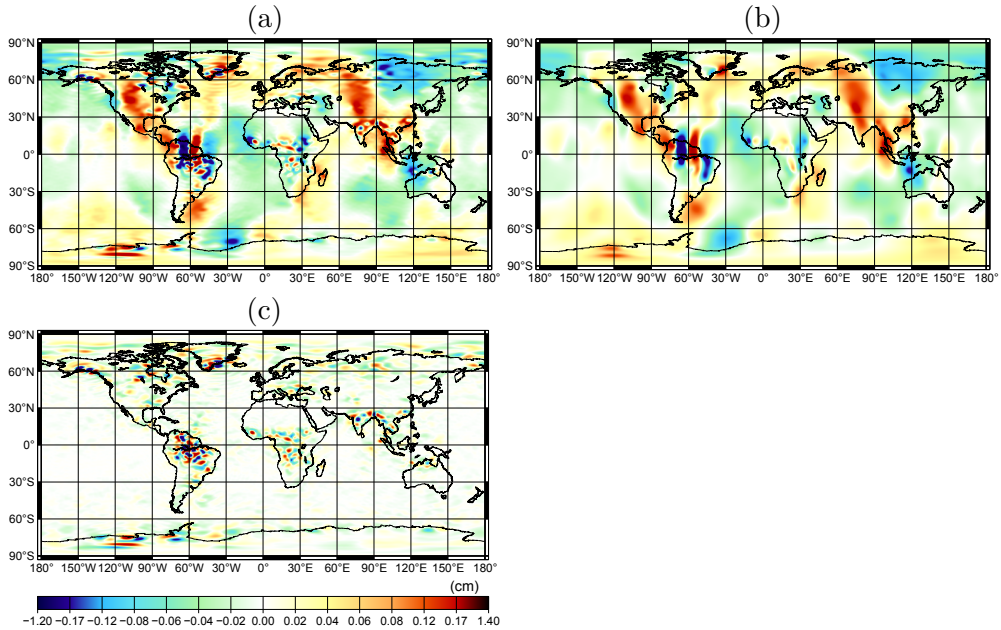


Figure 6.9: The impact of GOCE data onto the differential mass transport solution “December 2009 minus November 2009”: (a) the combined impact of GOCE SST and SGG data; (b) the impact of GOCE SST data only; and (c) the impact of GOCE SGG data only. All the results are presented in terms of equivalent water heights. The maps are generated on a $0.5^\circ \times 0.5^\circ$ grid. Their RMS and the maximum absolute values are: (a) 0.06 cm and 1.34 cm; (b) 0.05 cm and 0.67 cm; and (c) 0.03 cm and 1.18 cm.

I find it also remarkable that the impact of GOCE data spans a wide range of spatial scales. The reason for that becomes more clear if one looks into the impact of GOCE SST data and its gravity gradients, separately (Figs. 6.9b and 6.9c, respectively). The obtained maps allow me to conclude that the impact of GOCE SST data is mostly limited to the range of low spherical harmonic degrees. Its presence is visible worldwide, including the oceans, though correlations with the total mass transport signal are definitely present. The impact of GOCE gravity gradients, on the other hand, is observed as a collection of small-scale features, which is consistent with a relatively high sensitivity of these data to signals at high degrees. These small-scale features are strictly limited to areas where the mass transport signal is rather strong, i.e., mostly to the continental areas (such as Amazon, South Greenland, and Antarctica). The fact that the applied filter is aggressive the least in areas where relatively strong mass transport occurs makes the impact of GOCE data in those areas be subjected to less smoothing than in the rest of the globe. This makes the impact of GOCE data in those areas larger. The analysis of

the other solutions and the products derived on their basis leads to similar findings, and therefore, is not presented.

The obtained results prompt that it is insufficient to limit the analysis to the average impact of GOCE data, as it is done in Table 6.2. It is also necessary to consider the peak values (i.e., maximum absolute values) of the impact, which are expected to be associated with areas of relatively strong mass transport signals. This allows me to inspect whether or not at least in areas with relatively strong mass variations the impact of GOCE data can be substantial.

In Table 6.3, I present the peak values of the impact of GOCE data. The combined impact of GOCE SST and SGG data as well as the individual impact of data of each type are considered. One can see that the majority of the peak values are identified either at the southeast coast of Greenland or in the Amazon river basin, i.e., indeed in areas where the mass transport signal is particularly strong.

To understand the numbers presented in Table 6.3 better, I compare them with the signal at the vicinity of the geographical location where the peak impact of GOCE data is identified. The monthly solutions are unfortunately not quite useful for such a comparison. The signal in the monthly solutions is measured relatively with respect to a reference level, which can be chosen, generally speaking, arbitrarily. In the case of this study, this level is defined as the mean over the considered eleven monthly solutions. This means, for instance, that in areas where the signal is predominately characterized with a linear trend, the signal is relatively small in the middle of the considered time interval and increases towards the edges. Of course, one can easily manipulate this signal by choosing a different reference level. Hence, to make the comparison more objective, I hereafter focus only on the differential solutions and the linear trend.

The peak impact of GOCE SST data onto the differential solutions reaches 1 cm in terms of equivalent water heights. It is observed in the Amazon river basin for the differential solution “May 2010 minus April 2010”. From the corresponding map (Fig. 6.10a), it can be observed that this impact appears like stripes elongated in the North-South direction with the peak value over the Amazon river, where the total mass transport signal is maximum, too (Fig. 6.10c). Since such a spatial pattern is typical for errors in GRACE-based solutions, I cautiously interpret the identified impact as an attempt of GOCE SST data to mitigate those inaccuracies. The combined impact of the GOCE SST and SGG data (Fig. 6.10b) stays at the same level as that of the GOCE SST data alone, but the spatial pattern somewhat changes. On top of the features elongated in the meridional directions, I observe a collection of small-scale features due to a relatively high sensitivity of GOCE gravity gradients to signals at high degrees. A comparison of the impact with the

Table 6.3: The peak values of the impact of GOCE data onto the optimally filtered monthly solutions and the products derived on their basis. All the results are shown in terms of equivalent water heights. They are extracted from maps generated on a $0.5^\circ \times 0.5^\circ$ grid.

Product		GOCE SST and SGG data combined	GOCE SST data alone	GOCE SGG data alone
	Time interval	June 2010	May 2010	March 2010
Monthly solutions	Peak value (cm)	0.90	0.73	0.71
	Location	67.25°N, 33.75°W (Greenland)	3.25°S, 63.75°W (Amazon)	3.75°S, 61.75°W (Amazon)
	Time interval	Dec. 2009 minus Nov. 2009	May 2010 minus Apr. 2010	Dec. 2009 minus Nov. 2009
Differential solutions	Peak value (cm)	1.34	1.02	1.18
	Location	3.75°S, 60.25°W (Amazon)	3.25°S, 63.75°W (Amazon)	3.75°S, 60.25°W (Amazon)
Linear trend Nov. 2009 – Dec. 2010	Peak value (cm/yr)	0.57	0.16	0.51
	Location	67.25°N, 36.75°W (Greenland)	15.75°S, 48.75°W	67.25°N, 36.75°W (Greenland)

total signal observed in the Amazon river basin for the differential solution under consideration (Fig. 6.10c) shows that the observed impact in relative terms remains minor: not more than 2 %. The same conclusion can be drawn from the graph of differential GRACE-only and combined solutions shown along a selected East-West profile (Fig. 6.10d), which is marked with a black line in the aforementioned three maps.

The peak impact of the GOCE SGG data onto the differential solutions is slightly above 1 cm in terms of equivalent water heights. It is also observed in the Amazon river basin, but in this case for the differential solution “De-

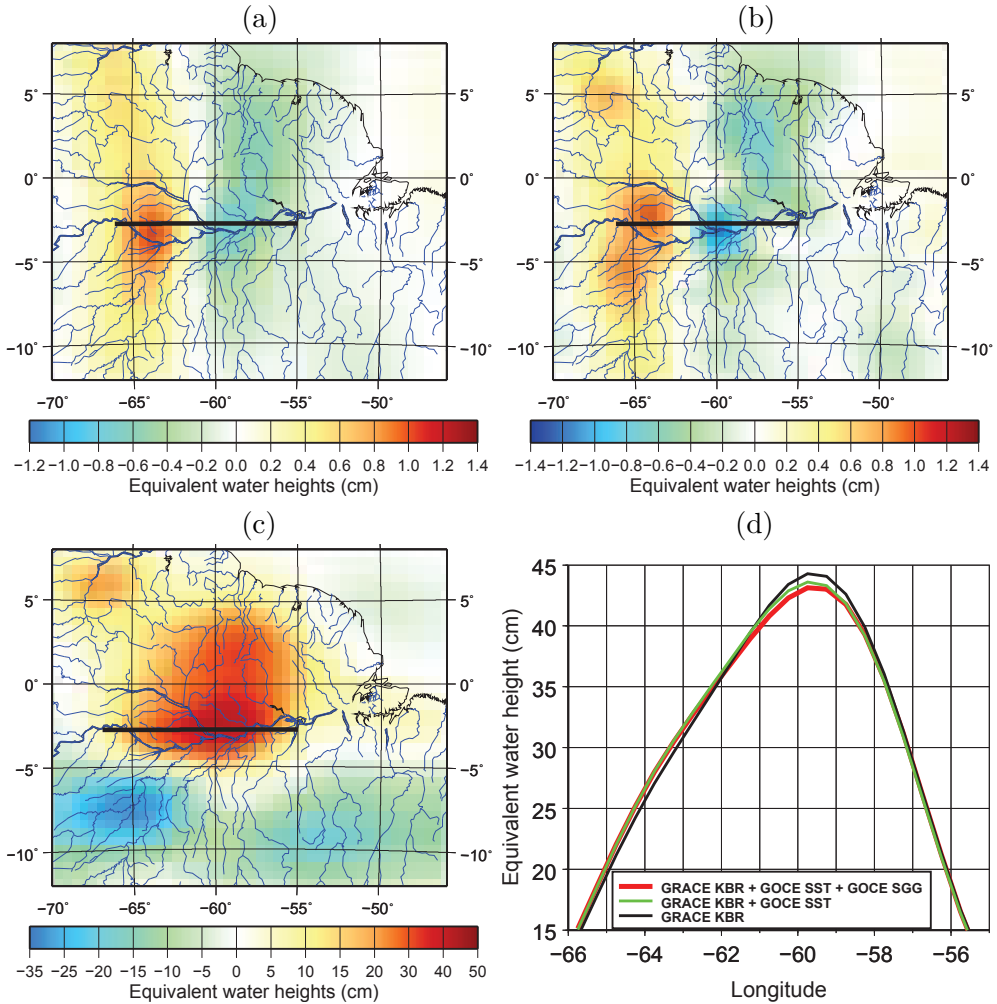


Figure 6.10: Results based on the differential solution “May 2010 minus April 2010” over the Amazon river basin in terms of equivalent water heights: (a) the impact of the GOCE SST data alone; (b) the impact of the GOCE SST and SGG data combined; (c) the total mass transport signal recovered from GRACE KBR data; and (d) the GRACE-only and combined estimations of mass transport along a selected East-West profile, which is marked by a thick black line in the maps. All the results are shown in terms of equivalent water heights.

cember 2009 minus November 2009” (Fig. 6.11a). The peak impact is located near the city of Manaus, where the Rio Negro river joins the Amazon river. The seasonal variations of water level in Manaus harbour reach several meters. Hence, this location is characterized by a relatively strong though highly localized signal. Therefore, the observed impact of the GOCE gravity gradients can be interpreted as an attempt to improve the spatial resolution of

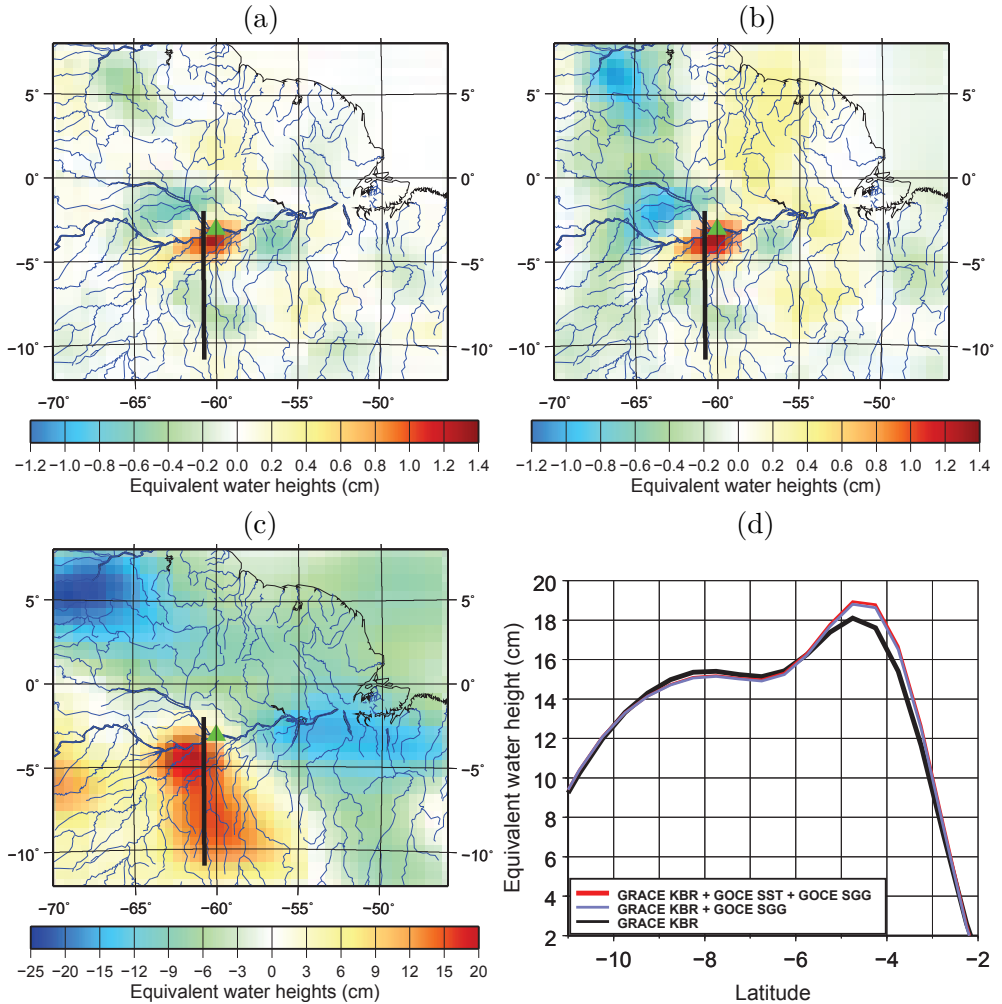


Figure 6.11: Results based on the differential solution “December 2009 minus November 2009” over the Amazon river basin in terms of equivalent water heights: (a) the impact of the GOCE SGG data alone; (b) the impact of the GOCE SST and SGG data combined; (c) the total mass transport signal recovered from KBR data; and (d) the GRACE-only and combined estimations of mass transport along a selected North-South profile, which is marked with a black line in the maps. The location of Manaus is marked in the maps with a green triangle. The results are in terms of equivalent water heights.

the GRACE-only differential solution, in which the signal in the sub-basins to the south from the Amazon and in the Amazon itself can hardly be separated (Fig. 6.11c). Given the total signal for the differential solution under consideration being about 20 cm (Figs. 6.11c and 6.11d), the peak impact of the GOCE gravity gradients is about 5%. The peak impact of the GOCE

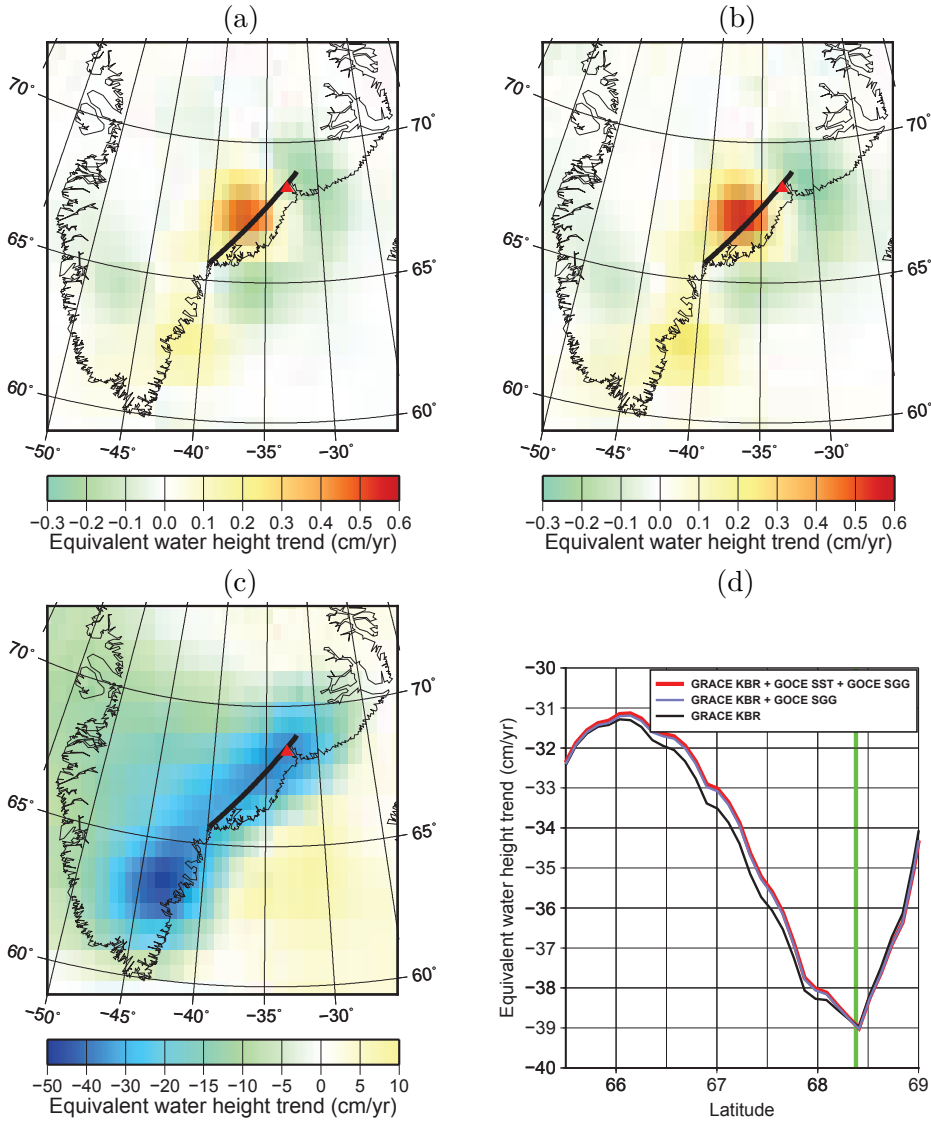


Figure 6.12: Results based on the estimated linear trend over the southeast Greenland in terms of equivalent water heights: (a) the impact of the GOCE SGG data alone; (b) the impact of the GOCE SST and SGG data combined; (c) the total mass transport signal recovered from GRACE KBR data; and (d) the GRACE-only and GRACE/GOCE combined estimations of mass transport along a selected profile crossing the Kangerdlugssuaq glacier along the coast, which is marked in the maps with a thick black line. The location of the Kangerdlugssuaq glacier is also marked in the maps with a red triangle and in the profile picture with a vertical green line. All the results are shown in terms of equivalent water heights. The maps are generated on a $0.5^\circ \times 0.5^\circ$ grid.

SST and SGG data combined is also found at this location and for the same differential solution. The spatial pattern of the combined impact (Fig. 6.11b) is somewhat similar to that of the GOCE gravity gradients alone. The incorporation of the GOCE SST data has only resulted in the appearance of faint meridional stripes. That is, it has a similar effect as mentioned earlier in the case of the differential solution “May 2010 minus April 2010”. According to Table 6.3, the peak of the combined impact is 1.34 cm of equivalent water heights, i.e., 6 – 7 % of the total signal under consideration. These findings are consistent with Fig. 6.11d, in which the GRACE-only and GRACE/GOCE combined estimations of the mass variations are plotted along a North-South profile near Manaus, which is marked with a black line in the three maps discussed above.

As far as the linear trend is concerned, the peak impact of the GOCE SGG data alone and that of the GOCE SST and SGG data combined are both identified at the southeast coast of Greenland (Figs. 6.12a and 6.12b, respectively). These impacts are of almost similar peak value, which is slightly above 0.5 cm/yr (Table 6.3). They show a similar spatial pattern, too. This spatial pattern is characterized by a localized positive feature situated to the south from the Kangerdlugssuaq glacier, which is characterized by massive ice mass loss in the past few years. In the GRACE-only solution, shown in Fig. 6.12c, the mass loss signal, which is centred at the Kangerdlugssuaq glacier, spreads over a relatively large distance along the coast. Then, the impact of the GOCE data can be interpreted as an attempt to increase the spatial resolution of the GRACE-only solution near the Kangerdlugssuaq glacier. This can also be observed in Fig. 6.12d, in which the GRACE-only and the combined estimations of mass variations are shown along a profile crossing the aforementioned glacier along the coast. Since the total signal observed at the considered location is about 30 – 40 cm/yr (Figs. 6.12c and 6.12d), the observed impact of the GOCE data does not exceed 2 %.

The peak impact of the GOCE SST data alone in the context of the linear trend is even less: only 0.16 cm/yr. Thus, I do not find it justified to discuss it in any further detail.

6.3.3 Attempt of an alternative definition of impact of GOCE data

It could be argued that the impact of the GOCE data quantified with the described methodology might be even somewhat overestimated. Currently, this quantification is made on the basis of the pairs of filtered solutions, the optimal filter applied to the GRACE-only and the one applied to the combined GRACE/GOCE solution in each pair being defined differently. That is, the filter is defined for each solution using the corresponding noise covariance

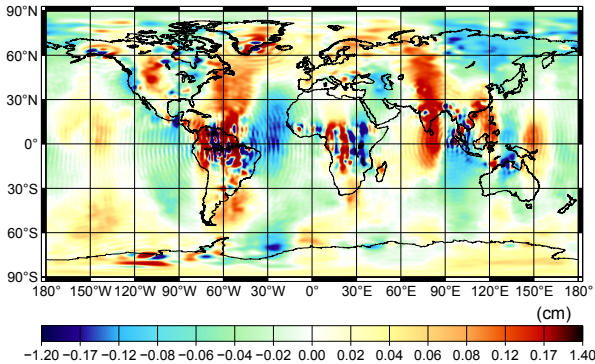


Figure 6.13: The same as Fig.6.9a, but the GRACE-only and the combined GRACE/GOCE unconstrained solutions are filtered consistently using the optimal filter built for the combined GRACE/GOCE solution. The RMS and peak values are 0.09 cm and 4.09 cm, respectively.

matrix, which is obviously unique for each solution. Therefore, the obtained impact can be interpreted as a combination of two effects: an effect onto unconstrained solutions and an effect onto the optimal filters. The latter effect, however, cannot be possibly related to the added value of GOCE data in the true sense of the word, because the construction of the optimal filter requires a stochastic model of data noise and not the data themselves at all. Such a stochastic model can be built by numerical simulations, without real GOCE data whatsoever. To eliminate the effect of GOCE data onto optimal filters, I make an attempt to re-estimate the impact of GOCE data, having applied the same filter to both the GRACE-only and GRACE/GOCE combined solutions in each pair. For that purpose, I utilize the optimal filter built for the combined GRACE/GOCE solution. Such a filter is less aggressive than that designed for the GRACE-only solutions. Therefore, additional signals that may potentially be present in GOCE data are not suppressed anymore. The impact obtained in this way for the differential solution “December 2009 minus November 2009” is shown in Fig. 6.13.

A comparison of this figure with Fig. 6.9a (i.e., its counterpart when different filters are applied to the GRACE-only and combined GRACE/GOCE solutions in the pair under consideration) allows me to conclude that the utilization of the same filters, in fact, does not reduce the difference between the GRACE-only and combined GRACE/GOCE solutions. On the contrary, it leads to a contamination of the obtained impact with additional high-frequency inaccuracies. Most probably, this is a consequence of the fact that the GRACE-only unconstrained solutions as compared to the combined GRACE/GOCE ones are characterized by a higher level of random noise. However, a suppression of this noise in the solutions of the later type should not be associated with an added value of GOCE data. As the experiments previously discussed have shown, this suppression can also be done with a better filter, namely, with the filter designed for the GRACE-only solutions deliberately. Thus, the application of the optimal filters built for the GRACE-only and combined

GRACE/GOCE solutions separately, as it is explained in section 6.3.2, leads to a fairer quantification of the added value of GOCE data than the application of same filters.

6.4 Summary, discussion, and conclusions

Temporal variations of the Earth's gravity field are nowadays primarily monitored with KBR data collected by the GRACE mission. With the study presented in this chapter, I made an attempt to quantify the potential added value of SST and SGG data from the GOCE mission to signals retrieved by KBR data. To that end, the time-varying gravity field variations were represented by a time series of monthly solutions in terms of spherical harmonic coefficients up to degree 120. In this way, a time series of KBR-only solutions and three time series of GRACE/GOCE combined solutions were produced. The latter ones were generated based on a combination of KBR data with (i) GOCE SST data alone; (ii) GOCE SGG data alone; and (iii) a combination of the latter two data types. The differences between the combined solutions and the KBR-only ones were analyzed. In doing so, both unconstrained and optimally filtered solutions were considered. It was found that the impact of GOCE data in these two cases is radically different.

In the case of unconstrained solutions, GOCE data compete only with KBR data. The accuracy of data of the latter type is, however, limited. Firstly, KBR data describe the gravity field variations to a lower spherical harmonic degree than GOCE gravity gradients. Secondly, KBR data suffer from an anisotropic sensitivity, so that the East-West variations of the gravity field are recovered poorly. As a result, the usage of GOCE data allows the noise level to be reduced substantially: by 1 – 2 orders of magnitude. This is consistent with earlier findings of Ditmar and Liu (2007), which were based on synthetic GRACE and GOCE data. I showed in my study, however, that such a notable impact is not more than a stabilization effect, which is similar to that achievable with, e.g., a regularization. Thus, this impact cannot be referred to as the added value of GOCE data in the true sense of the word, because the observed improvement does not benefit from the information content of GOCE data and does not require the presence of the real GOCE satellite in orbit.

In order to quantify an impact for GOCE data that can be linked with the information content of these data, I considered solutions subsequent to a statistically optimal anisotropic filtering (Klees et al., 2008b; Liu et al., 2010). The application of such a filter can be understood as a regularization of a solution. Therefore, GOCE data in this context compete both with KBR data and with a priori information exploited in the regularization concept. Con-

sequently, the quantified impact of GOCE data reduces dramatically in this setup. I found that the average impact of GOCE data in this context stays at sub-millimeter level in terms of equivalent water heights. Due to the fact that the typical accuracy of GRACE-based solutions is of the order of 1 cm, the impact quantified in the study presented can be considered as minor, if not negligible.

A further analysis demonstrated that this impact is not distributed homogeneously over the globe. In fact, it reveals a rather strong spatial correlation with the total mass transport signal. This triggered an idea to look into the geographical locations and time intervals where the impact of GOCE SST and SGG data both individually and jointly is maximum. I found that the peak values of the impact of GOCE data stay at the level of 0.7 – 1.3 cm of equivalent water heights in the case of the monthly and differential (i.e., month-to-month) solutions. As far as the linear trends are concerned, the peak impacts reach 0.5 – 0.6 cm/yr in the same representation. Thus, these values approach the level of noise in GRACE solutions or even narrowly exceed it. Furthermore, a more in-depth analysis of selected maps of impact allowed this impact to be likely interpreted as an attempt of GOCE data to mitigate the known limitations of GRACE data. However, the observed impact remains rather small in comparison with the total signal. It does not exceed 5 – 7 % in all considered cases. Nevertheless, I find it premature to conclude that the modelling of mass redistribution cannot benefit from GOCE data. This is in view of several reasons:

First, the impact of GOCE data can be particularly significant in the case of strong but localized signals such as those associated with major earthquakes. However, a special care should be taken in such a case to reduce the so-called “omission error”. A way to do that is to compute spherical harmonic coefficients up to a sufficiently high degree (definitely above degree 120). An alternative way is to use regional parameterizations of the gravity field similar to those studied by, e.g., Wittwer (2009). To increase the potential benefit of GOCE data in this context further, it is also advisable to apply more advanced filters, which could be based on a more accurate stochastic model of signal than that adopted in the study presented. For instance, the stochastic description of the expected signal could be tuned for the peak signal values rather than based on the RMS signal computed from a long time series of time-varying solutions, as it is done in (Klees et al., 2008b; Liu et al., 2010). This will make the behaviour of the filters to be applied to unconstrained solutions less aggressive and, therefore, will allow GOCE data to compete with a priori information more successfully.

Second, the impact of GOCE data may be increased if the accuracy of these data is further improved. In this context, it will be definitely beneficial to use data of the latest releases, which are produced with an improved gradiometer

calibration scheme (Siemes et al., 2012). It is important to keep in mind that the history of GOCE data processing is much shorter than that of GRACE data processing. Thus, it is not unlikely that there is still a potential for further improvements. Another way to reduce propagated noise in GOCE data is to consider time-varying gravity field solutions based on a sufficiently long time series of data (spanning several months or even years), so that noise is averaged out. It goes without saying that the stochastic model of noise in all those cases must be adjusted to the actual noise level, which will make the filters less aggressive and will allow the resulting solutions to fully benefit from a reduced data noise (Siemes et al., 2013).

Finally, it is worth noticing that a combination of various circumstances will have a cumulative effect in increasing added value of GOCE data. For instance, a reduction of noise in GOCE gravity gradients to the level of $2 \text{ mE}/\sqrt{\text{Hz}}$ in the measurement band, which is in line with early estimations (e.g., Sünkel, 2000), in combination with a sufficiently strong but localized signal, such as the one triggered by the Sumatra-Andaman earthquake, may increase the signal-to-noise ratio to such an extent that a mass redistribution model of a reasonable quality can even be built on the basis of GOCE gravity gradients alone (Han and Ditmar, 2008).

7 GRACE global temporal gravity field modelling: DMT-2

7.1 Introduction

The primary objective of this chapter is to produce and present a new global time-varying gravity field model entitled DMT-2: Delft Mass Transport model, release 2. Similar to its predecessor, i.e., DMT-1 (Liu et al., 2010), the new model is produced with a stand-alone processing of GRACE KBR data. These data are transformed into monthly sets of residual range combinations with respect to an a priori static gravity field model. These residuals are computed in the same manner as described in chapter 2 (section 2.3.1). The exception is the scheme used to calibrate the GRACE satellites' accelerometers, which is somewhat improved in the development of DMT-2 (see section 7.2.1.1). On the basis of the monthly sets of residual range combinations, a time series of unconstrained monthly gravity field solutions is produced, which are composed of spherical harmonic coefficients with respect to the a priori static gravity field model. The solutions are complete to degree 120. Following Liu et al. (2010), the production of these solutions involves two iterations, in both of which solutions are produced to degree 120. Those computed at the first iteration are truncated at degree 13. The truncated solutions are included in the force model to compute solutions at the second iteration. Adding the solutions computed at the second iteration to those computed and truncated at the first iteration yields the final unconstrained monthly gravity field solutions. These solutions are then optimally filtered with the procedure described in (Klees et al., 2008b; Liu et al., 2010) as well as in the previous chapter. As compared to its predecessor, the new model benefits from a number of improvements applied in its development. This includes, among others, the usage of a more advanced frequency-dependent data weighting (which is realized by an accurate estimation of data noise on a monthly basis and subsequently by a detailed parameterization of the estimated noise with an ARMA process) and the usage of the release 2 of GRACE level-1B data. These improvements are described in this chapter and their contribution is quantified. DMT-2 currently covers the time interval February 2003 till December 2010, excluding June 2003 due to the lacking of GRACE data. In order to analyse its quality, I compare the new model with its predecessor in the context of the optimally filtered solutions.

On the basis of the DMT-2 optimally filtered solutions and their counterparts

produced with the same procedure but up to a reduced degree, I additionally perform an investigation on the spatial resolution achievable from KBR data in the context of the monthly global gravity field modelling. This is primarily to inspect whether it is necessary to perform the GRACE monthly gravity field modelling up to degree 120 or choosing a lower maximum degree could lead to a similar spatial resolution in these models.

Here is how the chapter is structured. Section 7.2 describes the improvements applied in the development of DMT-2 as compared to its predecessor when the unconstrained solutions are computed. A comparison between the DMT-2 unconstrained solutions and their DMT-1 counterparts is made in section 7.2, too. An analysis of the quality of these two models subsequent to the optimal filtering is presented in section 7.3. In that section, I additionally obtain and present a quantification of the contribution of some of the improvements applied in the development of DMT-2. In section 7.4, I present the results of an investigation performed on the spatial resolution achievable from KBR data in the context of the monthly global gravity field modelling. Section 7.5 summaries the chapter and its findings.

7.2 Unconstrained gravity field solutions

In the first subsection, I illustrate the improvements incorporated in the production of DMT-2 as opposed to its predecessor. In the second subsection, I make a comparison between the unconstrained solutions associated with these two models.

7.2.1 Improvements

The improvements applied in the production of DMT-2 are related to either the data, or the force model or the data processing methodology. The improvements of the former two types are described in the first subsection, whereas those of the latter type are discussed in the second subsection.

7.2.1.1 Data- and force model-related improvements

The data and the force model exploited in the production of DMT-2 as compared to those used when DMT-1 was compiled are subject to the following improvements:

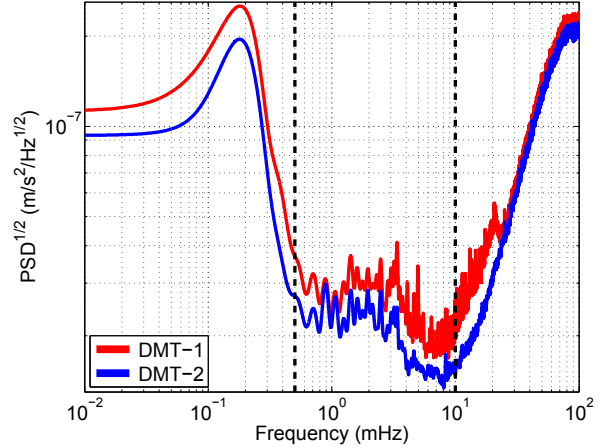
- (i) Usage of the latest release (i.e., release 2) of GRACE level-1B data. These data as compared to those from the previous releases are cleaned from, in particular, systematic inaccuracies in KBR data, which are identified and reported by Horwath et al. (2011).

- (ii) Usage of a latest a priori static gravity field model, i.e., DGM-1S (up to degree 250), instead of EIGEN-GL04C (up to degree 150).
- (iii) Usage of the latest release (i.e., release 5) of the AOD1B model (Dobslaw et al., 2013) instead of the previous release of this model.
- (iv) Usage of a state-of-the-art ocean tide model, i.e., EOT11a, instead of FES2004.
- (v) Usage of an improved scheme to calibrate the satellites' accelerometers. Similar to the scheme utilized in the production of the DMT-1 model, which is similar to that described in chapter 2, the improved scheme estimates one bias per axis per six-hour orbital arc. Unlike the old scheme, however, the improved one estimates only one scaling factor per component per month.

The force model exploited in the development of DMT-2 includes all the other ingredients listed in chapter 3 (section 3.2). The exceptions are the linear trends in the five low-degree spherical harmonic coefficients of the gravity field (i.e., \bar{c}_{20} , \bar{c}_{30} , \bar{c}_{40} , \bar{c}_{21} , and \bar{s}_{21}). It is obviously unjustified to include those linear trends in the force model in the production of a time-varying gravity field model. They represent a part of the temporal gravity field variations. Thus, their exclusion from the force model is to ensure that this part like the remaining part of the temporal gravity field signal is represented in the model to be produced. It is important to note that the incorporation of EOT11a into the force model and the implementation of the improved calibration scheme have been delivered by P. Inacio in the framework of his Ph.D. thesis currently being executed at the Delft University of Technology.

Figure 7.1 reflects the impact of the improvements in GRACE level-1B data and of those applied to the force model onto residual range combinations. This picture shows the $\text{PSD}^{\frac{1}{2}}$ of two sets of residuals of this type for July 2006 as an example. Those sets are computed in the production of DMT-1 and DMT-2, i.e., they are with respect to EIGEN-GL04C (up to degree 150) and DGM-1S (up to its maximum degree), respectively. The picture reveals a lower power for the residuals related to DMT-2. I interpret this as a reduction of noise in the residuals as a consequence of the aforementioned improvements. This noise reduction is observed in the entire spectrum. In the frequency range 0.5 – 10 mHz (which is marked in Fig. 7.1 with two vertical lines and comprises a significant part of the time-varying gravity field signal), it is mainly related to the usage of the latest release of GRACE level-1B data. Above the frequency 10 mHz, it is mainly associated with the usage of a better static gravity field model. Below the frequency 0.5 mHz, it is explained by a cumulative effect of the improvements incorporated into the force model.

Figure 7.1: The $\text{PSD}^{\frac{1}{2}}$ of the GRACE residual range combinations associated with DMT-1 and DMT-2 based on data of July 2006. The vertical lines mark the 0.5 mHz (3 cpr) and 10 mHz (54 cpr) frequencies. A Gaussian smoothing has been applied for a better visualization.



7.2.1.2 Methodology-related improvements

The data processing methodology used in the production of the DMT-2 unconstrained solutions as compared to that built by Liu (2008) for compiling the DMT-1 unconstrained solutions is subject to two adjustments: (i) improved elimination of the low-frequency noise and (ii) improved frequency-dependent data weighting.

Improved elimination of the low-frequency noise The first improvement concerns the seven-parameter high-pass filter, which is built and applied to monthly sets of residual range combinations to eliminate their low frequency noise, i.e., Eq. (3.1) in section 3.3.1. This filter in the production of DMT-1 is built based on a non-weighted least squares adjustment, whereas in the production of the new model it makes use of the new spatially-dependent data weighting, described in the previous chapter. As it was explained in that chapter, this improved estimation and elimination of the low-frequency noise minimizes the damping of the mass transport signals in areas where these signals are relatively strong. It is worth mentioning that the signal variances, which I used in the production of DMT-2 to form the spatially-dependent weight matrix, is based on signal variances derived from the DMT-1 optimally filtered monthly solutions in the time interval February 2003 – November 2010. The map of those standard deviations is almost similar to that shown in Fig. 6.1 in the previous chapter, and therefore, not shown here.

Improved frequency-dependent data weighting The second improvement lies within the realization of the frequency-dependent data weighting. The dependency of residual data noise on frequency in the production of DMT-1 was represented with a sketchy analytical function. Moreover, one

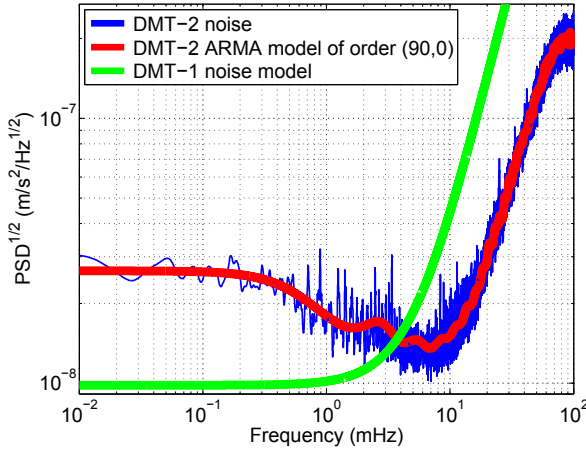


Figure 7.2: The $\text{PSD}^{\frac{1}{2}}$ of noise and of stochastic models of noise in GRACE residual range combinations: noise estimated in the production of DMT-2 for July 2006 (blue); its best-fitting ARMA model (red); and the analytical model of noise exploited when DMT-1 was produced (green).

single function was used to approximate noise in all months. In the production of the new model, however, I account for this dependency with detailed ARMA models of noise built iteratively as described in the previous chapter. Furthermore, I built these ARMA models on a monthly basis to account for a notable time-variability of noise, which was shown earlier in chapters 3 and 6. The DMT-2-type frequency-dependent data weighting approach allows statistically optimal solutions to be compiled even if noise gradually changes in time. Figure 7.2 shows the $\text{PSD}^{\frac{1}{2}}$ of noise in GRACE residual range combinations for July 2006 (as an example) and its best fitting ARMA model built in the development of DMT-2. For a comparison, the $\text{PSD}^{\frac{1}{2}}$ of the analytical function used to approximate noise in the production of DMT-1 is plotted in this picture, too. The picture indicates that the noise models built and used in the production of DMT-2 approximate the actual noise much better than in the case of DMT-1. The impact of the new frequency-dependent data weighting onto the solutions turns out to be substantial. I will prove (in section 7.3) that the improved frequency-dependent data weighting clearly outperforms all the other aforementioned improvements applied in the production of DMT-2 combined. The impact of this improvement in the context of the optimally filtered solutions is quantified in the next section.

7.2.2 DMT-2 versus DMT-1: unconstrained solutions

In order to make a comparison of DMT-2 with its predecessor, I derive the linear trend from the corresponding unconstrained monthly gravity field solutions. Since DMT-1 does not include the solution for December 2010, for the sake of consistency, I derive the linear trend for both models (in this section and in the next one) for the time interval February 2003 – November 2010. To compute the linear trend, I use the same procedure as the one described

Figure 7.3: The linear trend in terms of per degree geoid height derived from the DMT-1 and DMT-2 unconstrained monthly gravity field solutions in the time interval February 2003 till November 2010.

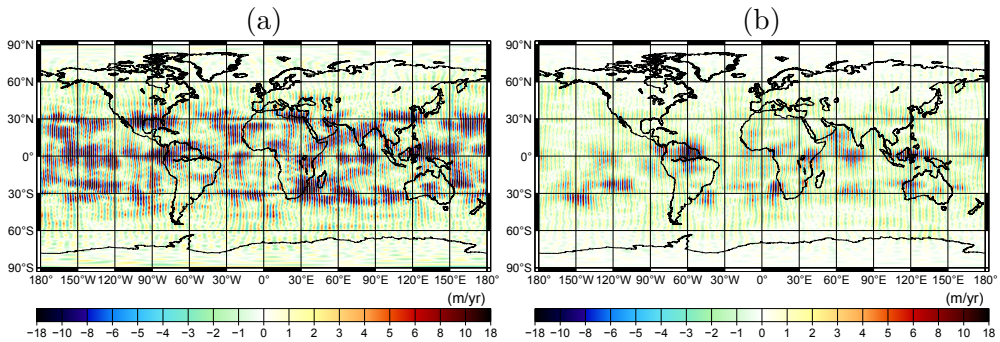
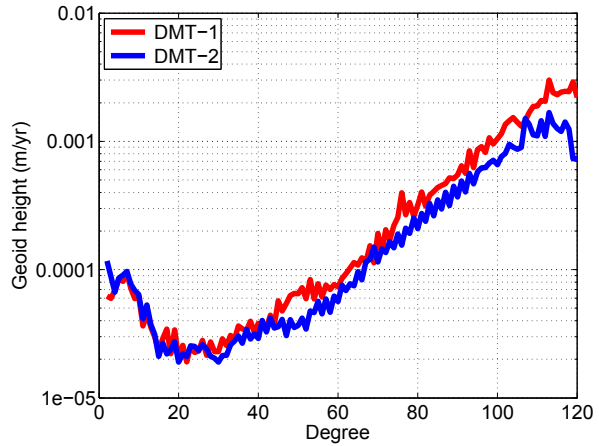


Figure 7.4: The linear trend in terms of equivalent water heights derived from the (a) DMT-1 and (b) DMT-2 unconstrained monthly gravity field solutions up to degree 120 in the time interval February 2003 till November 2010. The maps are generated on a $0.5^\circ \times 0.5^\circ$ grid. Their RMS values are (a) 2.9 m/yr and (b) 1.7 m/yr.

in the previous chapter (section 6.2.2). The computed linear trends are shown in Fig. 7.3 in the spectral domain in terms of per degree geoid height and in Fig. 7.4 in the spatial domain in terms of equivalent water heights up to degree 120. The latter picture indicates that the DMT-2 unconstrained solutions as compared to those from DMT-1 are less striped: by about 40 % in terms of RMS equivalent water heights. According to Fig. 7.3, this reduction of stripes is mainly associated with the coefficients above approximately degree 25. Nevertheless, given the outcome of the investigation presented in the previous chapter, I do not consider the presence of less stripes in an unconstrained gravity field model as a reliable indicator of a higher quality. Thus, in the next section, I compare the quality of DMT-1 and DMT-2 after the optimal filtering.

7.3 Optimally filtered gravity field solutions

As it was pointed out earlier, the optimal filtering of DMT-2 unconstrained solutions is performed with the same procedure as the one used in the production of DMT-1, i.e., in the same manner as described in (Klees et al., 2008b; Liu et al., 2010) as well as in the previous chapter. The difference between DMT-2 and its predecessor in this context is limited to the computation of the signal covariance matrix, i.e., \mathbf{D} . This matrix in the case of DMT-1 was estimated in the time interval February 2003 – December 2006, whereas it is now estimated in a longer time interval, namely, February 2003 – December 2010. This leads to a more representative estimation of the signal covariance matrix.

In the first subsection, I make a comparison between DMT-2 and its predecessor subsequent to the optimal filtering. I additionally discuss in that subsection the origin of the differences identified between these two models. In the second subsection, I obtain and present a quantification of the contribution of the new releases of GRACE level-1B data and the AOD1B model individually.

7.3.1 DMT-2 versus DMT-1: optimally filtered solutions

Figures 7.5a and 7.5b compares the DMT-1 and DMT-2 models in terms of the linear trend derived from the optimally filtered solutions in the time interval February 2003 – November 2010. The linear trend is computed with the same procedure as described in the previous chapter. In addition, the difference between these two variants of the linear trend is presented in Fig. 7.5d.

The picture reveals relatively large differences between the DMT-1 and DMT-2 models. These differences are observed in areas with relatively strong mass variations, such as Greenland, Antarctica, Himalayas, South Africa, and Patagonia in south Argentina. The map of the DMT-2 model as compared to that related to its predecessor reflects the mass variations in these areas with a much higher spatial resolution. For instance, the mass variations in Greenland are more concentrated along the coast and the retrieved signal amplitude is higher in the case of the DMT-2 model. This is consistently observed in all the aforementioned areas. According to the peak equivalent water heights provided in the caption of Fig. 7.5, the signal amplitude differences between these two models reach about 30 %.

I associate the higher spatial resolution of the DMT-2 model as compared to its processor almost entirely with the improved frequency-dependent data weighting exploited in the production of the new model. In order to prove this statement, I produce a preliminary variant of the DMT-2 model, hereafter referred to as DMT-2p, in the same time interval, with using the same force

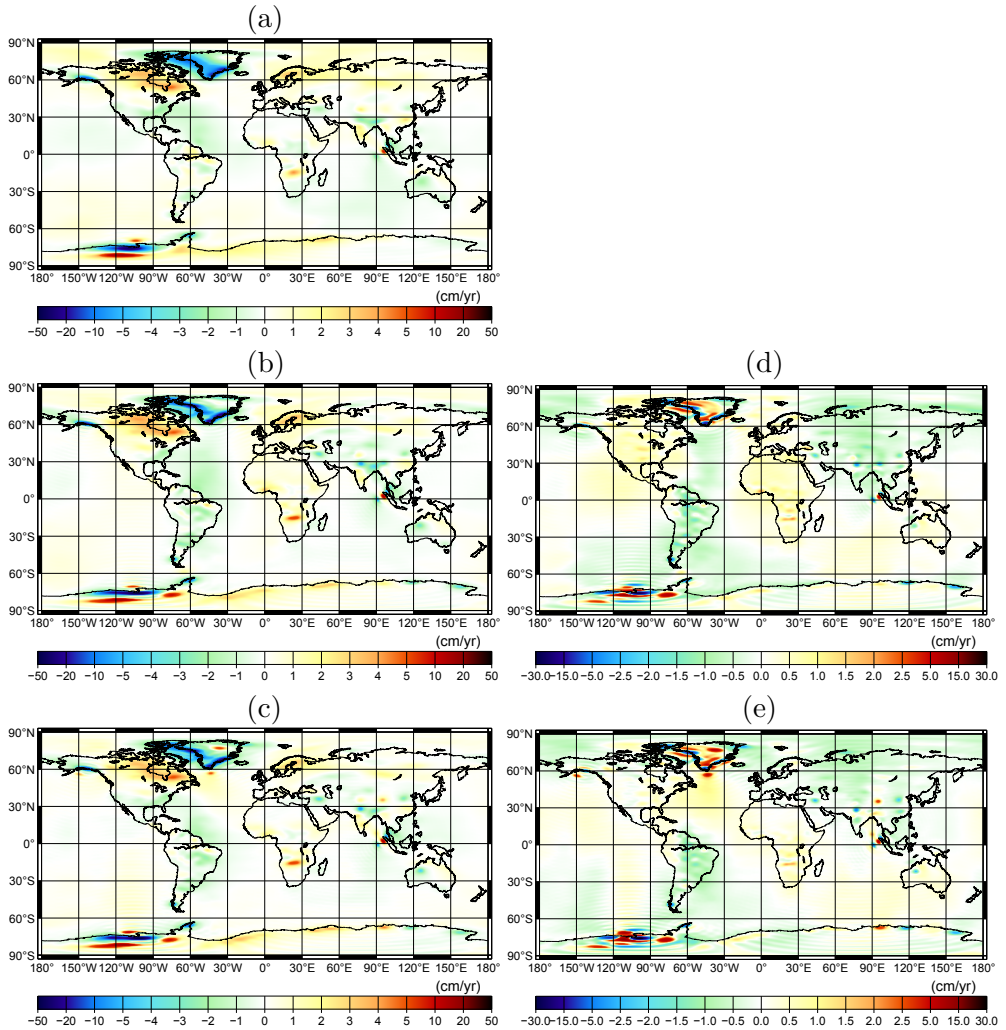


Figure 7.5: The linear trend estimated from the optimally filtered monthly mass transport solutions in the time interval February 2003 till November 2010: (a) DMT-1; (b) DMT-2; (c) DMT-2p; (d) the difference between DMT-1 and DMT-2; and (e) the difference between DMT-1 and DMT-2p. The maps are in terms of equivalent water heights up to degree 120. They are generated on a $0.5^\circ \times 0.5^\circ$ grid. Their RMS values are (a) 1.42 cm/yr, (b) 1.70 cm/yr, (c) 1.65 cm/yr, (d) 0.77 cm/yr, and (e) 0.82 cm/yr. Their peak values are (a) 39.7 cm/yr, (b) 51.0 cm/yr, (c) 55.0 cm/yr, (d) 29.3 cm/yr, and (e) 35.9 cm/yr.

model, with using the same release of GRACE level-1B data, and based on the same data processing methodology as in the case of DMT-1, but with the usage of the improved frequency-dependent data weighting methodology. The linear trend derived from the DMT-2p optimally filtered solutions in the

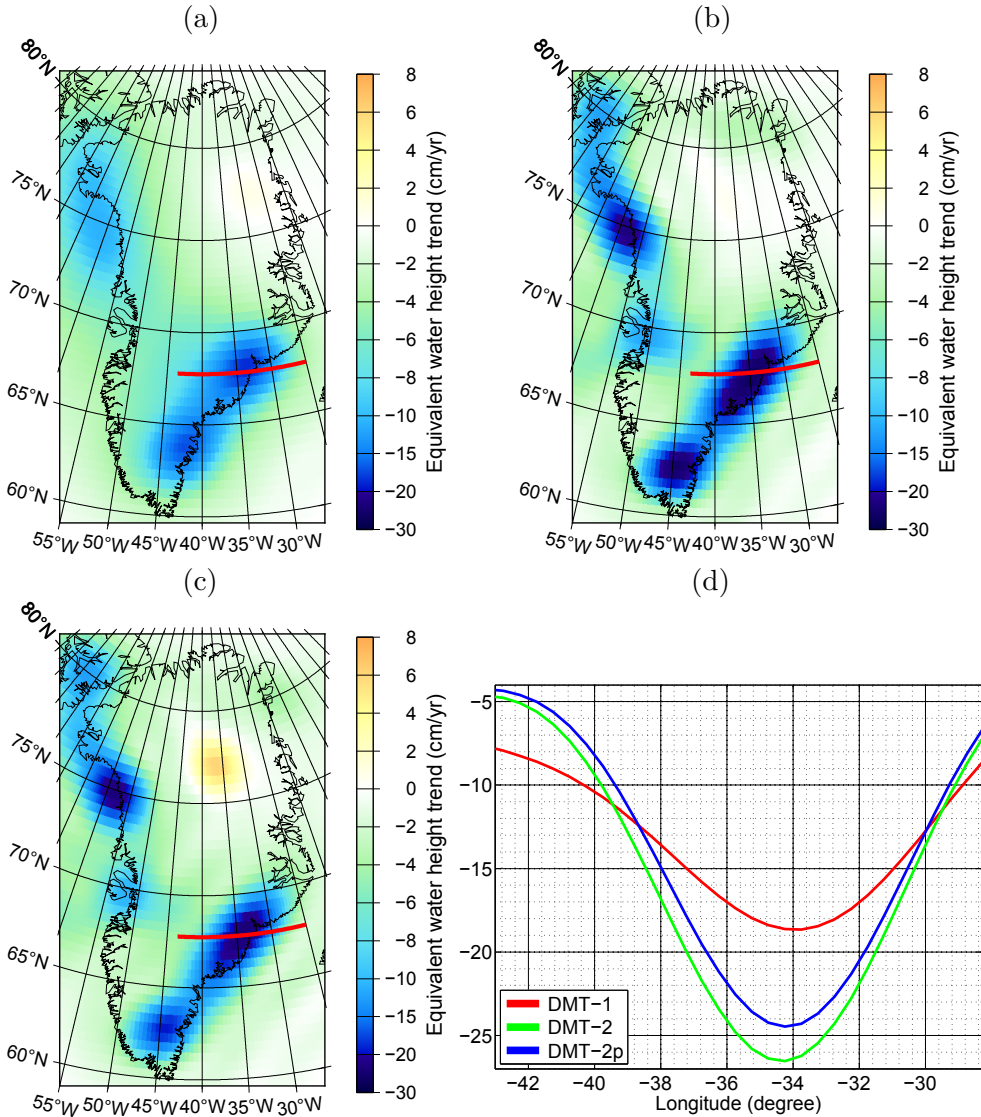


Figure 7.6: The linear trend estimated over the southeast Greenland from the filtered solutions (February 2003 – November 2010): (a) DMT-1; (b) DMT-2; (c) DMT-2p; and (d) the variations derived from these models along an East-West profile crossing the Kangerdlugssuaq glacier. The maps are in terms of equivalent water heights. Their RMS values are (a) 4.78 cm/yr, (b) 5.84 cm/yr, and (c) 5.35 cm/yr. Their peak values are (a) 18.7 cm/yr, (b) 26.5 cm/yr, and (c) 24.5 cm/yr.

time interval February 2003 – November 2010 is presented in Fig. 7.5c. Its difference from the linear trend derived from the DMT-1 model is exhibited in Fig. 7.5e. A quite good agreement is observed between the DMT-2 and DMT-

2p models as well as between the maps of differences of these two models from the DMT-1 model.

The crucial role of the improved frequency-dependent data weighting becomes even more convincing if I zoom into the aforementioned maps. Figure 7.6a – 7.6c shows the linear trend derived over the southeast Greenland from the DMT-1, and DMT-2, and DMT-2p optimally filtered solutions. In addition, Fig. 7.6d shows the linear trend retrieved from these models along a selected East-West profile crossing the Kangerdlugssuaq glacier. An inspection of the collection of the pictures presented in Fig. 7.6 confirms the statements above. The signals retrieved from DMT-2 or DMT2-p over the considered region are quite close to each other. They are both much higher than that observed in the case of DMT-1. This difference over, for instance, the Kangerdlugssuaq glacier, is 25 – 35 % of equivalent water heights. It is also worth noticing that the signal amplitude retrieved from DMT-2 is slightly larger than that from DMT-2p (by about 5 % over the Kangerdlugssuaq glacier). This can be explained by a cumulative contribution of the other improvements applied in the production of DMT-2 in addition to the improved frequency-dependent data weighting.

Finally, I find it worth noticing in Figs. 7.5c and 7.6c positive features in DMT-2p in sea areas close to the south Greenland and south Alaska. These features are most likely artifacts. They are not present in DMT-2. I explain this by the contribution of the other improvements applied in the production of DMT-2 in addition to the improved frequency-dependent data weighting. The absence of these artifact in DMT-2 is most probably due to the usage of the new release of GRACE level-1B data in the production of this model. However, this is my personal belief and it is yet to be verified.

7.3.2 Contribution of the latest releases of GRACE level-1B data and AOD1B model

A recent development in the area of the time-varying gravity field modelling is the distribution of the release 2 of GRACE level-1B data and release 5 of the AOD1B model. Therefore, I find it relevant to obtain and present a quantification of the contribution of the usage of these products in the context of the GRACE time-varying gravity field modelling. To that end, I produce two DMT-1-type preliminary models. In the production of each of these preliminary models, I consider all the improvements mentioned earlier used in the production of DMT-2 with the exception of the one whose contribution is to be quantified. Then, I compare the DMT-1-type preliminary models with DMT-2 and then analyse their differences. The produced preliminary models cover only a one-year time interval in January 2006 – December 2006. Thus, I make the comparison between all the three involved models for the

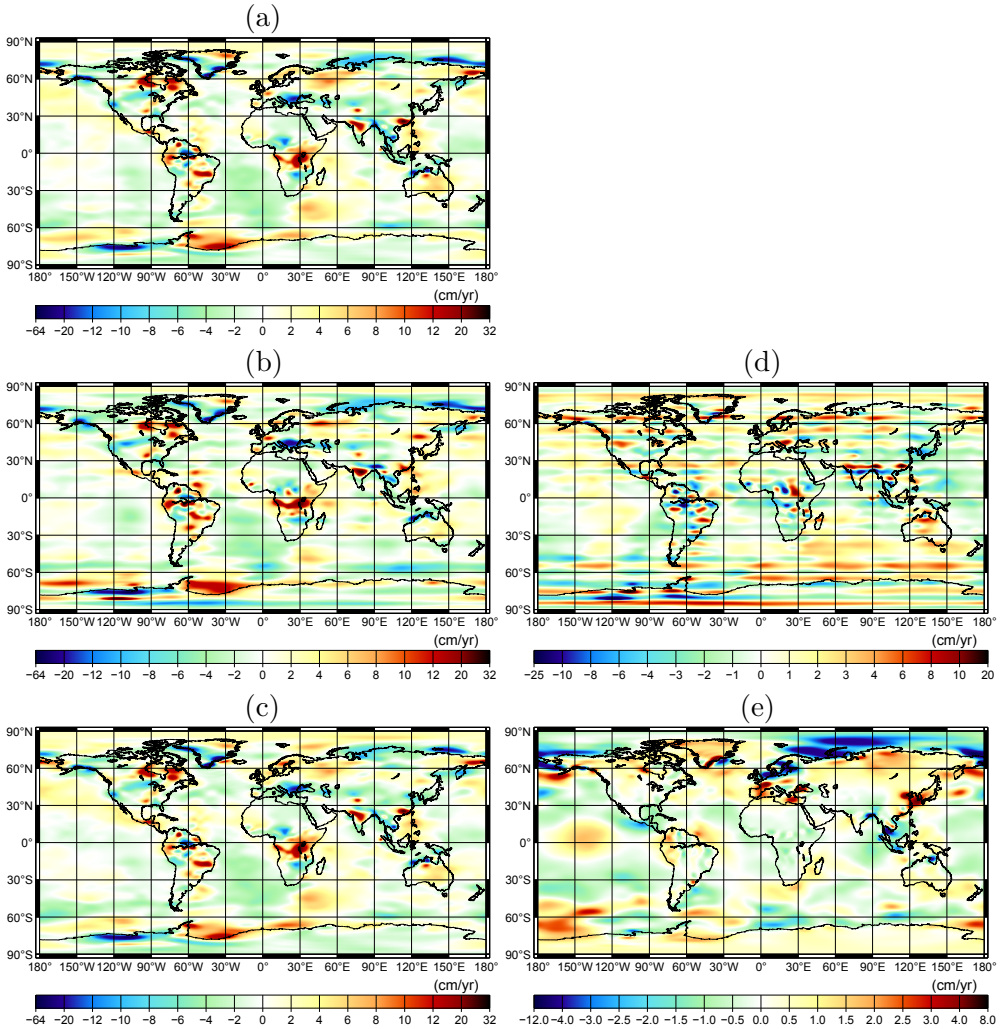


Figure 7.7: The linear trend estimated from the optimally filtered monthly mass transport solutions in the time interval January 2006 till December 2006: (a) DMT-2; (b) the DMT-1-type preliminary model produced with the previous releases of GRACE level-1B data (i.e., DMT-2 but based on the releases 0 and 1 of GRACE level-1B data); (c) the DMT-1-type preliminary model produced with the previous release of the AOD1B model (i.e., DMT-2 but based on the release 4 of the AOD1B model); (d) the difference between DMT-2 and the DMT-1-type preliminary model produced with the previous releases of GRACE level-1B data (i.e., the contribution of the release 2 of GRACE level-1B data); (e) the difference between DMT-2 and the DMT-1-type preliminary model produced with the previous release of the AOD1B model (i.e., the contribution of the release 5 of the AOD1B model). The maps are in terms of equivalent water heights up to degree 120. They are generated on a $0.5^\circ \times 0.5^\circ$ grid. Their RMS values are (a) 3.76 cm/yr, (b) 4.24 cm/yr, (c) 3.80 cm/yr, (d) 2.42 cm/yr, and (e) 1.13 cm/yr. Their peak values are (a) 46.27 cm/yr, (b) 63.74 cm/yr, (c) 48.20 cm/yr, (d) 24.84 cm/yr, and (e) 11.28 cm/yr.

linear trend derived from the corresponding optimally filtered solutions in this one-year time interval. It is worth mentioning that for the optimal filtering of the DMT-1-type preliminary unconstrained solutions, I utilize the signal covariance matrix estimated in the production of DMT-2. Furthermore, each DMT-1-type preliminary unconstrained solution is filtered on the basis of its own noise covariance matrix. Figure 7.7 presents DMT-2 and the two DMT-1-type preliminary models as well as the difference between the latter two models and the former one. The results reflect pronounced East-West artifacts in the DMT-1-type preliminary model produced with the previous releases of GRACE level-1B data. This is consistent with the findings of Horwath et al. (2011), who have identified and reported inaccuracies of this type in the polar areas. I, however, identify them all over the globe. These inaccuracies manifest themselves not only in the map of differences, but also in the map related to the DMT-1-type preliminary model itself. Furthermore, the results show relatively large differences in the arctic oceans between DMT-2 and the DMT-1-type preliminary model produced with the previous release of the AOD1B model. I associate these differences with improved oceanic models incorporated when the new release of the AOD1B model was produced (Dobslaw et al., 2013). Finally, it is worth noting that given the RMS and peak values provided in the caption of Fig. 7.7, the contribution of the new release of GRACE level-1B data outperforms that of the new release of the AOD1B model in the conducted experiment.

7.4 Maximum degree recoverable from KBR data in monthly gravity field modelling

With the usage of the latest release of GRACE level-1B data three monthly gravity field models have been released so far. They are produced by the Center for Space Research (CSR), GeoForschungsZentrum (GFZ), and Jet Propulsion Laboratories (JPL) (Bettadpur, 2012; Dahle et al., 2012; Watkin and Ning, 2012). Unlike DMT-2, these models are complete only to degree 60 (in the case of CSR) or 90 (in the case of GFZ and JPL). In principle, reduction of the maximal spherical harmonic degree may lead to a loss of some high-frequency information available in GRACE KBR data. Therefore, I find it important to perform an investigation on the spatial resolution achievable from these data in the context of the monthly gravity field modelling. To that end, I utilize DMT-2 and its clones computed up to degree 60 and 90. I compare the difference between these three models in terms of the linear trend derived from the optimally filtered solutions in the time interval February 2003 till December 2010. Figure 7.8 presents DMT-2 and its clones as well as the difference of the latter two models from the former one. Figure 7.8 re-

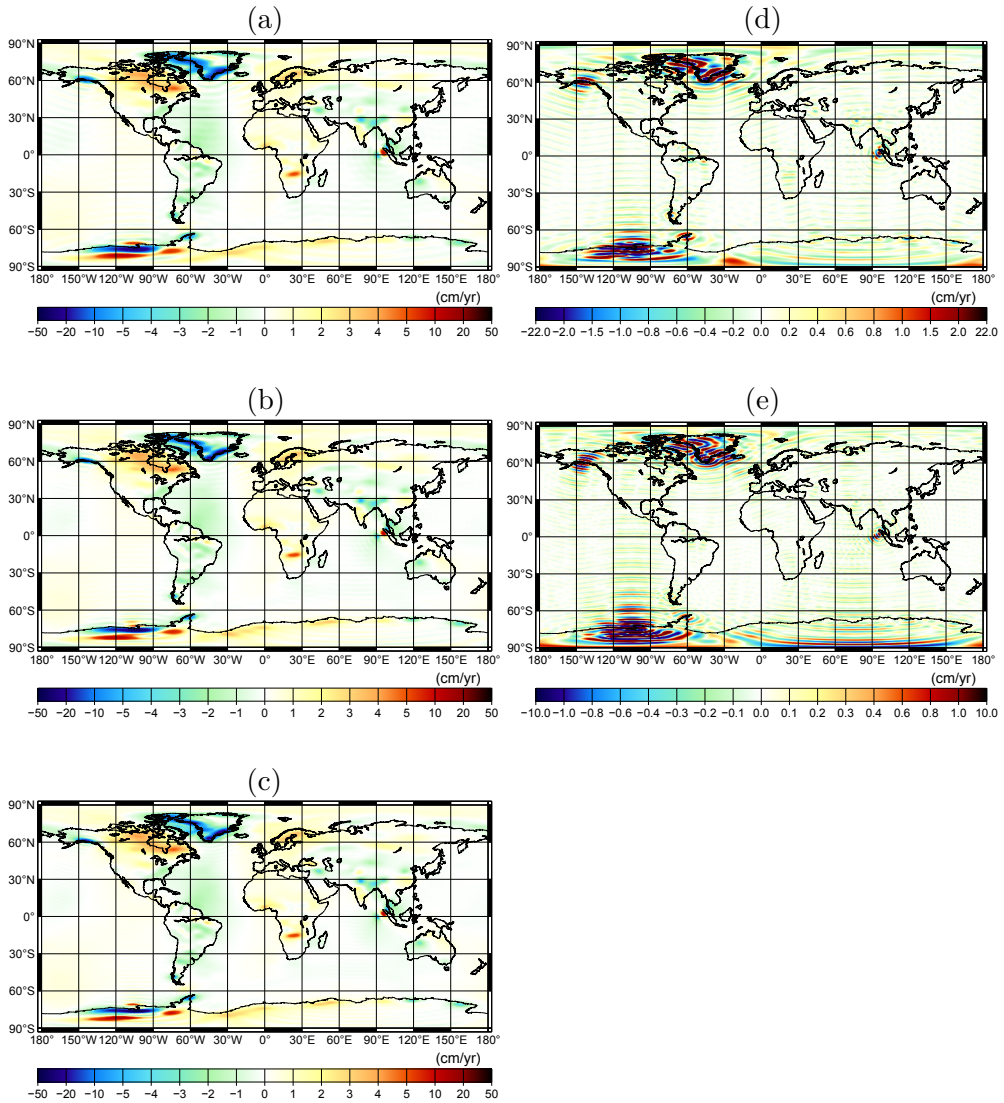


Figure 7.8: The linear trend estimated from the optimally filtered monthly mass transport solutions in the time interval February 2003 till December 2010: (a) a DMT-2 clone computed up to spherical harmonic degree 60; (b) a DMT-2 clone computed up to spherical harmonic degree 90; (c) DMT-2 (which is complete up to spherical harmonic degree 120); (d) the difference between DMT-2 and its clone computed up to spherical harmonic degree 60; and (e) the difference between DMT-2 and its clone computed up to spherical harmonic degree 90. The maps have been presented in terms of equivalent water heights. They have been generated on a $0.5^\circ \times 0.5^\circ$ grid. Their RMS values are (a) 1.60 cm/yr, (b) 1.67 cm/yr, (c) 1.71 cm/yr, (d) 0.62 cm/yr, and (e) 0.38 cm/yr. Their peak values are (a) 29.9 cm/yr, (b) 41.5 cm/yr, (c) 51.4 cm/yr, (d) 21.8 cm/yr, and (e) 10.1 cm/yr.

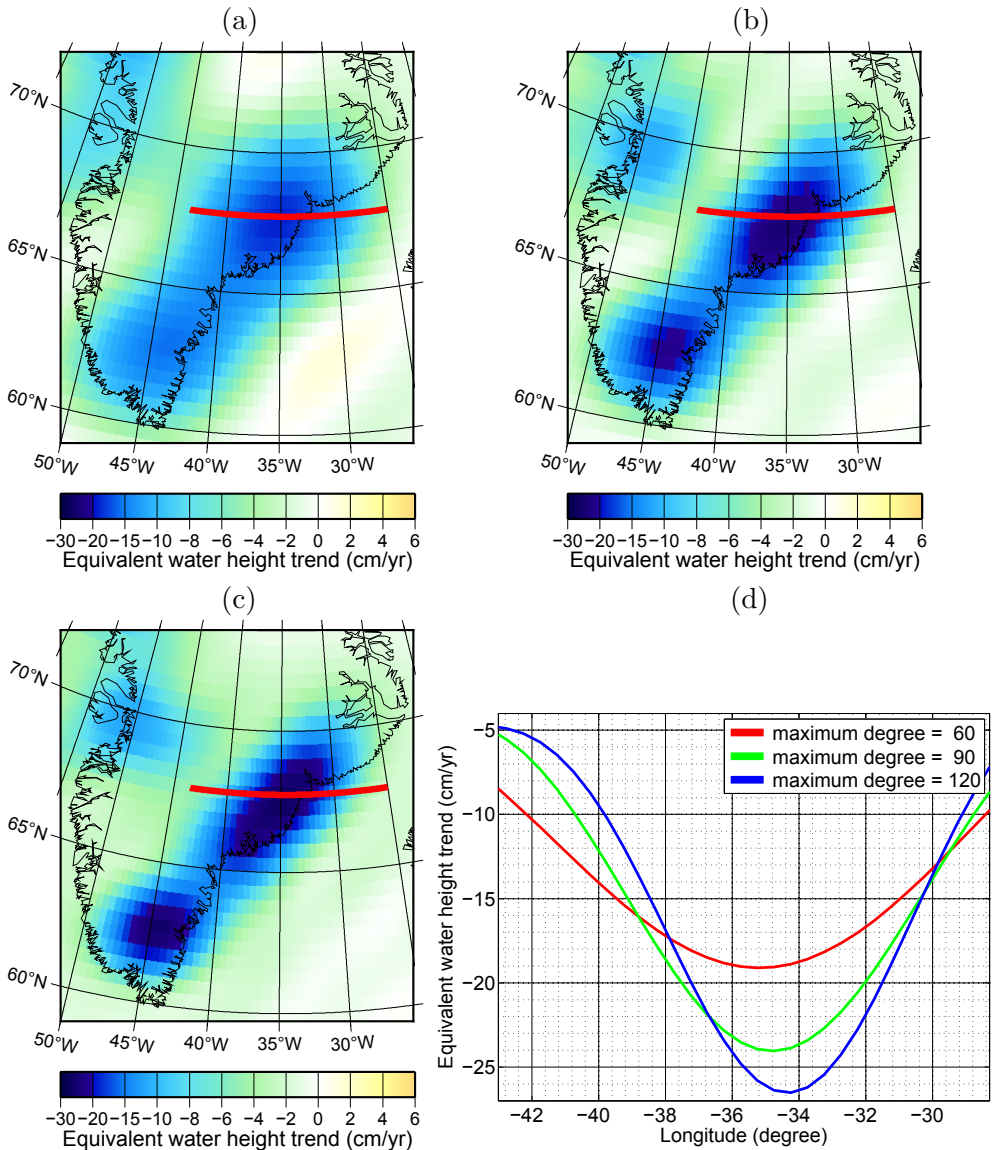


Figure 7.9: The linear trend estimated over the southeast Greenland from the optimally filtered monthly mass transport solutions in the time interval February 2003 till December 2010: (a) a DMT-2 clone computed up to spherical harmonic degree 60; (b) a DMT-2 clone computed up to spherical harmonic degree 90; (c) DMT-2; and (d) the mass variations along a selected East-West profile crossing the Kangerdlugssuaq glacier. The maps are presented in terms of equivalent water heights. They are generated on a $0.5^\circ \times 0.5^\circ$ grid. Their RMS values are (a) 5.55 cm/yr, (b) 5.81 cm/yr, and (c) 5.87 cm/yr. Their peak values are (a) 18.7 cm/yr, (b) 24.3 cm/yr, and (c) 26.53 cm/yr.

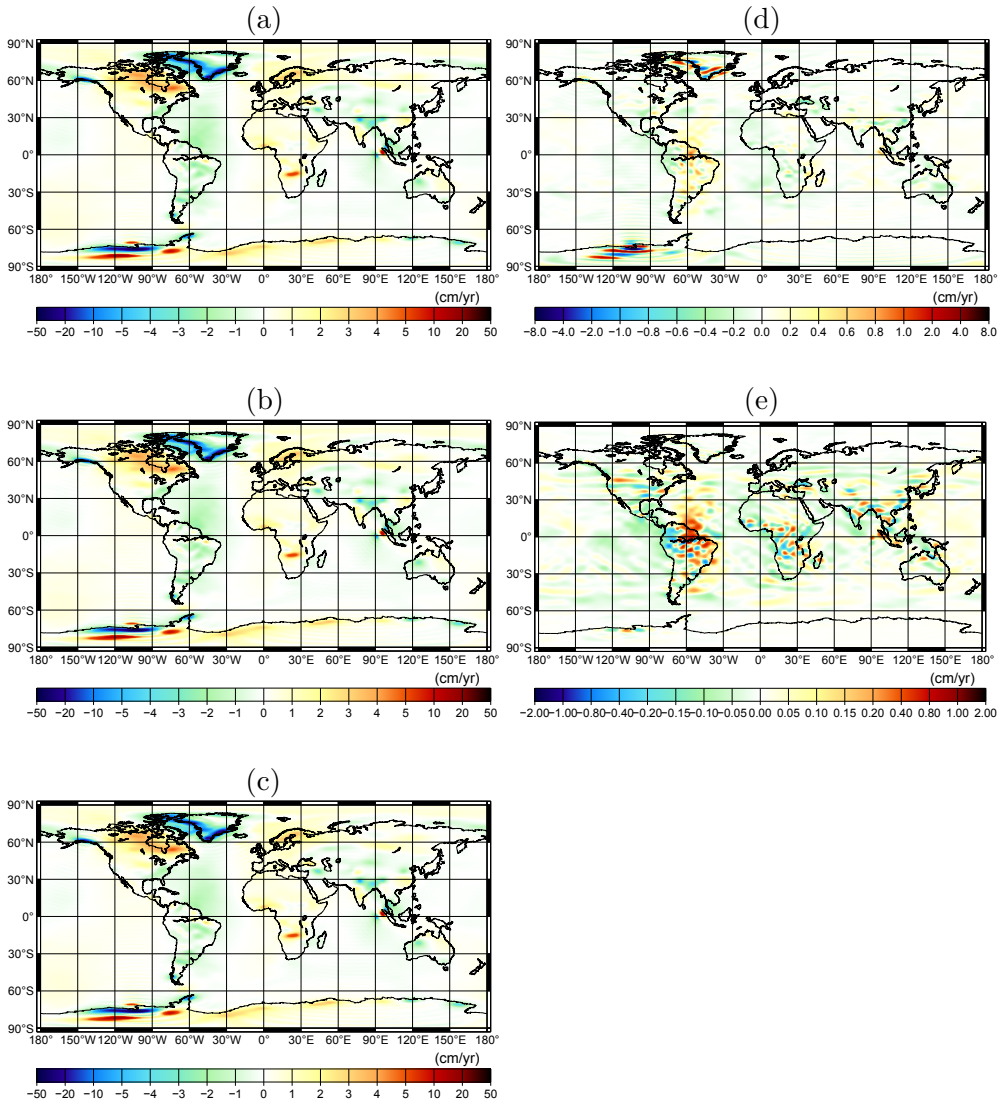


Figure 7.10: The linear trend estimated from the optimally filtered monthly mass transport solutions in the time interval February 2003 till December 2010: (a) a DMT-2 clone computed up to degree 60; (b) a DMT-2 clone computed up to degree 90; (c) DMT-2; (d) the difference between DMT-2 and its clone computed up to degree 60; and (e) the difference between DMT-2 and its clone computed up to degree 90. These pictures are the same as those shown in Fig. 7.8, but the unconstrained solutions of the DMT-2 clones are augmented above their maximum degrees up to degree 120 with zeros. The maps are in terms of equivalent water heights. They are generated on a $0.5^\circ \times 0.5^\circ$ grid. The RMS values are (a) 1.67 cm/yr, (b) 1.71 cm/yr, (c) 1.71 cm/yr, (d) 0.20 cm/yr, and (e) 0.07 cm/yr. Their peak values are (a) 43.99 cm/yr, (b) 51.36 cm/yr, (c) 51.39 cm/yr, (d) 7.52 cm/yr, and (e) 2.11 cm/yr.

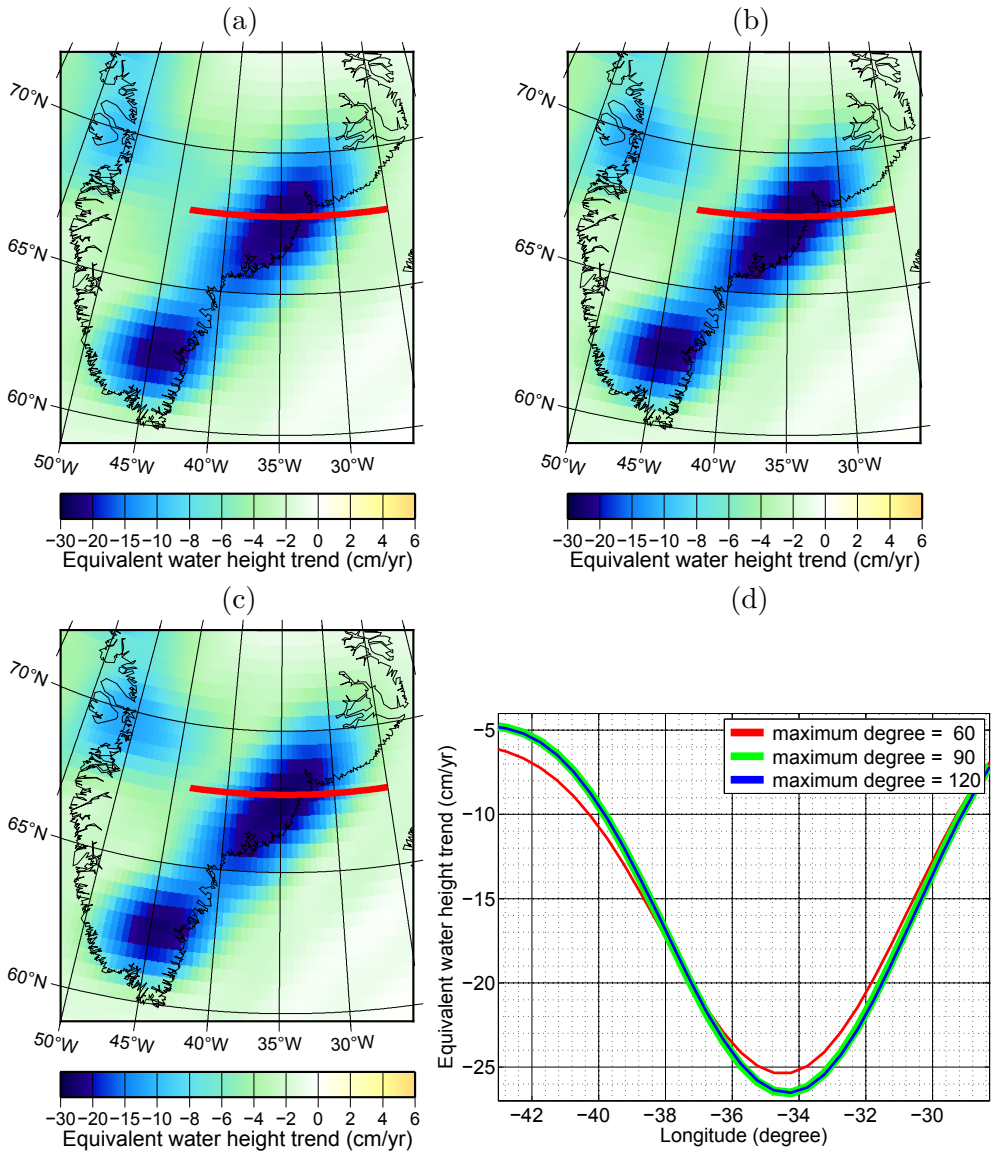


Figure 7.11: The linear trend estimated over the southeast Greenland from the optimally filtered monthly mass transport solutions in the time interval February 2003 till December 2010: (a) a DMT-2 clone complete up to degree 60; (b) a DMT-2 clone up to degree 90; (c) DMT-2; and (d) the mass variations along a selected East-West profile crossing the Kangerdlugssuaq glacier. These pictures are the same as those shown in Fig. 7.9, but the unconstrained solutions of the DMT-2 clones are augmented above their maximum degrees up to degree 120 with zeros. The maps are in terms of equivalent water heights. They are generated on a $0.5^\circ \times 0.5^\circ$ grid. The RMS values are (a) 5.73 cm/yr, (b) 5.87 cm/yr, and (c) 5.87 cm/yr. Their peak values are (a) 25.35 cm/yr, (b) 26.53 cm/yr, and (c) 26.53 cm/yr.

veals non-negligible differences between DMT-2 and its two considered clones. These differences are expectedly larger for the DMT-2 clone computed up to degree 60 as compared to that computed up to degree 90. The peak values of these differences, which are provided in the caption of Fig. 7.8, are well above the GRACE noise level. Importantly, these differences are observed in areas with relatively strong temporal gravity field variations. Furthermore, they are characterized by ring patterns due to the well known “Gibbs” phenomenon, which typically occurs when a spectral representation of a physical phenomenon is truncated at a too low frequency. I associate these differences with a higher spatial resolution of DMT-2 as compared to its considered clones. This can be clearly observed, e.g., in Greenland, where signal recovered from DMT-2 as compared to its clones is more concentrated along the coast, as one can expect.

To inspect the identified differences further, I zoom over the southeast Greenland in Fig. 7.9. This picture shows DMT-2 and its two considered clones. Additionally, I present in this figure the linear trend derived from these three models along a selected East-West profile crossing the Kangerdlugssuaq glacier. The picture demonstrates that the usage of the DTM-2 clones computed up to degree 60 and 90 instead of DMT-2 leads to an underestimation of the signal amplitude by about 30 % and 8 % in the case of the maximum degree 60 and 90, respectively.

Nevertheless, I find it essential to demonstrate that the higher spatial resolution of DMT-2 as compared to its clones must be almost entirely attributed to the filter applied at the post-processing stage and not to KBR data themselves. To that end, I conduct a new experiment in which the unconstrained solutions of the DMT-2 clones computed up to degree 60 and 90 are augmented above their maximum degree up to degree 120 with zeros. They are then subject to the optimal filtering in the same manner as applied to the solutions complete to degree 120. The results are presented in Figs 7.10 and 7.11. These two figures present the same materials as those respectively shown in Figs. 7.8 and 7.9, but for the new experiment. One can see in the new pictures that the DMT-2 clones computed up to a reduced maximum degree in the new experiment show much lower differences from DMT-2 as compared to those computed in the previous experiment. Given the GRACE noise level being 1 – 2 cm/yr of equivalent water heights in the monthly gravity field modelling, the differences in the case of the maximum degree 90 are now even below the GRACE noise level. This implies that the JPL and GFZ monthly gravity field models, which are complete to degree 90, probably do not suffer from a loss of information content of KBR data. As far as the CSR model is concerned, its re-computation to a higher degree is advised.

7.5 Summary and conclusions

A new global time varying gravity field model, entitled DMT-2, was produced on the basis of GRACE KBR data in the form of range combinations. The new model represents the gravity field variations with respect to DGM-1S on a monthly basis in terms of spherical harmonic coefficients up to degree 120. It is currently comprised of 94 monthly solutions covering the time interval February 2003 till December 2010, excluding June 2003 due to the absence of GRACE data. Both unconstrained and optimally filtered solutions are produced. As compared to its predecessor, namely, DMT-1, the new model benefits from a number of improvements applied in the course of its development: (i) the usage of the release 2 of GRACE level-1B data; (ii) the usage of the release 5 of the AOD1B model; (iii) the usage of a GRACE/GOCE static gravity field model, namely, DGM-1S, as the a priori one; (iv) the usage of a latest global ocean tide model, namely, EOT11a; (v) the usage of an improved calibration of GRACE satellites' accelerometers; (vi) the usage of an improved frequency-dependent data weighting methodology; and (vii) the usage of an improved estimation and elimination of the low-frequency noise in monthly sets of GRACE residual range combinations.

It was shown that DMT-2 substantially outperforms its predecessor in terms of spatial resolution. This improvement was proven to be almost entirely associated with the usage of a more advanced frequency-dependent data weighting, which is realized with an accurate estimation of data noise and subsequently a computation and incorporation of highly-detailed ARMA models of noise in monthly sets of residual range combinations. Furthermore, it was confirmed that the usage of the release 2 of GRACE level-1B data instead of the previous releases of these data leads to the elimination of East-West artifacts from the GRACE mass transport models all over the globe.

In addition, I showed that DMT-2 contains relatively strong signals above spherical harmonic degree 60 and 90, which are lost if an attempt is made to truncate this model. On the other hand, I demonstrated that the presence of these high-frequency signals must be almost entirely attributed to the filters applied and not to information content in GRACE KBR data.

Finally, it was found that the maximum spherical harmonic degree in the context of the GRACE monthly gravity field modelling should not be chosen lower than 90. It was shown that choosing a lower maximum degree may lead in the spatial domain to a non-negligible underestimation of the signal amplitude in areas with strong temporal gravity field variations.

8 GRACE-only global static gravity field modelling with EGM96 as a priori model

8.1 Introduction

The methodology adopted in chapter 3 in the production of DGM-1S cannot be applied to produce a static gravity field model of an acceptable quality if an inaccurate model is used as the a priori one. This is due to the fact that a priori orbits produced in that case would be too inaccurate. This means that GRACE satellites' line-of-sight unit vectors, i.e., $\mathbf{e}(t)$ in Eq. (2.4), which are computed from a priori orbits, would also be inaccurate. This would make the functional model, established by Eq. (2.4), inadequate. In this chapter, I investigate whether the methodology followed in the production of DGM-1S could be improved so that it could also lead to an accurate static gravity field model when a relatively old model such as EGM96 is exploited as the a priori one. When producing DEOS_CHAMP-01C from CHAMP kinematic orbit data, Ditmar et al. (2006) demonstrated that the average acceleration approach in the context of kinematic orbit data could yield a static gravity field model of a good quality even if EGM96 is used as the a priori model. Furthermore, Reubelt et al. (2012) have recently demonstrated a successful static gravity field modelling from GOCE kinematic orbit data with the point-wise acceleration approach even without using any a priori model for the static part of the gravity field. Apparently, this is possible due to the fact that satellite accelerations are related to spherical harmonic coefficients linearly. As far as GOCE gravity gradients are concerned, their links to spherical harmonic coefficients are linear as well (see Appendix B). Thus, the outcome of the gravity field retrieval on the basis of GOCE gravity gradients is independent from the quality of the a priori gravity field model, provided that no regularisation is applied. An attempt of the gravity field modelling based on GRACE KBR measurements, on the other hand, in one way or another heavily relies on the concept of the dynamic orbit integration, which depends on the a priori gravity field model. Therefore, I perform the investigation designated for this chapter only in the context of the GRACE mission.

To perform this investigation, I produce a GRACE-only static gravity field model using EGM96 as the a priori model. To that end, I consider both

data types of the GRACE mission, i.e., its KBR and kinematic orbit data. This is to ensure a fair comparison that is to be eventually made between the model produced in this research and alternative models produced and released by other research centres, which all use both data types. I produce GRACE-based residual data sets (residual range combinations and residual 3-D average acceleration vectors) in the same manner as described in chapter 2 (in sections 2.3.1 and 2.3.2, respectively). The force model exploited for this purpose accounts, in addition to EGM96, for all the other contributors listed in section 3.2. A number of modifications are to be applied to the GRACE data processing methodology to enable it to deal with relatively large inaccuracies in the a priori (dynamic) orbits caused by a relatively low quality of EGM96. Due to a practical limitation, which I explain in section 8.2.1, I apply the adjusted methodology to only GRACE data in 2006. The produced GRACE-only model is compared with AIUB-GRACE01S (Jäggi et al., 2008), i.e., another one-year GRACE-only static gravity field model produced by using EGM96 as the a priori one. AIUB-GRACE01S has been produced up to spherical harmonic degree 120. Thus, to ensure a fair comparison, I set the maximum degree in the model production as 120, too. Importantly, I impose no regularization to be consistent with AIUB-GRACE01S in this aspect as well.

Here is the outline of the chapter. In section 8.2, I describe modifications applied to the GRACE data processing methodology and quantify their effects, individually. The produced GRACE-only model is presented in section 8.3, where a preliminary analysis of its quality is made by comparing it and AIUB-GRACE01S with EGM2008. Furthermore, an independent validation of these two GRACE-only models is performed in section 8.3 by confronting them with GRACE KBR and GOCE SGG control data as described in chapter 4. Section 8.4 concludes and summarises the chapter.

8.2 Data processing modifications and their effects

Three modifications are applied to the methodology that was used to produce DGM-1S from GRACE data:

- (i) The GRACE residual range combinations are no longer subject to the empirical high pass filter of Eq. (3.1). When using a relatively poor a priori static gravity field model such as EGM96, the low frequency part of the spectrum of these residuals is overwhelmed by gravity signals, which are to be retrieved. Thus, the low-frequency noise is treated by defining and applying a so-called “geometrical correction”. Given relatively large inaccuracies in the a priori orbits based on EGM96, I find it essential to define and apply a similar correction in the context of GRACE satellites’

residual 3-D average acceleration vectors, too. All these corrections are defined in the first subsection.

- (ii) The ARMA models of noise in sets of residual data of both types are improved iteratively. This iterative scheme has already been described in chapter 6 (section 6.2.1.2).
- (iii) The a priori static gravity field model is also improved in an iterative manner. That is, the gravity field model produced at the first iteration, for instance, is exploited in the force model as the new a priori static gravity field model in order to retrieve the gravity field at the second iteration. A few iterations of this type are performed until a convergence is achieved.

Thus, the improved data processing methodology consists of two iterative schemes. To facilitate a distinction between them, they are hereafter referred to as the “noise model-related” and “a priori model-related” iterative schemes by which the ARMA models of noise in residual data sets and the a priori model of the gravity signal are to be improved, respectively. The former scheme occurs within the latter one.

A quantification of the effect of these three modifications is individually presented in the following three subsections, respectively. In doing so, a number of preliminary GRACE-only models are produced. These preliminary models are analysed in terms of per-degree geoid height differences with respect to EGM2008. As the reference, I include EGM96 and DGM-1S in the analysis, too.

8.2.1 Geometrical corrections and their effect

8.2.1.1 Geometrical correction of residual range combinations

Conceptually, GRACE residual range combinations reflect the discrepancy between the true (observed) and the a priori (computed) range combinations, provided that the latter ones are computed at the true GRACE satellites’ locations:

$$\delta\bar{g}_i = \frac{\mathbf{e}_{i-1} \cdot \mathbf{e}_i \rho_{i-1} - 2\rho_i + \mathbf{e}_i \cdot \mathbf{e}_{i+1} \rho_{i+1}}{(\Delta t)^2} - \left\{ \bar{\mathbf{a}}^{(0)}(\mathbf{r}_{2,i}) - \bar{\mathbf{a}}^{(0)}(\mathbf{r}_{1,i}) \right\} \cdot \mathbf{e}_i, \quad (8.1)$$

where the lower index $i = 1, 2, \dots$ corresponds to the measurement time $t_i = t_0 + i\Delta t$ with t_0 being an initial epoch, $\bar{\mathbf{a}}^{(0)}(\mathbf{r}_{j,i})$ is the a priori 3-D average acceleration vectors with $j = 1$ for GRACE-1 and $j = 2$ for GRACE-2. The computation of the right-hand side of Eq. (8.1) requires knowledge of the true GRACE satellites’ positions $\mathbf{r}_{j,i}$ and of the true line-of-sight unit vectors \mathbf{e}_i . Since both of these are unavailable, the a priori counterparts of these

quantities, i.e., $\mathbf{r}_{j,i}^{(0)}$ and $\mathbf{e}_i^{(0)}$, derived from the GRACE satellites' dynamic orbits, are utilized. In order to account for inaccuracies of these a priori counterparts, I introduce a geometrical correction that consists of a position-related correction, i.e.,

$$\delta_{\bar{g}_i}^{(p)} = \left\{ \bar{\mathbf{g}}^{(0)}(\mathbf{r}_{2,i}) - \bar{\mathbf{g}}^{(0)}(\mathbf{r}_{1,i}) \right\} \cdot \mathbf{e}_i^{(0)} - \left\{ \bar{\mathbf{g}}^{(0)}(\mathbf{r}_{2,i}^{(0)}) - \bar{\mathbf{g}}^{(0)}(\mathbf{r}_{1,i}^{(0)}) \right\} \cdot \mathbf{e}_i^{(0)}, \quad (8.2)$$

and two direction-related ones, i.e.,

$$\delta_{\bar{g}_i}^{(d)} = \left\{ \bar{\mathbf{g}}^{(0)}(\mathbf{r}_{2,i}^{(0)}) - \bar{\mathbf{g}}^{(0)}(\mathbf{r}_{1,i}^{(0)}) \right\} \cdot \mathbf{e}_i - \left\{ \bar{\mathbf{g}}^{(0)}(\mathbf{r}_{2,i}) - \bar{\mathbf{g}}^{(0)}(\mathbf{r}_{1,i}) \right\} \cdot \mathbf{e}_i^{(0)}, \quad (8.3)$$

and

$$\delta_{\bar{g}_i}^{(d')} = \frac{\mathbf{e}_{i-1} \cdot \mathbf{e}_i \rho_{i-1} - 2\rho_i + \mathbf{e}_i \cdot \mathbf{e}_{i+1} \rho_{i+1}}{(\Delta t)^2} - \frac{\mathbf{e}_{i-1}^{(0)} \cdot \mathbf{e}_i^{(0)} \rho_{i-1} - 2\rho_i + \mathbf{e}_i^{(0)} \cdot \mathbf{e}_{i+1}^{(0)} \rho_{i+1}}{(\Delta t)^2}. \quad (8.4)$$

Herein, $\bar{\mathbf{g}}^{(0)}$ is the a priori 3-D average gravitational acceleration vectors and $\mathbf{r}_{j,i}$ and \mathbf{e}_i are respectively positions and line-of-sight unit vectors derived from orbits of a higher quality than the a priori ones. Thus, the corrected values for the GRACE residual range combinations are obtained by the following expression:

$$\frac{\mathbf{e}_{i-1}^{(0)} \cdot \mathbf{e}_i^{(0)} \delta \rho_{i-1} - 2\delta \rho_i + \mathbf{e}_i^{(0)} \cdot \mathbf{e}_{i+1}^{(0)} \delta \rho_{i+1}}{(\Delta t)^2} - \delta_{\bar{g}_i}^{(p)} - \delta_{\bar{g}_i}^{(d)} + \delta_{\bar{g}_i}^{(d')}, \quad (8.5)$$

where $\delta \rho_i$ denotes a residual inter-satellite range.

8.2.1.2 Geometrical correction of residual 3-D average accelerations

In order to explain the need for a geometrical correction in the context of 3-D acceleration vectors, I recall that in my research unlike that performed by, e.g., Reubelt et al. (2012), I process GRACE kinematic orbits by producing dynamic orbits (see section 2.3.2). The implication is that an a priori gravity field model is needed. If this model is of a poor quality, it would affect the quality of a priori orbits. This would affect in a negative manner the functional model established by Eq. (2.2). To appropriately treat this, I define a geometrical correction in the context of kinematic orbits, too. To that end, it is sufficient to look into the conceptual definition of residual 3-D average acceleration vectors:

$$\delta \bar{\mathbf{g}}_{j,i} = \frac{\mathbf{r}_{j,i-1} - 2\mathbf{r}_{j,i} + \mathbf{r}_{j,i+1}}{(\Delta t)^2} - \bar{\mathbf{a}}^{(0)}(\mathbf{r}_{j,i}). \quad (8.6)$$

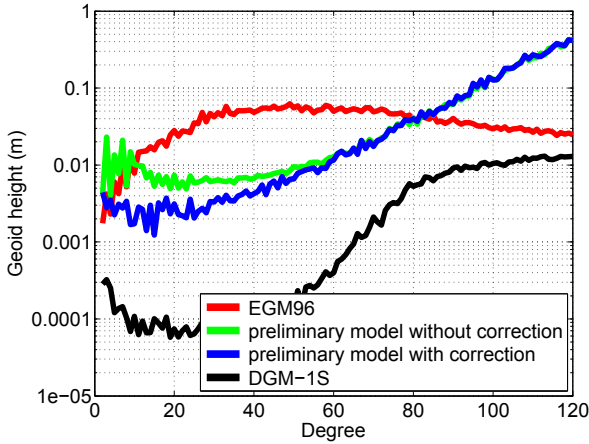


Figure 8.1: Two preliminary one-year GRACE-only unconstrained gravity field models based on GRACE residual range combinations and residual 3-D average acceleration vectors at the first a priori model-related and noise model-related iterations in the absence of the geometrical corrections and after its application. The results are presented in terms of per-degree geoid height differences from EGM2008.

The second term in the right-hand side of this expression, i.e., the a priori 3-D average acceleration vector, has to be evaluated at the true satellite locations, i.e., $\mathbf{r}_{j,i}$, which are obviously unavailable. In practice, a priori orbits $\mathbf{r}_{j,i}^{(0)}$ are used, instead. Thus, a geometrical correction is defined to account for errors in those a priori orbits:

$$\delta_{\mathbf{g}_{j,i}}^{(p)} = \bar{\mathbf{g}}^{(0)}(\mathbf{r}_{j,i}) - \bar{\mathbf{g}}^{(0)}(\mathbf{r}_{j,i}^{(0)}), \quad (8.7)$$

where $\mathbf{r}_{j,i}$ are positions derived from an orbit of a higher quality than the a priori one. Then, residual 3-D average acceleration vectors are computed as follows:

$$\frac{\mathbf{r}_{j,i-1} - 2\mathbf{r}_{j,i} + \mathbf{r}_{j,i+1}}{(\Delta t)^2} - \bar{\mathbf{a}}^{(0)}(\mathbf{r}_{j,i}^{(0)}) + \delta_{\mathbf{g}_{j,i}}^{(p)}. \quad (8.8)$$

8.2.1.3 Effect of geometrical corrections

Obviously, the computation of the geometrical correction requires that the true GRACE satellites' orbits or at least orbits of a higher quality than their dynamic ones are accessible, so that more accurate estimations of the satellites' positions and line-of-sight unit vectors can be produced. In this chapter, I utilize GRACE satellites' reduced-dynamic orbits as orbits of a higher quality to compute geometrical corrections in the context of residual data of both types. Of the GRACE satellites' reduced-dynamic orbits that are at my disposal, only those of 2006 are determined independently from a GRACE-based a priori static gravity field model. As a matter of fact, EGM96 was used to determine those orbits in 2006, too. Therefore, I limit the computations only to GRACE data in 2006 to ensure independency from any GRACE-based a priori knowledge.

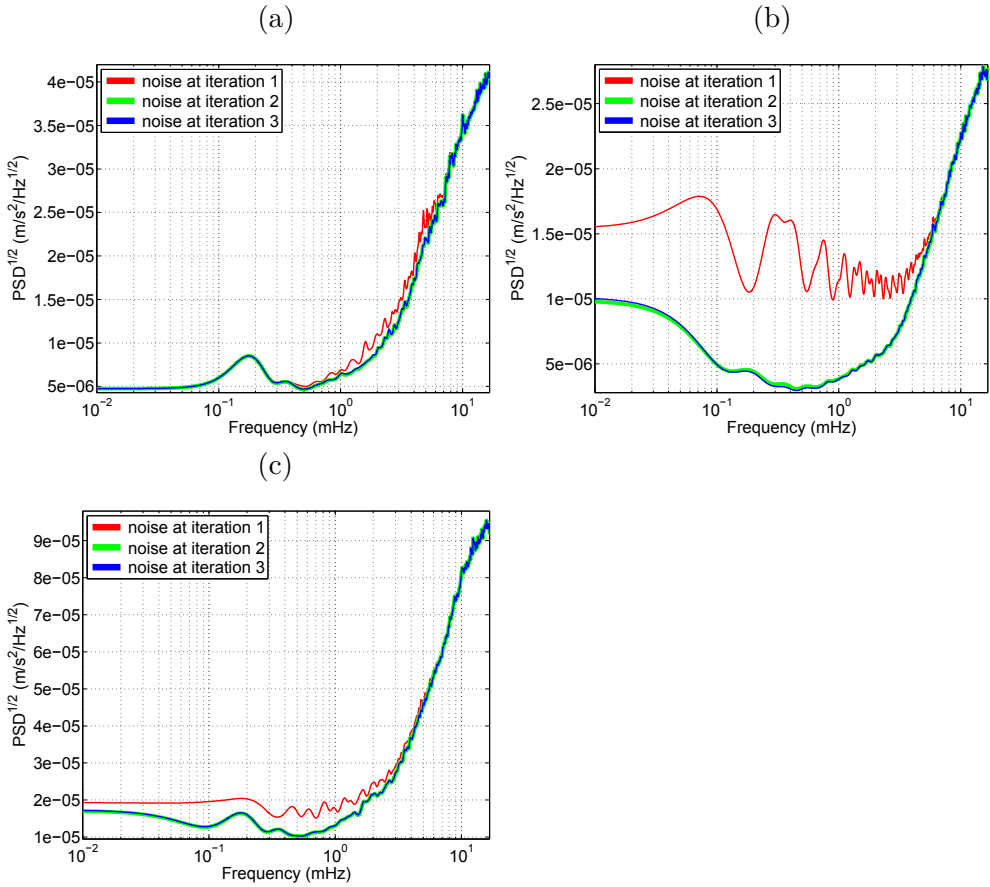


Figure 8.2: The noise $\text{PSD}^{\frac{1}{2}}$'s of the (a) along-track, (b) cross-track, and (c) radial components of the GRACE trailing satellite's residual 3-D average acceleration vectors based on data of 2006. They are obtained at the first, second, and third iterations of the noise model-related iterative scheme within the first a priori model-related iteration in the presence of the geometrical corrections. A Gaussian smoothing has been applied for a better visualization.

Figure 8.1 presents two preliminary one-year GRACE-only unconstrained gravity field models produced at the first a priori model-related iteration and noise model-related iteration in the absence of the geometrical corrections and subsequent to their application. These results are shown in terms of per-degree geoid height differences from EGM2008. This picture indicates a non-negligible model improvement below spherical harmonic degree 60 due to the application of the geometrical corrections. This encourages me to apply the geometrical corrections in computing further results presented in the next two subsections.

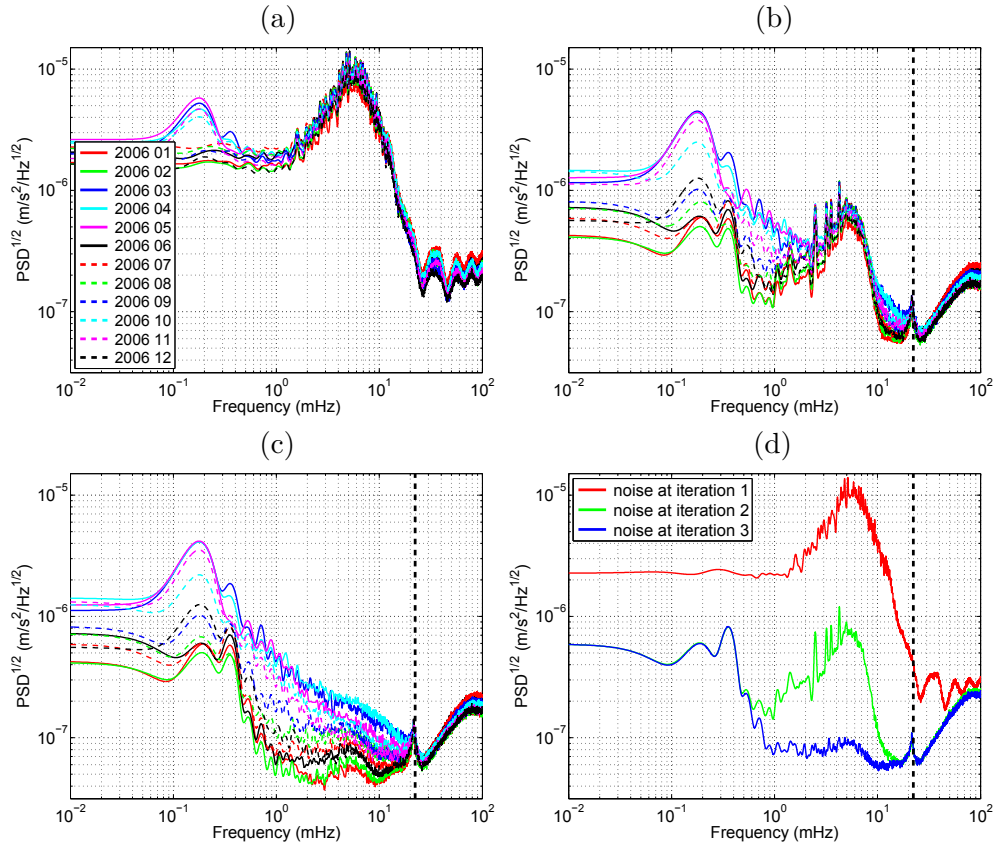
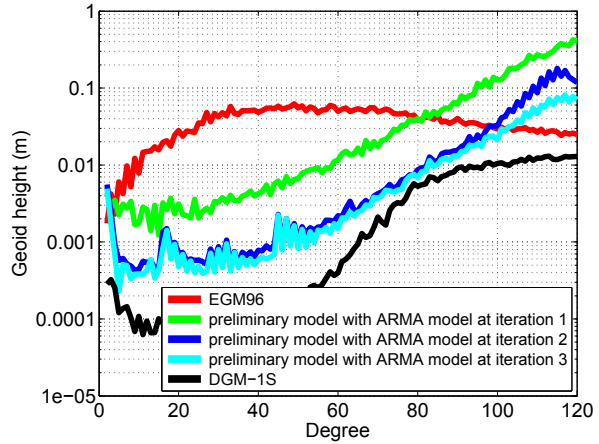


Figure 8.3: The noise $\text{PSD}^{\frac{1}{2}}$ of the GRACE residual range combinations based on data of 12 months of 2006 at the (a) first, (b) second, and (c) third iterations of the noise model-related iterative scheme within the first a priori model-related iteration in the presence of the geometrical corrections. Furthermore, the last picture shows results for the first, second, and third iterations for July 2006. The vertical line in the last three pictures marks the frequency 22 mHz (120 cpr). A Gaussian smoothing has been applied for a better visualization.

8.2.2 An iterative improvement of noise models

In this section, I demonstrate the effect of an iterative improvement of noise models in the GRACE residual data of both types within the first a priori model-related iteration. Three ARMA models of noise are built iteratively in the case of each data type. The noise $\text{PSD}^{\frac{1}{2}}$'s estimated in these three iterations are plotted in Figs. 8.2 and 8.3 for the sets of residual 3-D average acceleration vectors and residual range combinations, respectively. In the former case, only noise $\text{PSD}^{\frac{1}{2}}$'s for the trailing satellite are shown, because those for the leading one turn out to be quite similar. The noise PSD 's of the

Figure 8.4: Three preliminary one-year GRACE-only unconstrained gravity field models produced with ARMA models of noise in residual data sets built at the first, second, and third iterations of the noise model-related iterative scheme within the first a priori model-related iteration in the presence of the geometrical corrections. They are presented in terms of per-degree geoid height differences from EGM2008.



residual 3-D accelerations are based on the whole data set of 2006. Those in the case of residual range combinations are built on a monthly basis individually. This is to account for a rather strong time variability of noise in these residuals, which can be observed in Fig. 8.3. Figures 8.2 and 8.3 show that the noise estimates substantially reduce as the noise model-related iterative scheme progresses. In the case of the residual 3-D average acceleration vectors, two iterations seem to be sufficient. Only a minor reduction of noise estimates and only at the cross-track component is achieved at the third attempt. In the case of the residual range combinations, however, a substantial reduction of noise estimates is observed not only at the second iteration, but also at the third one. After that, a convergence of results is achieved (not shown). I find it worth noticing the peaks in the noise estimates obtained for the residual range combination at the second and third iterations at the frequency 22 mHz (or 120 cpr), which is marked in Figs. 8.3b – 8.3d by a vertical, dashed line. These peaks simply reflect the fact that the gravity field modelling is performed up to only degree 120.

To demonstrate that the achieved reduction of noise estimates is essential, I present in Fig. 8.4 three preliminary one-year GRACE-only unconstrained gravity field models obtained at these three iterations. They are presented in terms of per-degree geoid height differences from EGM2008. This picture reveals a substantial model improvement at the second iteration. This improvement is observed in the entire range of degrees. A minor model improvement is observed at the third iteration, too. A further iteration has a negligible effect (not shown). Thus, within the next a priori model-related iterations, I proceed with the ARMA models of residual data noise built at the third iteration of the noise model-related iterative scheme.

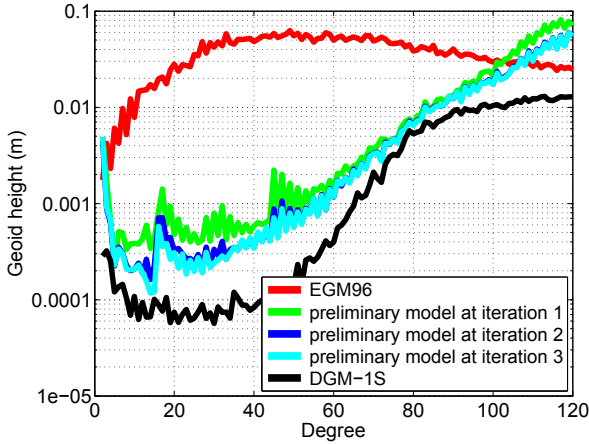


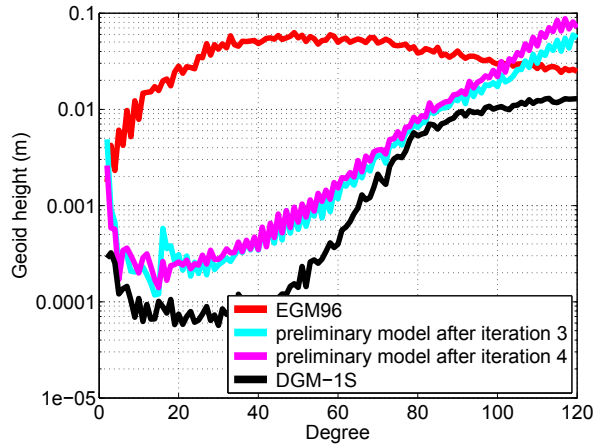
Figure 8.5: Three preliminary one-year GRACE-only unconstrained models produced within the first, second, and third a priori model-related iterations in presence of geometrical corrections. The noise ARMA models used to produce each of them are built at the third iteration of the noise model-related iterative schemes run within the corresponding a priori model-related iteration. The models are presented in terms of per-degree geoid height differences from EGM2008.

8.2.3 An iterative improvement of the static gravity model

Figure 8.5 presents three preliminary one-year GRACE-only unconstrained gravity field models produced at the first three a priori model-related iterations in terms of per-degree geoid height differences from EGM2008. The picture indicates a non-negligible model improvement at the second iteration, which can be observed in the entire range of degrees. Performing the third iteration only leads to a minor model improvement, which is barely observed in the range of low degrees. After that, a convergence of results is achieved (not shown).

A point of concern in Fig. 8.5 is the jump around spherical harmonic degree 17, which consistently appears in all these three preliminary gravity field models presented in this picture, including the one produced at the third iteration. In order to identify the cause of this jump, I performed an investigation in the so-called “trial-and-error” fashion. That investigation led me to a hypothesis that this jump might be related to some inaccuracies in the GRACE satellite’ reduced dynamic orbits, which are utilized to compute the geometrical corrections. In order to inspect this hypothesis, I perform a fourth a priori model-related iteration without applying these geometrical corrections. The model produced in this iteration together with the one produced at the previous iteration is presented in Fig. 8.6 in terms of per-degree geoid height differences with respect to EGM2008. One can clearly see that the aforementioned jump disappears in the model produced at the fourth iteration. Nevertheless, the model produced at this iteration, as opposed to the model produced at the third iteration, experiences a loss of quality. This loss is particularly pronounced at high degrees. In spite of that, I consider the model

Figure 8.6: Two preliminary one-year GRACE-only unconstrained gravity field models produced at the third and the fourth a priori model-related iterations in terms of per-degree geoid height differences with respect to the EGM2008 model. At the third iteration the geometrical correction is applied, whereas at the fourth iteration it is not.



produced at the fourth iteration as the definitive gravity field model of this chapter. Although, it is not an official product, I give this model its own name: TUD-GRACE01S.

8.3 Assessment of TUD-GRACE01S

In the first subsection, a preliminary assessment of TUD-GRACE01S is made by comparing it and AIUB-GRACE01S with EGM2008. In the second subsection, an independent validation of these two unconstrained GRACE-only models is performed by confronting them with GRACE KBR and GOCE SGG control data using the methodology described in chapter 4.

8.3.1 Preliminary comparison

Figure 8.7 presents TUD-GRACE01S and AIUB-GRACE01S in terms of per-degree geoid height differences from EGM2008. EGM96 and DGM-1S are also shown in this picture as a reference. TUD-GRACE01S as compared to AIUB-GRACE01S consistently shows smaller or at least similar per-degree geoid height errors below degree 100. Above that degree, however, the latter model shows a slightly better agreement with EGM2008.

8.3.2 Validation

In this section, I utilize the methodology described in chapter 4 to perform an independent validation of TUD-GRACE01S and AIUB-GRACE01S. To that end, I exploit the same sets of control data as those used in chapter 4. It is worth noting that those data have not been used in the production of the GRACE-only models under consideration. I perform the validation in both

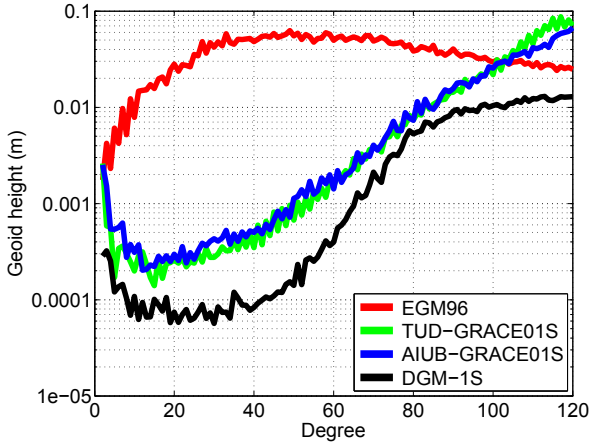


Figure 8.7: Per-degree geoid height differences with respect to EGM2008.

the frequency and spatial domain. The results of the validation against the GRACE KBR and GOCE SGG test data are presented in the first and second subsections, respectively.

8.3.2.1 Validation against GRACE KBR control data

Figure 8.8 exhibits the $\text{PSD}^{\frac{1}{2}}$ of the GRACE misfit range combinations associated with the two GRACE-only models under consideration. The results are based on the control KBR data of February 2010. The frequency ranges shown in Figs. 8.8a and 8.8b are those in which some differences in the model performances can be identified. According to Fig. 8.8a, TUD-GRACE01S shows a higher quality than AIUB-GRACE01S below 20 mHz (i.e., 108 cpr), which can be associated with signals at spatial scales of larger than 200 km half wavelength. Nonetheless, Fig. 8.8b indicates a better performance of AIUB-GRACE01S in a higher frequency range, i.e., 20 – 22 mHz (108 – 120 cpr), which is associated with signals at spatial scales of 180 – 200 km half wavelength.

Figure 8.9 presents the GRACE $1^\circ \times 1^\circ$, $3^\circ \times 3^\circ$, and $6^\circ \times 6^\circ$ block-mean misfit range combinations obtained in the case of the TUD-GRACE01S and AIUB-GRACE01S models on the basis of the one-year set of GRACE KBR control data in 2010. These pictures consistently reveal smaller misfits for the TUD-GRACE01S model. The RMS misfits, provided in the caption of Fig. 8.9, indicate a better performance of this model by about 4 %, 39 %, and 51 % in the case of $1^\circ \times 1^\circ$, $3^\circ \times 3^\circ$, and $6^\circ \times 6^\circ$ block-mean sets of misfit range combinations, respectively.

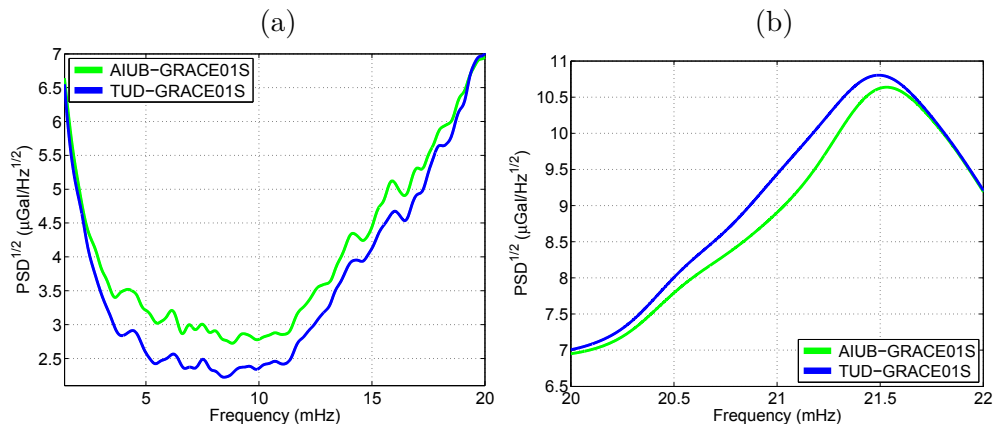


Figure 8.8: $\text{PSD}^{\frac{1}{2}}$ the GRACE misfit range combinations for February 2010 in the frequency ranges (a) 1.5 – 20 mHz and (b) 20 – 22 mHz. A Gaussian smoothing has been applied to facilitate the comparison.

8.3.2.2 Validation against GOCE SGG control data

Figure 8.10 shows $\text{PSD}^{\frac{1}{2}}$ of the xx component of the GOCE misfit gravity gradients for the two GRACE-only models under consideration. The results are based on the control gravity gradients in May 2011. The frequency ranges shown in Figs. 8.10a and 8.10b are the ones in which some differences in the model performances are identified. Figure 8.10a narrowly indicates a higher quality of the TUD-GRACE01S model in the frequency range 8 – 20 mHz (43 – 108 cpr), whereas Fig. 8.10b shows the opposite in a higher frequency range, i.e., 21 – 22 mHz (113 – 120 cpr). Although the identified performance differences are minor, it is important that they are consistent with the results presented earlier based on the GRACE KBR control data. The results based on the yy gravity gradient component are not shown here, due to a relatively low ability of this component to reveal model performance differences in the spectral domain, as it was already discussed in chapter 4. The results based on the xz and zz components are not exhibited either, because they reflect the same behaviour for the two models under consideration as those associated with the xx component.

Figure 8.11 presents the GOCE $1^\circ \times 1^\circ$ block-mean misfit gravity gradients for the xx , yy , and zz components obtained for the two models under assessment. The maps related to the xz gravity gradient component are not shown because of a relatively low sensitivity of this component, which was already discussed in chapter 4. Both models demonstrate an almost similar fit to the GOCE control gravity gradients at the xx component. However, AIUB-GRACE01S

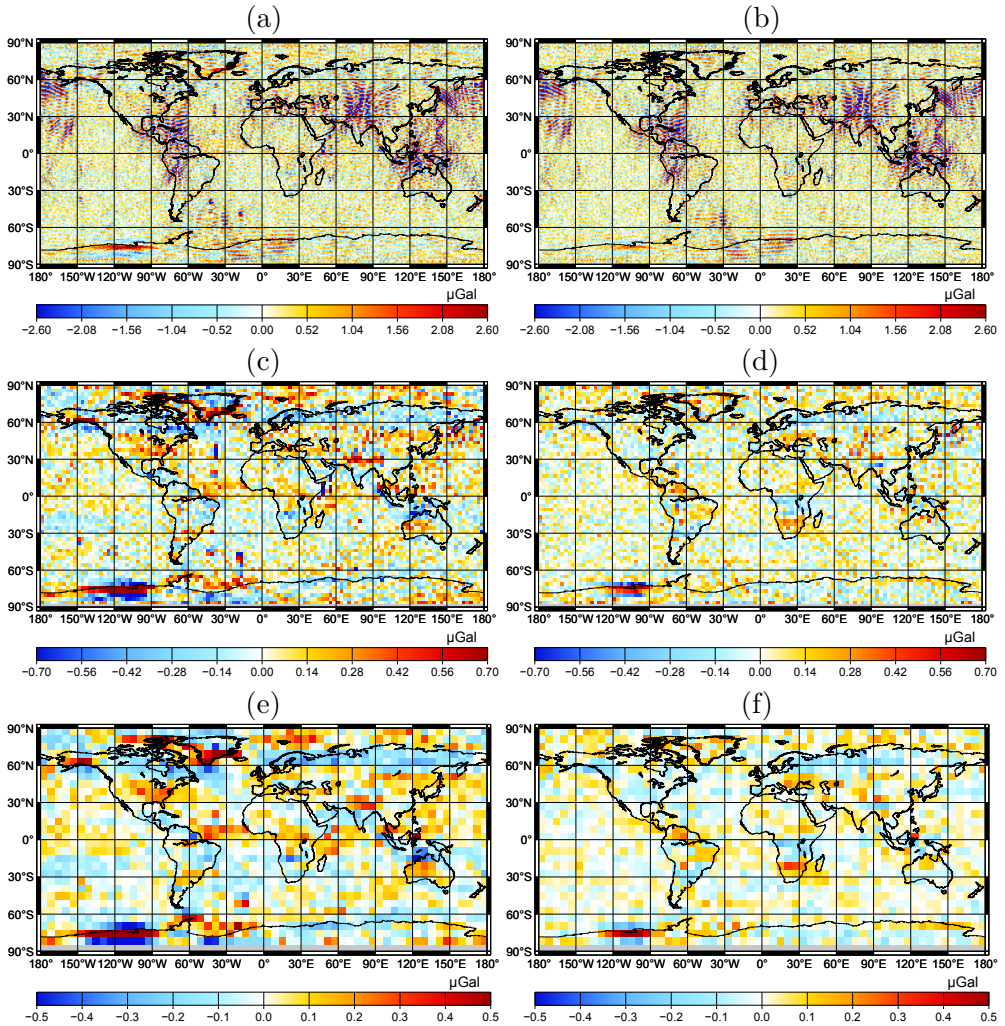


Figure 8.9: The GRACE $1^\circ \times 1^\circ$ (top), $3^\circ \times 3^\circ$ (middle), and $6^\circ \times 6^\circ$ (bottom) block-mean misfit range combinations obtained for AIUB-GRACE01S (left) and TUD-GRACE01S (right) on the basis of the 1-year GRACE KBR control data set in 2010. The RMS misfits are (a) $0.901 \mu\text{Gal}$, (b) $0.863 \mu\text{Gal}$, (c) $0.237 \mu\text{Gal}$, (d) $0.145 \mu\text{Gal}$, (e) $0.168 \mu\text{Gal}$, and (f) $0.083 \mu\text{Gal}$.

matches these data at the yy and zz components better than TUD-GRACE01S by about 1 % and 3 %, respectively. I explain these results by a slightly lower quality of TUD-GRACE01S at relatively high degrees, as it can be observed in Fig. 8.7.

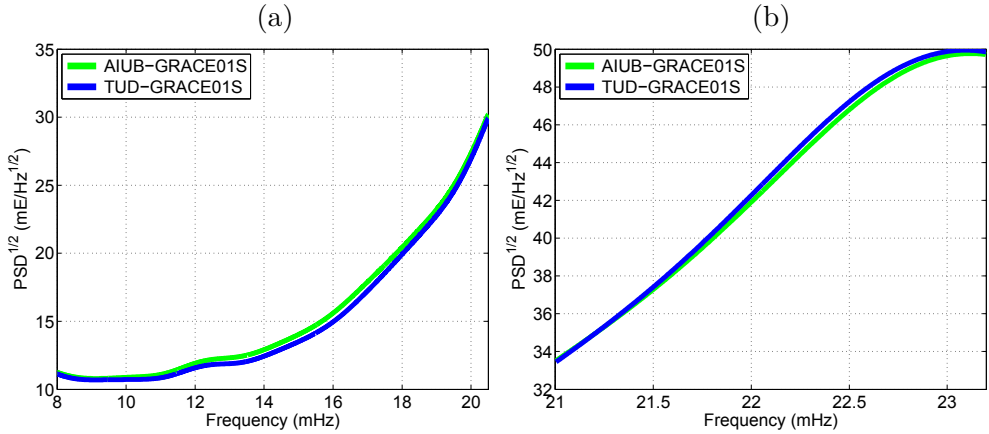


Figure 8.10: $\text{PSD}^{\frac{1}{2}}$ of the xx component of the GOCE misfit gravity gradient tensor for May 2011 in the frequency ranges (a) 8 – 20.5 mHz and (b) 21 – 23.2 mHz. A Gaussian smoothing has been applied to facilitate the comparison.

8.4 Summary and conclusions

As it was pointed out in chapter 3, a state-of-the-art static gravity field model was used as the a priori model in the production of DGM-1S. Therefore, I found it indispensable to perform an investigation to demonstrate that the methodology followed in the production of DGM-1S could be adjusted so that it could offer a successful static gravity field retrieval even if a relatively old model, such as EGM96, is used as the a priori guess. I performed this investigation in the context of only the GRACE mission. Of all the data contributed to DGM-1S, GRACE KBR measurements are the only ones that require the usage of an a priori guess for the gravity field. A number of modifications were implemented. First, a geometrical correction was defined and applied to the residual range combinations to appropriately deal with their low-frequency noise. On the other hand, these residuals were no longer subject to the empirical high-pass filter of Eq. (3.1). A similar correction was defined and applied to the residual 3-D average acceleration vectors. Second, an accurate estimation of noise in the residual data was obtained with an iterative scheme similar to that described in chapter 6. It was shown that the results converge after three iterations. The contribution of this iterative approach was found to be substantial in the entire range of degrees. Third, the static gravity field model, used to compute a priori (dynamic) orbits, was updated in an iterative manner, too. It was shown that it only takes three iterations until a convergence of the results is achieved. Having applied these three modifications, I produced TUD-GRACE01S: a one-year GRACE-only unconstrained

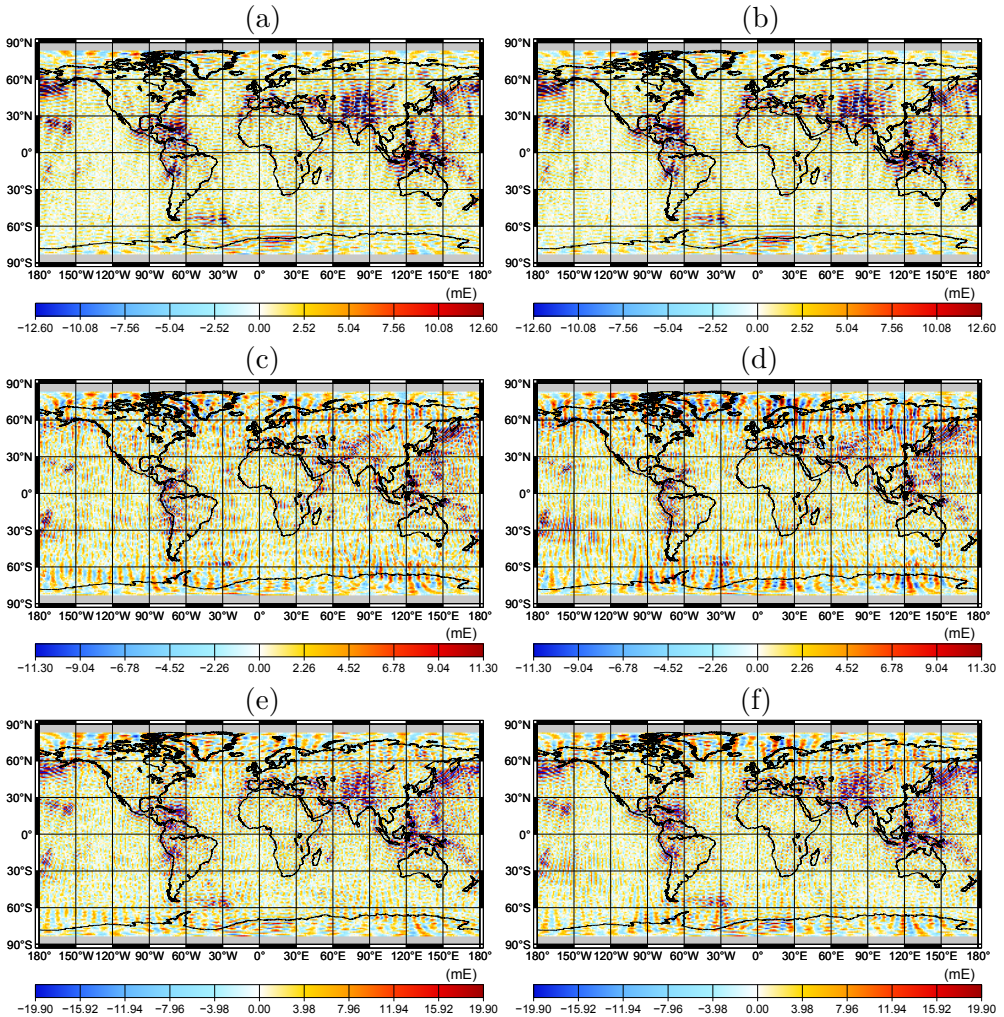


Figure 8.11: The GOCE $1^\circ \times 1^\circ$ block-mean residual gravity gradients for the xx (top), yy (middle), and zz (bottom) components obtained for AIUB-GRACE01S (left) and TUD-GRACE01S (right). The RMS misfits are (a) 4.187 mE, (b) 4.187 mE, (c) 3.655 mE, (d) 3.754 mE, (e) 6.587 mE, and (f) 6.624 mE.

static gravity field model complete up to spherical harmonic degree 120. In doing so, I used EGM96 as the a priori guess. For a comparison, I considered AIUB-GRACE01S, which is the only publicly available one-year GRACE-only unconstrained static gravity field model. Importantly, AIUB-GRACE01S has been also produced using EGM96 as the a priori guess and is also complete up to spherical harmonic degree 120. Then, I validated TUD-GRACE01S and AIUB-GRACE01S by confronting them with GRACE KBR and GOCE SGG sets of control data with the methodology presented in chapter 4. The valida-

tion indicated, in general, a similar performance of these two models. However, some differences in the performance were identified. The KBR-based validation in the frequency domain indicated a higher accuracy of TUD-GRACE01S below 20 mHz (i.e., below 108 cpr). However, the opposite was observed in a higher frequency range: 20 – 22 mHz (i.e., 108 – 120 cpr). In the spatial domain, TUD-GRACE01S showed a better agreement with GRACE KBR control data: by about 4 % in terms of RMS misfits. Both models demonstrated a similar match to GOCE control gravity gradients at the xx component. AIUB-GRACE01S matched these data at the yy and zz components slightly better than TUD-GRACE01S: by about 1 % and 3 %, respectively.

The outcome of the validation leads me to the following main conclusion: a GRACE-only global static gravity field modelling with a competitive quality is possible with the range combination approach even without a high-quality a priori static gravity field model.

9 Understanding low-frequency noise in GRACE KBR data

Ditmar et al. (2012) investigated noise in GRACE KBR measurements. They performed the investigation, in particular, in the frequency domain, including in the range of low frequencies. My contribution to that study was to identify the origin of the increased level of noise in the low-frequency part (below 2 – 3 cpr). In this chapter, I document that contribution.

9.1 Introduction

A new approach was proposed in chapter 6 based on a spatially-dependent data weighting scheme to deal with the increased level of noise in GRACE residual range combinations in the range of low frequencies (below 2 – 3 cpr). In this chapter, I present a method by which I identify the origin of this noise. To that end, I utilize the functional model proposed by Rummel (1979) in the so-called “classical acceleration approach”. Thus, I find it essential to describe the link between the range combination approach and the classical acceleration approach. This is the subject of section 9.2.1. In section 9.2.2, I identify the origin of the low-frequency noise in GRACE residual range combinations. Section 9.3 summarises the findings of the research and concludes with a discussion.

9.2 Methodology

9.2.1 Linking the average acceleration approach to the classical acceleration approach

There is a close link between the approach based on GRACE range combinations and the classical acceleration approach, proposed by Rummel (1979). According to the latter approach, the along-track component of the GRACE point-wise inter-satellite accelerations can be derived from KBR measurements as follows:

$$a_i^{(x')} = \ddot{\rho}_i - \frac{1}{\rho_i} \left\{ \left(v_i^{(y')} \right)^2 + \left(v_i^{(z')} \right)^2 \right\}. \quad (9.1)$$

Herein, x' , y' , and z' refer to the axes of a local Cartesian frame that is defined at a given measurement epoch such that (i) the x' -axis is parallel to the line-

of-sight, which is directed from the trailing satellite to the leading one; (ii) the z' -axis is directed upwards, being orthogonal to the x' -axis and belonging to the plane defined by the satellites' locations and the center of mass of the Earth; and (iii) the y' -axis is orthogonal to x' - and z' -axes, complementing the frame to a right-handed one. The origin of this local frame coincides with the center of the Earth. The lower index i corresponds to the measurement time $t_i = t_0 + i\Delta t$, where $i = 1, 2, \dots$ and t_0 is an initial epoch. Quantities v_i and a_i respectively denote components of the inter-satellite velocity and acceleration vectors at epoch i . A particular component of these vectors is denoted with the corresponding upper index: (x'), (y'), or (z'). The first term on the right-hand side of Eq. (9.1) is the inter-satellite range-acceleration (i.e., the second order time-derivative of the inter-satellite range), which is directly derived from KBR data (Case et al., 2004). This term is provided as a part of GRACE level-1b data (i.e., in KBR1B product). The second term in the right-hand side of Eq. (9.1) represents a centrifugal acceleration, which is the consequence of the fact that the aforementioned local frame, which is coupled with the line-of-sight direction, is a non-inertial one. This centrifugal acceleration term has to be obtained as accurately as possible for which purpose GRACE satellites' precise dynamic orbits, i.e., those that are produced with a state-of-the-art force model, are typically used. By neglecting the out-of-plane motion, this centrifugal acceleration term can be represented as

$$-\frac{1}{\rho_i} \left\{ \left(v_i^{(y')} \right)^2 + \left(v_i^{(z')} \right)^2 \right\} \approx -\frac{1}{\rho_i} \left(v_i^{(z')} \right)^2. \quad (9.2)$$

Now, let me return to the concept of range combinations. Since $\mathbf{e}_i \cdot \mathbf{e}_{i\pm 1} = \cos \theta_{i\pm}$ (i.e., that θ_{i-} and θ_{i+} are the angles between the line-of-sight direction at the current epoch and the one at the previous and subsequent epochs, respectively), Eq. (2.4) can be re-written as

$$\bar{a}_i = \frac{\rho_{i-1} - 2\rho_i + \rho_{i+1}}{(\Delta t)^2} - \frac{(1 - \cos \theta_{i-})\rho_{i-1} + (1 - \cos \theta_{i+})\rho_{i+1}}{(\Delta t)^2}. \quad (9.3)$$

The first term in the right-hand side of this expression is obviously a finite-difference analogy of the inter-satellite range-acceleration, i.e., the first term in the left-hand side of Eq. (9.1). Let me consider the second term in the right-hand side of Eq. (9.3). Taking into account the identity $1 - \cos \theta = 2 \sin^2 \left(\frac{\theta}{2} \right)$, it can be re-written as

$$\frac{2 \sin^2 \left(\frac{\theta_{i-}}{2} \right) \rho_{i-1} + 2 \sin^2 \left(\frac{\theta_{i+}}{2} \right) \rho_{i+1}}{(\Delta t)^2}. \quad (9.4)$$

Now, let $\theta(t)$ be the angle between the line-of-sight direction at an arbitrary moment and the line-of-sight direction at the time t_i ($\theta(t) < 0$ for $t < t_i$ and

$\theta(t) > 0$ for $t > t_i$). Variations of the angle $\theta(t)$ mostly reflect the rotation of the satellites in a given orbital plane. Therefore, it follows from simple geometrical considerations that

$$\sin \theta(t) \approx -\frac{d^{(z'_i)}(t)}{\rho(t)}, \quad (9.5)$$

where $d^{(z'_i)}(t)$ is the z'_i -component of the current GRACE inter-satellite offset vector. With a further assumption that the function $\theta(t)$ is approximately linear in the time interval $[t_i - \Delta t, t_i + \Delta t]$, the angles $\frac{\theta_{i-}}{2}$ and $\frac{\theta_{i+}}{2}$ reflect the line-of-sight orientation at the moments $t_i - \frac{\Delta t}{2}$ and $t_i + \frac{\Delta t}{2}$, respectively, i.e.,

$$\left\{ \begin{array}{l} \sin \left(\frac{\theta_{i-}}{2} \right) \approx -\frac{d^{(z'_i)}(t_i - \frac{\Delta t}{2})}{\rho(t_i - \frac{\Delta t}{2})} \\ \sin \left(\frac{\theta_{i+}}{2} \right) \approx -\frac{d^{(z'_i)}(t_i + \frac{\Delta t}{2})}{\rho(t_i + \frac{\Delta t}{2})}. \end{array} \right. \quad (9.6)$$

Furthermore, let $d^{(z'_i)}(t)$ be a linear function at the vicinity of the time t_i . Since by definition it follows that $d^{(z'_i)}(t_i) = 0$, one can readily obtain:

$$\left\{ \begin{array}{l} d^{(z'_i)}(t_i - \frac{\Delta t}{2}) \approx -\frac{v_i^{(z')} \Delta t}{2} \\ d^{(z'_i)}(t_i + \frac{\Delta t}{2}) \approx \frac{v_i^{(z')} \Delta t}{2}. \end{array} \right. \quad (9.7)$$

Then, the substitution of Eqs. (9.6) and (9.7) into Eq. (9.4) allows the second term in Eq. (9.3) to be re-written as

$$-\frac{(v_i^{(z')})^2}{2} \left(\frac{\rho_{i-1}}{\rho^2(t_i - \frac{\Delta t}{2})} + \frac{\rho_{i+1}}{\rho^2(t_i + \frac{\Delta t}{2})} \right). \quad (9.8)$$

Assuming that the inter-satellite range shows only minor variations, i.e., that $\rho(t_i - \Delta t) \approx \rho(t_i - \frac{\Delta t}{2}) \approx \rho(t_i) \approx \rho(t_i + \frac{\Delta t}{2}) \approx \rho(t_i + \Delta t)$, one finally arrives at: $-\frac{1}{\rho_i} (v_i^{(z')})^2$. This is equal to the centrifugal acceleration term given by Eq. (9.2). It is important to recall that this conclusion is achieved when assuming that the angle θ and the z' -component of the inter-satellite offset vector change linearly, whereas the inter-satellite range is constant. Obviously, all these assumptions are satisfied in a sufficiently close vicinity of the time t_i . This means that range combinations can be considered as a finite-difference approximation of the along-track component of the point-wise inter-satellite accelerations, i.e., Eq. (9.1). That is, the data of these two types become equivalent when $\Delta t \rightarrow 0$.

9.2.2 Identifying the origin of the low-frequency noise in residual range combinations

This section aims at identifying the origin of the low-frequency noise in GRACE residual range combinations. To achieve this objective, an accurate estimation of the total noise in these residuals has to be first obtained. To that end, I produce residual range combinations as described in chapter 2 (see section 4.2.2) on the basis of a state-of-the-art force model in which the monthly variations of the gravity field are also taken into account using DMT-2. The exploited force model uses DGM-1S. Importantly, it also accounts for all the other dynamic forces listed in chapter 3 (see section 3.2).

The PSD^{1/2} of the estimated total noise in 12 months of 2006 is plotted as an example in Figs. 9.1 and 9.2. One can clearly see in Figs. 9.1 and 9.2 the increased noise level in the range of low frequencies below 2 – 3 cpr. To identify its origin, I utilize Eq. (9.1) and re-write it as:

$$a_i^{(x')} = \ddot{\rho}_i - \frac{1}{\rho_i} (\mathbf{v}_{\perp,i})^2, \quad (9.9)$$

where the term $\mathbf{v}_{\perp,i} = \sqrt{(v_i^{(y')})^2 + (v_i^{(z')})^2}$ is the GRACE inter-satellite velocity vector projected onto the plane orthogonal to the line-of-sight direction. It mostly represents the radial component of the inter-satellite velocity vector. It can be easily computed as follows:

$$\mathbf{v}_{\perp,i} = \sqrt{\|\mathbf{v}_i\|^2 - \dot{\rho}_i^2}, \quad (9.10)$$

where \mathbf{v}_i is the inter-satellite velocity vector and $\|\mathbf{v}_i\|$ is its Euclidean norm. They are computed from GRACE satellites' precise dynamic orbits. I recall that these orbits are produced by the orbit integration (see chapter 2) performed in the course of estimation of the total noise in residual range combinations. The term $\dot{\rho}_i$ in Eq. (9.10) is inter-satellite range-rate, which is directly obtained from ranging measurements (Case et al., 2004). Range rates are provided as a part of GRACE level-1B data (i.e., in KBR1B product). To identify the origin of the low-frequency noise, one only needs to look into noise in the second term of the right-hand side of Eq. 9.9: $\frac{1}{\rho_i} (\mathbf{v}_{\perp,i})^2$. This is due to the fact that noise associated with the first term in this equation, i.e., $\ddot{\rho}_i$, manifests itself in the high-frequency range, and therefore, is irrelevant in the context of my study. The noise associated with the second term in Eq. (9.9) can be estimated by applying the error propagation law as follows:

$$\frac{2}{\rho_i} \mathbf{v}_{\perp,i} \sigma_{\mathbf{v}_{\perp,i}}. \quad (9.11)$$

This noise is caused by inaccurately known GRACE satellites' relative velocities. Thus, I hereafter refer to it as “relative velocity noise”, in which $\sigma_{\mathbf{v}_{\perp,i}}$ is

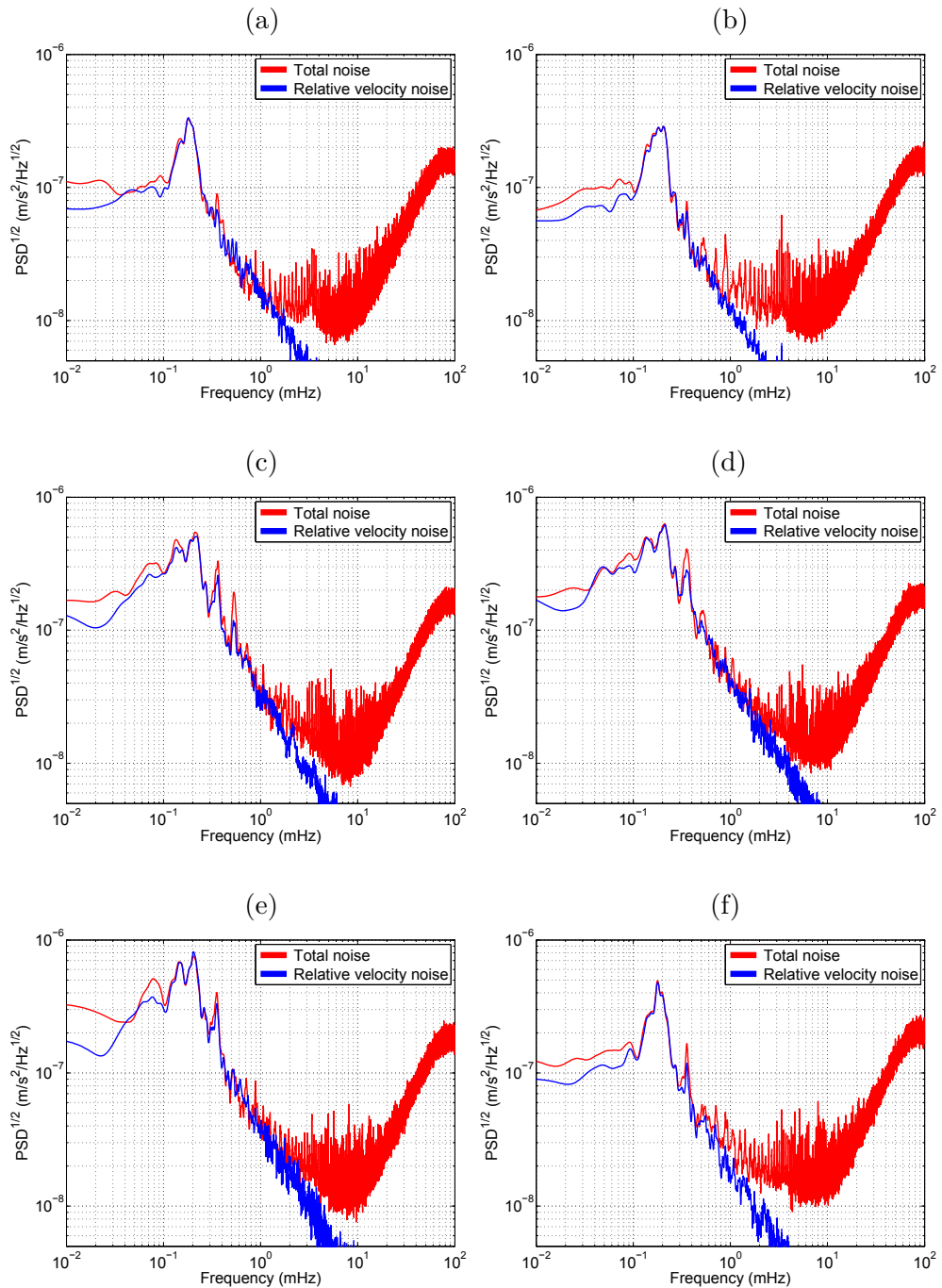


Figure 9.1: The $\text{PSD}^{1/2}$ of the total noise and relative velocity noise in GRACE residual range combinations in (a) January, (b) February, (c) March, (d) April, (e) May, and (f) June 2006.

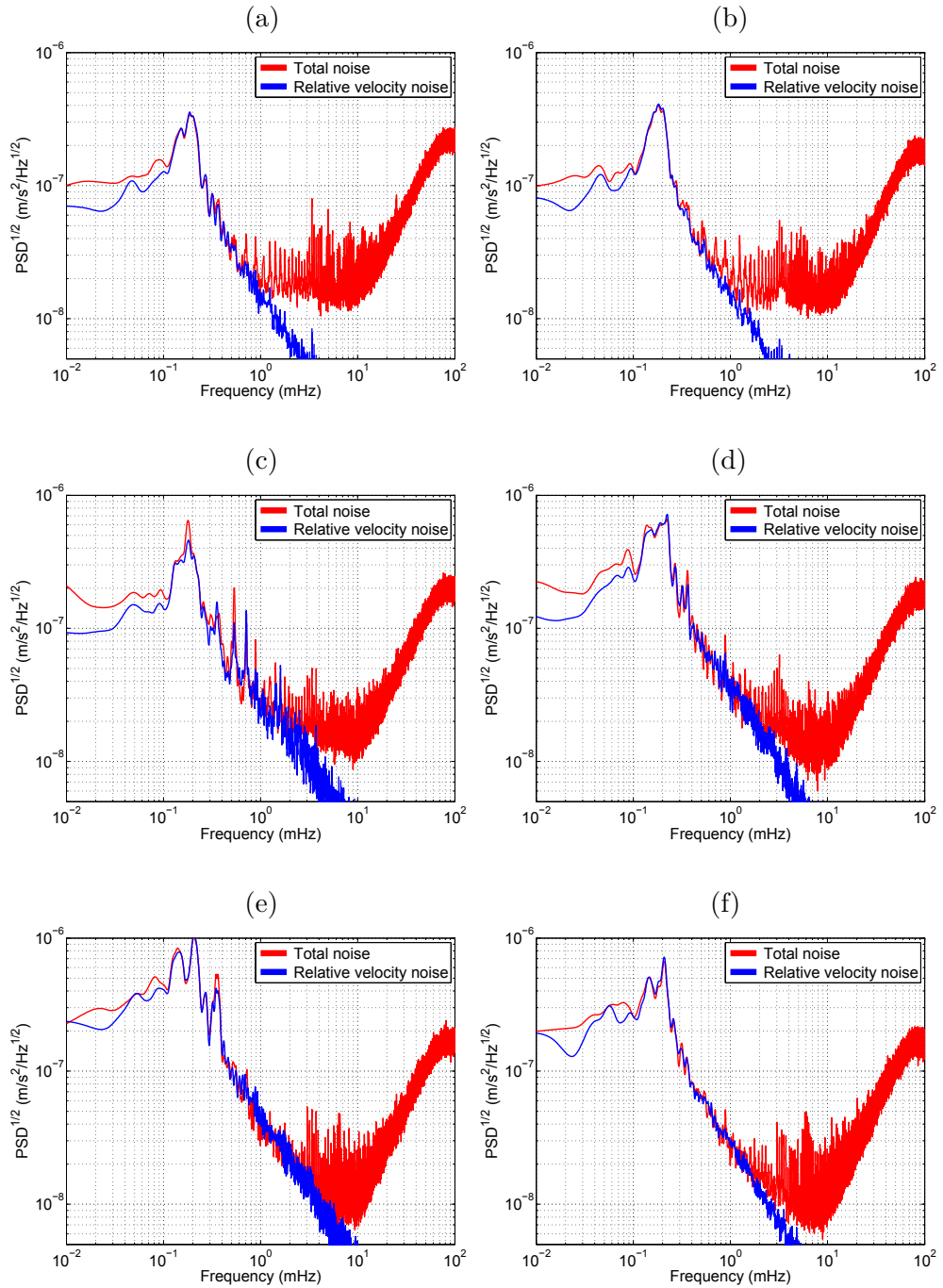


Figure 9.2: The $\text{PSD}^{1/2}$ of the total noise and relative velocity noise in GRACE residual range combinations in (a) July, (b) August, (c) September, (d) October, (e) November, and (f) December 2006.

the error in the projection of the inter-satellite velocity vector onto the plane orthogonal to the line-of-sight direction. Assuming that stochastic properties of noise in the velocities derived from dynamic orbits are the same at all components, I approximate $\sigma_{\mathbf{v}_{\perp,i}}$ with the residual inter-satellite range-rates, which are estimated as the observed range-rates minus those based on the precise dynamic orbits. The procedure to compute the inter-satellite range-rates from GRACE satellites' dynamic orbits is already described in chapter 4 (see section 4.4).

The PSD ^{$\frac{1}{2}$} of the estimated relative velocity noise is presented for the 12 months of 2006 in Figs. 9.1 and 9.2 together with that of the total noise. As one can clearly see, there is an almost perfect agreement between the relative velocity noise and the total noise in the residual range combinations at the low-frequency part of the spectrum. Importantly, such an agreement is observed in all 12 months of 2006. The conclusion is that above-defined relative velocity noise is primarily responsible for the presence of the low-frequency noise in GRACE residual range combinations. The implication is that the increased level of noise in GRACE residual range combinations can be eliminated or at least mitigated by producing GRACE satellites' orbits of a higher quality than their precise dynamic ones and exploiting those improved orbits to obtain and apply a geometrical correction, which was already defined in the previous chapter.

9.3 Summary, discussion, and conclusions

The increased noise level in GRACE residual range combinations in the range of low frequencies (i.e., up to 2 – 3 cpr) was found to be the consequence of an inaccurately known GRACE satellites' dynamic orbits. More specifically, inaccuracies in the radial component of the GRACE inter-satellite velocity vectors were found to be responsible for the aforementioned low-frequency noise. Because they implicitly lead to an insufficiently accurate computation of the centrifugal accelerations, which are caused by the rotation of the line-of-sight.

I conclude by saying that although I performed this investigation in the context of the functional model based on the concept of range combinations, the presence of the strong low frequency noise in KBR data may play a significant role in a general case, too. After all, the GRACE inter-satellite measurement principle is nothing but gravity gradiometry along one axis: the line-of-sight (Keller and Sharifi, 2005). The GRACE gradiometer, like any other gravity gradiometer, senses not only the gravity gradients, but also a centrifugal force caused by the rotation of the line-of-sight. And just like in the case of any other gravity gradiometer, this force needs to be corrected for, for which pur-

pose independent information about the frame rotation, i.e., about the radial component of the inter-satellite velocity vector, must be available. Inaccuracies in such information definitely reduce the overall quality of the resulting gravity field models.

The outcome of the presented investigation implies that a more accurate determination of GRACE satellites' orbits may allow the low-frequency noise in GRACE observable based on its KBR data to be eliminated or at least mitigated. This may substantially improve the quality of KBR-based gravity field models.

10 Conclusions and recommendations

In this chapter, I (i) highlight the most important products and findings of the research executed in the framework of my dissertation (the first subsection); and (ii) provide a list of recommendations regarding tasks that could be executed in the future as a continuation of the research (the second subsection).

10.1 Conclusions

In view of the research objectives defined and listed in chapter 1 (section 1.2), the study executed in this thesis led to the following outcomes. They are listed in the same order as the research objectives in chapter 1.

1. A new global model of the static part of the Earth's gravity field, entitled DGM-1S, was produced on the basis of GRACE KBR data, GOCE gravity gradients, and GRACE and GOCE kinematic orbits. The model is complete to spherical harmonic degree 250. In the production of this model, a frequency-dependent data weighting was applied to all the data to account for the colored noise in those data and ensure their optimal combination. To that end, noise in each data set was estimated and its stochastic description was built with an ARMA process. Furthermore, the added value of GOCE data to the static gravity field modelling was studied. It was found that a usage of kinematic orbit data delivered by the GOCE mission might not improve a static gravity field model if GRACE data and GOCE gravity gradients are already incorporated. This implies that the added value of the GOCE mission to the static gravity field retrieval is fully linked to its measurements of gravity gradients. In addition, it was found that GOCE gravity gradients contribute to the static gravity field modelling above degree 150. Furthermore, it was shown that satellite-only GRACE/GOCE combined models are contaminated with high-frequency random inaccuracies. Those inaccuracies were identified mostly above degree 200. Finally, it was found that satellite-only GRACE/GOCE models show a relatively low performance in a few parts of the Pacific ocean. Causes of this phenomenon are still to be investigated.
2. A new methodology was proposed to validate global static gravity field models. It is based on an analysis of the ability of a model to fore-

cast independent GRACE KBR data and GOCE gravity gradients, i.e., those data that have not been used in the production of models under assessment. The proposed methodology allows the quality of models to be assessed in different geographical regions as well as in the spectral domain. The methodology was applied to a number of recent models produced without and with GOCE data. The study clearly demonstrated, among others, the ability of the proposed methodology to reveal performance differences between models, despite the fact that the duration of control data sets was much shorter than that of the data sets used in the production of tested models. In that study, DGM-1S and some alternative models, e.g., GOCO02S, were considered. The obtained results demonstrated a competitive quality of DGM-1S as compared to the other combined satellite-only GRACE/GOCE models.

3. The proposed validation methodology allowed the added value of the GOCE mission to the static gravity field modelling to be further analysed. To that end, I compared the validation results for the combined GRACE/GOCE satellite-only models with those obtained for state-of-the-art models produced without GOCE data, namely, EGM2008 and ITG-Grace2010s. Prior to this comparison, I found it essential to compare these two models with each other to find out which one is a better benchmark in a given geographical region. A better performance of EGM2008 as compared to ITG-Grace2010s in the world's oceans and in the continental areas well surveyed by terrestrial gravimetry was found based on GOCE control gravity gradients. On the other hand, ITG-Grace2010s was found to be of a much higher quality in the continental areas poorly surveyed with terrestrial gravimetry. Those findings led me to the conclusion that a fair quantification of the added value of the GOCE mission has to be based on a comparison of satellite-only GRACE/GOCE models with ITG-Grace2010s in the gravimetrically poorly surveyed continental areas and with EGM2008 in the gravimetrically well-surveyed ones as well as in the world's oceans. In view of that conclusion, the GRACE control KBR data did not allow this added value to be seen in the gravimetrically poorly-surveyed continental areas. However, the GOCE control gravity gradients did show that the usage of GOCE data increases the model accuracy there by 23 – 36 %. Both the control KBR and gravity gradiometry data allowed the GOCE mission's added value to be seen in the gravimetrically well surveyed continental areas (improvements by 6 – 9 % and 4 – 16 %, respectively) and in the world's oceans (improvements by about 11 % and 12 %, respectively). Importantly, it was shown that this identified added value is almost entirely related to the coefficients below degree 200.

4. The proposed validation methodology also allowed me to inspect how successfully GRACE and/or GOCE data have been combined with surface gravity measurements, i.e., terrestrial gravimetry/satellite altimetry data, in the production of ultra-high degree global static gravity field models, namely, EGM2008 and EIGEN-6C. To that end, these two models were compared with their satellite-only counterparts: ITG-Grace03 and EIGEN-6S, respectively. The comparison revealed that EGM2008 has experienced a substantial (by 62 – 69 % based on GOCE control gravity gradients) loss of information content of GRACE data in areas poorly surveyed with terrestrial gravimetry measurements. A similar problem was also identified in the case of EIGEN-6C, but in a much less pronounced manner. Finally, it was found based on the GRACE control KBR data that EGM2008 as compared to its satellite-only counterpart has also experienced a minor performance degradation in the world's oceans and in the gravimetrically well-surveyed continental areas. The GOCE control gravity gradients, on the other hand, revealed a substantial gain in EGM2008 in these regions.
5. An investigation on the potential added value of the GOCE mission to the GRACE-based modelling of temporal gravity field variations was performed. The investigation was conducted both in the context of unconstrained solutions and after an optimal anisotropic filtering. The impact identified for GOCE data in those two cases were found to be radically different. A substantial impact was identified before filtering. It was shown, however, that the impact identified in the context of unconstrained solutions is mostly related to the stabilization effect of GOCE data onto linear system of equations and not driven by GOCE data information content. The impact identified after filtering, which was regarded in my analysis as the quantification of the GOCE mission's added value to the time-varying gravity field modelling, was found to be small. In some instances, however, that impact was found to be slightly above GRACE noise level. Those instances were observed in areas with strong mass transport. Importantly, indications were found that the quantified added value could be interpreted as an attempt of GOCE data to alleviate some well-known limitations of the GRACE mission.
6. A new global model of monthly gravity field variations, i.e., DMT-2, was produced based on KBR data in the time interval February 2003 – December 2010. The new model was found to outperform its predecessor, DMT-1, in terms of spatial resolution. The higher spatial resolution of the new model is found to be mostly related to the usage of a more advanced data weighting approach (which is realized by building and

incorporating highly detailed ARMA models of noise in GRACE residuals on a monthly basis). In addition, the new model benefits from the usage of the release 2 of GRACE level-1B data. It was confirmed that the usage of these data leads to elimination of globally distributed East-West artifacts. Furthermore, it was shown that GRACE monthly gravity field models produced up to degree 120 as compared to those complete to degree 60 or 90 are of a higher spatial resolution. The latter models underestimate the signal amplitude and show ring artifacts in areas where strong mass variations occur. Nevertheless, it was shown that the higher spatial resolution of models produced up to degree 120 is almost entirely related to the optimal filtering and not driven by the information content of KBR data. Finally, it was found that maximum degree in the unconstrained GRACE-based monthly gravity field modelling should not be lower than 90. Computing a model of this kind to a lower degree could lead to a loss of signal.

7. The methodology followed in the production of DGM-1S was adjusted so that it could be used even when a relatively inaccurate model, such as EGM96, is defined as the a priori guess. The model produced with the adjusted methodology was compared with AIUB-GRACE01S (i.e., an alternative model produced at University of Bern). A high quality of the model produced in my study was proven in an independent validation. The outcome allowed me to conclude that a GRACE-only global static gravity field modelling with a competitive quality is possible with the range combination approach even without a high-quality a priori model.
8. The increased noise level in GRACE KBR data in the range of low frequencies (i.e., up to 2 – 3 cpr) was found to be mainly caused by inaccuracies in the computed orbits. In particular, errors in the radial component of inter-satellite velocities play an important role. This implies that a more accurate determination of GRACE orbits may substantially improve the quality of KBR-based gravity field models.

10.2 Recommendations

It is recommended that the following tasks are executed in the future:

1. Computing a new combined GRACE/GOCE static gravity field model (to replace DGM-1S) based on the latest releases of GRACE and GOCE data. In doing so, longer data sets shall be used. Definitely, this shall include all data to be acquired by the GOCE mission by the end of its lifetime (i.e., some time in November 2013). Furthermore, following two tasks shall be executed prior to the production of the new model.

- (i) In the production of DGM-1S, I did not clean GRACE KBR data from long-term (e.g., monthly) temporal gravity field variations. However, I tend to believe that models of a higher quality (at least in a degree range to which KBR data are sensitive) could be produced if these nuisance signals are removed from KBR measurements using a GRACE-based mass transport model.
 - (ii) In the production of DGM-1S, I applied a Kaula-type regularization at high degrees. In doing so, I computed the optimal value of the regularization parameter by minimizing geoid height differences from EGM2008 over the whole globe. Given a high quality of EGM2008 in the oceanic areas as well as in the gravimetrically well-surveyed continental areas, I tend to believe that the approach followed to compute the regularization parameter is practically justified. Nevertheless, a usage of a variance component estimation, such as the one proposed by Kusche (2003), for computing the optimal regularization parameter is more appealing from a scientific standpoint. Furthermore, the regularization shall be applied in a spatially varying fashion taking into account the signal magnitude in different regions.
2. Further validation of the developed global static gravity field models using, in particular, in situ oceanographic measurements of geostrophic current velocities.
 3. Extending the methodology proposed to validate global static gravity field models using sets of GRACE and GOCE control data. To that end, sets of misfits of GRACE range combinations and GOCE gravity gradients from satellite altitude are inverted into corresponding sets of misfit spherical harmonic coefficients. These coefficients shall allow model performance differences to be computed and analysed in terms of misfit geoid heights and gravity anomalies. This will allow a more sensible measure of the model quality to be achieved.
 4. Calibrating GRACE noise covariance matrices in the context of time-varying gravity field modelling. A problem is that GRACE noise covariance matrices do not realistically describe errors in the corresponding models at the vicinity of the poles. They underestimate the actual errors in the models there. The reason is that the density of GRACE observation points near the poles is extremely high. Therefore, the propagation of errors in GRACE data into solutions yields too small errors in areas at the vicinity of poles, which is unrealistic. This overestimation of accuracy of GRACE solutions manifests a serious problem at the stage of the optimal filtering. An application of the filter proposed by Klees et al.

(2008b) with ignoring this issue would lead to East-West stripes in the filtered mass transport model all over the globe. A pragmatic approach to deal with this problem is to empirically manipulate noise in GRACE models at the vicinity of poles until the aforementioned East-West artifacts disappear. This pragmatic approach was proposed and implemented by Liu et al. (2010) when they computed DMT-1. I also used that approach in my research in the context of GRACE monthly gravity field modelling. A more justified approach to deal with the aforementioned problem would be, however, to obtain a more realistic estimation of noise in GRACE models. To that end, inaccuracies in force models exploited in processing GRACE data shall be taken into account when building GRACE noise covariance matrices.

5. The high-frequency content of GOCE gravity gradients implies, in particular, a potential ability of these data to detect large and localized mass transport signals. An example of such signals is the mass deformation caused by large earthquakes. Thus, an investigation shall be performed on GOCE mission's ability to detect and study mass redistribution caused by such events. To that end, the experience collected in the proposed methodology to validate global static gravity field models shall be used. That is, two sets of block-mean misfit gravity gradients shall be produced: before and after a considered earthquake, e.g., the one occurred in Japan in 2012. The conclusion shall be drawn by comparing the aforementioned two sets of block-mean misfit gravity gradients. The same analysis could also be applied to GRACE sets of misfit range combinations. This shall allow the abilities of the GRACE and GOCE missions to detect large earthquakes to be compared.
6. Validating DMT-2 with sets of independent data delivered by, e.g., satellite laser/radar altimetry missions.
7. Investigating the maximum spatial resolution achievable in the context of the GRACE-based time-varying gravity field modelling with an optimal filtering applied. To that end, time-varying gravity field models produced up to various maximum degrees shall be validated and compared by confronting them with independent data, such as satellite laser/radar altimetry measurements.
8. Developing tools to improve the quality of GRACE satellites' orbits to eliminate or mitigate the low-frequency noise in KBR data. A suggestion is to incorporate additional inputs, such as KBR measurements, into the orbit determination procedure.

Appendix A Linking 3-D average acceleration vectors to spherical harmonic coefficients

This appendix describes the link between 3-D average acceleration vectors $\bar{\mathbf{a}}(t)$ in an inertial frame, e.g., the CRF, and spherical harmonic coefficients. As it was pointed out in chapter 2, all data are cleaned from nuisance signals, which are associated with, e.g., tidal or non-gravitational perturbations. The reduced quantities are 3-D average gravitational acceleration vectors $\bar{\mathbf{g}}(t)$. To link them to spherical harmonic coefficients, the link between their point-wise counterparts $\mathbf{g}(t)$ and these coefficients needs to be first established. Assuming that spherical coordinates λ , ϕ and r are related to the satellite's centre of mass at the measurement time t , this link reads as follows:

$$\mathbf{g}(\lambda, \phi, r) = \mathbf{R}_{\text{LNOF} \rightarrow \text{CRF}} \nabla V(\lambda, \phi, r), \quad (\text{A.1})$$

where $\nabla V(\lambda, \phi, r)$ denotes the gradient of the gravitational potential in the spherical coordinate system. Given the representation of the gradient operator in the spherical coordinate system (Kellogg, 1929; Kreyszig, 1978), it reads as follows:

$$\nabla V(\lambda, \phi, r) = \begin{bmatrix} \frac{1}{r \cos \phi} \frac{\partial V}{\partial \lambda} \\ \frac{1}{r} \frac{\partial V}{\partial \phi} \\ \frac{\partial V}{\partial r} \end{bmatrix}, \quad (\text{A.2})$$

where

$$\begin{cases} \frac{\partial V}{\partial \lambda} \approx \frac{GM}{R} \sum_{n=0}^L \left(\frac{R}{r}\right)^{n+1} \sum_{m=0}^n (-m \bar{c}_{nm} \sin m\lambda + m \bar{s}_{nm} \cos m\lambda) \bar{P}_{nm}(\sin \phi) \\ \frac{\partial V}{\partial \phi} \approx \frac{GM}{R} \sum_{n=0}^L \left(\frac{R}{r}\right)^{n+1} \sum_{m=0}^n (\bar{c}_{nm} \cos m\lambda + \bar{s}_{nm} \sin m\lambda) \bar{P}'_{nm}(\sin \phi) \\ \frac{\partial V}{\partial r} \approx -\frac{GM}{R^2} \sum_{n=0}^L (n+1) \left(\frac{R}{r}\right)^{n+2} \sum_{m=0}^n (\bar{c}_{nm} \cos m\lambda + \bar{s}_{nm} \sin m\lambda) \bar{P}_{nm}(\sin \phi). \end{cases} \quad (\text{A.3})$$

The spherical coordinates λ , ϕ and r in Eq. (A.1) are defined with respect to a local Cartesian coordinate system to which it is often referred to as the Local North-Oriented Frame (LNOF): a right-handed frame whose origin coincides with the satellite's centre of mass and its axes point the North, West, and

upwards. The term $\mathbf{R}_{\text{LNOF} \rightarrow \text{CRF}}$ in Eq. (A.1) symbolises the rotation matrix from this frame into the inertial one:

$$\mathbf{R}_{\text{LNOF} \rightarrow \text{CRF}} = \mathbf{R}_{\text{LNOF} \rightarrow \text{TRF}} \mathbf{R}_{\text{TRF} \rightarrow \text{CRF}}, \quad (\text{A.4})$$

in which $\mathbf{R}_{\text{LNOF} \rightarrow \text{TRF}}$ denotes the rotation matrix from the LNOF into the TRF, i.e.,

$$\mathbf{R}_{\text{LNOF} \rightarrow \text{TRF}} = \begin{bmatrix} -\cos \lambda \sin \phi & \sin \lambda & \cos \lambda \cos \phi \\ -\sin \lambda \sin \phi & -\cos \lambda & \sin \lambda \cos \phi \\ \cos \phi & 0 & \sin \phi \end{bmatrix}. \quad (\text{A.5})$$

The matrix $\mathbf{R}_{\text{TRF} \rightarrow \text{CRF}}$ in Eq. (A.4) symbolizes the rotation from the TRF into the CRF, which can be computed based on the Earth's rotation parameters provided by the IERS (e.g., McCarthy and Petit, 2004).

Having the link between 3-D point-wise gravitational acceleration vectors with spherical harmonic coefficients established, the average counterparts of these accelerations can also be linked to these coefficients by obtaining an analytical expression for Eq. (2.3). To that end, let a sequence of 3-D point-wise gravitational acceleration vectors be assumed to be known in the time interval $[t - q\Delta t, t + q\Delta t]$ with step Δt where q is an integer number. These accelerations can be uniquely approximated as a polynomial of degree $2q$:

$$\mathbf{g}^{(i)}(t + s) = \sum_{j=0}^{2q} \mathbf{c}_j^{(i)}(t) s^j, \quad (\text{A.6})$$

where $s \in [-q\Delta t, q\Delta t]$, the scalar terms $\mathbf{c}_j^{(i)}(t)$ are the coefficients of the polynomial per vector component, and the scalar function $\mathbf{g}^{(i)}(t + s)$ represents one of the vector components of the point-wise acceleration vectors with i (being 1, 2, or 3) referring to the vector component. The coefficients $\mathbf{c}_j^{(i)}(t)$ can be found explicitly as the solution of a Vandermonde-type system of linear equations:

$$\mathbf{c}^{(i)} = \mathbf{V}^{-1} \mathbf{g}^{(i)}, \quad (\text{A.7})$$

with

$$\mathbf{c}^{(i)} = \left[\mathbf{c}_0^{(i)}(t) \quad \mathbf{c}_1^{(i)}(t) \quad \cdots \quad \mathbf{c}_{2q}^{(i)}(t) \right]^T, \quad (\text{A.8})$$

$$\mathbf{g}^{(i)} = \left[\mathbf{g}^{(i)}(t - q\Delta t) \quad \cdots \quad \mathbf{g}^{(i)}(t) \quad \cdots \quad \mathbf{g}^{(i)}(t + q\Delta t) \right]^T, \quad (\text{A.9})$$

and

$$\mathbf{V} = \begin{bmatrix} 1 & -q\Delta t & \cdots & (-q\Delta t)^{2q} \\ 1 & -(q-1)\Delta t & \cdots & -(q-1)\Delta t)^{2q} \\ \vdots & \vdots & & \vdots \\ 1 & q\Delta t & \cdots & (q\Delta t)^{2q} \end{bmatrix}. \quad (\text{A.10})$$

The substitution of Eq. (A.6) into Eq. (2.3) yields an analytical expression for integral (2.3) per vector component:

$$\begin{aligned}
\bar{\mathbf{g}}^{(i)}(t) &= \int_{-\Delta t}^{\Delta t} \frac{\Delta t - |s|}{(\Delta t)^2} \mathbf{g}^{(i)}(t+s) ds = \\
&= \int_{-\Delta t}^0 \frac{\Delta t + s}{(\Delta t)^2} \sum_{j=0}^{2q} \mathbf{c}_j^{(i)}(t) s^j ds + \int_0^{\Delta t} \frac{\Delta t - s}{(\Delta t)^2} \sum_{j=0}^{2q} \mathbf{c}_j^{(i)}(t) s^j ds = \\
&= \frac{1}{\Delta t} \sum_{j=0}^{2q} \mathbf{c}_j^{(i)}(t) \int_{-\Delta t}^{\Delta t} s^j ds + \frac{1}{(\Delta t)^2} \sum_{j=0}^{2q} \mathbf{c}_j^{(i)}(t) \int_{-\Delta t}^0 s^{j+1} ds - \frac{1}{(\Delta t)^2} \sum_{j=0}^{2q} \mathbf{c}_j^{(i)}(t) \int_0^{\Delta t} s^{j+1} ds = \\
&= \frac{1}{\Delta t} \sum_{j=0}^{2q} \frac{\mathbf{c}_j^{(i)}(t) s^{j+1}}{j+1} \Big|_{-\Delta t}^{\Delta t} + \frac{1}{(\Delta t)^2} \sum_{j=0}^{2q} \frac{\mathbf{c}_j^{(i)}(t) s^{j+2}}{j+2} \Big|_{-\Delta t}^0 - \frac{1}{(\Delta t)^2} \sum_{j=0}^{2q} \frac{\mathbf{c}_j^{(i)}(t) s^{j+2}}{j+2} \Big|_0^{\Delta t} = \\
&= \frac{1}{\Delta t} \sum_{j=0}^{2q} \frac{\mathbf{c}_j^{(i)}(t)}{j+1} \left((\Delta t)^{j+1} - (-\Delta t)^{j+1} \right) - \frac{1}{(\Delta t)^2} \sum_{j=0}^{2q} \frac{\mathbf{c}_j^{(i)}(t)}{j+2} \left((-\Delta t)^{j+2} + (\Delta t)^{j+2} \right) = \\
&= \sum_{j=0}^{2q} \mathbf{c}_j^{(i)}(t) \left(\frac{(\Delta t)^j + (-\Delta t)^j}{j+1} - \frac{(-\Delta t)^j + (\Delta t)^j}{j+2} \right) = \\
&= 2 \sum_{j=0}^{2q} \mathbf{c}_j^{(i)}(t) (\Delta t)^j p_j \left(\frac{1}{j+1} - \frac{1}{j+2} \right), \tag{A.11}
\end{aligned}$$

where $p_j = 1$ and $= 0$ for even and odd j 's, respectively (with $j = 0, 1, \dots$, and $2q$). Thus, the average acceleration vector per component can be analytically represented as follows:

$$\bar{\mathbf{g}}^{(i)}(t) = \mathbf{w}^T \mathbf{c}^{(i)}, \tag{A.12}$$

where

$$\mathbf{w} = \left[w_0 \quad w_1 \quad \dots \quad w_{2q} \right]^T \tag{A.13}$$

with $w_j = 2(\Delta t)^j \left(\frac{1}{j+1} - \frac{1}{j+2} \right)$ and $= 0$ for even and odd j 's, respectively. From Eqs. (A.7) and (A.12) it follows that the average acceleration vectors per component can be directly related to the vector of point-wise accelerations as:

$$\bar{\mathbf{g}}^{(i)}(t) = \mathbf{f}^T \mathbf{g}^{(i)}, \tag{A.14}$$

with

$$\mathbf{f} = (\mathbf{V}^T)^{-1} \mathbf{w} \tag{A.15}$$

being a vector composed of so-called “filter coefficients”. Importantly, these coefficients are constant. Thus, they can be computed just once. In my study, the order of the averaging filter is always chosen as 16 (i.e., $q = 8$). It has been shown by Ditmar and van Eck van der Sluijs (2004) that a higher order does not make any practical difference.

Appendix B Linking gravity gradients in the instrument frame to spherical harmonic coefficients

This appendix explains the links between GOCE measured gravity gradients in the GRF and spherical harmonic coefficients. Let x , y , and z respectively be the along-track, cross-track, and nadir axes of the GRF. Then, the links between measured gravity gradients in the GRF and spherical harmonic coefficients read as follows:

$$\begin{bmatrix} \frac{\partial^2 V}{\partial x^2} & \frac{\partial^2 V}{\partial x \partial y} & \frac{\partial^2 V}{\partial x \partial z} \\ \frac{\partial^2 V}{\partial x \partial y} & \frac{\partial^2 V}{\partial y^2} & \frac{\partial^2 V}{\partial y \partial z} \\ \frac{\partial^2 V}{\partial x \partial z} & \frac{\partial^2 V}{\partial y \partial z} & \frac{\partial^2 V}{\partial z^2} \end{bmatrix} = \mathbf{R}_{\text{LNOF} \rightarrow \text{GRF}} \mathbf{G}(\lambda, \phi, r) \mathbf{R}_{\text{LNOF} \rightarrow \text{GRF}}^T \quad (\text{B.1})$$

The left-hand side of this equation denotes the gravity gradient tensor measured by the GOCE satellite in the GRF. The term in the middle in the right-hand side of this equation is the gravity gradient tensor in the spherical coordinate system, which is associated with the LNOF (see Appendix A). Given the representation of the gradient operator in the spherical coordinate system (Kellogg, 1929; Kreyszig, 1978), this term reads as follows (Heiskanen and Moritz, 1967):

$$\mathbf{G}(\lambda, \phi, r) = \quad (\text{B.2})$$

$$\begin{bmatrix} \frac{1}{r^2 \cos^2 \phi} \frac{\partial^2 V}{\partial \lambda^2} + \frac{1}{r} \frac{\partial V}{\partial r} - \frac{\tan \phi}{r^2} \frac{\partial V}{\partial \phi} & \frac{1}{r^2 \cos \phi} \left(\frac{\partial^2 V}{\partial \lambda \partial \phi} + \tan \phi \frac{\partial V}{\partial \lambda} \right) & \frac{1}{r^2 \cos \phi} \left(r \frac{\partial^2 V}{\partial \lambda \partial r} - \frac{\partial V}{\partial \lambda} \right) \\ \frac{1}{r^2 \cos \phi} \left(\frac{\partial^2 V}{\partial \lambda \partial \phi} + \tan \phi \frac{\partial V}{\partial \lambda} \right) & \frac{1}{r^2} \frac{\partial^2 V}{\partial \phi^2} + \frac{1}{r} \frac{\partial V}{\partial r} & \frac{1}{r} \frac{\partial^2 V}{\partial \phi \partial r} - \frac{1}{r^2} \frac{\partial V}{\partial \phi} \\ \frac{1}{r^2 \cos \phi} \left(r \frac{\partial^2 V}{\partial \lambda \partial r} - \frac{\partial V}{\partial \lambda} \right) & \frac{1}{r} \frac{\partial^2 V}{\partial \phi \partial r} - \frac{1}{r^2} \frac{\partial V}{\partial \phi} & \frac{\partial^2 V}{\partial r^2} \end{bmatrix}. \quad (\text{B.3})$$

The second order derivatives of the gravitational potential in Eq. (B.3) can be obtained easily from Eq. (2.1):

$$\left\{ \begin{array}{l} \frac{\partial^2 V}{\partial \lambda^2} \approx \frac{GM}{r} \sum_{n=0}^L \left(\frac{R}{r}\right)^n \sum_{m=0}^n -m^2 (\bar{c}_{nm} \cos m\lambda + \bar{s}_{nm} \sin m\lambda) \bar{P}_{nm}(\sin \phi) \\ \frac{\partial^2 V}{\partial \phi^2} \approx \frac{GM}{r} \sum_{n=0}^L \left(\frac{R}{r}\right)^n \sum_{m=0}^n (\bar{c}_{nm} \cos m\lambda + \bar{s}_{nm} \sin m\lambda) \bar{P}_{nm}''(\sin \phi) \\ \frac{\partial^2 V}{\partial r^2} \approx \frac{GM}{r^3} \sum_{n=0}^L (n+1)(n+2) \left(\frac{R}{r}\right)^n \sum_{m=0}^n (\bar{c}_{nm} \cos m\lambda + \bar{s}_{nm} \sin m\lambda) \bar{P}_{nm}(\sin \phi) \\ \frac{\partial^2 V}{\partial \lambda \partial \phi} \approx \frac{GM}{r} \sum_{n=0}^L \left(\frac{R}{r}\right)^n \sum_{m=0}^n -m (\bar{c}_{nm} \sin m\lambda - \bar{s}_{nm} \cos m\lambda) \bar{P}_{nm}'(\sin \phi) \\ \frac{\partial^2 V}{\partial \lambda \partial r} \approx \frac{GM}{r^2} \sum_{n=0}^L (n+1) \left(\frac{R}{r}\right)^n \sum_{m=0}^n m (\bar{c}_{nm} \sin m\lambda - \bar{s}_{nm} \cos m\lambda) \bar{P}_{nm}(\sin \phi) \\ \frac{\partial^2 V}{\partial \phi \partial r} \approx \frac{GM}{r^2} \sum_{n=0}^L -(n+1) \left(\frac{R}{r}\right)^n \sum_{m=0}^n (\bar{c}_{nm} \cos m\lambda + \bar{s}_{nm} \sin m\lambda) \bar{P}_{nm}'(\sin \phi). \end{array} \right. \quad (\text{B.4})$$

The term $\mathbf{R}_{\text{LNOF} \rightarrow \text{GRF}}$ in Eq. (B.1) denotes the rotation matrix from the LNOF into GRF:

$$\mathbf{R}_{\text{LNOF} \rightarrow \text{GRF}} = \mathbf{R}_{\text{LNOF} \rightarrow \text{TRF}} \mathbf{R}_{\text{TRF} \rightarrow \text{CRF}} \mathbf{R}_{\text{CRF} \rightarrow \text{GRF}}. \quad (\text{B.5})$$

The first two rotation matrices in the right-hand side of this equation, namely, $\mathbf{R}_{\text{LNOF} \rightarrow \text{TRF}}$ and $\mathbf{R}_{\text{TRF} \rightarrow \text{CRF}}$, are already addressed in Appendix A. The last one, namely, $\mathbf{R}_{\text{CRF} \rightarrow \text{GRF}}$, offers frame transformation from the CRF into the GRF. This matrix can be computed from the quaternions provided by the GOCE attitude determination system.

Bibliography

- Albertella A, Rummel R (2009) On the spectral consistency of the altimetric ocean and geoid surface: a one-dimensional example, *J Geod*, 83: 805–815, doi: 10.1007/s00190-008-0299-5.
- Altamimi Z, Collilieux X, Métivier L (2011) ITRF2008: an improved solution of the international terrestrial reference frame, *J Geod*, 85: 457–473, doi: 10.1007/s00190-011-0444-4.
- Andersen OB, Knudsen P (2009) DNSC08 mean sea surface and mean dynamic topography models, *J Geophys Res*, 114, C11001, doi: 10.1029/2008JC005179.
- Bamber JL, Riva REM, Vermeersen BLA, LeBrocq AM (2009) Reassessment of the potential sea-level rise from a collapse of the West Antarctic ice sheet, *Science*, 324: 901–903, doi: 10.1126/science.1169335.
- Baur O, Sneeuw N (2011) Assessing Greenland ice mass loss by means of point-mass modeling: a viable methodology, *J Geod*, 85: 607–615, doi: 10.1007/s00190-011-0463-1.
- Baur O (2013) Greenland mass variation from time-variable gravity in the absence of GRACE, *Geophys Res Lett*, 40: 4289–4293, doi: 10.1002/grl.50881.
- Bettadpur S (2007) CSR Level-2 processing standards document for product release 04, GRACE 327-742, Revision 3.1.
- Bettadpur S (2012) CSR level-2 processing standards document for level-2 product release 05, GRACE 327-742.
- Beutler G, Jäggi A, Mervart L, Meyer U (2010a) The celestial mechanics approach: theoretical foundations, *J Geod*, 84: 605–624, doi: 10.1007/s00190-010-0401-7.
- Beutler G, Jäggi A, Mervart L, Meyer U (2010b) The celestial mechanics approach: application to data of the GRACE mission, *J Geod*, 84: 661–681, doi: 10.1007/s00190-010-0402-6.
- Beutler G, Jäggi A, Meyer U, Prange L, Bock H, Dach R, Mervart L (2011) Gravity field determination at AIUB: from CHAMP and GRACE to GOCE, *Geophys Res Abs*, 13, EGU2011-6174.

- Bock H, Jäggi A, Švehla D, Beutler G, Hugentobler U, Visser P (2007) Precise orbit determination for the GOCE satellite using GPS, *Adv Space Res*, 39: 1638–1647, doi: 10.1016/j.asr.2007.02.053.
- Bock H, Jäggi A, Meyer U, Visser P, van den IJssel J, van Helleputte T, Heinze M, Hugentobler U (2011) GPS-derived orbits for the GOCE satellite, *J Geod*, 85: 807–818, doi: 10.1007/s00190-011-0484-9.
- Bouman J, Koop R, Tscherning CC, Visser P (2004) Calibration of GOCE SGG data using high-low SST, terrestrial gravity data and global gravity field models, *J Geod*, 78: 124–137, doi: 10.1007/s00190-004-0382-5.
- Braitenberg C, Ebbing J (2009) The GRACE-satellite gravity and geoid fields in analysing large-scale, cratonic or intracratonic basins, *Geophysical Prospecting*, 57: 559–571, doi: 10.1111/j.1365-2478.2009.00793.x.
- Bruinsma SL, Marty JC, Balmino G, Biancale R, Förste C, Abrikosov O, Neumayer H (2010a) GOCE gravity field recovery by means of the direct numerical method, *Proceedings of the ESA Living Planet Symposium*, 28 June – 2 July, 2010, Bergen, Norway.
- Bruinsma SL, Lemoine J-M, Biancale R, Valès N (2010b) CNES/GRGS 10-day gravity field models (release 2) and their evaluation, *Adv Space Res*, 45: 587–601, doi: 10.1016/j.asr.2009.10.012.
- Burša M, Raděj K, Šíma Z, True SA, Vátrt V (1997) Determination of the geopotential scale factor from Topex/Poseidon satellite altimetry, *Studia geoph et geod*, 41: 203–216, doi: 10.1023/A:1023313614618.
- Burša M, Kenyon S, Kouba J, Šíma Z, Vátrt V, Vitek V, Vojtíšková M (2007) The geopotential value W_0 for specifying the relativistic atomic time scale and a global vertical reference system, *J Geod*, 81: 103–110, doi: 10.1007/s00190-006-0091-3.
- Case K, Kruizinga GLH, Wu S-C (2004) GRACE Level-1B data product user handbook, Jet Propulsion Laboratory, California Institute of Technology, JPL D-22027.
- Chao BF (2005) On inversion for mass distribution from global (time-variable) gravity field, *J Geodyn*, 39: 223–230, doi: 10.1016/j.jog.2004.11.001.
- Colombo OL (1984) The global mapping of gravity with two satellites, Netherlands Geodetic Commission, Publication on Geodesy, Delft, The Netherlands.

- Colombo OL (1986) Notes on the mapping of the gravity field using satellite data, in Sünkel H (ed.), *Mathematical and Numerical Techniques in Physical Geodesy*, Lecture notes in Earth Sciences, vol. 7, pp. 261–315, doi: 10.1007/BFb0010134.
- Dahle C, Flechtner F, Gruber C, König D, König R, Michalak G, Neumayer K-H (2012) GFZ GRACE level-2 processing standards document for level-2 product release 05, Technical Report STR12/02, doi: 10.2312/GFZ.b103-12020.
- Desai SD (2002) Observing the pole tide with satellite altimetry, *J Geophys Res*, 107(C11), 3186, doi: 10.1029/2001JC001224.
- Ditmar P, Klees R (2002) A method to compute the Earth's gravity field from SGG/SST data to be acquired by the GOCE satellite, Delft University Press, DUP Science, Delft, The Netherlands.
- Ditmar P, Klees R, Kostenko F (2003a) Fast and accurate computation of spherical harmonic coefficients from satellite gravity gradiometry data, *J Geod*, 76: 690–705, doi: 10.1007/s00190-002-0298-x.
- Ditmar P, Kusche J, Klees R (2003b) Computation of spherical harmonic coefficients from gravity gradiometry data to be acquired by the GOCE satellite: regularization issues, *J Geod*, 77: 465–477, doi: 10.1007/s00190-003-0349-y.
- Ditmar P, van Eck van der Sluijs AA (2004) A technique for modeling the Earth's gravity field on the basis of satellite accelerations, *J Geod*, 78: 12–33, doi: 10.1007/s00190-003-0362-1.
- Ditmar P, Kuznetsov V, van Eck van der Sluijs AA, Schrama E, Klees R (2006) DEOS_CHAMP-01C-70: a model of the Earth's gravity field computed from accelerations of the CHAMP satellite, *J Geod*, 79: 586–601, doi: 10.1007/s00190-005-0008-6.
- Ditmar P, Liu X (2007) Synergy of the GOCE and GRACE satellite missions, *Proceedings of the Third International GOCE User Workshop*, 6 – 8 November, 2006, ESA/ESRIN Frascati, Rome, Italy.
- Ditmar P, Klees R, Liu X (2007) Frequency-dependent data weighting in global gravity field modeling from satellite data contaminated by non-stationary noise, *J Geod*, 81: 81–96, doi: 10.1007/s00190-006-0074-4
- Ditmar P (2009) *Satellite Gravity and the Geosphere*, Lecture note, Delft University of Technology, Delft, The Netherlands.

- Ditmar P, Bezdek A, Liu X, Zhao Q (2009) On a feasibility of modeling temporal gravity field variations from orbits of non-dedicated satellites, in Sideris MG (ed.), *Observing our changing Earth*, International Association of Geodesy Symposia, vol. 133, pp. 307–313, doi: 10.1007/978-3-540-85426-5_36.
- Ditmar P, Liu X, Klees R, Revtova E, Vermeersen B, Riva R, Siemes C, Zhao Q (2010) Regular gravity field variations and mass transport in the Earth's system from DEOS models based on GRACE satellite data, in Mertikas SP (ed.), *Gravity, Geoid and Earth Observation*, International Association of Geodesy Symposia, vol. 135, pp. 595–602, doi: 10.1007/978-3-642-10634-7_79.
- Ditmar P, Teixeira da Encarnação J, Farahani HH (2012) Understanding data noise in gravity field recovery on the basis of inter-satellite ranging measurements acquired by the satellite gravimetry mission GRACE, *J Geod*, 86: 441–465, doi: 10.1007/s00190-011-0531-6.
- Dobslaw H, Flechtner F, Bergmann-Wolf I, Dahle C, Dill R, Esselborn S, Sasgen I, Thomas M (2013) Simulating high-frequency atmosphere-ocean mass variability for de-aliasing of satellite gravity observations: AOD1B RL05, *J Geophys Res*, 118: 3704–3711, doi: 10.1002/jgrc.20271.
- Drinkwater MR, Floberghagen R, Haagmans R, Muzi D, Popescu A (2003) GOCE: ESA's first Earth explorer core mission, *Space Sci Rev*, 00: 1–14.
- Farahani HH, Ditmar P, Klees R, Teixeira da Encarnação J, Liu X, Zhao Q, Guo J (2013a) Validation of static gravity field models using GRACE K-band ranging and GOCE gradiometry data, *Geophys J Int*, 194: 751–771, doi: 10.1093/gji/ggt149.
- Farahani HH, Ditmar P, Klees R, Liu X, Zhao Q, Guo J (2013b) The static gravity field model DGM-1S from GRACE and GOCE data: computation, validation and an analysis of GOCE mission's added value, *J Geod*, 87: 843–867, doi: 10.1007/s00190-013-0650-3.
- Farahani HH, Ditmar P, Klees R (2013c) Assessment of the added value of data from the GOCE satellite mission to time-varying gravity field modeling, *J Geod*, doi: 10.1007/s00190-013-0674-8 (in press).
- Fehringer M, Floberghagen R, Frommknecht B (2012) The status of the GOCE mission, *AGU Fall Meeting Abs*, G34A-01.
- Fey AL, Gordon D, Jacobs CS (2009) The second realization of the International Celestial Reference Frame by Very Long Baseline Interferometry,

- IERS Technical Note 35, Verlag des Bundesamtes für Kartographie und Geodäsie, Frankfurt am Main, Germany.
- Flechtner F (2007a) GFZ Level-2 processing standards document for product release 04, GRACE 327-743, GR-GFZ-STD-001.
- Flechtner F (2007b) AOD1B product description document for Product Releases 01 to 04, GRACE 327-750, GR-GFZ-AOD-0001.
- Flechtner F, Dahle C, Neumayer KH, König R, Förste C (2010) The release 04 CHAMP and GRACE EIGEN gravity field models, in Flechtner F, Gruber T, Güntner A, Mandea M, Rothacher M, Schöne T, Wickert J (eds.), *System Earth via Geodetic-Geophysical Space Techniques*, pp. 41–58, doi: 978-3-642-10228-8.
- Floberghagen R, Fehringer M, Lamarre D, Muzi D, Frommknecht B, Steiger C, Piñeiro J, da Costa A (2011) Mission design, operation and exploitation of the Gravity field and steady-state Ocean Circulation Explorer mission, *J Geod*, 85: 749–758, doi: 10.1007/s00190-011-0498-3.
- Földvály L, Švehla D, Gerlach C, Wermuth M, Gruber T, Rummel R, Rothacher M, Frommknecht B, Peters T, Steigenberger P (2005) Gravity model TUM-2Sp based on the energy balance approach and kinematic CHAMP orbits, in Reigber C, Lühr H, Schwintzer P, Wickert J (eds.), *Earth Observation with CHAMP – Results from Three Years in Orbit*, pp. 13–18, doi: 10.1007/3-540-26800-6_2.
- Förste C, Schmidt R, Stubenvoll R, Flechtner F, Meyer U, König R, Neumayer H, Biancale R, Lemoine J-M, Bruinsma S, Loyer S, Barthelmes F, Esselborn S (2008a) The GeoForschungsZentrum Potsdam/Groupe de Recherche de Géodésie Spatiale satellite only and combined gravity field models: EIGEN-GL04S1 and EIGEN-GL04C, *J Geod*, 82: 331–346, doi: 10.1007/s00190-007-0183-8.
- Förste C, Flechtner F, Schmidt R, Stubenvoll R, Rothacher M, Kusche J, Neumayer H, Biancale R, Lemoine J-M, Barthelmes F, Bruinsma S, König R, Meyer U (2008b) EIGEN-GL05C – A new global combined high-resolution GRACE-based gravity field model of the GFZ-GRGS cooperation, *Geophys Res Abs*, 10, EGU2008-A-03426.
- Förste C, Bruinsma S, Shako R, Marty J-C, Flechtner F, Abrikosov O, Dahle C, Lemoine J-M, Neumayer H, Biancale R, Barthelmes F, König R, Balmino G (2011) EIGEN-6 – A new combined global gravity field model including GOCE data from the collaboration of GFZ-Potsdam and

- GRGS-Toulouse, *Geophys Res Abs*, 13, EGU2011-3242-2, http://icgem.gfz-potsdam.de/ICGEM/documents/Foerste-et-al-EGU_2011-01.pdf.
- Gatti A, Reguzzoni M, Venuti G (2013) The height datum problem and the role of satellite gravity models, *J Geod*, 87: 15–22, doi: 10.1007/s00190-012-0574-3.
- van Gelderen M, Koop R (1997) The use of degree variances in satellite gradiometry, *J Geod*, 71: 337–343, doi: 10.1007/s001900050101.
- Gerlach C, Földvary L, Švehla D, Gruber T, Wermuth M, Sneeuw N, Frommknecht B, Oberndorfer H, Peters T, Rothacher M, Rummel R, Steigenberger P (2003) A CHAMP-only gravity field model from kinematic orbits using the energy integral, *Geophys Res Lett*, 30(20), 2037, doi: 10.1029/2003GL018025.
- Gerlach C, Rummel R (2013) Global height system unification with GOCE: a simulation study on the indirect bias term in the GBVP approach, *J Geod*, 87: 57–67, doi: 10.1007/s00190-012-0579-y.
- Goiginger H, Hock E, Rieser D, Mayer-Gurr T, Maier A, Krauss S, Pail R, Fecher T, Gruber T, Brockmann JM, Krasbutter I, Schuh W-D, Jaggi A, Prange L, Hausleitner W, Baur O, Kusche J (2011) The combined satellite-only global gravity field model GOCO02S, *Geophys Res Abs*, 13, EGU2011-10571, <http://www.goco.eu>.
- Gourdeau L, Lemoine JM, Rio M-H, Hernandez F (2003) Estimating mean dynamic topography in the tropical Pacific ocean from gravity and altimetry satellites, *Geophys Res Lett*, 30(20), 2062, doi: 10.1029/2003GL018200.
- Gruber T (2009) Evaluation of the EGM2008 gravity field by means of GPS-leveling and sea surface topography solutions, *Newton’s Bulletin BurGravimetricque International (BGI)/Int, Geoid Service (IGeS)*, ISSN 1810-8555, Issue 4, pp. 3–17.
- Gruber T, Rummel R, Abrikosov O, van Hees R (2010) GOCE Level 2 product data handbook, European Space Agency, GO-MA-HPF-GS-0110, Issue 4, Revision 3.
- Gruber T, Visser P, Ackermannm Ch, Hosse M (2011) Validation of GOCE gravity field models by means of orbit residuals and geoid comparisons, *J Geod*, 85: 845–860, doi: 10.1007/s00190-011-0486-7.
- Han S-C (2003) Efficient global gravity field determination from satellite-to-satellite tracking (SST), Technical Report No. 467, Ohio State University, Columbus, Ohio, USA.

- Han S-C (2004) Efficient determination of global gravity field from satellite-to-satellite tracking mission, *Celestial Mechanics and Dynamical Astronomy*, 88(1): 69–102, doi: 10.1023/B:CELE.0000009383.07092.1f.
- Han S-C, Shum CK, Matsumoto K (2005) GRACE observations of M2 and S2 ocean tides underneath the Filchner-Ronne and Larsen ice shelves, *Antarctica, Geophys Res Lett*, 32(20), doi: 10.1029/2005GL024296.
- Han S-C, Ditmar P (2008) Localized spectral analysis of satellite gravity fields for recovering time-variable mass redistributions, *J Geod*, 82: 423–430, doi: 10.1007/s00190-007-0194-5.
- Han S-C, Shum CK, Bevis M, Ji C, Kuo1 C-Y (2006) Crustal dilatation observed by GRACE after the 2004 Sumatra-Andaman earthquake, *Science*, 313: 658–662, doi: 10.1126/science.1128661.
- Han S-C, Sauber J, Riva REM (2011) Contribution of satellite gravimetry to understanding seismic source processes of the 2011 Tohoku-Oki earthquake, *Geophys Res Lett*, 38, L24312, doi: 10.1029/2011GL049975.
- Heiskanen WA, Moritz H (1967) *Physical Geodesy*, W. H. Freeman, San Francisco, USA.
- Hirt C, Gruber T, Featherstone WE (2011) Evaluation of the first GOCE static gravity field models using terrestrial gravity, vertical deflections and EGM2008 quasigeoid heights, *J Geod*, 85: 723–740, doi: 10.1007/s00190-011-0482-y.
- Horwath M, Lemoine J-M, Biancale R, Bourgogne S (2011) Improved GRACE science results after adjustment of geometric biases in the Level-1B K-band ranging data, *J Geod*, 85: 23–38, doi: 10.1007/s00190-010-0414-2.
- Ihde J, Wilmes H, Müller J, Denker H, Voigt C, Hosse M (2010) Validation of satellite gravity field models by regional terrestrial data sets, in Flechtner F, Gruber T, Güntner A, Mandea M, Rothacher M, Schöne T, Wickert J (eds.), *System Earth via Geodetic-Geophysical Space Techniques*, pp. 277–296, doi: 10.1007/978-3-642-10228-8_22.
- Jäggi A, Beutler G, Mervart L (2008) GRACE gravity field determination using the celestial mechanics approach – first results, IAG Symposium on Gravity, Geoid, and Earth Observation 2008, June 23 – 27 2008, Chania, Greece.
- Jäggi A, Beutler G, Meyer U, Prange L, Dach R, Mervart L (2009) AIUB-GRACE02S – Status of GRACE gravity field recovery using the celestial

- mechanics approach, IAG Scientific Assembly 2009, 31 August – 4 September, 2009, Buenos Aires, Argentina.
- Jäggi A, Beutler G, Mervart L (2010) GRACE gravity field determination using the celestial mechanics approach – first results, in Mertikas SP (ed.), *Gravity, Geoid and Earth Observation*, vol. 135, pp. 177–184, doi: 10.1007/978-3-642-10634-7_24.
- Jäggi A, Bock H, Prange L, Meyer U, Beutler G (2011) GPS-only gravity field recovery with GOCE, CHAMP, and GRACE, *Adv Space Res*, 47: 1020–1028, doi: 10.1016/j.asr.2010.11.008.
- Jäggi A, Beutler G, Meyer U, Prange L, Dach R, Mervart L (2012) AIUB-GRACE02S – Status of GRACE gravity field recovery using the celestial mechanics approach, in Kenyon S, Pacino MC, Marti U (eds.), *Geodesy for Planet Earth*, vol. 136, pp. 161–170, doi: 10.1007/978-3-642-20338-1_20.
- Jekeli C (1999) The determination of gravitational potential differences from satellite-to-satellite tracking, *Celestial Mechanics and Dynamical Astronomy*, 75: 85–101, doi: 10.1023/A:1008313405488.
- Jekeli C (2000) Heights, the Geopotential, and vertical datums, Technical Report No. 459, Ohio State University, Columbus, Ohio, USA.
- Keller W, Sharifi MA (2005) Satellite gradiometry using a satellite pair, *J Geod*, 78: 544–557, doi: 10.1007/s00190-004-0426-x.
- Kellogg OD (1929) *Foundations of potential theory*, Courier Dover Publications, ISBN 0486601447, 9780486601441.
- Kim J (2000) Simulation study of a low-low satellite-to-satellite tracking mission, PhD Thesis, Center for Space Research, The University of Texas at Austin, Texas, USA.
- Klees R, Broersen P (2002) How to handle colored noise in large least-squares problems – Building the optimal filter, Delft University Press, DUP Science, Delft, The Netherlands.
- Klees R, Ditmar P, Broersen P (2003) How to handle colored observation noise in large least-squares problems, *J Geod*, 76: 629–640, doi: 10.1007/s00190-002-0291-4.
- Klees R, Ditmar P (2004) How to handle colored noise in large least-squares problems in the presence of data gaps? in Sansò F (ed.), *V Hotine-Marussi Symposium on Mathematical Geodesy*, International Association of Geodesy Symposia, vol. 127, pp. 39–48, doi: 10.1007/978-3-662-10735-5_6.

- Klees R, Zapreeva EA, Winsemius HC, Savenije HHG (2007) The bias in GRACE estimates of continental water storage variations, *Hydrol Earth Syst Sci*, 11: 1227–1241, doi: 10.5194/hess-11-1227-2007.
- Klees R, Liu X, Wittwer T, Gunter BC, Revtova EA, Tenzer R, Ditmar P, Winsemius HC, Savenije HHG (2008a) A comparison of global and regional GRACE models for land hydrology, *Surv Geophys*, 29: 335–359, doi: 10.1007/s10712-008-9049-8.
- Klees R, Revtova EA, Gunter BC, Ditmar P, Oudman E, Winsemius HC, Savenije HHG (2008b) The design of an optimal filter for monthly GRACE gravity models, *Geophys J Int*, 175: 417–432, doi: 10.1111/j.1365-246X.2008.03922.x.
- Knudsen P, Bingham R, Andersen O, Rio M-H (2011) A global mean dynamic topography and ocean circulation estimation using a preliminary GOCE gravity model, *J Geod*, 85: 861–879, doi: 10.1007/s00190-011-0485-8.
- Koch K-R, Kusche J (2002) Regularization of geopotential determination from satellite data by variance components, *J Geod*, 76: 259–268, doi: 10.1007/s00190-002-0245-x.
- Kreyszig E (1978) *Introductory Functional Analysis with applications*, ISBN 0471507318, 9780471507314
- Kroes R, Montenbruck O, Bertiger W, Visser P (2005) Precise GRACE baseline determination using GPS, *GPS Solut*, 9: 21–31, doi: 10.1007/s10291-004-0123-5
- Kurtenbach E, Mayer-Gürr T, Eicker A (2009) Deriving daily snapshots of the Earth's gravity field from GRACE L1B data using Kalman filtering, *Geophys Res Lett*, 36, L17102, doi: 10.1029/2009GL039564.
- Kusche J (2003) A Monte-Carlo technique for weight estimation in satellite geodesy, *J Geod*, 76: 641–652, doi: 10.1007/s00190-002-0302-5.
- Kusche J, Klees R (2002) Regularization of gravity field estimation from gravity gradiometry data, *J Geod*, 76: 359–368, doi: 10.1007/s00190-002-0257-6.
- Kusche J (2007) Approximate decorrelation and non-isotropic smoothing of time-variable GRACE-type gravity field models, *J Geod*, 81: 733–749, doi: 10.1007/s00190-007-0143-3.
- Kusche J, Schmidt R, Petrovic S, Rietbroek R (2009) Decorrelated GRACE time-variable gravity solutions by GFZ, and their validation using a hydrological model, *J Geod*, 83: 903–913, doi: 10.1007/s00190-009-0308-3.

- Lemoine FG, Kenyon SC, Factor JK, Trimmer RG, Pavlis NK, Chinn DS, Cox CM, Klosko SM, Luthcke SB, Torrence MH, Wang YM, Williamson RG, Pavlis EC, Rapp RH, Olson TR (1998) The development of the joint NASA GSFC and the National Imagery and Mapping Agency NIMA geopotential model EGM96, Goddard Space Flight Center, National Aeronautics and Space Administration, NASA Technical Paper, NASA/TP-1998-206861, Greenbelt, Maryland, USA.
- Liu X (2008) Global gravity field recovery from satellite-to-satellite tracking data with the acceleration approach, PhD Thesis, Delft University of Technology, Delft, The Netherlands.
- Liu X, Ditmar P, Siemes C, Slobbe DC, Revtova E, Klees R, Riva R, Zhao Q (2010) DEOS Mass Transport model (DMT-1) based on GRACE satellite data: methodology and validation, *Geophys J Int*, 181: 769–788, doi: 10.1111/j.1365-246X.2010.04533.x.
- Losch M, Sloyan BM, Schröter J, Sneeuw N (2002) Box inverse models, altimetry and the geoid: Problems with the omission error, *J Geophys Res*, 107(C7), doi: 10.1029/2001JC000855.
- Luthcke SB, Zwally HJ, Abdalati W, Rowlands DD, Ray RD, Nerem RS, Lemoine FG, McCarthy JJ, Chinn DS (2006) Recent Greenland ice mass loss by drainage system from satellite gravity observations, *Science*, 314: 1286–1289, doi: 10.1126/science.1130776
- Lyard F, Lefevre F, Letellier T, Francis O (2006) Modelling the global ocean tides: modern insides from FES2004, *Ocean Dyn*, 56: 394–415, doi: 10.1007/s10236-006-0086-x.
- Mayer-Gürr T, Ilk KH, Eicker A, Feuchtinger M (2005) ITG-CHAMP01: a CHAMP gravity field model from short kinematic arcs over a one-year observation period, *J Geod*, 78: 462–480, doi: 10.1007/s00190-004-0413-2.
- Mayer-Gürr T (2006) Gravitationsfeldbestimmung aus der Analyse kurzer Bahnbögen am Beispiel der Satellitenmissionen CHAMP und GRACE, PhD Thesis, University of Bonn, Bonn, Germany.
- Mayer-Gürr T, Eicker A, Kurtenbach E, Ilk K-H (2010a) ITG-GRACE: Global static and temporal gravity field models from GRACE data, in Flechtner F, Gruber T, Güntner A, Manda M, Rothacher M, Schöne T, Wickert J (eds.), *System Earth via Geodetic-Geophysical Space Techniques*, pp. 159–168, doi: 10.1007/978-3-642-10228-8_13.

- Mayer-Gürr T, Eicker A, Kurtenbach E (2010b) ITG-Grace2010: The new GRACE gravity field release computed in Bonn, Geophys Res Abs, 12, EGU2010-2446.
- Mayer-Gürr T, Rieser D, Höck E, Brockmann JM, Schuh W-D, Krasbutter I, Kusche J, Maier A, Krauss S, Hausleitner W, Baur O, Jäggi A, Meyer U, Prange L, Pail R, Fecher T, Gruber T (2012) The new combined satellite only model GOCO03S, International Symposium on Gravity, Geoid and Height Systems (GGHS) 2012, Venice, Italy, <http://www.goco.eu>.
- McCarthy DD, Petit G (2004) IERS conventions (2003) IERS Technical Note 32, Verlag des Bundesamtes für Kartographie und Geodäsie, Frankfurt am Main, Germany.
- Meyer U, Jäggi A, Beutler G (2012) Monthly gravity field solutions based on GRACE observations generated with the Celestial Mechanics Approach, Earth and Planetary Science Letters, 345: 72–80, doi: 10.1016/j.epsl.2012.06.026.
- Migliaccio F, Reguzzoni M, Gatti A, Sansò F, Herceg M (2011) A GOCE-only global gravity field model by the space-wise approach, Proceedings of the Fourth International GOCE User Workshop, 31 March – 1 April, 2011, Munich, Germany.
- Montenbruck O, Gill E (2000) Satellite orbits: models, methods and applications, ISBN 978-3-642-58351-3.
- Montenbruck O, van Helleputte T, Kroes R, Gill E (2005) Reduced dynamic orbit determination using GPS code and carrier measurements, Aerospace Science and Technology, 9: 261–271, doi: 10.1016/j.ast.2005.01.003.
- Müller J (2003) GOCE gradients in various reference frames and their accuracies, Adv Geosci, 1: 33–38, doi: 10.5194/adgeo-1-33-2003.
- Nesvorný D, Šíma Z (1994) Refinement of the geopotential scale factor R_0 on the satellite altimetry basis, Earth, Moon and Planets, 65: 79–88, doi: 10.1007/BF00572201.
- Pail R, Goiginger H, Mayrhofer R, Schuh W-D, Brockmann JM, Krasbutter I, Höck E, Fecher T (2010a) Global gravity field model derived from orbit and gradiometry data applying the time-wise method, Proceedings of the ESA Living Planet Symposium, 28 June – 2 July, 2010, Bergen, Norway.
- Pail R, Goiginger H, Schuh W-D, Höck E, Brockmann JM, Fecher T, Gruber T, Mayer-Gürr T, Kusche J, Jäggi A, Rieser D (2010b) Combined satellite

- gravity field model GOCO01S derived from GOCE and GRACE, *Geophys Res Lett*, 37, L20314, doi: 10.1029/2010GL044906.
- Pail R, Bruinsma S, Migliaccio F, Förste C, Goiginger H, Schuh W-D, Höck E, Reguzzoni M, Brockmann JM, Abrikosov O, Veicherts M, Fecher T, Mayrhofer R, Krasbutter I, Sansò F, Tscherning CC (2011) First GOCE gravity field models derived by three different approaches, *J Geod*, 85: 819–843, doi: 10.1007/s00190-011-0467-x.
- Pavlis NK, Holmes SA, Kenyon SC, Factor JK (2008) An Earth gravitational model to degree 2160: EGM2008, *Geophys Res Abs*, 10, EGU2008-A-01891.
- Pavlis NK, Holmes SA, Kenyon SC, Factor JK (2012) The Development and Evaluation of the Earth Gravitational Model 2008 (EGM2008), *J Geophys Res*, doi: 10.1029/2011JB008916 (in press).
- Perosanz F, Marty JC, Balmino G (1997) Dynamic orbit determination and gravity field model improvement from GPS, DORIS and laser measurements on Topex/Poseidon satellite, *J Geod*, 71: 160–170, doi: 10.1007/s001900050084.
- Prange L, Jäggi A, Beutler G, Dach R, Mervart L (2008) Gravity field determination at the AIUB – The Celestial Mechanics Approach, in Sideris MG (ed.), *Observing our Changing Earth*, International Association of Geodesy Symposia, vol. 133, pp. 353–362, doi: 10.1007/978-3-540-85426-5_42.
- Rapp RH (1997) Use of potential coefficient models for geoid undulation determinations using a spherical harmonic representation of the height anomaly geoid undulation difference, *J Geod*, 71: 282–289, doi: 10.1007/s001900050096.
- Rapp RH, Jekeli C (1980) Accuracy of the determination of mean anomalies and mean geoid undulations from a satellite gravity field mapping mission, Technical Report No. 307, Ohio State University, Columbus, Ohio, USA.
- Reigber C (1989) Gravity field recovery from satellite tracking data, in Sansò F, Rummel R (eds.), *Theory of Satellite Geodesy and Gravity Field Determination*, Lecture Notes in Earth Sciences, vol. 25, pp. 197–234, doi: 10.1007/BFb0010552.
- Reigber C, Bock R, Förste C, Grunwaldt L, Jakowski N, Lühr H, Schwintzer P, Tilgner C (1996) CHAMP phase B executive summary, GFZ, STR96/13, Potsdam, Germany.
- Reigber C, Schwintzer P, Lühr H (1999) The CHAMP geopotential mission, *Boll Geof Teor Appl*, 40: 285–289.

- Reigber C, Balmino G, Schwintzer P, Biancale R, Bode A, Lemoine J-M, König R, Loyer S, Neumayer H, Marty J-C, Barthelmes F, Perosanz F, Zhu SY (2002) A high-quality global gravity field model from CHAMP GPS tracking data and accelerometry (EIGEN-1S), *Geophys Res Lett*, 29(14), doi: 10.1029/2002GL015064, 2002.
- Reigber C, Schwintzer P, Neumayer K-H, Barthelmes F, R König, Förste C, Balmino G, Biancale R, Lemoine J-M, Loyer S, Bruinsma S, Perosanz F, Fayard T (2003) The CHAMP-only Earth gravity field model EIGEN-2, *Adv Space Res*, 31: 1883–1888, doi: 10.1016/S0273-1177(03)00162-5.
- Reigber C, Jochmann H, Wunsch J, Petrovic S, Schwintzer P, Barthelmes F, Neumayer K-H., König R, Förste C, Balmino G, Biancale R, Lemoine J-M., Loyer S, Perosanz F (2004) Earth gravity field and seasonal variability from CHAMP, in Reigber C, Lühr H, Schwintzer P, Wickert J (eds.), *Earth Observation with CHAMP – Results from Three Years in Orbit*, pp. 25–30, 10.1007/3-540-26800-6_4.
- Reubelt T, Austen G, Grafarend EW (2003) Harmonic analysis of the Earth’s gravitational field by means of semi-continuous ephemerides of a low Earth orbiting GPS-tracked satellite, Case study: CHAMP, *J Geod*, 77: 257–278, doi: 10.1007/s00190-003-0322-9.
- Reubelt T, Götzelmann M, Grafarend EW (2006) Harmonic analysis of the Earth’s gravitational field from kinematic CHAMP orbits based on numerically derived satellite accelerations, in Flury J, Rummel R, Reigber C, Rothacher M, Boedecker G, Schreiber U (eds.), *Observation of the Earth System from Space*, pp. 27–42, doi: 10.1007/3-540-29522-4_3.
- Reubelt T, Baur O, Weigelt M, Roth M, Sneeuw N (2012) GOCE long-wavelength gravity field recovery from 1s-sampled kinematic orbits using the acceleration approach, *IAG Symposium on Gravity, Geoid and Height Systems*, 9 – 12 October 2012, Venice, Italy.
- Ricard Y, Chambat F, Lithgow-Bertelloni C (2006) Gravity observations and 3D structure of the Earth, *Comptes Rendus Geoscience*, 338: 992–1001, doi: 10.1016/j.crte.2006.05.013.
- Rio M-H, Hernandez F (2004) A mean dynamic topography computed over the world ocean from altimetry, in situ measurements, and a geoid model, *J Geophys Res*, 109, C12032, doi: 10.1029/2003JC002226.
- Rio M-H, Guinehut S, Larnicol G (2011) New CNES-CLS09 global mean dynamic topography computed from the combination of GRACE data,

- altimetry, and in situ measurements, *J Geophys Res*, 116, C07018, doi: 10.1029/2010JC006505.
- Rummel R (1979) Determination of short-wavelength components of the gravity field from satellite-to-satellite tracking or satellite gradiometry – an attempt to an identification of problem areas, *Man Geod*, 4: 107–148.
- Rummel R (1980) Geoid heights, geoid differences, and mean gravity anomalies from low-low satellite-to-satellite tracking – An error analysis, Technical Report No. 306, Ohio State University, Columbus, Ohio, USA.
- Rummel R, Yi W, Stummer C (2011) GOCE gravitational gradiometry, *J Geod*, 85: 777–790, doi: 10.1007/s00190-011-0500-0.
- Sandwell DT, Smith WHF (2009) Global marine gravity from retracked Geosat and ERS-1 altimetry: Ridge segmentation versus spreading rate, *J Geophys Res*, 114, B01411, doi: 10.1029/2008JB006008.
- Sasgen I, Martinec Z, Fleming K (2006) Wiener optimal filtering of GRACE data, *Studia Geophysica et Geodaetica*, 50: 499–508, doi: 10.1007/s11200-006-0031-y.
- Savcenko R, Bosch W (2012) EOT11a – Empirical ocean tide model from multi-mission satellite altimetry, Report No. 89, Deutsches Geodätisches Forschungsinstitut (DGFI), München, Germany.
- Schall J, Eicker A, Kusche J (2013) The ITG-Goce02 gravity field model from GOCE orbit and gradiometer data based on the short arc approach, *J Geod* (in review).
- Scharroo R, Visser P (1998) Precise orbit determination and gravity field improvement for the ERS satellites, *J Geophys Res*, 103(C4): 8113–8127, doi: 10.1029/97JC03179.
- Schutz BE, Tapley BD, Abusali PAM, Rim HJ (1994) Dynamic orbit determination using GPS measurements from Topex/Poseidon, *Geophys Res Lett*, 21(19), 2179–2182, doi: 10.1029/94GL01040.
- Siemes C, Haagmans R, Kern M, Plank G, Floberghagen R (2012) Monitoring GOCE gradiometer calibration parameters using accelerometer and star sensor data: methodology and first results, *J Geod*, 86: 629–645, doi: 10.1007/s00190-012-0545-8.
- Siemes C, Ditmar P, Riva REM, Slobbe DC, Liu X, Farahani HH (2013) Estimation of mass change trends in the Earth’s system on the basis of GRACE satellite data, with application to Greenland, *J Geod*, 87: 69–87, doi: 10.1007/s00190-012-0580-5.

- Slobbe DC, Simons FJ, Klees R (2012) The spherical Slepian basis as a means to obtain spectral consistency between mean sea level and the geoid, *J Geod*, 86: 609–628, doi: 10.1007/s00190-012-0543-x.
- Smith DA (1998) There is no such thing as “The” EGM96 geoid: Subtle points on the use of a global geopotential model, IGeS Bulletin No. 8, International Geoid Service, pp. 17–28, Milan, Italy.
- Standish EM (1998) JPL planetary and lunar ephemerides, DE405/LE405, Jet Propulsion Laboratory, IOM 312.F – 98 – 048.
- Süinkel H (2000) From Eötvös to mGal, Final report, ESA/ESTEC Contract 13392/98/NL/GD, European Space Agency, Noordwijk, The Netherlands.
- Swenson S, Wahr J, Milly PCD (2003) Estimated accuracies of regional water storage variations inferred from the Gravity Recovery and Climate Experiment (GRACE), *Water Resour Res*, 39(8), 1223, doi: 10.1029/2002WR001808.
- Swenson S, Wahr J (2006) Post-processing removal of correlated errors in GRACE data, *Geophys Res Lett*, 33, L08402, doi: 10.1029/2005GL025285.
- Tapley BD, Bettadpur S, Watkins M, Reigber C (2004a) The gravity recovery and climate experiment: Mission overview and early results, *Geophys Res Lett*, 31, L09607, doi: 10.1029/2004GL019920.
- Tapley BD, Bettadpur S, Ries JC, Thompson PF, Watkins MM (2004b) GRACE measurements of mass variability in the Earth system, *Science*, 305: 503–505, doi: 10.1126/science.1099192.
- Tapley BD, Ries JC, Bettadpur S, Chambers DP, Cheng MK, Condi F, Gunter B, Kang Z, Nagel P, Pastor R, Pekker T, Poole S, Wang F (2005) GGM02 – An improved Earth gravity field model from GRACE, *J Geod*, 79: 467–478, doi: 10.1007/s00190-005-0480-z.
- Tapley BD, Ries JC, Bettadpur S, Chambers D, Cheng M, Condi F, Poole S (2007) The GGM03 mean Earth gravity model from GRACE, AGU Fall Meeting Abs, G42A-03.
- Visser P, van den IJssel J, Van Helleputte T, Bock H, Jäggi A, Beutler G, Švehla D, Hugentobler U, Heinze M (2009) Orbit determination for the GOCE satellite, *Adv Space Res*, 43: 760–768, doi: 10.1016/j.asr.2008.09.016.
- Wahr J, Molenaar M, Bryan F (1998) Time variability of the Earth’s gravity field: Hydrological and oceanic effects and their possible detection using GRACE, *J Geophys Res*, 103(B12): 30205–30229, doi: 10.1029/98JB02844.

- van der Wal W, Wu P, Sideris MG, Shum CK (2008) Use of GRACE determined secular gravity rates for glacial isostatic adjustment studies in North-America, *J Geodyn*, 46: 144–154, doi: 10.1016/j.jog.2008.03.007.
- Watkin M, Ning YD (2007) JPL level-2 processing standards document for product release 04, GRACE 327-744.
- Watkin M, Ning YD (2012) JPL level-2 processing standards document for product release 05, GRACE 327-744.
- Weigelt M, van Dam T, Jäggi A, Prange L, Tourian MJ, Keller W, Sneeuw N (2013) Time-variable gravity signal in Greenland revealed by high-low satellite-to-satellite tracking, *J Geophys Res*, 118: 3848–3859, doi: 10.1002/jgrb.50283.
- de Witte S (2011) GOCE XML Parser, European Space Agency, GO-TN-HPF-GS-0192, Issue 2, Revision 7.
- Wittwer T (2009) Regional gravity field modelling with radial basis functions, PhD Thesis, Delft University of Technology, Delft, The Netherlands.
- Wouters B, Chambers D, Schrama EJO (2008) GRACE observes small-scale mass loss in Greenland, *Geophys Res Lett*, 35, L20501, doi: 10.1029/2008GL034816.
- Wunsch C, Gaposchkin EM (1980) On using satellite altimetry to determine the general circulation of the oceans with application to geoid improvement, *Rev Geophys*, 18: 725–745, doi: 10.1029/RG018i004p00725.
- Zhang, ZZ, Chao BF, Lu Y, Hsu H-T (2009) An effective filtering for GRACE time-variable gravity: Fan filter, *Geophys Res Lett*, 36, L17311, doi: 10.1029/2009GL039459.
- Zhao Q (2004) Research on precise orbit determination theory and software for both GPS navigation constellation and LEO satellites, PhD Thesis, Wuhan University, Wuhan, China.

Samenvatting

Het modeleren van het statische en tijdsvariabele aardse zwaartekrachtveld op basis van een combinatie van GRACE en GOCE data De belangrijkste focus van dit proefschrift is het op mondiale schaal modeleren van het statische en tijdsvariabele deel van het aardse zwaartekrachtveld op basis van data afkomstig van de Gravity Recovery And Climate Experiment (GRACE) en de Gravity field and the steady-state Ocean Circulation Explorer (GOCE) satellietmissies. Daarnaast wordt een nieuwe methode voorgesteld voor het valideren van mondiale zwaartekrachtveldmodellen. Verder is de toegevoegde waarde van GOCE data op de bepaling van het statische en tijdsvariabele zwaartekrachtveld vastgesteld. Ten laatste is de laagfrequente ruis in van GRACE K-band ranging (KBR) data afgeleide waarnemingen bestudeerd en is een nieuwe manier voorgesteld hoe met deze ruis om te gaan.

Modelering van het mondiale statische zwaartekrachtveld op basis van GRACE/GOCE: DGM-1S Een nieuw mondiaal statisch zwaartekrachtveldmodel met de naam DGM-1S (Delft Gravity Model, release 1, Satellite-only) is berekend uit een statistisch optimale combinatie van GRACE en GOCE data. Het model is gebaseerd op bijna zeven jaren GRACE KBR data, vier jaren kinematische banen van de GRACE satellieten, 14 maanden kinematische banen van de GOCE satelliet en 10 maanden GOCE Satelliet Gravity Gradiometry (SGG) data. De kinematische baan en KBR data zijn verwerkt met behulp van een variant op de versnellingsmethode, waarin deze data door middel van een 3-punt differentiatie zijn getransformeerd in respectievelijk “driedimensionale (3-D) gemiddelde versnellingsvectoren” en “afstandscombinaties” (\approx versnellingen tussen beide satellieten). Zwaartekrachtgradiënten zijn verwerkt in het referentiestelsel van het instrument. Stochastische modellen van de ruis in de data zijn berekend met een auto-regressive moving-average (ARMA) proces. Het gebruik van ARMA modellen garandeert (i) dat gekleurde ruis in de data op de juiste manier wordt meegenomen en (ii) dat alle data in statistisch optimale zin worden gecombineerd. DGM-1S is berekend tot sferisch harmonische graad 250, waarbij Kaula regularisatie is toegepast voor de coëfficiënten van graad 180 en hoger. Uit onze resultaten volgt (a) dat het gebruik van de GOCE kinematische banen niet tot een beter statisch zwaartekrachtveldmodel leidt als GRACE data en GOCE zwaartekrachtgradiënten ook worden meegenomen en (b) dat de bijdrage van de GOCE zwaartekrachtgradiënten zich in een

gecombineerd GRACE/GOCE model manifesteert boven graad 150. Ter validatie zijn de DGM-1S, GOCO01S, EIGEN-6S (alleen het statische deel) en de GOCO02S geoïde modellen gebruikt om modellen van de gemiddelde dynamische zee topografie te berekenen door ze af te trekken van het DNSC08 model van het gemiddelde zeeniveau. De resulterende modellen zijn vergeleken met het state-of-the-art CNES-CLS09 model van de gemiddelde dynamische zee topografie. Het model berekent met behulp van DGM-1S komt hier het beste mee overeen. Verder suggereren de resultaten dat de GRACE/GOCE modellen die uitsluitend gebaseerd zijn op satellietdata, boven graad 200 worden beïnvloed door een relatief sterke, hoogfrequente ruis. Daarnaast laten de tests zien dat er nog steeds problemen zijn met deze modellen in de Pacifische oceaan, waar aanzienlijke afwijkingen met EGM2008 zijn gedetecteerd.

Validatie van mondiale zwaartekrachtveldmodellen: kwantificatie van de toegevoegde waarde van GOCE en een onderzoek naar de optimaliteit van de datacombinatie in modellen die zijn berekend met oppervlakte data

De mate waarin satellietgravimetrie data geschikt is voor het valideren van mondiale modellen van het statische zwaartekrachtveld is onderzocht. Twee typen van data zijn voor de controle gebruikt: GRACE KBR data en GOCE zwaartekrachtgradiënten. De validatie is gebaseerd op een analyse van de verschillen tussen de waargenomen data en data gesynthetiseerd uit verschillende modellen waaronder het te valideren statische zwaartekrachtveldmodel. De methode is toegepast op acht modellen: EGM2008 (afgebroken bij graad 250), EIGEN-6C (alleen het statische deel en afgebroken bij graad 250), twee modellen uitsluitend gebaseerd op GRACE data (ITG-Grace03 en ITG-Grace2010s) en vier GRACE/GOCE modellen: GOCO01S, EIGEN-6S (alleen het statische deel), GOCO02S en DGM-1S. De validatie laat zien dat beide datatypen verschillen in de modelperformance waarneembaar maken, ondanks de veel kortere tijdsintervallen die de controle datasets bestrijken vergeleken met de tijdsintervallen van de datasets die zijn gebruikt in de berekening van de modellen. De KBR en SGG controle data laten voor EGM2008 relatief hoge onnauwkeurigheden zien in respectievelijk het frequentiebereik van 5 – 22 mHz (27 – 120 cycles-per-revolution, cpr) en het frequentiebereik van 10 – 28 mHz (54 – 150 cpr). De SGG dataset laat ook onnauwkeurigheden in het frequentiebereik van 25 – 37 mHz (135 – 200 cpr) zien van ITG-Grace2010s. De validatie in het ruimtedomein laat zien dat de performance van EGM2008 minder is dan die van de GRACE/GOCE modellen. Het kwadratisch gemiddelde van de verschillen (RMS) tussen de waargenomen en de uit modellen afgeleide zz componenten van de zwaartekrachtgradiënten laten een verschil van 76 – 83 % in performance zien in de continentale gebieden waar nauwelijks terrestrische zwaartekrachtdata voorhanden is (de Himalaya's, Zuid-Amerika

en Equatoriaal Afrika). Dit verschil wordt grotendeels verklaard door een informatieverlies van ITG-Grace03 toen in de berekening van EGM2008 dit model werd gecombineerd met terrestrische zwaartekrachtdata/satelliet altimetrie data. Verder zijn de ontdekte verschillen in performance 4 – 16 % in de continentale gebieden die een goede dekking hebben met deze data (Australië, Noord-Eurazië en Noord-Amerika) en 11 % in de oceanen. Deze verschillen zijn gerelateerd aan de toegevoegde waarde van de GOCE missie in het bepalen van het statische zwaartekrachtveld. Het is aangetoond dat EIGEN-6C ook informatie verliest op het moment dat alle data gecombineerd worden, maar wel in een mindere mate. In Zuid-Amerika, bijvoorbeeld, doet dit model het slechts 12 % slechter dan zijn tegenhanger EIGEN-6S dat berekend is op basis van uitsluitend satelliet data. De GRACE/GOCE modellen hebben in de continentale gebieden waar nauwelijks terrestrische metingen beschikbaar zijn een 23 – 36 % hogere nauwkeurigheid dan ITG-Grace2010s, wat is toegekend aan de toegevoegde waarde van de GOCE missie. We laten zien dat de gekwantificeerde toegevoegde waarde nagenoeg geheel zit in de coëfficiënten beneden graad 200. DGM-1S en GOCO02S laten bijna dezelfde performance zien ten opzichte van de GOCE controle zwaartekrachtgradiënten, niettegenstaande dat het eerste model een iets betere overeenkomst heeft met de KBR controle data. Beide modellen komen beter met beide typen controle data overeen dan EIGEN-6S.

Bepaling van de toegevoegde waarde van de GOCE missie voor de modelering van het tijdsvariabele zwaartekrachtveld Temporele zwaartekrachtveldvariëaties afgeleid uit KBR data lijden onder anderen aan een beperkte ruimtelijke resolutie en een relatief lage nauwkeurigheid van de oost-west componenten. Ik heb onderzocht of het bepalen van deze variëaties kan worden verbeterd door ook GOCE data te gebruiken. Om dit te onderzoeken heb ik maandelijkse oplossingen tot graad 120 berekend (i) uit alleen KBR data en (ii) door middel van een statistisch optimale combinatie van KBR data met GOCE kinematische banen en zwaartekrachtgradiënten. De impact van de GOCE data is geanalyseerd voor de ongefilterde oplossingen en de oplossingen verkregen na optimale anisotrope filtering. De impact in deze twee gevallen is totaal verschillend. In het geval van de ongefilterde oplossingen reduceert het toevoegen van GOCE data de ruis 1 – 2 ordes van grootte. Ik laat echter zien dat deze reductie een stabilisatie-effect is en niet is bepaald door het informatiegehalte van de GOCE data. Voor de gefilterde oplossingen blijft de impact in termen van gelijkwaardige water hoogten gemiddeld genomen op sub-millimeter niveau. Maximaal is de impact 1 cm. Dit geldt zowel voor de gecombineerde impact van de GOCE kinematische banen en de GOCE zwaartekrachtgradiënten als voor de impact van deze datatypen

afzonderlijk. De relatieve impact is niet groter dan 5 – 7 % van de signaalamplitude, omdat de impact altijd zichtbaar is op de locaties waar het tijdsvariabele zwaartekrachtssignaal sterk is. Niettemin zie ik er niet van af te concluderen dat de toegevoegde waarde van GOCE data voor het bepalen van temporale zwaartekrachtveldveranderingen altijd verwaarloosbaar is. En aantal scenario's zijn besproken waarin de impact van GOCE data groter zou kunnen zijn dan is gekwantificeerd in deze situatie.

Modelering van tijdsvariaties in het mondiale zwaartekrachtveld:

DMT-2 Het Delft Mass Transport model, release 2 (DMT-2) is net als zijn voorganger (DMT-1) berekend uit GRACE KBR data. Het model bestaat uit een tijdreeks van 94 maandelijks oplossingen (februari 2003 – december 2010). Elke oplossing (ongefilterd en gefilterd) bestaat uit sferisch harmonische coëfficiënten tot graad 120 en is uitgedrukt ten opzichte van DGM-1S. De verbeteringen toegepast in de berekening van dit model ten opzichte van zijn voorganger DMT-1 zijn: (i) een verbeterde schatting en eliminatie van de laagfrequente ruis in de residuele afstandscombinaties, zodat sterke massatransport signalen niet worden gedempt, (ii) een verbeterde frequentieafhankelijke weging van de data waardoor het mogelijk is om oplossingen te berekenen die statistisch optimaal zijn, (iii) het gebruik van release 2 van de GRACE level-1B data, (iv) het gebruik van een recent berekend, a priori statisch zwaartekrachtveldmodel, namelijk DGM-1S, (v) het gebruik van release 5 van het AOD1B model van niet-getijde massaherverdeling in de atmosfeer en de oceanen, (vi) het gebruik van het recent berekende oceaan getijmodel EOT11a, (vii) een verbeterde kalibratie van de versnellingsmeters die zich in de GRACE satellieten bevinden. Het is aangetoond dat DMT-2 zijn voorganger ver achter zich laat in termen van ruimtelijke resolutie, wat bewezen is veroorzaakt te zijn door de geavanceerdere frequentieafhankelijke weging van de data. Verder is het bevestigd dat het gebruik van release 2 van de GRACE level-1B data leidt tot een eliminatie van de artefacten in oost-west richting. Ten laatste laten we zien dat voor de maandelijks zwaartekrachtveldmodelering de keuze van een maximale sferisch harmonische graad lager dan 120 kan leiden tot een onderschatting van de signaalamplitude en de aanwezigheid van het zogenoemde “Gibbs” fenomeen in de buurt van gebieden waar sterke massavariaties optreden. Echter, de hoge ruimtelijke resolutie van modellen berekent tot graad 120 kan bijna volledig worden toegekend aan de optimale filtering en is niet te danken aan het informatiegehalte in de ongefilterde sferisch harmonische coëfficiënten.

De bijdragen in dit proefschrift De belangrijkste bijdragen van dit proefschrift zijn:

1. Berekening van een nieuw mondiaal zwaartekrachtveldmodel met een competitieve kwaliteit.
2. Ontwikkeling van een nieuwe methode om mondiale statische zwaartekrachtveldmodellen te valideren.
3. Het kwantificeren van de toegevoegde waarde van de GOCE missie aan het modeleren van het statische en tijdsvariabele zwaartekrachtveld.
4. Onderzoeken in hoeverre de combinatie van data in modellen die zijn berekend op basis van zowel satelliet gravimetrie en oppervlakte data optimaal is. Dit baant de weg voor de ontwikkeling van betere strategieën om satelliet en oppervlakte gravimetrische data met elkaar te combineren in het berekenen van toekomstige modellen.
5. Berekening van een nieuw model van de tijdvariaties in het zwaartekrachtveld uit GRACE data, DMT-2.
6. Het laten zien van het belang van een nauwkeurige berekening, en het op de juiste manier benutten van statistische modellen van de ruis in satelliet gravimetrie data in de context van modellering van het mondiale zwaartekrachtveld.
7. Het achterhalen van de oorsprong van de laagfrequente ruis in GRACE KBR data en het voorstellen van een nieuwe manier om hiermee om te gaan.

Acknowledgements

First and foremost, I wish to express my sincere gratitude to my co-promotor and daily supervisor, P. Ditmar, who continually supported me in the course of my research with his remarkable patience and solid knowledge. His critical remarks and detailed corrections helped me tremendously to improve the quality of the thesis and of the articles that I took the lead to write in the framework of my thesis. Words simply fail to express how grateful I am for those inputs. Additionally, his inversion software built in the context of global gravity field modelling using satellite gravimetry data proved essential in my research.

I would like to thank my promotor, R. Klees, for providing me with the opportunity to carry out this research and for his continuous support. His critical remarks in various periodical progress meetings proved essential in guiding the research. In addition, his software built and documented in (Klees and Broersen, 2002) for a parameterization of stochastic properties of colored noise in data played a key role in my research.

I am thankful to the members of the doctoral committee for evaluating the dissertation and for their constructive recommendations, which helped me to enhance the thesis.

The Nederlandse organisatie voor Wetenschappelijk Onderzoek (Netherlands Organisation for Scientific Research, NWO) is gratefully acknowledged for financing my research. The Stichting Nationale Computerfaciliteiten (National Computing Facilities Foundation, NCF) supported the research by providing the high-performance computing facilities. This support is gratefully acknowledged as well.

I wish to extend my gratitude to X. Liu and C. Siemes (formerly at Delft University of Technology), who graciously shared their knowledge with me and provided me with invaluable suggestions. Q. Zhao and J. Guo (GNSS Research Centre of Wuhan University) are gratefully acknowledged for computing and providing kinematic and reduced-dynamic orbits of the GRACE satellites in the time interval January 2006 – December 2010. I am grateful to Q. Zhao also for his PANDA (Positioning And Navigation Data Analyst) software, which I used to compute dynamic orbit of the GRACE satellites in my research. I am thankful to D. C. Slobbe (Delft University of Technology) for proofreading the summary of the thesis and for a careful translation of it and of the propositions of the thesis into Dutch. I would like to acknowledge P. Inacio (Delft University of Technology) for upgrading the global ocean tide model in the PANDA software and implementing an improved calibration

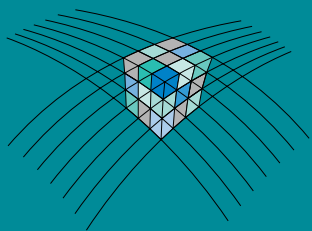
of GRACE satellites' accelerometers within this software, when I processed GRACE KBR data in the course of production of DMT-2. I wish to thank J. Teixeira da Encarnação (Delft University of Technology) for mutually beneficial collaborations, which were reflected in two articles, which I have addressed in the preface of chapters 4 and 9.

The GRACE level-1B data were provided by the Jet Propulsion Laboratory, JPL, whereas the GOCE level-2 data by the European Space Agency, ESA. The reduced-dynamic orbits of the GRACE satellites in the time interval February 2003 – December 2005 were provided by P. Visser, R. Kroes, and T. van Helleputte (Delft University of Technology). The transformation of GRACE KBR data into range combinations was done with a collection of codes created by X. Liu in the course of (Liu, 2008). The optimal anisotropic filtering of GRACE-based time-varying gravity field models was performed with a software built by C. Siemes in the course of production of the DMT-1 model (Liu et al., 2010). The synthesis of global static gravity field models into geoid ones, executed in the validation of these models on the basis of a control model of the oceanic mean dynamic topography, was performed with the GEOPOT07 software (Smith, 1998). The DNSC08 model of the mean sea surface, which I exploited to transform these synthesized geoid models into models of the oceanic mean dynamic topography, was provided by the National Space Institute of Technical University of Denmark. The CNES-CLS09 model of the oceanic mean dynamic topography, which I utilized as a control in a validation of global static gravity field models, was provided by the AVISO data services. These supports are gratefully acknowledged and highly appreciated.

Last but not least, I would like to express my appreciation to my family, particularly my parents and my sisters, for their love, continuous support, and encouragement in the course of the years of my research. For that, I am grateful forever.

Curriculum vitae

Hassan H. Farahani was born in Tehran, Iran in May the 3rd 1980. He received his B.Sc. degree in Civil and Surveying Engineering from University of Tabriz, Tabriz, Iran (September 2001 – September 2003), and later his M.Sc. degree in Geodesy from University of Tehran, Tehran, Iran (September 2001 – September 2003). His M.Sc. thesis was defended on August 2003 and awarded with honor. In January 2009, he started his Ph.D. research in Geodesy under the supervision of Dr. P. Ditmar and Prof. Dr.-Ing. habil. R. Klees at the section of Physical and Space Geodesy at Delft University of Technology, Delft, the Netherlands. Since April 2013, he has been a post-doctoral researcher in Geodesy at the same research group. In the framework of his postdoctoral research, he is involved in a project dedicated to regional geoid modelling, which is being led by Prof. Dr.-Ing. habil. R. Klees.



KONINKLIJKE NEDERLANDSE
AKADEMIE VAN WETENSCHAPPEN